UNIVERSITY OF OKLAHOMA

GRADUATE COLLEGE

EFFECTS OF EQUIVALENCE RATIO AND IODINE NUMBER ON NO_X EMISSIONS FROM THE FLAMES OF BIOFUELS AND HYDROCARBONS

A DISSERTATION

SUBMITTED TO THE GRADUATE FACULTY

in partial fulfillment of the requirements for the

Degree of

DOCTOR OF PHILOSOPHY

By

NORMAN DON LOVE JR.
Norman, Oklahoma
2009

EFFECTS OF EQUIVALENCE RATIO AND IODINE NUMBER ON NO_X EMISSIONS FROM FLAMES OF BIOFUELS AND HYDROCARBONS

A DISSERTATION APPROVED FOR THE
SCHOOL OF AEROSPACE AND MECHANICAL ENGINEERING

BY

_____
Dr. S.R. Gollahalli (Co-chair)

_____
Dr. R.N Parthasarathy (Co-chair)

_____
Dr. M. C. Altan

_____
Dr. D. V. Papavassiliou

_____
Dr. A.R. Choudhuri

"*Instruct a wise man and he will be wiser still;*
teach a righteous man and he will add to his learning"
Proverbs 9:9 (New International Version)

Acknowledgements

I would first like to thank God who has blessed me with physical health, financial support, mental strength, and the people around me who have made this dissertation possible.

One of the most important people who have made this dissertation possible and supported me continuously over the past three years is my wife. She has helped me in many ways, whether it was late nights eating dinner in the lab, helping to run experiments, proof reading papers, or just listening. She has always encouraged me and for these things I am thankful. I would also like to thank my father who has acted as a 'sixth member' in my committee. He helped guide me through the beginning of the program, listened to me, always provided wise council by sharing of his experiences, and helped me in many more ways than I can describe. I would also like to thank my mother for being a model of hard work and dedication. She attended graduate school and held a full-time job while I have been in Oklahoma, her continued success and love has helped motivate me to finish.

Next I would like to extend my thanks to my committee chair Professor Gollahalli for his guidance and for allowing me the opportunity to succeed. Over the last four years he has not only sharpened my technical abilities but has also taught me valuable lessons which I can carry out of the program and apply to all aspects of life. From these lessons I believe I have grown a great deal, albeit painfully at times. I also thank Professor Gollahalli for financially supporting me

over the past four and a half years, allowing me to focus solely on the completion of the degree. I thank my committee chair Professor Parthasarathy who has shown me what it is to be dedicated and passionate about teaching. His understanding of engineering principles and mathematics has helped me throughout the program and will stay with me after I leave. I also thank Professor Parthasrathy for his guidance and advice throughout my degree. I believe both my advisors have shown me how to effectively communicate through writing and speaking and I thank them for that as well. Next I would like to thank Dr. Ahsan Choudhuri from the University of Texas at El Paso and my other committee members Professor Altan and Professor Papavassiliou for their participation, time, and comments on this dissertation.

A special thank you to the students of the combustion lab past and present who have also helped through their friendships and technical discussions with me, these include: Dr. Chendhil Periasamy, Mr. Jaime Erazo, Mr. Pablo Barajas, Mr. Axzel Sequera, Mr. Carlos Mendez, Mr. Balasaheb Dahifale, Mr. Vinay Singh, Mr. Cristian Aldana, and Mr. Nikhil Dhamale.

I also thank the Aerospace and Mechanical Engineering Machine Shop Billy Mayes and Greg Williams for their ability to construct and machine excellent quality products both for this project and for the Combustion Laboratory.

Finally, the financial support provided by the Secretary Oklahoma Department of Energy, the U.S. Department of Education through the Graduate Assistance in Areas of National Need Fellowship, and the John Zink Company is gratefully acknowledged.

Table of Contents

Acknowledgements iv
Table of Contents vi
List of Tables ix
List of Figures x
Abstract xvi

Chapter 1 Introduction and Background

1.1 Diesel Fuel 3
1.2 Biodiesel Fuel 4
1.2.1 Transesterification 5
1.3 Dodecane and Methyl Stearate Fuels 7
1.4 Brief Description of Combustion in a Diesel Engine 9
1.5 Literature Review 11
1.5.1 Diesel and Biodiesel Combustion in Engines 11
1.5.2 Diesel and Biodiesel Flames 15
1.5.3 Numerical Studies of Biodiesel Combustion 17
1.6 Significane of NO_x 19
1.7 Project Impact 21
1.8 Objectives 23
1.9 Organization of the Dissertation 25

Chapter 2 Experimental Setup and Procedure

2.1 Laboratory Combustion Chamber 30
2.2 Burner and Fuel Delivery System 31
2.3 Instrumentation 33
2.3.1 Flame Visualization 33
2.3.2 Temperature Profiles 34
2.3.3 Global Emissions/In-Flame Species Concentration Profiles 35
2.3.4 Radiative Emissions 37
2.3.5 PLIF Instrumentation 39
2.3.6 Soot Volume Fraction Measurements 42
2.4 Stoichiometric Calculations 44
2.5 Reynolds Number Calculations 45
2.6 Description of Test Matrix 46

Chapter 3 Development of Experimental Technique

3.1 Burner and Fuel Delivery System Development 55
3.1.1 Flat Flame Burner 56
3.1.2 Counter Flow Burner 57
3.1.3 Bunsen Burner 58
3.1.4 Tubular Burner 59
3.1.5 Heating the Setup 60
3.1.6 Fuel delivery System Development 61
3.2 Effect of Liquid Fuel Injection Rate 63
3.3 Effect of Methane in Fuel of Flames 64
3.4 Validation of Experimental Setup 66
3.4.1 Radiative Fraction 66
3.4.2 Comparison with Published Values of Emission Index 68
3.4.3 Equivalence Ratio 70
3.5 Chapter Summary 71

Chapter 4 Global Flame Properties

4.1 Flame Appearance and Length 83
4.1.1 Effect of Equivalence Ratio 83
4.1.2 Effect of Iodine Number on Flame Length 86
4.2 Radiative Fraction 87
4.2.1 Effect of Equivalence Ratio 87
4.2.2 Effect of Iodine Number on Radiative Heat Fraction 90
4.3 Emission Index Results 91
4.3.1 Effect of Equivalence Ratio on NO Emission 91
4.3.2 Effect of Iodine Number on NO Emission 93
4.3.3 Effect of Equivalence Ratio on CO Emission 94
4.3.4 Effect of Iodine Number on CO Emission 96
4.4 Chapter Conclusions 97

Chapter 5 Flame Structure

5.1 Temperature Profiles 109
5.1.1 Effect of Equivalence Ratio on Temperature 109
5.1.2 Effect of Iodine Number on Temperature 114
5.2 Soot Volume Fraction 116
5.2.1 Effect of Equivalence Ratio on Soot Volume Fraction 117
5.2.2 Effect of Iodine Number on Soot Volume Fraction 121
5.3 Intermediate Species Concentrations 122
5.3.1 OH Radical Distributions 122
5.3.2 CH Radical Distributions 127
5.4 In-Flame Species Concentration Profiles 131
5.4.1 Nitric Oxide (NO) 131
5.4.2 Carbon Monoxide (CO) 135

5.4.3 Carbon Dioxide (CO_2) 137
5.4.4 Oxygen (O_2) 139
5.5 Liquid and Vapor Biofuel Flames 141
5.6 Chapter Conclusions 142

Chapter 6 Computational Results

6.1 Governing Equations 213
6.1.1 Model Assumptions 213
6.1.2 Continuity and Momentum Equations 214
6.1.3 Energy Equation 215
6.1.4 Species Transport Equation 216
6.1.5 Equilibrium Calculations 217
6.1.6 Non-Equilibrium Calculations 218
6.2 Reaction Models 220
6.3 Grid Development 222
6.4 Results 224
6.4.1 Dodecane Equilibrium Model 225
6.4.2 Biodiesel Equilibrium Model 228
6.4.3 Non- Equilibrium Model 230
6.5 Chapter Summary and Conclusions 233

Chapter 7 Summary and Conclusions

7.1 Summary of Results 255
7.1.1 Development of Experimental Technique 257
7.1.2 Primary Mechanism of Formation of NO 258
7.2 Conclusions 260
7.3 Practical Implications 262
7.4 Recommendations for Further Study 263

References 264

Appendix A 271

Appendix B 273

Appendix C 275

Appendix D 278

Appendix E 280

Appendix F 283

List of Tables

Table 1.1: Composition and properties of No. 2 diesel fuel 27
Table 1.2: Composition and properties of B100 biodiesels soy methyl ester and canola methyl ester 27
Table 1.3: Composition and properties of n-dodecane and methyl state 28
Table 2.1 Parts and Instrumentation used for the present study 47
Table 2.2 Stoichiometric air/fuel ratio calculated by mass for all fuels tested 48
Table 2.3 Nominal Experimental Conditions 48
Table 2.4 Estimated experimental uncertainties 48
Table 2.5a Test Matrix (Global Properties) 49
Table 2.5b Test Matrix (Flame Structure Measurements) 49
Table 3.1 Composition and properties of other tested fuels 73
Table 3.2 Nominal operating conditions for Mode 1 and Mode 2 73
Table 3.3 Comparison of present experimental results to those in literature 74
Table 3.4 Equivalence ratios for fuels tested at both flow rates under mode 2 condition 75
Table 5.1 Adiabatic flame temperature of all fuels at stoichiometry 144
Table 6.1 Material Properties for fuel mixture with air 234
Table 6.2 Under - Relaxation Parameters 234
Table 6.3 Discretization Methods 234
Table 6.4 Boundary Conditions 235

List of Figures

Chapter 1 Introduction and Background

Figure 1.1: Transesterification process 29
Figure 1.2: Example reactor for biodiesel production 29

Chapter 2 Experimental Setup and Procedure

Figure 2.1 Laboratory combustion chamber and fuel supply train 50
Figure 2.2 Schematic diagram of the experimental setup with burner 51
Figure 2.3 Schematic drawing of the thermocouple and traverse used for temperature measurements 51
Figure 2.4 Schematic diagram of the global emissions sampling setup and quartz probe 52
Figure 2.5 Schematic diagram of in-flame emissions experimental setup and water cooled stainless steel probe 52
Figure 2.6 Top view drawing of the global radiative emission setup 53
Figure 2.7 Experimental setup for PLIF measurements 53
Figure 2.8 Schematic drawing of experimental setup used for soot volume fraction measurements 54

Chapter 3 Development of Experimental Technique

Figure 3.1 Digital camera photographs (not shown to scale) of the four burners considered: a) flat flame burner, b) counter flow burner, c) Bunsen burner, and d) tubular burner 76
Figure 3.2 Schematic drawing of the initial experimental setup 77
Figure 3.3 Schematic drawing of the final experimental setup 77
Figure 3.4 Example radiative heat flux for CME and diesel for an average manual injection flow rate of 2 cm^3/min 78
Figure 3.5 Example radiative heat flux for CME and diesel for syringe pump injection flow rate of 0.82 cm^3/min 79
Figure 3.6 Radiative heat fraction plotted against liquid fuel flow rate for No. 2 Diesel and CME for Mode 1 and Mode 2 conditions 79
Figure 3.7 Radiative fraction of heat release for four fuels at (top) 0.82 cm^3/min and (bottom) 1.60 cm^3/min in comparison to values available in literature 80
Figure 3.8 Visible flame images for tested fuels under mode 2 conditions at 0.82 cm^3/min 80
Figure 3.9 EI NO and EI CO for diesel, CME, Pentane, and Heptane 81

Chapter 4 Global Flame Properties

Figure 4.1 Digital photograph of all fuels tested at ϕ = 1.2 with scale (exposure time of 1/25 seconds) 99
Figure 4.2 Digital photograph of all fuels tested at ϕ = 2 with scale (exposure time of 1/25 seconds) 100
Figure 4.3 Digital photograph of all fuels tested at ϕ = 3 with scale (exposure time of 1/25 seconds) 101
Figure 4.4 Digital photograph of all fuels tested at ϕ = 7 with scale (exposure time of 1/25 seconds) 102
Figure 4.5 Measured visible flame length for all fuels at ϕ = 1.2, 2, 3, and 7 103
Figure 4.6 Visible flame length plotted against iodine number at ϕ = 1.2, 2, 3, and 7 103
Figure 4.7 Radiative heat fraction (F) values at ϕ = 1.2, 2, 3, and 7 for all fuels tested 104
Figure 4.8 Radiative heat fraction plotted against iodine number for ϕ = 1.2, 2, 3, and 7 104
Figure 4.9 EINO for all fuels tested at ϕ = 1.2, 2, 3, and 7 105
Figure 4.10 EINO plotted against iodine number for ϕ = 1.2, 2, 3, and 7 105
Figure 4.11 EICO for all fuels tested at ϕ = 1.2, 2, and 3 106
Figure 4.12 EICO for all fuels at ϕ = 7 106
Figure 4.13 EICO plotted against iodine number for ϕ = 1.2, 2, 3, and 7 107

Chapter 5 Flame Structure

Figure 5.1 Temperature profiles of diesel at ϕ =1.2 144
Figure 5.2 Temperature profiles of diesel at ϕ =2 145
Figure 5.3 Temperature profiles of diesel at ϕ =3 145
Figure 5.4 Temperature profiles of diesel at ϕ =7 146
Figure 5.5 Temperature profiles of CME at ϕ =1.2 146
Figure 5.6 Temperature profiles of CME at ϕ =2 147
Figure 5.7 Temperature profiles of CME at ϕ =3 147
Figure 5.8 Temperature profiles of CME at ϕ =7 148
Figure 5.9 Temperature profiles of SME at ϕ =1.2 148
Figure 5.10 Temperature profiles of SME at ϕ =2 149
Figure 5.11 Temperature profiles of SME at ϕ =3 149
Figure 5.12 Temperature profiles of SME at ϕ =7 150
Figure 5.13 Temperature profiles of dodecane at ϕ =1.2 150
Figure 5.14 Temperature profiles of dodecane at ϕ =2 151
Figure 5.15 Temperature profiles of dodecane at ϕ =3 151
Figure 5.16 Temperature profiles of dodecane at ϕ =7 152
Figure 5.17 Temperature profiles of methyl stearate at ϕ =1.2 152
Figure 5.18 Temperature profiles of methyl stearate at ϕ =2 153
Figure 5.19 Temperature profiles of methyl stearate at ϕ =3 153

Figure 5.20 Temperature profiles of methyl stearate at ϕ =7 154
Figure 5.21 Peak temperatures at ϕ =1.2, 2, 3, and 7 plotted against Iodine Number 154
Figure 5.22 Diesel soot volume fraction profiles at ϕ =1.2 155
Figure 5.23 Diesel soot volume fraction profiles at ϕ =2 155
Figure 5.24 Diesel soot volume fraction profiles at ϕ =3 156
Figure 5.25 Diesel soot volume fraction profiles at ϕ =7 156
Figure 5.26 CME soot volume fraction profiles at ϕ =1.2 157
Figure 5.27 CME soot volume fraction profiles at ϕ =2 157
Figure 5.28 CME soot volume fraction profiles at ϕ =3 158
Figure 5.29 CME soot volume fraction profiles at ϕ =7 158
Figure 5.30 SME soot volume fraction profiles at ϕ =1.2 159
Figure 5.31 SME soot volume fraction profiles at ϕ =2 159
Figure 5.32 SME soot volume fraction profiles at ϕ =3 160
Figure 5.33 SME soot volume fraction profiles at ϕ =7 160
Figure 5.34 Dodecane soot volume fraction profiles at ϕ =1.2 161
Figure 5.35 Dodecane soot volume fraction profiles at ϕ =2 161
Figure 5.36 Dodecane soot volume fraction profiles at ϕ =3 162
Figure 5.37 Dodecane soot volume fraction profiles at ϕ =7 162
Figure 5.38 Methyl stearate soot volume fraction profiles at ϕ =1.2 163
Figure 5.39 Methyl stearate soot volume fraction profiles at ϕ =2 163
Figure 5.40 Methyl stearate soot volume fraction profiles at ϕ =3 164
Figure 5.41 Methyl stearate soot volume fraction profiles at ϕ =7 164
Figure 5.42 Peak $f_v/f_{v,max}$ at ϕ =1.2, 2, 3, and 7 plotted against Iodine Number. 165
Figure 5.43 OH PLIF images of all fuels at ϕ =1.2 166
Figure 5.44 OH PLIF images of all fuels at ϕ =2 166
Figure 5.45 OH PLIF images of all fuels at ϕ =3 167
Figure 5.46 OH PLIF images of all fuels at ϕ =7 167
Figure 5.47 CH PLIF images of all fuels at ϕ =1.2 168
Figure 5.48 CH PLIF images of all fuels at ϕ =2 168
Figure 5.49 CH PLIF images of all fuels at ϕ =3 169
Figure 5.50 CH PLIF images of all fuels at ϕ =7 169
Figure 5.51 Diesel NO concentration profiles at ϕ =1.2 170
Figure 5.52 Diesel NO concentration profiles at ϕ =2 170
Figure 5.53 Diesel NO concentration profiles at ϕ =3 171
Figure 5.54 Diesel NO concentration profiles at ϕ =7 171
Figure 5.55 CME NO concentration profiles at ϕ =1.2 172
Figure 5.56 CME NO concentration profiles at ϕ =2 172
Figure 5.57 CME NO concentration profiles at ϕ =3 173
Figure 5.58 CME NO concentration profiles at ϕ =7 173
Figure 5.59 SME NO concentration profiles at ϕ =1.2 174
Figure 5.60 SME NO concentration profiles at ϕ =2 174
Figure 5.61 SME NO concentration profiles at ϕ =3 175
Figure 5.62 SME NO concentration profiles at ϕ =7 175

Figure 5.63 Dodecane NO concentration profiles at ϕ =1.2 176
Figure 5.64 Dodecane NO concentration profiles at ϕ =2 176
Figure 5.65 Dodecane NO concentration profiles at ϕ =3 177
Figure 5.66 Dodecane NO concentration profiles at ϕ =7 177
Figure 5.67 Methyl stearate NO concentration profiles at ϕ =1.2 178
Figure 5.68 Methyl stearate NO concentration profiles at ϕ =2 178
Figure 5.69 Methyl stearate NO concentration profiles at ϕ =3 179
Figure 5.70 Methyl stearate NO concentration profiles at ϕ =7 179
Figure 5.71 Peak NO concentrations versus Iodine Number at all conditions ... 180
Figure 5.72 Diesel CO concentrations at ϕ =1.2 for three axial locations 181
Figure 5.73 Diesel CO concentrations at ϕ =2 for three axial locations 181
Figure 5.74 Diesel CO concentrations at ϕ =3 for three axial locations 182
Figure 5.75 Diesel CO concentrations at ϕ =7 for three axial locations 182
Figure 5.76 CME CO concentrations at ϕ =1.2 for three axial locations 183
Figure 5.77 CME CO concentrations at ϕ =2 for three axial locations 183
Figure 5.78 CME CO concentrations at ϕ =3 for three axial locations 184
Figure 5.79 CME CO concentrations at ϕ =7 for three axial locations 184
Figure 5.80 SME CO concentrations at ϕ =1.2 for three axial locations 185
Figure 5.81 SME CO concentrations at ϕ =2 for three axial locations 185
Figure 5.82 SME CO concentrations at ϕ =3 for three axial locations 186
Figure 5.83 SME CO concentrations at ϕ =7 for three axial locations 186
Figure 5.84 Dodecane CO concentrations at ϕ =1.2 for three axial locations 187
Figure 5.85 Dodecane CO concentrations at ϕ =2 for three axial locations 187
Figure 5.86 Dodecane CO concentrations at ϕ =3 for three axial locations 188
Figure 5.87 Dodecane CO concentrations at ϕ =7 for three axial locations 188
Figure 5.88 Methyl stearate CO concentrations at ϕ =1.2 for three axial locations 189
Figure 5.89 Methyl stearate CO concentrations at ϕ =2 for three axial locations 189
Figure 5.90 Methyl stearate CO concentrations at ϕ =3 for three axial locations 190
Figure 5.91 Methyl stearate CO concentrations at ϕ =7 for three axial locations 190
Figure 5.92 Diesel CO_2 concentrations at ϕ =1.2 for three axial locations..... 191
Figure 5.93 Diesel CO_2 concentrations at ϕ =2 for three axial locations..... 191
Figure 5.94 Diesel CO_2 concentrations at ϕ =3 for three axial locations..... 192
Figure 5.95 Diesel CO_2 concentrations at ϕ =7 for three axial locations..... 192
Figure 5.96 CME CO_2 concentrations at ϕ =1.2 for three axial locations 193
Figure 5.97 CME CO_2 concentrations at ϕ =2 for three axial locations 193
Figure 5.98 CME CO_2 concentrations at ϕ =3 for three axial locations 194
Figure 5.99 CME CO_2 concentrations at ϕ =7 for three axial locations 194
Figure 5.100 SME CO_2 concentrations at ϕ =1.2 for three axial locations..... 195
Figure 5.101 SME CO_2 concentrations at ϕ =2 for three axial locations..... 195
Figure 5.102 SME CO_2 concentrations at ϕ =3 for three axial locations..... 196

Figure 5.103 SME CO_2 concentrations at ϕ =7 for three axial locations..... 196
Figure 5.104 Dodecane CO_2 concentrations at ϕ =1.2 for three axial locations. 197
Figure 5.105 Dodecane CO_2 concentrations at ϕ =2 for three axial locations.... 197
Figure 5.106 Dodecane CO_2 concentrations at ϕ =3 for three axial locations.... 198
Figure 5.107 Dodecane CO_2 concentrations at ϕ =7 for three axial locations.... 198
Figure 5.108 Methyl stearate CO_2 concentrations at ϕ =1.2 for three axial locations 199
Figure 5.109 Methyl stearate CO_2 concentrations at ϕ =2 for three axial locations 199
Figure 5.110 Methyl stearate CO_2 concentrations at ϕ =3 for three axial locations 200
Figure 5.111 Methyl stearate CO_2 concentrations at ϕ =7 for three axial locations 200
Figure 5.112 Diesel O_2 concentrations at ϕ =1.2 for three axial locations 201
Figure 5.113 Diesel O_2 concentrations at ϕ =2 for three axial locations 201
Figure 5.114 Diesel O_2 concentrations at ϕ =3 for three axial locations 202
Figure 5.115 Diesel O_2 concentrations at ϕ =7 for three axial locations 202
Figure 5.116 CME O_2 concentrations at ϕ =1.2 for three axial locations..... 203
Figure 5.117 CME O_2 concentrations at ϕ =2 for three axial locations..... 203
Figure 5.118 CME O_2 concentrations at ϕ =3 for three axial locations..... 204
Figure 5.119 CME O_2 concentrations at ϕ =7 for three axial locations..... 204
Figure 5.120 SME O_2 concentrations at ϕ =1.2 for three axial locations 205
Figure 5.121 SME O_2 concentrations at ϕ =2 for three axial locations 205
Figure 5.122 SME O_2 concentrations at ϕ =3 for three axial locations 206
Figure 5.123 SME O_2 concentrations at ϕ =7 for three axial locations 206
Figure 5.124 Dodecane O_2 concentrations at ϕ =1.2 for three axial locations ... 207
Figure 5.125 Dodecane O_2 concentrations at ϕ =2 for three axial locations 207
Figure 5.126 Dodecane O_2 concentrations at ϕ =3 for three axial locations 208
Figure 5.127 Dodecane O_2 concentrations at ϕ =7 for three axial locations 208
Figure 5.128 Methyl stearate O_2 concentrations at ϕ =1.2 for three axial locations 209
Figure 5.129 Methyl stearate O_2 concentrations at ϕ =2 for three axial locations 209
Figure 5.130 Methyl stearate O_2 concentrations at ϕ =3 for three axial locations 210
Figure 5.131 Methyl stearate O_2 concentrations at ϕ =7 for three axial locations 210

Chapter 6 Computational Results

Figure 6.1 Schematic drawing of the computational domain 236
Figure 6.2 Variation of grid sensitivity for (a) original grid, (b) adaptation 1, and (c) adaptation 2 237
Figure 6.3 Temperature variation with grid size for the (a) near the burner at x = 0.024 m, (b) at x = 0.048 m, and (c) far from the burner at x = 0.071 m for n-dodecane/air 238
Figure 6.4 Temperature distributions for n-dodecane and biodiesel heated fuel/air jets in region of interest up to 15 cm above injector exit..... 239
Figure 6.5 Mass fraction of n-dodecane and biodiesel in heated fuel/air jets in region of interest up to 15 cm above injector exit 239
Figure 6.6 Mass fraction of O_2 in n-dodecane and biodiesel in heated fuel/air jets in region of interest up to 15 cm above injector exit 240
Figure 6.7 Carbon Monoxide concentration profiles for n – dodecane at (a) x = 0.02375 m, (b) x = 0.0475 m, and (c) 0.07125 m for equilibrium model..... 241
Figure 6.8 Carbon Dioxide concentration profiles for n – dodecane at (a) x = 0.02375 m, (b) x = 0.0475 m, and (c) 0.07125 m for equilibrium model..... 242
Figure 6.9 Temperature profiles for n – dodecane at (a) x = 0.02375 m, (b) x = 0.0475 m, and (c) 0.07125 m for equilibrium model..... 243
Figure 6.10 Oxygen concentration profiles for n – dodecane at (a) x = 0.02375 m, (b) x = 0.0475 m, and (c) 0.07125 m for equilibrium model..... 244
Figure 6.11 NO concentration profiles for n – dodecane at (a) x = 0.02375 m, (b) x = 0.0475 m, and (c) 0.07125 m for equilibrium model 245
Figure 6.12 Carbon Monoxide concentration profiles for biodiesel at (a) x = 0.02375 m, (b) x = 0.0475 m, and (c) 0.07125 m for equilibrium model..... 246
Figure 6.13 Carbon Dioxide concentration profiles for biodiesel at (a) x = 0.02375 m, (b) x = 0.0475 m, and (c) 0.07125 m for equilibrium model..... 247
Figure 6.14 Temperature profiles for biodiesel at (a) x = 0.02375 m, (b) x = 0.0475 m, and (c) 0.07125 m for equilibrium model..... 248
Figure 6.15 Oxygen concentration profiles for biodiesel at (a) x = 0.02375 m, (b) x = 0.0475 m, and (c) 0.07125 m for equilibrium model 249
Figure 6.16 NO concentration profiles for biodiesel at (a) x = 0.02375 m, (b) x = 0.0475 m, and (c) 0.07125 m for equilibrium model..... 250
Figure 6.17 Jet reactor network schematic diagram and actual model in CHEMKIN used for non-equilibrium model..... 251
Figure 6.18 NO concentration profiles using non-equilibrium model for biodiesel at (a) x = 0.02375 m, (b) x = 0.0475 m, and (c) 0.07125 m 252
Figure 6.19 NO concentration profiles using non-equilibrium model for n-dodecane at (a) x = 0.02375 m, (b) x = 0.0475 m, and (c) 0.07125 m 253
Figure 6.20 Predicted mole fraction of CH for both fuels at (a) x = 0.02375 m, (b) x = 0.0475 m, and (c) 0.07125 m..... 254

Abstract

Increased energy consumption in the United States has led to a demand for the development of new bio-derived fuels. As biofuels are used more frequently in diesel and gasoline engines, it has become increasingly important to test the emissions resulting from the combustion of these fuels from internal combustion engines. This study was motivated by the need to test these fuels, predict the combustion characteristics of fuels used in engines, and provide quick feedback to fuel researchers on the combustion characteristics. Therefore, this dissertation presents a technique to characterize the combustion properties of liquid fuels based on the chemistry of the fuel alone. The first part of the dissertation describes the development of a method for the rapid characterization of combustion properties, such as emission index and flame radiation. The technique provided a way of comparing the particulate and pollutant emissions from flames of hydrocarbon fuels to those of new fuels such as biodiesel. Burner conditions were selected to make flame properties sensitive primarily to fuel chemistry. The technique was validated through a comparison of measured radiative heat release fraction and pollutant (NO and CO) emission indices available in literature. It was seen that the present values compared well with the emission indices documented during engine testing and in other flame configurations. Approximately a 10% increase was observed in NO pollutant when biofuels where burned compared to diesel as in engine studies. Findings showed that use of this technique can assist fuel researchers in the development of new fuels since pollutant and sooting

tendency data obtained were similar to those from diesel engines. This technique in comparison to engine studies, however, requires only small amounts of fuel, time, and provides a method to compare fuels on a normalized basis.

Based on the observation that the biofuels produced more NO than diesel, it was desired to determine the cause for the increase in NO. For the second part of the dissertation, the equivalence ratio and iodine number were varied and their effect on the formation of NO was studied for four different fuels: canola methyl ester, soy methyl ester, diesel, and normal dodecane fuels. Measurements of intermediate species, flame temperatures, soot volume fraction, and global emissions were made for this purpose. At the lowest equivalence ratio of 1.2, the biofuel flames showed higher NO concentration values for in-flame measurements than diesel flames. NO production was primarily due to the Zeldovich mechanism for both biodiesel and diesel, since high temperatures were recorded, high concentrations of OH were observed, and NO concentration increased downstream of the burner, indicating a dependence on residence time. At higher equivalence ratios from 2 to 7, similar to those predicted to exist in diesel engines, NO production was much higher for the biofuel flames. The Fenimore mechanism was thought to be dominant at this condition, since the CH radical population was high in regions of peak measured NO concentration. A correlation between iodine number and peak NO concentration was also observed. Fuels with lower iodine number values (diesel and methyl stearate) produced less CH and NO concentrations, while fuels with higher iodine numbers (SME and CME) produced the highest CH and NO concentrations. It is thought that the

double bonds present in unsaturated fuels, such as SME, facilitated the production of more CH. This coupled with the presence of the oxygen in the biofuels accelerated the formation of NO.

Chapter 1
Introduction and Background

Worldwide energy consumption primarily comes from combustion of fossil fuels such as petroleum, coal, or natural gas. According to the Energy Information Administration over 80 percent of all energy used in the United States derives from fossil fuel sources and is predicted to continue to increase. This demand has caused a growing dependence on foreign countries to supply the fuel needed in the U.S. The political and economic pressure from this has resulted in efforts to develop alternative fuels which show a promising and realistic alternative for future use.

In 2008, 29 percent of the total energy consumed in the United States was used for transportation. As an alternative, renewable, sustainable and environmentally-friendly energy sources are being developed to meet the demand of the transportation industry. Examples of transportation based alternative energy sources currently include the hydrogen fuel cell, methane based combustion engines, and solar powered vehicles. However, the use of these technologies in automobiles has been limited since significant modifications are needed to effectively run an engine that normally operates on gasoline or diesel fuel.

Another alternative energy source that has become popular for engines is biofuel. Biofuels are renewable, can be made from various feedstocks grown in the U.S., have energy content similar to that of gasoline and diesel fuels, and can run in standard engines and combustors with minor modifications. Some biofuels in use today include biodiesels and ethanol used in diesel and gasoline engines.

This chapter provides a general overview of combustion characteristics of diesel and biodiesel as well as other fuels used in this study. The literature pertaining to the current investigation, statement of the problem, significance of the project, and organization of the report are also included.

1.1 Diesel Fuel

Petroleum based diesel fuels are widely used in agricultural, power generation, commercial, and transportation industries. Because of its wide range of uses, diesel is divided into five primary categories: No. 1, 2, 4, 5 and 6 fuel oils each having varying physical properties (density and viscosity). For automotive transportation purposes No. 2 diesel is most commonly used and will be considered for the present study (Chevron Technical Report, 1998). No. 2 diesel fuel is derived from crude oil sources, consisting of various hydrocarbons including paraffin, naphthalene, and aromatic. Each of these hydrocarbon components contains distinct molecular weights, structures, and carbon chain lengths. For example, No. 2 diesel fuel can contain up to 75% saturated hydrocarbons (paraffins), 25% unsaturated hydrocarbons (aromatic or naphthalene) and range in carbon chain length from 10 to 22. For this study, No. 2 diesel fuel will be used with an assumed average chemical formula, chemical composition, and physical properties presented in Table 1.1 (ATSDR, 1995, McCormick et al., 2001, Strong et al., 2004, Annamalai and Puri, 2007).

1.2 Biodiesel Fuel

Raw vegetable oils, which some consider the earliest biofuels, were first used in the 19th century to run diesel engines (Strong et al., 2004). Several of the vegetable oils were typically chosen because of their availability for a particular region or relatively low price. Using these vegetable oils directly, however, has been shown to be disagreeable for most cases primarily because of their high viscosities, tendency to cause carbon deposits on piston heads, difficult cold weather starting, gum formation causing plugging of injectors, and engine knocking due to low cetane numbers (Ma and Hanna, 1999). Rather than using vegetable oils directly, they are now transesterified which reduces the viscosity, improves the reaction rate, increases yield, and reduces problems with engine knocking and injector clogging while making the use of biofuel practical. Transesterified biodiesels are those that are currently available for use in engines today and include those used in the present study.

1.2.1 Transesterification

Triglycerides (e.g., vegetable oils) undergo a process called transesterification in order to be used effectively in diesel engines. This process alters the original molecular structure of the triglyceride to produce biodiesel as it is defined by the American Society for Testing and Materials (ASTM D6751-03a). Mixing the triglyceride at an elevated temperature (~100^{o}C) with an alcohol (e.g. ethanol or methanol) and catalyst (e.g. sodium hydroxide) results in the formation of methyl ester biodiesels (if methanol is used) and ethyl ester biodiesels (if ethanol is used) as well as a glycerol product which can later be used in food, medical, pharmaceutical, or cosmetic products. Figure 1.1 presents an example of a typical reaction for biodiesel fuel.

An example of a reactor for biodiesel is also shown in Figure 1.2. The oil, alcohol, and catalyst are sent through a steam heated coil in the upper part of the reactor. In this section the triglyceride reacts to form the products, biodiesel and glycerol. The products are then neutralized, passed to the lower section of the reactor, and remaining alcohol vapor is collected through the top. The esters that form have lighter densities and accumulate above the heavier glycerol product and are siphoned and stored. Resulting molecular structures and composition of the esters vary based on the oil that is used to make the fuel. Table 1.2 presents the composition by weight of soy and canola methyl esters, as well as their molecular compositions and heating values (Lang et al., 2001, McCormick et al., 2001, Adams et al., 2004, Strong et al. 2004). For the present study, biodiesels were acquired commercially, hence transesterified by an external manufacturer,

purchased from a vendor, and were assumed to have the properties listed in Table 1.2.

1.3 Dodecane and Methyl Stearate Fuels

The diesel and biodiesel fuels are composed of a mixture of several components including aromatics and paraffins for diesel and several fatty acids for biodiesel. For this reason, single component fuels with varying iodine number that best represented the diesel and biodiesel fuels, dodecane and methyl stearate, were selected.

Diesel fuel is composed of 75% paraffins of which 41% are straight or iso paraffins. Dodecane, a straight chain single component paraffin, was selected because it provided similar molecular composition, carbon chain length, and energy content comparable to the midpoint of diesel. Furthermore, dodecane is a single component fuel and does not contain aromatics. Aromatics found in diesel have been shown to adversely affect combustion characteristics (Ladommatos et al., 1997).

Similarly, a single component fatty acid methyl ester found in biodiesel, methyl stearate (MS), was selected. MS has similar energy content and carbon chain length when compared to typical biodiesel fuels such as the soy methyl ester (SME) and canola methyl ester (CME) used in this study. Additionally, MS is a saturated fuel containing no double bonds. This molecular characteristic is demonstrated by the low iodine number, and can be seen in Table 1.3. The iodine number was defined as the amount of iodine absorbed by a chemically unsaturated fuel, thus it is a measure of how unsaturated the fuel of interest is; it is typically expressed in centigrams of iodine absorbed per gram of sample (percentage by weight of iodine absorbed).

By using these single component fuels a comparison can be done with diesel and biodiesel fuels to determine the effects of the additional components and iodine number. The physical and chemical properties of dodecane and methyl stearate are presented in Table 1.3 (Krisnangkura, 1991, McCormick et al., 2001, Santana et al., 2006, Annamalai and Puri, 2007).

1.4 Brief Description of Combustion in a Diesel Engine

In this section the terms and variables associated with the combustion process in a diesel engine will be defined. These terms will be consistently used throughout this chapter.

The diesel engine relies on compression for the ignition of the fuel/air mixture. Air drawn into the engine's combustion chamber, or piston cylinder, is compressed by the piston causing temperature and pressure to increase. Fuel is then injected as a finely dispersed spray into the cylinder, evaporated, mixed with the hot air, and burned. The resulting combustion process that occurs can be divided into three primary steps: (1) ignition delay (2) uncontrolled combustion, and (3) controlled combustion. Timing and length of each of these steps directly impacts the resulting emissions and depends on the physical and chemical properties of the fuel and engine used.

The first step, ignition delay, refers to the amount of time between the beginning of injection and ignition of the fuel. Droplet size of the injected fuel, cetane number (a measure of the fuel's ignition/combustion quality), air temperature, and mixture ratio of the fuel and air are variables that can affect the ignition delay. During this stage the fuel spray breaks up and evaporates into the surrounding air in the cylinder.

The second step, uncontrolled combustion, describes the initial combustion of the injected fuel/air mixture. Autoignition during this phase causes high temperature and pressure increases. The rise in pressure in this process is dependent on the amount of fuel injected and vaporized prior to ignition.

Following the rapid autoignition of the fuel and air, controlled combustion then begins. Controlled combustion is sustained by the injection and mixing rate of the fuel and air in the cylinder. As the piston moves downward the pressure and temperature are reduced and combustion process ceases.

When using any engine it is important to consider certain characteristics such as the fuel consumption rate, thermal and combustion efficiency, power output, and pollutants emitted. Compression ignition engines typically produce higher efficiencies and have lower fuel consumption rates than spark ignition engines. The tradeoff, however, is found in the relatively large amounts of particulate matter (PM) and NO_x produced by the compression engine. The current project *does not* simulate the combustion environment of the diesel engine; rather, it simplifies the process by removing several variables (high pressure, droplet evaporation, injection timing), as is further discussed later in this chapter.

1.5 Literature Review

1.5.1 Diesel and Biodiesel Combustion in Engines

Biodiesel and conventional petroleum-based diesel fuels have been extensively studied in internal combustion engines. A study by Scholl and Sorenson (1993) investigated the effects of using soy methyl ester in a four cylinder, four stroke, 3L, normally aspirated direct injection diesel engine and compared their results to those produced with conventional diesel fuel. NO_x production was 2100 ppm for soy methyl ester and 1700 ppm for conventional diesel engine with standard injection timing. The authors determined that the difference was due to variation in ignition delay of the two fuels. Flynn et al. (1999) studied diesel fuel spray combustion in an engine. These authors found that fuel droplets were completely vaporized within 22-27 mm from the injector exit. After this, the heated fuel vapor burned with entrained air from the cylinder at high equivalence ratios in the range of 4 to 8. Around this region a thin diffusion flame front oxidized soot, CO, and other unburned fuel fragments. NO_x was produced along the boundaries of the diffusion flame interface where the temperature was high. Another study by Durbin et al. (2000) used neat (B100) biodiesel and diesel in 4 heavy duty diesel truck engines including a 1988 Ford F-250 7.3L, 1990 Dodge Ram 250 5.9L, 1995 Ford F-350 7.3L, and 1996 Dodge Ram 5.9L. Results showed that production of NO_x with biodiesel was also higher in 3 of the 4 engines in comparison to diesel. Wang et al. (2000) used a fuel blend B35 in Cummins 855-14L and DDC Series 60-11.1L engines and showed that NO_x emissions were higher for the B35 blend than for the diesel fuel in the

Cummins engine. The slight increase in NO_x with biodiesel fuels was attributed to the shorter ignition delay caused by biodiesel's higher cetane number. The ignition delay for biodiesel fuels advanced the combustion timing, increased peak temperature and pressure, and resulted in higher NO_x formation.

McCormick et al. (2001) used diesel and various biodiesel fuels in a six cylinder, direct injected, turbocharged, four stroke cycle engine rated at 345 bhp at 1800 rpm. Pollutant emissions of NO_x were measured from the exhaust of methyl esters of canola, soy, and stearate along with 17 other biofuels and diesel. NO_x emissions per unit power were found to be 5.1, 5.2, 4.3, and 4.6 g/bhp-h for commercially available methyl canola, soy, stearate, and diesel respectively. In this study, differences in the NO_x emissions were correlated to both chemical (iodine number) and physical properties (density, rate of fuel injection). Highly saturated fuels, such as methyl stearate, and fuels with higher cetane numbers were shown to produce the lowest NO_x emissions. Graboski et al. (2003) investigated the effect of the composition of 28 neat biodiesels, four B20 blends, and diesel fuel in a six cylinder, four stroke, direct injected, turbocharged, intercooled, 11.1 L, 345 bhp engine. They found that NO_x emissions were higher for the unsaturated fuels, whether neat biodiesel or biodiesel blend, when compared to diesel fuel with the exception of highly saturated fuels such as methyl stearate. The EPA (EPA, 2002) has also shown that B100 and B20 soy biodiesel and blend produced 13% and 2% more NO_x, respectively, in heavy duty highway engines than the conventional diesel fuel.

In general, pollutant emission studies have shown that a majority of biodiesels produced more NO_x than commercially available diesel fuel. Some authors in the aforementioned investigations attributed higher peak temperature and pressure, as resulting from shorter ignition delay caused by the higher cetane number of biodiesels, to increased NO_x formation. Alternatively, other studies have attributed the increase to chemical parameters, showing that biodiesels with lower iodine numbers produced lower NO_x emissions. These investigations, however, have difficulty in determining the cause of increased NO_x generation seen with biodiesel fuels. This is largely due to the complexity of the engine studies which require knowledge of many factors and their effect on NO_x production. To better understand the combustion and formation of pollutants within engines, some authors have used spectroscopic techniques to observe regions of radical formation in the cylinder.

Nakagawa et al. (1997) obtained distributions of OH radicals and NO using the planar laser induced fluorescence (PLIF) and laser induced fluorescence (LIF). The authors used a modified single cylinder motor driven engine with diesel fuel spray issuing from a single hole injection nozzle. OH radicals were present in a band-like zone outside the region of flame luminescence. NO was shown to be distributed just outside the observed flame luminescence zone and increased during the end of the combustion process. Since the formation of NO occurred slightly after the time of peak heat release, the authors attributed NO formation primarily to the extended Zeldovich mechanism. Fayoux et al. (2004) also studied the formation of OH in the combustion chamber of a Homogenous

Charge Compression Ignition (HCCI) engine running on blended fuels of n-heptane and n-octane. OH radicals were shown to increase during the period of main heat release and followed regions of high temperature premixed combustion and zones of low oxidation of unburned hydrocarbons. Another study by Demory et al. (2006) used PLIF to qualitatively study NO and OH radical concentrations of diesel fuel in the cylinder of a rapid compression machine. As in the previous studies discussed, the authors observed that for the main part of the mixing controlled phase, regions of OH radicals formed in a thin band around the recorded flame front. Literature pertaining to the combustion of neat biodiesel and blends inside an optically accessible engine is limited, therefore is not presented.

As can be seen above the advantages of optically accessible engines include the study of actual in-cylinder combustion processes. However, since this is complex and requires knowledge of many factors and their effect on the pollutant emission generation it can be more effectively used if the combustion of these fuels in a controlled laminar flame environment is fully understood.

1.5.2 Diesel and Biodiesel Flames

Ladommatos et al. (1997) studied the effects of aromatic hydrocarbons on soot formation in laminar diffusion flames of various diesel fuel blends. Fuels were vaporized prior to combustion and sent to a 10 mm stainless steel burner and the sooting flame heights measured. Diesel fuel blends varied in the number of aromatics present ranging from 57 to <0.2% composition by mass. By measuring the flame heights the authors observed the effects of the aromatics to be significant. Flames without aromatics, <0.2%, were found to begin to soot at nearly four times the flame length as those composed of 57%. A related study by Bryce et al. (2000) showed quantified soot distributions in diesel blends using laser induced incandescence. By capturing images of the flames of the blended diesel fuels with aromatic content ranging from <1 to 24% by volume, regions of fuel pyrolysis, soot formation, soot growth, and soot oxidation were shown. McEnally and Pfefferle (2007) predicted sooting tendencies of aromatic hydrocarbons in a coflow methane/air non-premixed flame doped with 400 ppm of the test hydrocarbon. Testing of 143 fuels similar to diesel including aromatics such as toluene and tetralin showed that the yield sooting tendencies were strongly dependent on molecular structure. Perez et al. (2007) also investigated the effects of molecular structure on particulate matter and NO emissions of oxygenated hydrocarbons. The authors tested six ester isomers pairs on a Hencken diffusion flame burner, where methane was the carrier gas for the tested esters. Sooting tendencies increased with increased carbon chain length. Additionally, methyl butanoate and butyl methanoate esters were observed to increase NO

emissions while addition of smaller esters methyl ethanoate and ethyl methanoate decreased NO emissions when compared to the methane/air baseline which was also attributed to carbon chain length.

Wang et al. (2007) documented the lower extinction limits of biofuels such as ethanol, dimethyl ester, and methyl butanoate from a counterflow configuration over a range of equivalence ratios. The primary goal of their study was to enhance the basic knowledge of the combustion of biofuels. Another fundamental study by Jha et al. (2008) presented relative flame temperatures of 13 component methyl esters found in biodiesel. This was accomplished by burning the fuels in a laminar diffusion wick generated flame. Relative flame temperature measurements were acquired using an infrared camera. It was observed that fuels with higher calorific values had lower flame temperatures and saturated components with lower carbon chain lengths led to increased flame temperatures.

The studies listed have enhanced the understanding of the combustion behavior of both diesel and biodiesel fuels by measurement of in-flame soot concentrations, temperature profiles, and global pollutant emissions. Other authors have developed detailed and reduced kinetic models to numerically simulate the combustion of biodiesel. With these models, knowledge of chemical interactions occurring and the formation of pollutants are further enhanced.

1.5.3 Numerical Studies of Biodiesel and Diesel Combustion

Methane (CH_4) which only contains one carbon atom considers 325 elementary reactions involving 53 species (GRI-Mech 3.0). Biodiesel, composed of several fatty acid methyl esters, ranges in carbon chain length from 15 to 21. Similarly, diesel is composed of various different types of paraffins and aromatic compounds. This implies that a kinetic model for a diesel/biodiesel fuel would be large and computationally taxing. For this reason chemical kinetic models of diesel and biodiesel fuels as they are sold commercially are currently unavailable. Without chemical kinetic models accurate predictions of temperatures, intermediate radicals, and pollutant concentrations cannot be achieved. To resolve this problem authors have used surrogate fuels which are significantly smaller in length and computational requirements.

Fisher et al. (2000) developed detailed chemical kinetic models for the combustion of biodiesels by using surrogate fuels methyl butanoate ($C_5H_{10}O_2$) and methyl formate ($C_2H_4O_2$). The mechanisms presented in the paper by Fisher et al. (2000) were tested against the limited available data obtained under low temperature, subatmospheric conditions in closed vessels, using pressure measurements as the main diagnostic. Weiss et al. (2006) also numerically simulated the formation of NO_x in biodiesels. For the study the effect of double bonds in a well-mixed balloon model was used and showed the time history of a fuel jet injected into a combustion chamber with constant inflow of hot oxidizer. Combustion of methyl butanoate and methyl trans 2- butenoate ($C_5H_8O_2$) fuels showed that higher temperatures occurred for the latter. The authors attributed

higher temperatures to the presence of the additional double bonds which increased NO formation by the thermal mechanism. Dooley et al. (2008) also developed a detailed kinetic model for biodiesel by using the surrogate methyl butanoate. They accomplished this by measuring data from shock tube and rapid compression machine at various conditions and also collected existing data from literature simulations of: opposed flow diffusion flames, jet stirred reactors, and flow reactors. Authors have developed and made publicly available the chemical kinetic models for a surrogate fuel methyl butanoate ($C_5H_{10}O_2$) (Fisher et al., 2000, Weiss et al., 2006, Dooley et al. 2008). Thus, the numerical portion of this dissertation will use the kinetic model provided by Dooley et al. (2008) for methyl butanoate.

For diesel fuel, fuels such as n-hepatne, n-dodecane, n-hexadecane, and mixtures of these with toluene have all been used to simulate the combustion of diesel (Kitamura et al., 2001, Farell et al., 2007, Westbrook et al., 2009). Normal dodecane has been shown to have similar thermo-physical and transport properties to that of diesel (Farell et al., 2007, Blin-Simiand et al., 2001, Ranzi et al., 2001). It has been used previously and found to be a satisfactory surrogate for diesel according to a review by Farell et al. (2007). Also, since experimental data in this dissertation was obtained for n-dodecane, the predictive mechanism would provide a direct comparison. Hence, the kinetic model provided by Westbrook et al. (2009) was used; the model consists of 5030 reactions and 1282 total species for the combustion of n-dodecane.

1.6 Significane of NO_x

NO_x is a closely regulated emission by the Environmental Protection Agency (EPA). Its contribution to pollution causes dangerous health effects to humans, animals, and the environment. NO_x has been shown to cause respiratory irritation, reduce lung function, induce asthma attacks, permanent lung damage, and destroy plant life (Fernando et al., 2006). Additionally, NO_x is involved in the formation of acid rain which can cause damage to manmade structures. The increased acidity of waterways also harms wildlife that occupies lakes or rivers.

The two most common types of NO_x are nitric oxide (NO) and nitrogen dioxide (NO_2). In the presence of hot stagnant air and sunlight NO_x can convert to hazardous ground level ozone. NO_x plays a role in the catalytic destruction of the lowest layer of atmosphere (stratosphere) ozone (O_3) (Turns, 2000). Investigation of causes of NO_x formation and reduction of the pollutant through exhaust gas recirculation (EGR), catalytic converters, and modifications to injection timing has been a well researched topic for conventional engines. The harmful nature of NO_x emissions and their prevention have been studied extensively.

NO_x formation pathways that are relevant for this study can be described by a few primary mechanisms: (1) the thermal or Zeldovich mechanism which dominates in high temperature combustion (above 1800K), (2) intermediate N_2O mechanism which is most important in lean low temperature combustion processes, and (3) prompt or Fenimore mechanism which dominates in rich combustion (Turns, 2000).

The thermal or extended Zeldovich mechanism is given by three reactions:

$$O + N_2 \leftrightarrow NO + N$$

$$N + O_2 \leftrightarrow NO + O$$

$$N + OH \leftrightarrow NO + H$$

Another mechanism contributing to NO_x in lean low temperature combustion is the N_2O intermediate mechanism, important in gas turbine combustion (Erazo, 2008, Habib, 2008). The three step reaction for this mechanism is given by:

$$O + N_2 + M \leftrightarrow N_2O + M$$

$$H + N_2O \leftrightarrow NO + NH$$

$$O + N_2O \leftrightarrow NO + NO$$

The third mechanism is known as the prompt or Fenimore involving hydrocarbon reaction with molecular nitrogen. This reaction has been shown to be dominant in stoichiometric and rich mixtures. Hydrocarbon radicals react with molecular nitrogen to form amines (e.g. HCN) or cyano (e.g. CN) compounds (Turns, 2000). These compounds are then intermediately connected to the formation of NO. The Fenimore mechanism is shown below:

$$CH + N_2 \leftrightarrow HCN + N$$

$$C + N_2 \leftrightarrow CN + N$$

1.7 Project Impact

Knowledge of the combustion characteristics of petroleum based diesel and oxygenated biofuels have been enhanced through measurements in engines, flames, and numerical simulations. However, there currently exists a lack of advancements in this field to:

1. Test fuels using a common technique that successfully characterizes their combustion properties attributable to the molecular structure of fuels

- This can provide a relative scale/technique by which various fuels and their combustion properties can be compared.

2. Analyze the pollutant emissions of these fuels based on fuel chemistry alone

- By the elimination of effects such as high pressure, droplet evaporation, turbulence, and injection timing this can be accomplished. Burning fuel vapor in a controlled laminar flame environment removes most physical variables that are encountered in more complex combustors.

3. Capture the combustion properties of various fuels using only small quantities (<50ml)

- This is needed since in bench-scale experiments in the development of new fuels, e.g., catalytic modification of existing fuels in the laboratory, the yield of new fuels is very small, on the order of milliliters. Therefore, as new fuels are developed and produced in small (<50ml) amounts, fuel

developers need to have the combustion and pollutant formation potential of their new products to optimize the fuel production conditions and to alter the molecular structure of the new products.

4. Determine the cause for NO_x increase for biodiesel when compared to conventional diesel

- Determining the cause(s) of NO_x formation can be used to modify the chemistry of the fuel or reduce unwanted pollutant emissions in the future.

1.8 Objectives

As mentioned in the previous section there currently exist several methods to measure the combustion characteristics (e.g. pollutant emissions) of diesel and biodiesel fuels. A common technique to test liquid fuels based on chemistry alone would eliminate complicated variables and reduce variations from study to study. The technique should also be capable of using only a small amounts of fuel (<50 ml). Once the developed technique has been established, it is desired to study the increased formation of NO_x observed in biodiesel fuels when compared to conventional petroleum based diesel.

Hence, this dissertation will present a two part study which will describe:

(1) The development and validation of a technique to rapidly assess the combustion properties of liquid fuels in a laminar combustion environment using small amounts of fuel and

(2) An investigation of the cause of the increase in NO_x produced by biodiesel when compared to diesel.

For the first part of the project the appropriate setup was developed to complete the objective and was based on the listed criteria:

- Laminar flow maintained in order to avoid the effects of flow parameters and thus measure combustion properties attributable to the fuel chemistry alone
- Pre-vaporize liquid fuel and supply it in gaseous form to the burner in order to avoid the atomization and vaporization effects in the test section
- Appropriate burner that provides an attached flame for a range of fuels to avoid the complex effects of flame liftoff
- Small amounts of fuel in testing (<50 ml)

Once the technique was established, the goals were extended to answer the second portion of this report by determining the following:

- The primary mechanism(s) (Zeldovich, Fenimore, etc.) which contributes to increased NO_x formation for biofuels on a chemical basis alone.
- The effect of chemical parameter iodine number on the NO_x formation of diesel and biofuels.

1.9 Organization of the Dissertation

An introduction to the problem, description of hydrocarbon and oxygenated fuels used in the study, literature review, and discussion of the objectives is given in Chapter 1.

Chapter 2 presents the experimental techniques and instrumentation used in the present investigation.

Chapter 3 details the validation of the experimental setup and method to characterize the combustion properties tested fuels.

Chapter 4 describes the results for the global flame properties. This includes flame appearance, flame length, emissions indices for NO and CO, and radiation parameters.

Chapter 5 presents the results and discussion for the experimentally obtained data involving the internal structure of the flame. This includes measured flame temperatures, concentration profiles of stable species (CO, CO_2, and NO), soot volume fraction, and PLIF images of intermediate species.

Chapter 6 contains the numerical portion of the report: the governing equations, reaction models, grid parameters, grid independence measurements, and comparison of computational results with experimental.

Finally, in Chapter 7 a general discussion of the dissertation is given followed by recommendations for future studies.

Table 1.1: Composition and properties of No. 2 diesel fuel (ATSDR, 1995, McCormick et al., 2001, Strong et al., 2004, Annamalai and Puri, 2007)

No. 2 Diesel	
Hydrocarbon Type	**% By Volume**
Paraffins (n and iso)	41.3
Monocycloparaffins	22.1
Bicycloparaffins	9.6
Tricycloparaffins	2.3
Total saturated hydrocarbons	75.3
Alkylbenzenes	5.9
Teralins	4.1
Dinaphthenobenzenes	1.8
Naphthalenes	8.2
Acenaphthenes	2.6
Acenaphthylenes	1.4
Phenanthrenes	0.7
Total aromatic hydrocarbons	24.7
Iodine Number	8.6
Assumed Molecular Formula	$C_{14.4}H_{24.9}$
LHV (MJ/kg)	42.6
Density (kg/m^3)	850
Cetane Number	45
Final BP (^{o}C)	345

Table 1.2: Composition and properties of B100 biodiesels soy methyl ester and canola methyl ester (Lang et al., 2001, McCormick et al., 2001, Adams et al., 2004, Strong et al. 2004)

Fatty Acid	**SME composition (% by weight)**	**CME Composition (% by weight)**
Palmitic	6.5	4.2
Stearic	4.9	2.2
Oleic	20.5	67.2
Linoleic	68.0	18.9
Linolenic	0.0	7.4
Eicosenoic	0.0	0.0
Erucic	0.0	0.0
Iodine Number	141.6	115.0
Assumed Molecular Formula	$C_{18.8}H_{34.6}O_2$	$C_{19}H_{36}O_2$
LHV (MJ/kg)	37.0	37.4
Density (kg/m^3)	887	881
Cetane Number	47	55
Final BP (^{o}C)	346	405

Table 1.3: Composition and properties of n-dodecane and methyl state (Krisnangkura, 1991, McCormick et al., 2001, Santana et al., 2006, Annamalai and Puri, 2007)

Fuel	Dodecane	Methyl Stearate
Type	alkane (n-paraffin)	Fatty Acid Ester (saturated)
Iodine Number	-	0.5
Molecular Formula	$C_{12}H_{26}$	$C_{19}H_{38}O_2$
LHV (MJ/kg)	44.4	37.4
Density (kg/m^3)	749	868
Cetane Number	87	86.9
BP (^{o}C)	216	430

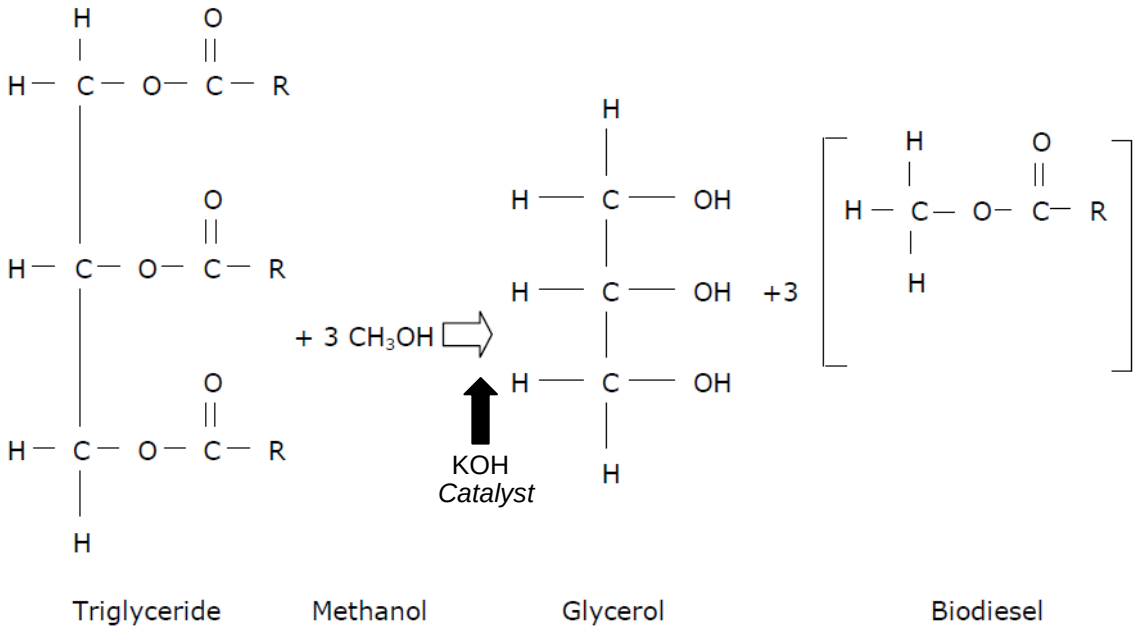

Figure 1.1: Transesterification process

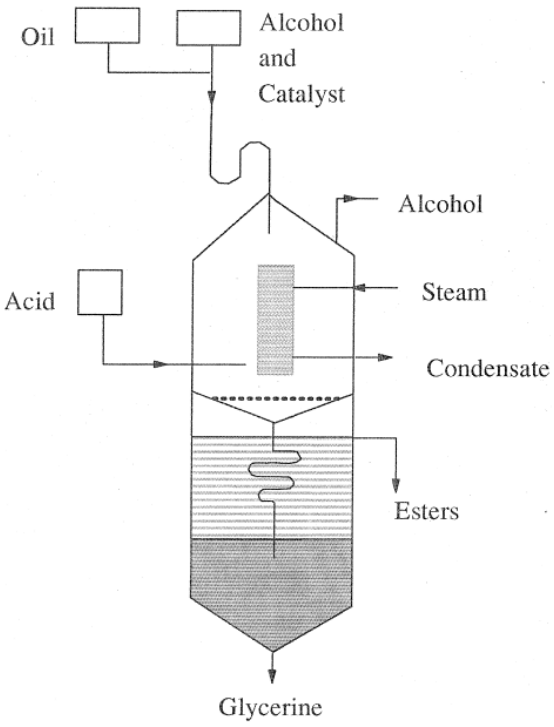

Figure 1.2: Example reactor for biodiesel production (Ma and Hanna, 1999)

Chapter 2
Experimental Setup and Procedure

To effectively complete the objectives of this report, selection of the appropriate instrumentation and setup was essential. Details of the experimental setup and its components are discussed here along with the background for the measurement techniques. A list of the instruments used (Table 2.1), operating conditions (Table 2.3), and test matrix (Table 2.5) are also presented in this chapter.

2.1 Laboratory Combustion Chamber

All experiments were conducted in a vertical steel test chamber of cross section 76 cm x 76 cm and 100 cm height. The burner used for the experimental was housed within the chamber at its bottom center. The walls of the chamber contained windows provided with removable slotted metal sheet covers measuring 96 cm x 25 cm to allow optical (laser, photography) and instrument (thermocouple, emissions probe) access. A schematic drawing of the combustion chamber can be found in Fig. 2.1. The top of the combustion chamber was open to atmosphere through an exhaust duct. The ambient pressure of the laboratory was maintained slightly above the atmospheric pressure (~20 Pa) to provide a positive draft inside the test chamber so that combustion products flowed through the exhaust duct and did not leak into the main laboratory facility.

2.2 Burner and Fuel Delivery System

Several burners, including flat-flame, counter flow, Bunsen burners, and circular tubular burners were tested with various vaporized liquid fuels. The porous medium in the flat-flame burner became clogged due to soot or coking. The cooling provision in the flat flame burner made it difficult to control the heat input necessary to vaporize the liquid fuels and avoid their condensation. The counterflow burner's complex design and varying wall thickness made it difficult to provide sufficiently uniform heating to completely vaporize the liquid fuel. The Bunsen burner also posed problems because precise control and measurement of the air flow rate supplied to the flame were inaccurate. Therefore, a stainless steel circular burner (ID = 9.5mm, Fig.2.2) with a beveled rim was chosen. The burner could be manufactured quickly, heated easily, and provided a stable, laminar, repeatable flame.

Fuels tested in this study were in liquid form hence it was required that they be completely vaporized and delivered to the burner. By pre-vaporizing the fuel, the fluid mechanics effects associated with droplet evaporation were eliminated and allowed the fuels to be burned in a laminar flame environment. To vaporize the fuel effectively, but not cause liquid phase pyrolysis and lead to coking of the fuel, high temperature heating tape was used and is listed in Table 2.1. The heating tape was wrapped around the 12.7 mm (OD) stainless steel feed line tubing. The heating tape was connected to a proportional temperature controller which was continuously monitored as were the air inlet and exit temperatures through K-type (chromel-alumel) thermocouples embedded in the feed line, Fig.

2.2. Maintained temperature was selected to be 430^{o}C based on the final boiling points of the tested fuels. The temperature was sufficiently high enough above the final boiling point of the fuels so as to completely vaporize the injected fuel and low enough so as to prevent coking in the feedlines. After several test runs with fuel, the inside of the tubing was examined for unburned fuel or coking to ensure that nothing accumulated within the tube walls.

The liquid fuel was delivered to the heated carrier gas (air) stream through a high temperature silica-based septum with a 50 cm^3 capacity syringe. A syringe pump was used to supply the liquid fuel through the syringe. The heated line was long enough to ascertain that the liquid fuel was completely vaporized in the air stream before exiting the burner. The volume flow rate of the carrier gas was monitored using a calibrated rotameter. The resulting mixed fuel and air mixture was ignited at the exit of the burner with an external pilot flame which was removed after ignition.

2.3 Instrumentation

2.3.1 Flame Visualization

Visible flame images were acquired using an 8 mega pixel digital AF SLR camera (EOS Digital Rebel XT/EOS 350D). The images were obtained under similar lighting conditions with a dark background at 1/25 second shutter speed. Images were taken perpendicular to the flame which was assumed axis symmetric. Using an appropriate software (GIMP version 2.6.6) the amount of pixels were counted and converted into the length scale using a calibration reference.

Flame length was determined by counting the number of pixels from the tip of the burner to the farthest point of visible luminosity. This pixel count was then converted into a length scale using the calibration reference. Ten images per flame condition were taken at arbitrary time intervals and the resultant flame lengths were averaged.

2.3.2 Temperature Profiles

For flame temperature measurements an in house made platinum-13% rhodium-platinum (R-type) thermocouple with wire diameter of 0.12 mm and bead diameter of 0.25 mm was used. The thermocouple was mounted onto a two dimensional linear traversing mechanism. Profiles were taken at three axial locations, 25%, 50%, and 75% of the visible flame height. Data were acquired from the thermocouple through the use of LabVIEW 7.1 data acquisition software at a sample rate of 2 Hz over a 60 second time interval at each point. Thermocouple data were then corrected for radiative and conductive losses. This setup can be seen in Fig. 2.3.

2.3.3 Global Emissions/In-Flame Species Concentration Profiles

Global emission measurements were measured by collecting gas samples through a 1 mm diameter tip uncooled quartz probe. The tube expanded to a 6 mm ID tube uncooled quartz probe placed at the top of a Pyrex flue gas collector, Fig. 2.4. The Pyrex flue gas collection funnel was placed 25 cm above the burner tip exit so that post combustion products were mixed and could be collected. The collected gas samples were passed through a filter and ice-chilled water bath to remove particulates and moisture. A NOVA model 376WP portable flue gas analyzer was used to measure the concentrations of NO, CO, CO_2, and O_2. The O_2, CO, and NO sensors were electrochemical 'fuel cell' type sensors which produced small electrical outputs proportional to the volumetric concentration of the gas being detected. The CO_2 instrument used a non-dispersive infrared (NDIR) to determine the concentration. The analyzers were calibrated with standard zero and reference gases before measurements were taken.

For global emissions, in order to correct for dilution of the product gases from ambient air entrainment the emission index was used (Turns, 2000). The emission index expresses the amount of pollutant formed per unit mass of the fuel burnt, Eq. (2.1).

$$EI_i = \left(\frac{\chi_i}{\chi_{CO} + \chi_{CO_2}} \right) \left(\frac{N \cdot MW_i}{MW_f} \right) \cdot 1000 \qquad (2.1)$$

where χ_i represents the mole fraction, N is the number of carbon atoms in the mixture, and MW_i and MW_f are the molecular weight of species i and fuel. It was assumed that all of the fuel carbon appeared either as CO_2 or CO. This

assumption was justified in the present case because the flames tested were not smoking, thus, there was no solid carbon in the exhaust; also, the amount of carbon radicals was expected to be at concentration levels of parts per million (ppm).

In flame species concentration profiles (CO_2, O_2, NO) were taken with a custom made water cooled stainless steel gas sample probe, Fig. 2.5. The probe consisted of a short 1.75 mm inner diameter and 3.2 mm outer diameter stainless steel tube cemented with high temperature ceramic adhesive into a stainless steel 4.6 mm inner diameter 6.35 mm outer diameter holder. This probe could withstand the high temperatures produced by the flames which tended to soften quartz tubing. Additionally, the diameter of the sampling probe was large enough not to clog from soot accumulation on the inlet.

For in flame concentration measurements the sampling probe was mounted on a two dimensional linear traversing mechanism. Measurements were taken with the probe placed perpendicular to the burner centerline. The probe was radially traversed at 2 mm intervals and at the same axial positions as the temperature measurements.

2.3.4 Radiative Emissions

A wide view-angle (150^o) high sensitivity pyrheliometer was used to measure the total radiation from the flame (q_{total}). The pyrheliometer had a linear output with a sensitivity of 23.65 $W/m^2/mV$. The pyrheliometer was located far enough (50 cm) from the burner, so that its view-angle covered the entire flame length and the flame could be assumed as a point source, thus was farther than 1.5 flame lengths to satisfy the inverse square law. A data-acquisition board along with suitable software was used to sample the measured radiative heat flux. Each test was run for a time duration of 3 minutes with a sampling rate of 2 Hz, allowing the heat flux to reach a steady value. The data was averaged over this sample time. Next, after the flame was extinguished the background radiation ($q_{background}$) was obtained and used for correction of the total radiation ($q_{corrected}$).

$$q_{corrected} = q_{total} - q_{background} \tag{2.2}$$

In order to use the measured radiative heat flux to characterize the fraction of energy emitted from the flame in the form of radiation the radiative fraction of heat released (F) was used. This also allowed a comparison of different fuels.

$$F = \frac{4\pi \ell^2 \cdot q_{corrected}}{\dot{m} \cdot LHV_{fuel}} \tag{2.3}$$

where ℓ was the distance from the flame centerline to the pyrheliometer, $q_{corrected}$ was the corrected radiative heat flux measured, $\dot{m}$ was the mass flow rate of the liquid fuel, and LHV_{fuel} was the lower heating value of the liquid fuel tested. A schematic drawing of this setup can be seen in Fig. 2.6.

2.3.5 PLIF Instrumentation

Planar Laser Induced Fluorescence (PLIF) has been used extensively to determine the relative population densities of intermediate radicals within a combustion test medium. For PLIF measurements, a wavelength-controlled narrowband light source (laser) is used to excite molecules of a desired species to a higher energy level. The incident photons absorbed at each point are re-emitted with a modified spectral distribution. The re-emitted photons, a form of molecular scattering and radiation termed fluorescence, are of interest for PLIF measurements. By capturing emitted fluorescence a non-intrusive method for measurement of various flow field properties, such as species concentration, with low temporal (5-20 ns) and spatial resolution can be accomplished.

The laser system used for the measurements included a Quanta-Ray GCR 200 pulsed Nd:YAG laser and Quanta- Ray MOPO-730 Optical Parametric Oscillator (OPO) with Frequency Doubler Option (FDO). The GCR 200 generated a laser beam at a wavelength of 355 nm, which pumped the OPO. The OPO was a coupled dual oscillator system including the power oscillator, which was seeded by the narrow output maser oscillator. The gain in the OPO system was accomplished from the nonlinear interaction between the intense optical wave (laser) and crystal having a large nonlinear polarizability coefficient. Tuning of wavelengths of the passing laser was obtained by altering the angle of the OPO crystals made from Type I Beta Barium Borate (BBO) crystal. The tuning wavelengths range from 190 – 2000 nm (ultraviolet to infrared) when using the FDO.

PLIF measurements were acquired by using a laser and a Princeton Instruments Model ICCD 576-G/RB-E camera with narrow bandwidth filter (± 10 nm), which reduced effects of background noise or stray light. A focusing lens was also placed in front of the camera to focus the images onto the ICCD array. The output beam of the OPO/FDO was directed with a highly reflective optical turning mirror onto a cylindrical lens creating a laser sheet. The laser sheet created a 2-D sheet of radical fluorescence which was directed into the testing section. Florescence images were then acquired at 90^{o} to the incident laser sheet. A schematic diagram of this setup can be seen in Fig. 2.7. A dual channel digital delay with a gate pulse generator was used to control and synchronize the imaging process with the laser. The gate pulse generator was triggered using the Q-switch advance synchronizing signal.

The laser was tuned to the corresponding excitation wavelength of OH (283.5 nm) and later for CH (431 nm). OH was pumped at the Q_1 (6) transition in the OH $A^2\Sigma \leftarrow X^2\Pi$ system of the (1,0) band and the resulting fluorescence from the (1,1) band (315 nm) was collected. CH PLIF was done using the transition of (0,0) band near 431 nm of the $A^2\Delta \leftarrow X^2\Pi$ system. In case of CH the transition was highly diagonal hence the excitation and detection were done on the same band.

PLIF images were captured from a flame region panning from the injector exit to 5 cm above the burner. Because of the limited field of view of the ICCD camera composite images of the flames were overlapped and used. Images are presented as normalized signal intensities providing a qualitative representation. Signal intensities were normalized by dividing all readings by the maximum value

detected by the ICCD for a fuel; this is further discussed in Chapter 5. A total of 40 images were acquired using WinView /32 ver 2.5.23.0 data acquisition software and averaged.

2.3.6 Soot Volume Fraction Measurements

A 5 mW Helium-Neon laser (λ = 632.8 nm) was used as a light source with a power detector that was placed opposite to the light source after passage through the flame. A schematic drawing of the setup used for soot volume fraction is presented Fig. 2.8. The beam attenuation due to the presence of soot was obtained by measuring the intensity of light with and without the flame field. The burner remained stationary, requiring the laser and power detector to be placed on traversing mechanisms to obtain radial and axial profiles. The laser and power meter were moved equal distances in the radial direction and traversed in the axial direction at the same locations where flame temperature and in flame species concentrations had been recorded. The power detector provided both digital and voltage outputs. Voltage readings from the power detector were sent into a data acquisition board with Labview 7.1 and were digitally sampled at the rate of 2 Hz for 1 minute. The average of the collected power readings at each location was then used in the calculation of soot volume fraction. Equation (2.4) presents the relationship used for the calculation of this parameter. This relationship derives from the application of Beer's Law and Mie's theory as seen in a paper by Yagi and Iino (1962) for a propane-air flame. This relationship has been used by several authors including Bryce et al. (2000) who studied the soot distributions in a diesel-air flame and combustion in a diesel engine. Pickett and Siebers (2004) also used this relationship for a constant volume, high pressure and temperature, constant volume combustion of a diesel fuel jet flame.

$$f_v = \frac{-\ln\left(\frac{I_o}{I_s}\right)\cdot\lambda}{k_\lambda \cdot \delta} \tag{2.4}$$

For Eq. (2.4) I_s was the incident laser intensity, I_o the attenuated laser intensity, k_λ the spectral extinction coefficient based on the refractive indices of the soot, λ the laser wavelength, and the δ the flame thickness.

For the flame thickness calculations the visible flame images, assuming axisymmetry, of each fuel were used and processed with GIMP 2.6.6 visual software. Further, the spectral extinction coefficient was assumed to follow Eq. (2.5) defined by Bryce et al. (2000), where the refractive index of soot had a value of 1.80 + i0.58 at a signal wavelength of 633 nm. For Eq. (2.5) η and κ represented the real and imaginary parts of the refractive index, respectively.

$$k_\lambda = \frac{36\pi\eta_\lambda\kappa_\lambda}{\left(\eta_\lambda^2 - \kappa_\lambda^2 + 2\right)^2 + 4\eta_\lambda^2\kappa_\lambda^2} \tag{2.5}$$

2.4 Stoichiometric Calculations

The fuels used in the present study were assumed to have a general chemical formula based on the average composition of the hydrocarbons or fatty acid methyl ester components that comprised the diesel and biodiesel fuels. The chemical equation used for the calculation of the stoichiometric air/fuel ratio for oxygenated or hydrocarbon fuels can be seen in Eq. (2.6):

$$C_xH_{2y}O_{2z} + a\,(O_2 + 3.76N_2) \rightarrow xCO_2 + y\,H_2O + (3.76a)\,N_2 \qquad (2.6)$$

where;

$$a = x + \frac{y}{2} - z \qquad (2.7)$$

And the stoichiometric air/fuel ratio by mass can be calculated by Eq. (2.8):

$$AF_{stoic} = \frac{a(32 + 3.76 \cdot 28)}{12x + 2y + 32z} \qquad (2.8)$$

Calculation of the AF_{stoic} by mass for diesel, canola methyl ester, soy methyl ester, methyl stearate, and dodecane is presented in Table 2.2.

2.5 Reynolds Number Calculations

The range of tested equivalence ratios was based on the premixed to partially premixed combustion that occurs in some combustors. The change in equivalence ratio was accomplished by varying the volumetric air flow rate and maintaining the fuel flow rate constant. The mixture flow rates were kept so as to maintain laminar flow hence a low Reynolds number (Re) at the exit of the injector. Viscosities for the vaporized fuel and air mixture were calculated with data from Maxwell (1968) and the Eqs. (2.9-10) from Kanury (1975).

$$\mu_{mixture} = \sum_{i=1}^{n} \frac{\chi_i \mu_i}{\sum_{j=1}^{n} \chi_j \Omega_{ij}} \tag{2.9}$$

$$\Omega_{ij} = \frac{1}{\sqrt{8}} \left(1 + \frac{MW_i}{MW_j} \right)^{-1/2} \left[1 + \left(\frac{\mu_i}{\mu_j} \right)^{1/2} \left(\frac{MW_j}{MW_i} \right)^{1/4} \right]^2 \tag{2.10}$$

Where χ_i is mole fraction of the species i, n is total number of species in the mixture, μ_i is the viscosity of the species i, and MW_i is the molecular weight of species i. Table 2.3 lists the nominal experimental conditions and range of Re for the fuels.

Experimental uncertainties are also given in Table 2.4. The values shown are based on the student-t distribution 95% confidence interval.

2.6 Description of Test Matrix

Experiments presented in this dissertation were performed to complete the initial objectives which were to:

1. Develop a method for the rapid characterization of the combustion properties of liquid fuels and validate this technique using only small amounts of fuel.
2. Determine the dominant mechanism(s) (Zeldovich, Fenimore, etc.) and effect of chemical parameter iodine number on the increased NO_x formation for biofuels on when compared to diesel on a chemical basis alone.

Chapter 3 presents the development and validation of the method of rapid characterization of combustion properties of liquid fuels in detail. This newly developed method was then extended to complete the second objective.

Table 2.5a and Table 2.5b describe the conditions and fuels used for both the global and flame structure measurements required for the second objective. Each of the five fuels was tested over a range of equivalence ratios from 1.2 to 7. This range was selected to simulate the premixed to partially premixed combustion that occurs locally in diesel engines and rich burn zones of utility furnaces. Fuels also provided a range of the chemical parameter iodine number from 0.5 to 141.6.

Table 2.1 Parts and Instrumentation used for the present study

Key Parts and Instrumentation	**Manufacturer/ Model Number**
Syringe Pump	Harvard Apparatus 975
50 cc Interchangeable Syringe	B-D Multifit 512135
High Temperature 11 mm Inlet Septa	Agilent 5183-4757
High Temperature Heavy Insulated Heat Tape	Omega Engineering Inc. STH051-080
Rotameter with Tantalum Ball	Lo-Flo with Tube Type SK ¼’’-15-G-5
Omega Temperature Control	Omega Engineering Inc. CN79022
Digital AF SLR 8 MP Camera	EOS Digital Rebel XT/EOS 350D
NO_x, CO, CO_2, O_2 Emission Analyzer	NOVA 376 WP
Type R and Type K Thermocouple	Omega Engineering Inc.
Radiometer	Hy-Cal P-8410-B-10-120-XC-400
Precision Laser Power Meter	Coherent FieldMate 1028297
5 mW He-Ne Laser	Spectra Physics 105-1
Pulsed Nd: YAG Laser	Spectra Physics GCR 250-10
Optical Parametric Oscillator (OPO)	Spectra Physics MOPO-730
Frequency Doubler (FDO)	Spectra Physics FDO 970
Photomultiplier Tube with Cooled Housing	Oriel Instruments 77345/77265
Photomultiplier Power Supply	Oriel Instruments 70705
Spectrometer with Holographic Grating	Oriel Instruments 77700 and 77740
Pulsed Laser Power Meter	Ophir Optronics Ltd. NOVA 30
ICCD Camera	Princeton Instrument ICCD-576E
Digital Gate Pulse Generator	Princeton Instrument PG – 200
Camera Controller	Princeton Instrument ST-138
ICCD Camera Image Acquisition Computer	Gateway P-200
Data Acquisition Hardware	National Instruments Labview Board SCB-100
Data Acquisition Software	National Instruments Labview 7.1
Data Acquisition Computer	Dell OptiPlex GX – 400
Image Acquisition Software	Princeton Instrument WinView
Traversing Mechanism	Unislide / Velmex Inc.

Table 2.2 Stoichiometric air/fuel ratio calculated by mass for all fuels tested

Fuel	$(A/F)_{stoic\ by\ mass}$
No. 2 Diesel	14.32
Dodecane	14.94
Canola Methyl Ester	12.52
Soy Methyl Ester	12.43
Methyl Stearate	12.67

Table 2.3 Nominal Experimental Conditions

Tubular Burner Diameter	Inner Diameter 9.5 mm Outer Diameter 12.7 mm
Volumetric Fuel Flow Rate (m^3/s)	2.67×10^{-8}
Air Flow Rate Range (m^3/s)	Diesel: $3.83 – 22.5 \times 10^{-5}$ Dodecane: $3.5 – 20.6 \times 10^{-5}$ CME: $3.5 – 20.6 \times 10^{-5}$ SME: $3.5 – 20.6 \times 10^{-5}$ MS: $3.5 – 20 \times 10^{-5}$
Injector Exit Reynolds Numbers (based on gas mixture density and viscosity at 430 ^oC)	125 – 745
Ambient Temperature	295 K
Ambient Pressure	101 KPa
Feedline Temperature	430 ^oC

Table 2.4 Estimated experimental uncertainties (± Percentage of Mean)*

Flame Length	12.5 %
Temperature	5 %
EI_{NO}	11 %
EI_{CO}	15 %
Concentration of NO_x	5 %
Concentration of CO	11 %
Concentration of O_2	4 %
Concentration of CO_2	8 %
Radiative Fraction	9.5 %
Soot Concentration	13.5 %

*values obtained at a 95% confidence level with student-t distribution

Table 2.5a Test Matrix (Global Properties)

Fuels	Iodine Number	Equivalence Ratio	Measured Parameters
Diesel	8.6	1.2, 2, 3, 7	Flame Length, Emission Index, Radiation
Dodecane	-	1.2, 2, 3, 7	
CME	115	1.2, 2, 3, 7	
SME	141.6	1.2, 2, 3, 7	
MS	0.5	1.2, 2, 3, 7	

Table 2.5b Test Matrix (Flame Structure Measurements)

Fuels	Iodine Number	Equivalence Ratio	Measured Parameters
Diesel	8.6	1.2, 2, 3, 7	OH/CH concentration, Temperature Profiles, Emission Profiles, Soot Volume Fraction
Dodecane	-	1.2, 2, 3, 7	
CME	115	1.2, 2, 3, 7	
SME	141.6	1.2, 2, 3, 7	
MS	0.5	1.2, 2, 3, 7	

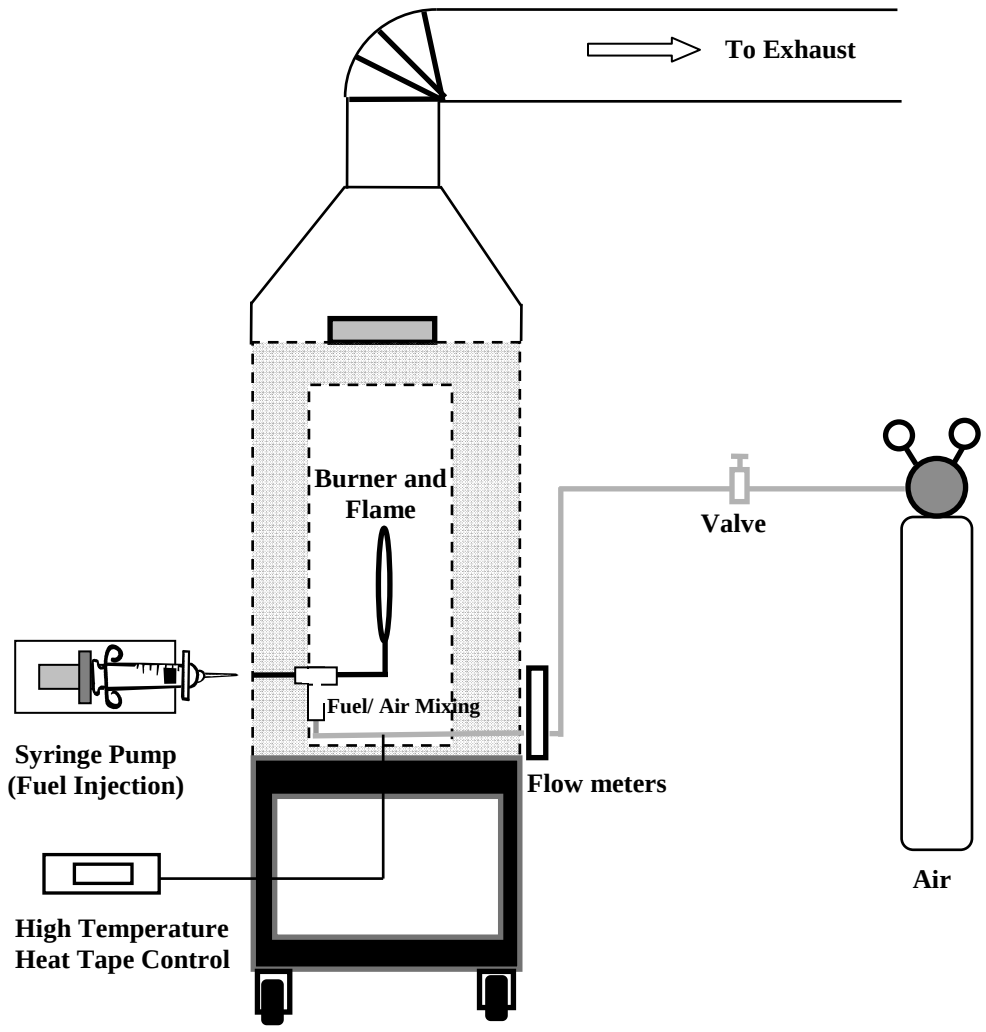

Figure 2.1 Laboratory combustion chamber and fuel supply train

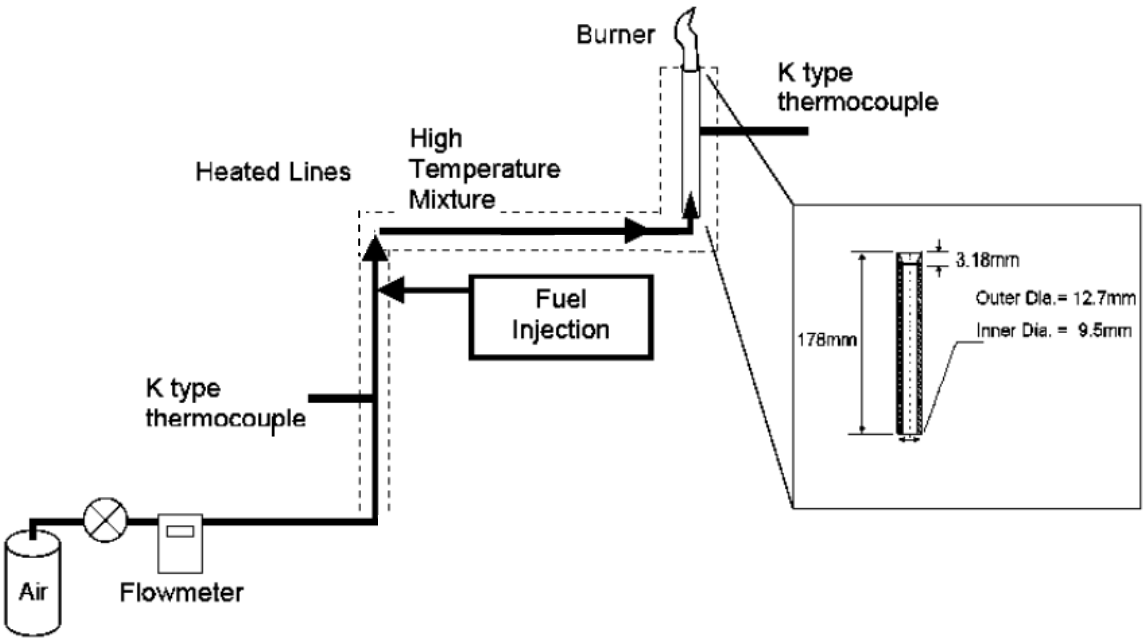

Figure 2.2 Schematic diagram of the experimental setup with burner

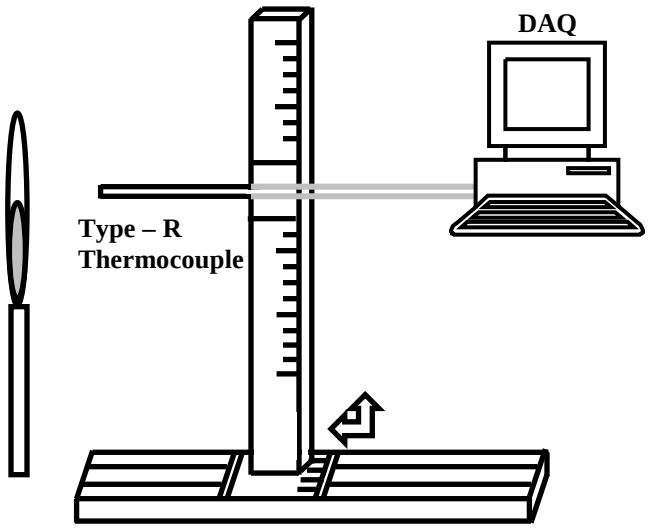

Figure 2.3 Schematic drawing of the thermocouple and traverse used for temperature measurements

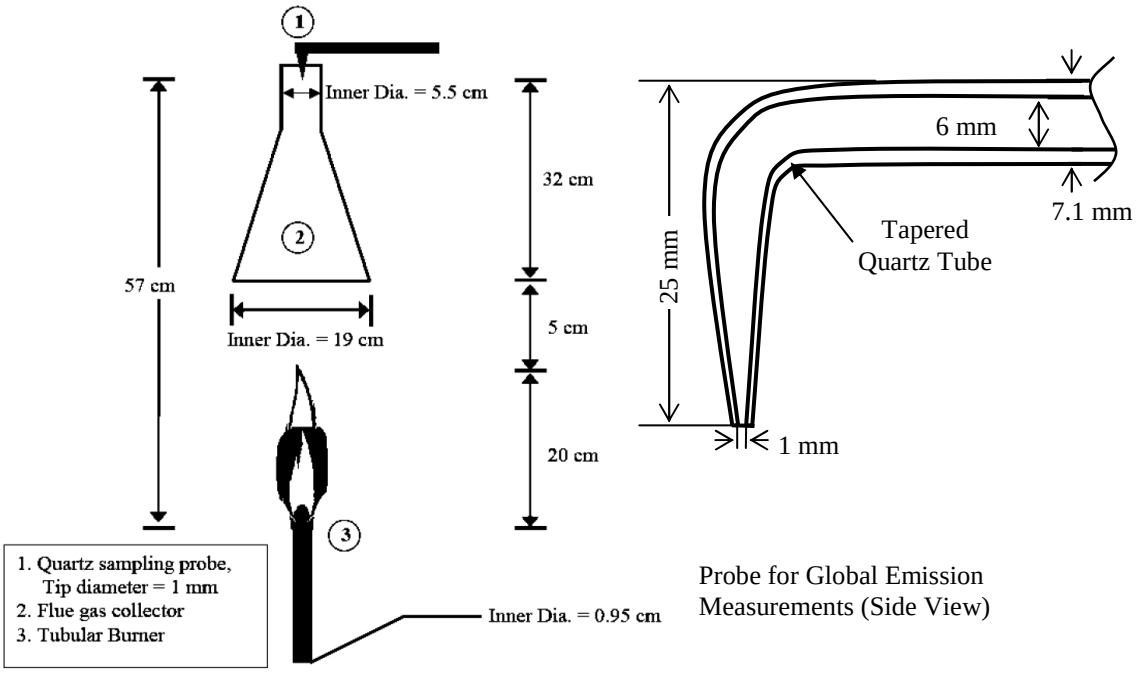

Figure 2.4 Schematic diagram of the global emissions sampling setup and quartz probe

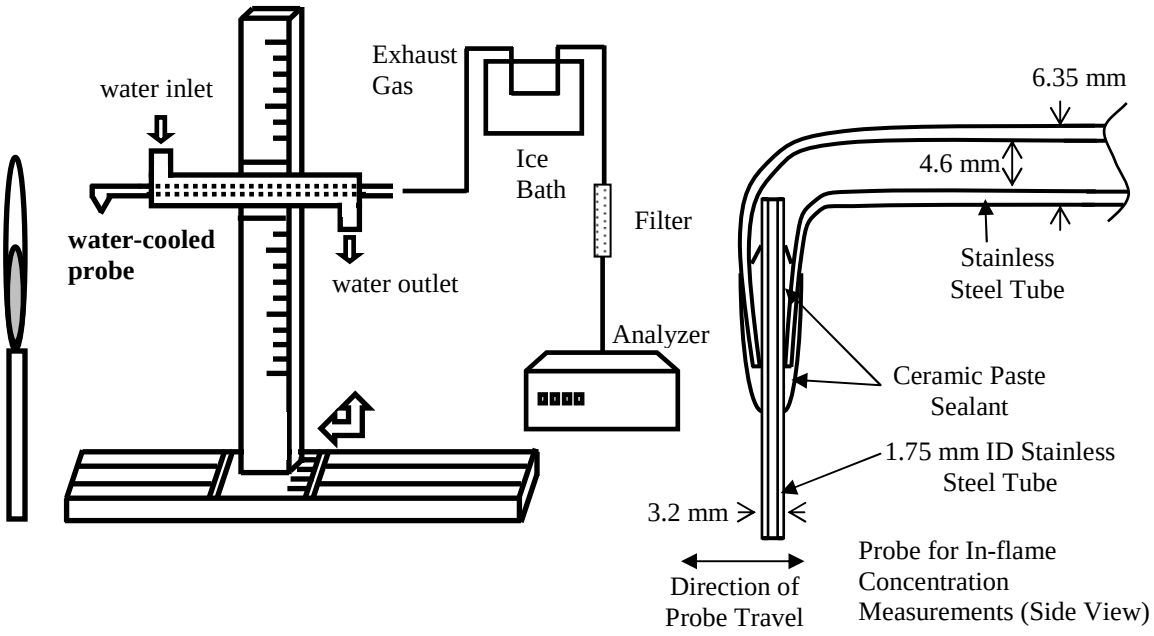

Figure 2.5 Schematic diagram of in-flame emissions experimental setup and water cooled stainless steel probe

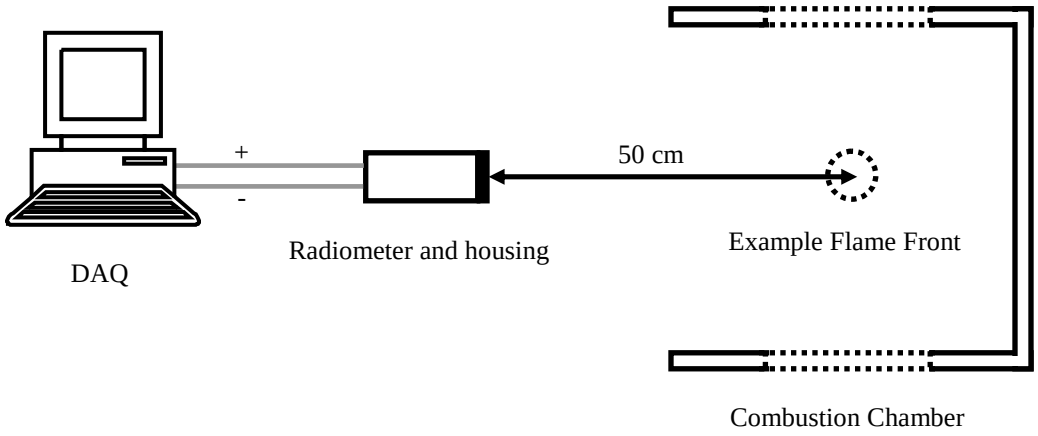

Figure 2.6 Top view drawing of the global radiative emission setup

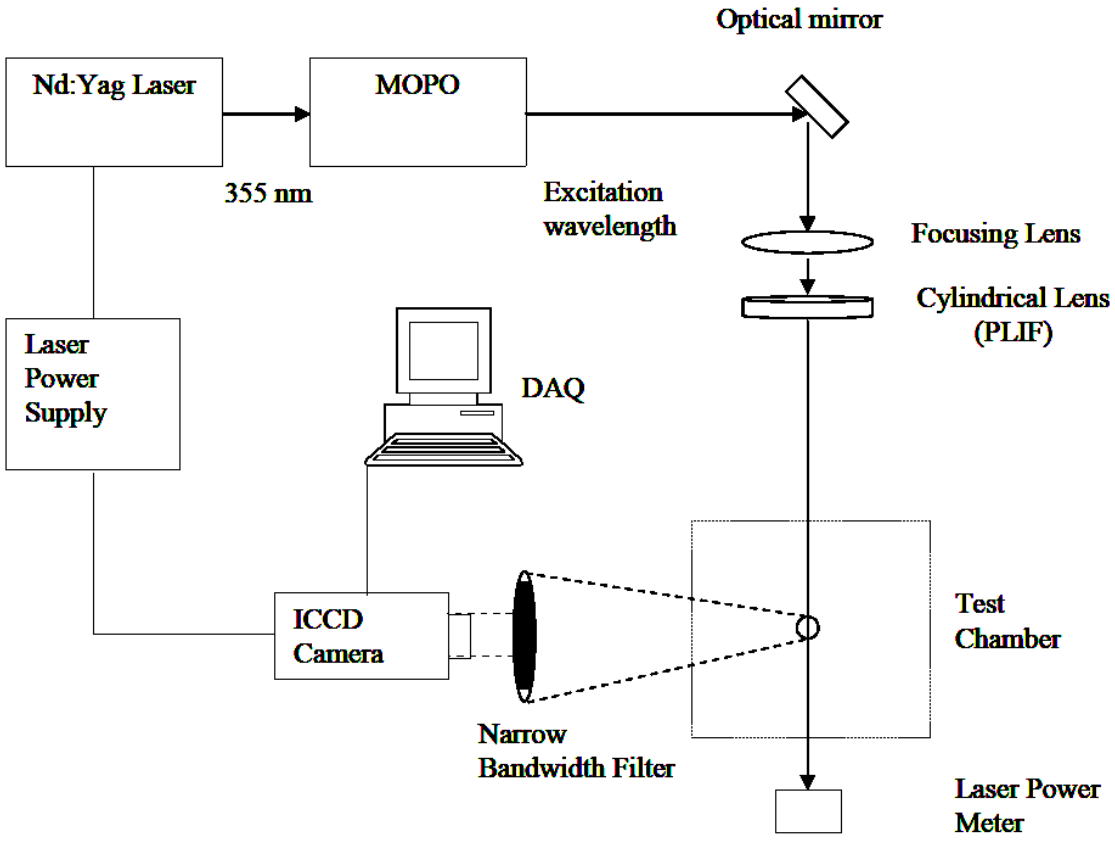

Figure 2.7 Experimental setup for PLIF measurements

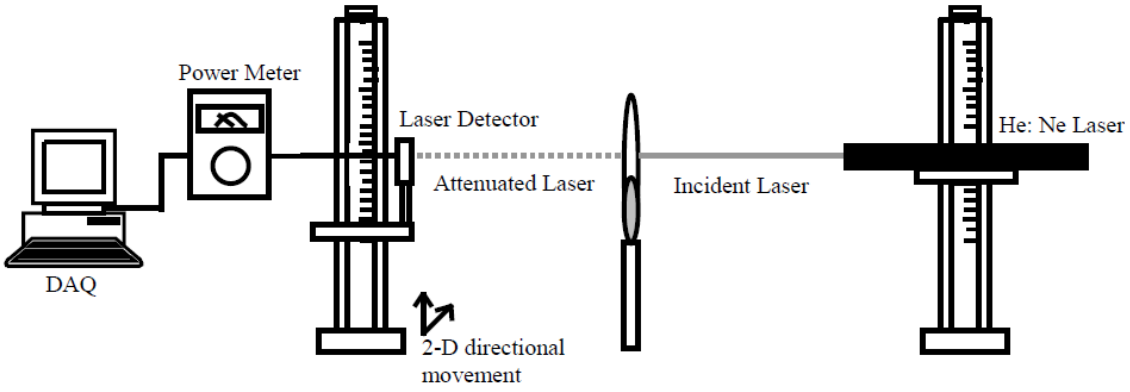

Figure 2.8 Schematic drawing of experimental setup used for soot volume fraction measurements

Chapter 3
Development of Experimental Technique

To meet the first objective, to rapidly assess the combustion properties of liquid fuels in a laminar combustion environment, the appropriate experimental apparatus was developed. This chapter extends on the description of the experimental setup used in Chapter 2 and describes its development and validation process in detail.

3.1 Burner and Fuel Delivery System Development

The burner selection process was based on the ability to:

- Maintain a laminar flame with combustion properties to be dependent only on fuel chemical properties (independent of flow characteristics)
- Heat reactants to temperatures that would vaporize the liquid fuel completely without coking.
- Support a variety of flames including premixed, partially premixed, and non premixed flames
- Provide repeatable measurements

There were four burners that were considered for the experimental setup including: flat flame, counter flow, Bunsen, and tubular burners. Digital camera photographs of the burners are presented in Fig. 3.1. A brief description of the burners and their implementation is also given in the following sections.

3.1.1 Flat Flame Burner

The first burner considered was the flat flame burner. The flat flame burner apparatus consisted of a cylindrical chamber with a 6 cm diameter porous medium disc constructed of sintered stainless steel at its top. A water cooling system extended throughout the entire system entering at the base of the burner and circulating throughout. The burner provides a laminar and uniform flame front, however, presented difficulties for this project. Specifically, heat input to the burner became difficult since the water cooling jacket acted to continuously cool the fuel/air mixture potentially condensing the liquid fuel in the porous medium. Another difficulty was to ensure that the porous medium did not clog due to soot or coking that occurred when burning fuels with high aromatic content such as diesel or toluene.

3.1.2 Counter Flow Burner

The next burner considered was a counter flow device. The counter flow burner was manufactured in the Aerospace and Mechanical Engineering machine shop. The burner nozzles were made from brass and aluminum and were surrounded with copper tubing. They were placed along the outer surface of the burner to remove excess heat transferred to the aluminum section of the burners. The two nozzles, identically manufactured, were placed above each other on a traversing mechanism allowing the adjustment of the axial separation between the burners. The contour of the burner nozzle was designed to produce a flow that was uniform and laminar at its exit. This burner, however, was not used since sufficient uniform heating to vaporize a liquid fuel was difficult due to the complex design of the burner.

3.1.3 Bunsen Burner

The Bunsen burner was the next considered. Fuel sent through the base of the burner caused air to be drawn in from the ambient environment through its inlet ports. The area of air ports increased or decreased allowing for more or less air, changing the equivalence ratio of the resulting premixed flame at the burner exit. This burner's simple design allowed for uniform heating along the surface, however, air drawn through the inlet ports could not be measured without performing complicated procedures. Therefore, this burner was also not used.

3.1.4 Tubular Burner

Because of its simple design, easily heated surface, and simple manufacturing procedure the tube burner was selected for this study. For low fuel and air flow rates this burner supports laminar lean and rich premixed, partially premixed, and non-premixed flames ideal for the present investigation. A drawing of this burner can be seen in Fig. 3.2.

3.1.5 Heating the Setup

In order to completely vaporize the liquid fuel the correct temperature needed to be selected and the appropriate method applied to heat to the setup. The boiling points of the fuels used in the present experiment can be seen in Tables 1.1-1.3 and Table 3.1. Based on their final boiling point of all fuels tested a temperature of 430^{o}C was selected for nominal operational conditions. In order to heat the experimental setup to this temperature 627 watt heating tapes were used. The heating tapes were wrapped around the 12.7 mm (OD) stainless steel tubing. Power was supplied to the tapes by a regulated proportional control. The proportional control was regulated by the temperature within the feed lines that were monitored with embedded K-Type thermocouples.

3.1.6 Fuel delivery System Development

A schematic of the initial experimental setup is shown in Fig. 3.2. Methane and air were passed through the heated lines to establish a premixed flame at the exit of the burner. Methane was used to ignite and stabilize the flame resulting from the vaporized liquid fuel. Flow rates of methane and air were monitored with mass flow meters and were kept constant for all conditions. In order to transfer the liquid fuel into the heated air stream a 3 cm^3 capacity hand injection syringe was initially chosen. Small amounts of fuel were injected through a high temperature septum placed the carrier gas stream. A known volume of liquid fuel was injected using the hand syringe. The time of injection was measured using a stopwatch; thus, the average liquid fuel flow rate was calculated. To determine the radiation heat flux from the fuel alone, data were taken from the methane flame and background 60 seconds prior to the liquid fuel injection and was subtracted from its value at all data points. Upon injection of the fuel vapors the flame length, luminosity, and radiation increased significantly; however, results obtained by this method were unsteady. Figure 3.4 shows an example of the radiation heat flux obtained from injecting the fuel with a hand operated syringe for CME and diesel fuel. The radiation heat value used in the calculation of the radiative fraction of heat released (F-values) seen in Eq. (2.3) was determined by determining the area under the curve in Fig. 3.4 using the Simpson's 3/8 Rule integration technique.

Manual injection was initially chosen for delivery of the fuel to the setup for its simplicity. However, unsteady flow rates and errors from approximations in

the integration of the radiation heat flux required a new technique to deliver the fuel. For these reasons a syringe pump was used which provided steady volumetric flow rates to the burner. The steady readings reduced errors in the calculation of the measured heat flux from the flame. Figure 3.5 shows a typical heat flux measurement, after subtraction of the methane and background radiation, using the syringe pump injection method. From Fig. 3.5 it can be seen that the initial and final radiation measurements were zero having a steep increase in the heat flux when the liquid vapor was introduced with a drop to zero once the supply of fuel vapor had ceased. The radiation heat flux remained flat during the duration of fuel burning, indicating that the liquid fuel supply was steady. An average value of the steady radiation heat flux was then used in the calculation of the radiative heat fraction, Eq. (2.3).

3.2 Effect of Liquid Fuel Injection Rate

The first set of experiments were conducted to determine the optimal conditions at which the measurements would be independent or weakly sensitive to burner operating variables other than the fuel. The fuel injection rate was one such variable. Figure 3.6 shows the variation of the radiative heat fraction with liquid fuel injection rate for No. 2 diesel and CME biodiesel flames. The measured radiative fraction values were in agreement with the results of Hura and Glassman (1987) for hydrocarbon fuels. Although the radiative heat fraction was weakly dependent on the fuel injection rate, the maximum values occurred at a particular injection rate (1.60 cm^3/min for CME B100 and 0.82 cm^3/min for the No. 2 diesel). Love et al. (2009) showed that for petroleum derived hydrocarbon fuels, the maximum radiative heat fraction occurred at the same injection rate, whereas the biofuels required a different flow rate for maximum radiation. This was thought to be due to the presence of oxygen in their fuel molecules. Thus, to compare maximum radiation potential of different families of fuels, it would be necessary to make a small adjustment to the fuel injection rate of the liquid fuels.

3.3 Effect of Methane in Fuel of Flames

After establishing the appropriate burner and fuel delivery system, which met the requirements listed in the objectives of this report, it was desired to determine the effect methane had on the combustion characteristics. Flame studies conducted up to this point had burned in a methane-air-liquid fuel vapor mixture. To quantify the effect of methane two conditions were considered:

Mode 1 – Vaporized fuel flame burning with a methane-air flame ($\phi_{methane,}$ shown on plots is the ratio of the stoichiometric air/methane mass flow ratio to the actual air/methane mass flow ratio.)

Mode 2 – Vaporized fuel flame burning with external ignition source and removed during the test

Figure 3.6 presents the radiative heat fraction of CME and diesel fuels plotted against fuel injection flow rate. The maximum uncertainties are shown as error bars. For Mode 1, the radiation associated with the premixed methane-air flame and the background was subtracted from the total measured radiation to quantify the value emitted from the combustion of fuel alone. For Mode 2, only the background radiation was subtracted since the methane supply was switched off at the onset of ignition. Table 3.2 shows the nominal operating conditions for both Mode 1 and Mode 2.

No measurable dependence of radiative fraction on the methane flame equivalence ratio was observed for Mode 1, indicating that the influence of pilot flame characteristics on the radiative emission of liquid fuels in these tests was insignificant (Fig. 3.6). However, the radiative heat fraction measured in Mode 1 flames was 5-10 % higher than the corresponding values in the Mode 2 tests. This was traced to the higher temperature, promoting injected fuel pyrolysis in the presence of the methane-air pilot flame in Mode 1. Therefore, Mode 2 was selected for further studies in order to eliminate the pilot flame effects.

3.4 Validation of Experimental Setup

3.4.1 Radiative Fraction

In order to validate the present experimental technique the values of radiative fraction of heat release measured in this study were compared with those reported in literature. Two additional fuels other than those listed in Chapter 1, toluene and kerosene, were tested to compare with values easily available in literature. The properties of these fuels can be found in Table 3.1. Figure 3.7 presents the values of radiative heat fraction for the fuels tested in the present study to the values available in literature. For this study toluene exhibited the highest radiative heat fraction (0.41) at 0.82 cm^3/min followed by kerosene (0.36), petroleum derived No. 2 diesel fuel (0.32), and CME B100 biodiesel fuel (0.23), in that order. The values did not change significantly even as the liquid fuel flow rate was doubled to 1.60 cm^3/min with toluene again producing the highest F-value (0.38) followed by kerosene (0.32), diesel (0.32), and CME (0.27). The toluene flame produced the highest amount of radiation for both cases, hence produced the highest amount of soot, whereas the biodiesel flame had the least radiative fraction and the least soot emission. These observations are in accordance with previous results from literature (Jassma and Borman, 1980, Koseki, 1989, Wade et al., 1995, Durbin et al., 2000, Pinto et al., 2005).

Figure 3.8 presents flames of No.2 diesel, kerosene, and toluene which were completely luminous yellow corresponding to the formation and combustion of soot throughout the flame which emitted continuum radiation at all wavelengths, hence higher radiative heat fraction values. For the CME biodiesel flame a blue

region was observed near the injector exit indicating the dominance of gas-phase oxidation reactions. In this region the molecularly bonded oxygen was available to participate in the oxidation of hydrogen, carbon monoxide, and nitrogen, thus resulting in the blue hue observed at the base of the flame and lower radiative emission.

The present measurements for No. 2 diesel fuel and kerosene agree within experimental uncertainties with findings from Koseki (1989). Radiative heat fraction measured for toluene, however, was slightly lower than that provided by Koseki (1989) for liquid pool fires and Wade et al. (1995) for liquid spray flames. The differences in the size of the flames which affect the optical thickness in radiation emission, and the differences in the fuel-air mixing conditions (homogeneous conditions in the present study as opposed to the heterogeneous reactions which become dominant in sooty flames account for the lower values in the present case). Nonetheless, the close agreement of the literature values with the current measurements establishes confidence and validates the current technique.

3.4.2 Comparison with Published Values of Emission Index

Global pollutant emissions from the flame were determined with the Emission Index which expresses the amount of pollutant formed per unit mass of fuel burnt. The global Emission Index of NO and CO were calculated with concentration measurements from gases sampled from the flames. Two additional fuels other than those listed in Chapter 1, pentane and heptane with properties shown in Table 3.1, were also tested to compare to values easily available in literature.

Measurements were taken at the injection rate corresponding to the maximum radiative heat fraction values of 0.82 and 1.60 cm^3/min, Fig. 3.9. The pentane flame produced the highest EI_{NO} value (1.03 g_{NO}/kg_{fuel}) followed by heptane (1.00 g_{NO}/kg_{fuel}), CME (0.71 g_{NO}/kg_{fuel}), and petroleum diesel (0.59 g_{NO}/kg_{fuel}) at the fuel injection rate of 0.82 cm^3/min. Results for EI_{NO} at the next fuel injection flow rate of 1.60 cm^3/min also showed that pentane produced the highest value (1.27 g_{NO}/kg_{fuel}), followed by heptane (1.05 g_{NO}/kg_{fuel}), CME (0.81 g_{NO}/kg_{fuel}), and diesel (0.75 g_{NO}/kg_{fuel}) in that order. A comparison between the values obtained in this study and those found in literature is presented in Table 3.3. Pentane and heptane flames from the present study produced values of EI_{NO} within experimental uncertainties to those of Jaasma and Borman (1980). Table 3.3 also shows that a relative comparison of EI_{NO} for CME and diesel agree with engine testing results. For the present study it has been shown that CME produced 9% higher NO emission than diesel fuel at a fuel injection flow rate of 1.60 cm^3/min which is comparable to results engine studies (Durbin et al., 2000, McCormick et al., 2001).

EI_{CO} measurements were also calculated at the two injection fuel flow rates corresponding to the maximum radiaitive heat fraction, 0.82 and 1.60 cm^3/min, Fig. 3.9. The inverse trend of EI_{NO} was observed for these measurements where pentane produced the lowest value (3.88 g_{CO}/kg_{fuel}) followed by heptane (4.6 g_{CO}/kg_{fuel}), CME (16.26 g_{CO}/kg_{fuel}), and petroleum diesel (36.5 g_{CO}/kg_{fuel}) at the fuel injection rate of 0.82 cm^3/min. Results for EI_{CO} at the next fuel injection flow rate of 1.60 cm^3/min also showed that pentane produced the lowest value (5.88 g_{CO}/kg_{fuel}), followed by heptane (11.22 g_{CO}/kg_{fuel}), CME (19.36 g_{CO}/kg_{fuel}), and diesel (41.5 g_{CO}/kg_{fuel}). A comparison between the values obtained for EI_{CO} in this study and those found in literature is also presented in Table 3.3. A relative comparison of EI_{CO} for CME and diesel also agree with engine testing results. For the present study it has been shown that CME produced 53% lower CO emission than diesel fuel at a fuel injection flow rate of 1.60 cm^3/min which was comparable to results engine studies that found lower CO exhaust emissions ranging from 20 to 50 % (Durbin et al., 2000, Dorado et al., 2003).

3.4.3 Equivalence Ratio

For all test conditions in this chapter the air flow rate was kept constant at 2300 cm^3/min as the fuel flow rate was varied from 0.49 to 2.2 cm^3/min. Flow rates of all fuels for this chapter were selected based on the maximum F values of hydrocarbon fuels such as toluene, kerosene, pentane, heptane, diesel and oxygenated fuel CME. This resulted in different equivalence ratios for each fuel tested. The calculated equivalence ratios are listed in Table 3.4.

3.5 Chapter Summary

A method for the rapid characterization of combustion properties, such as Emission Index and flame radiation, that required only small amounts of a liquid fuel was developed. The present technique provides a quick method of comparing existing and new fuels such as biodiesel. The burner conditions were selected to make flame properties sensitive primarily to fuel chemistry. The technique was validated through a comparison of measured radiative heat release fraction and pollutant (NO and CO) emission indices available in literature. All petroleum-derived fuels showed a higher radiative heat fraction than CME. The CME biodiesel flames also had lower emission index of CO and higher emission index of NO compared to those of the petroleum-derived diesel flame. It is seen that the present values compare well with the emission indices documented during *engine testing* and in other flame configurations. Thus, the present technique also provides a valid tool to determine the NO and CO emission potentials of new fuels. The present technique can serve as a valuable tool for fuel researchers and developers to obtain quick feedback on the combustion properties of the new fuels. Since the various measurements are conducted simultaneously, the entire experiment can be completed within twenty minutes. Moreover, the relative ease with which the current setup can be operated and the small amounts of fuel needed was an additional benefit of the present method.

The technique described in this chapter was used for fuel rich equivalence ratios near 7 corresponding to the points of maximum radiative heat fraction/sooting tendency of each fuel. The following chapters of the dissertation

investigate the effect of equivalence ratio, fuel composition, and mechanism of formation on the observable increase in NO with biofuels compared to petroleum derived fuels.

Table 3.1 Composition and properties of other tested fuels

Fuel	**Molecular Formula**	**LHV (MJ/kg)**	**Density (kg/m^3)**	**BP (^oC)**
Toluene	C_7H_8	40.9	867	110
Kerosene	$C_{13}H_{26}$	41.6	825	250
Heptane	C_7H_{16}	44.9	684	99
Pentane	C_5H_{12}	45.3	626	36

Table 3.2 Nominal operating conditions for Mode 1 and Mode 2

Tubular Burner Diameter	Inner Diameter 9.5 mm Outer Diameter 12.7 mm
Volumetric air flow rate (m^3/s)	3.83×10^{-5}
Volumetric fuel flow rate (m^3/s)	$7 – 36.7 \times 10^{-9}$
Volumetric methane flow rate (m^3/s) – Mode 1	$5 - 8.2 \times 10^{-6}$
Reynolds number (based on gas mixture density and viscosity at 430^oC)	100-300
Ambient Pressure	101 kPa
Ambient Temperature	295 K
Feedline Temperature	430^oC

Table 3.3 Comparison of present experimental results to those in literature

Author	Fuel	EINO	EICO	NOx	NO	CO	Instrument
Jaasma and Borman (1980)	Pentane Heptane	0.96 0.93	-	-	-	-	Moving Thread Burner
Durbin et al. (2000)	Diesel and biodiesel	-	-	10% higher for biodiesel than diesel	-	20% lower for biodiesel than diesel	Various heavy duty diesel engines
McCormick et al. (2001)	Various biodiesel fuels including CME and commercial diesel	-	-	10% higher for CME than for diesel	-	-	Six cylinder, direct injected, turbocharged, four stroke engine rated at 345 bhp at 1800 rpm
Dorado et al. (2003)	Transesterified waste olive oil and diesel	-	-	-	-	60 % lower for OME than for diesel	2500 cc, three cylinder, four stroke, direct injection diesel engine
Lin and Lin (2007)	Soy Methyl Ester	-	15.2	-	-	-	Isuzu four stroke, four cylinder, 88hp, direct injection, 3800 cc diesel engine
Love et al. (2007) [1]	Pentane Heptane CME Diesel SME	1.27 1.05 0.81 0.75 0.86	5.88 11.22 19.36 41.1 18.33	-	8% higher for CME than diesel	53% lower for diesel than for CME	Tube Burner

[1] Injection flow rate of 1.60 cm^3/min

Table 3.4 Equivalence ratios for fuels tested at both flow rates under mode 2 condition

Fuel	Φ at 0.82 cm^3/min	Φ at 1.60 cm^3/min
Diesel	3.62	7.06
CME	3.28	6.39
Kerosene	3.57	6.97
Toluene	3.46	6.75
Pentane	2.84	5.53
Heptane	3.07	5.99

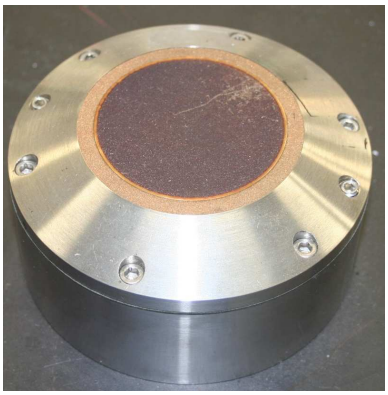

a

b

c

d

Figure 3.1 Digital camera photographs (not shown to scale) of the four burners considered: a) flat flame burner, b) counter flow burner, c) Bunsen burner, and d) tubular burner

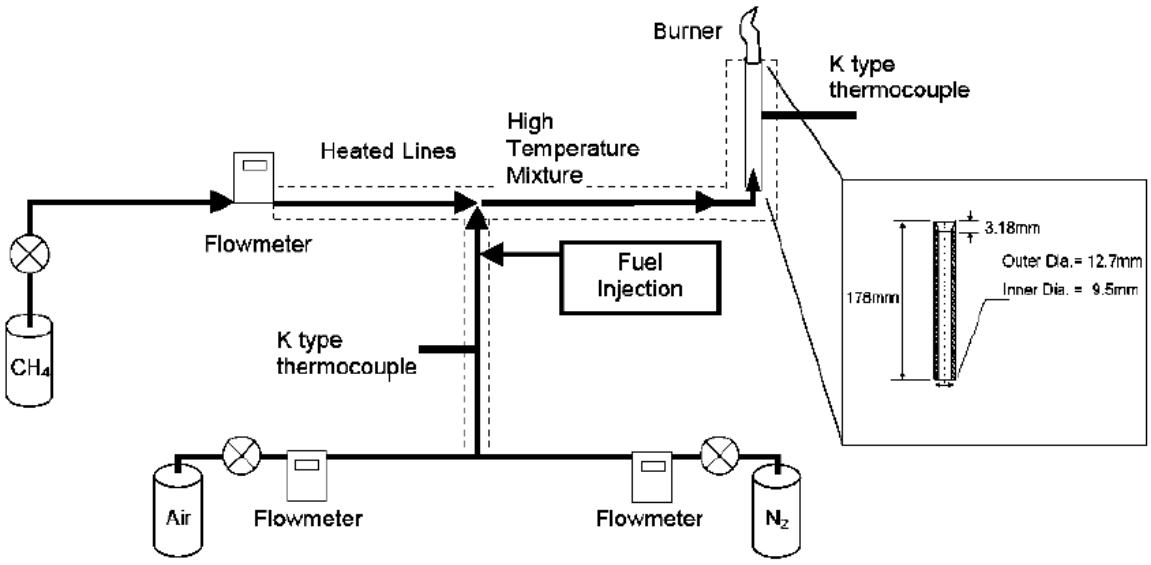

Figure 3.2 Schematic drawing of the initial experimental setup

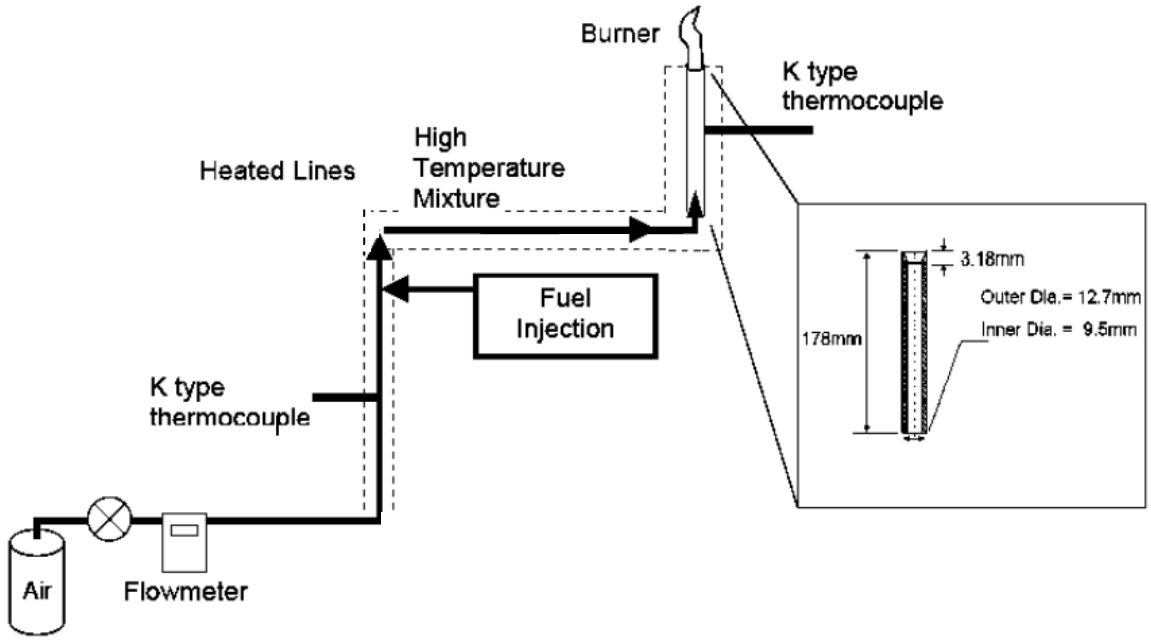

Figure 3.3 Schematic drawing of the final experimental setup

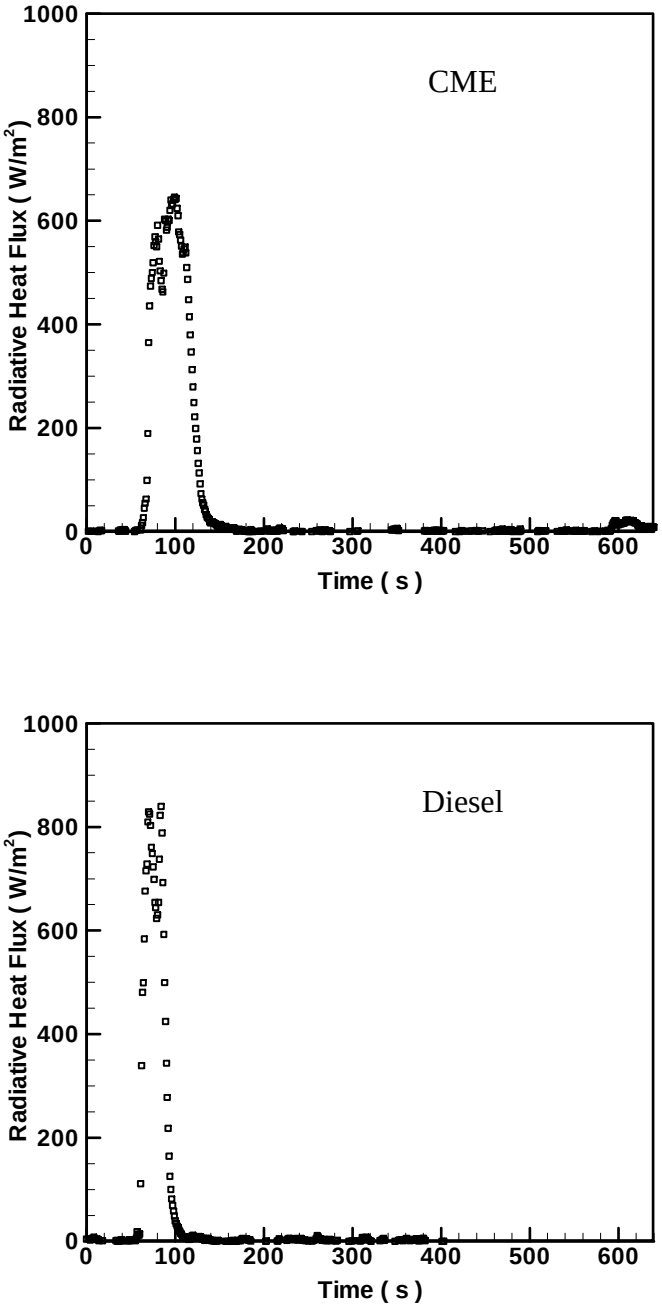

Figure 3.4 Example radiative heat flux for CME and diesel for an average manual injection flow rate of 2 cm^3/min

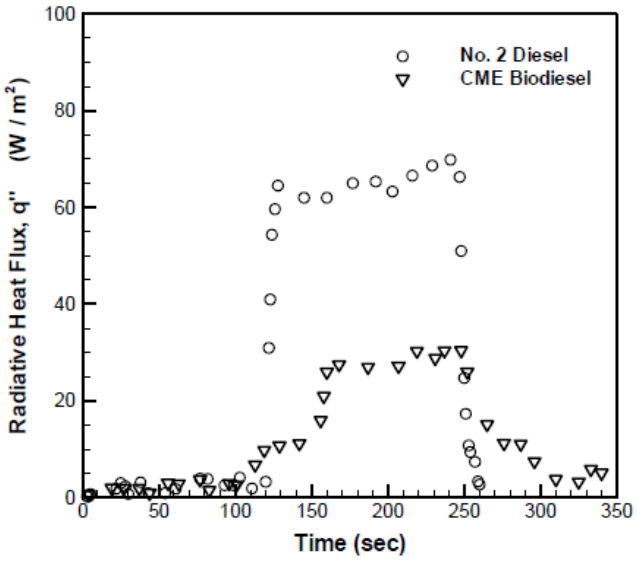

Figure 3.5 Example radiative heat flux for CME and diesel for syringe pump injection flow rate of 0.82 cm^3/min

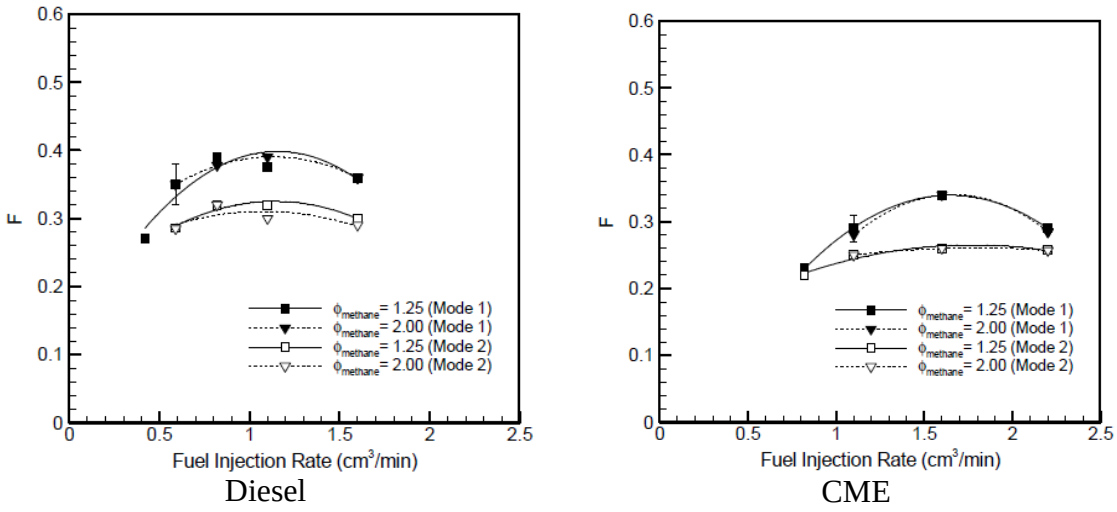

Figure 3.6 Radiative heat fraction plotted against liquid fuel flow rate for No. 2 Diesel and CME for Mode 1 and Mode 2 conditions

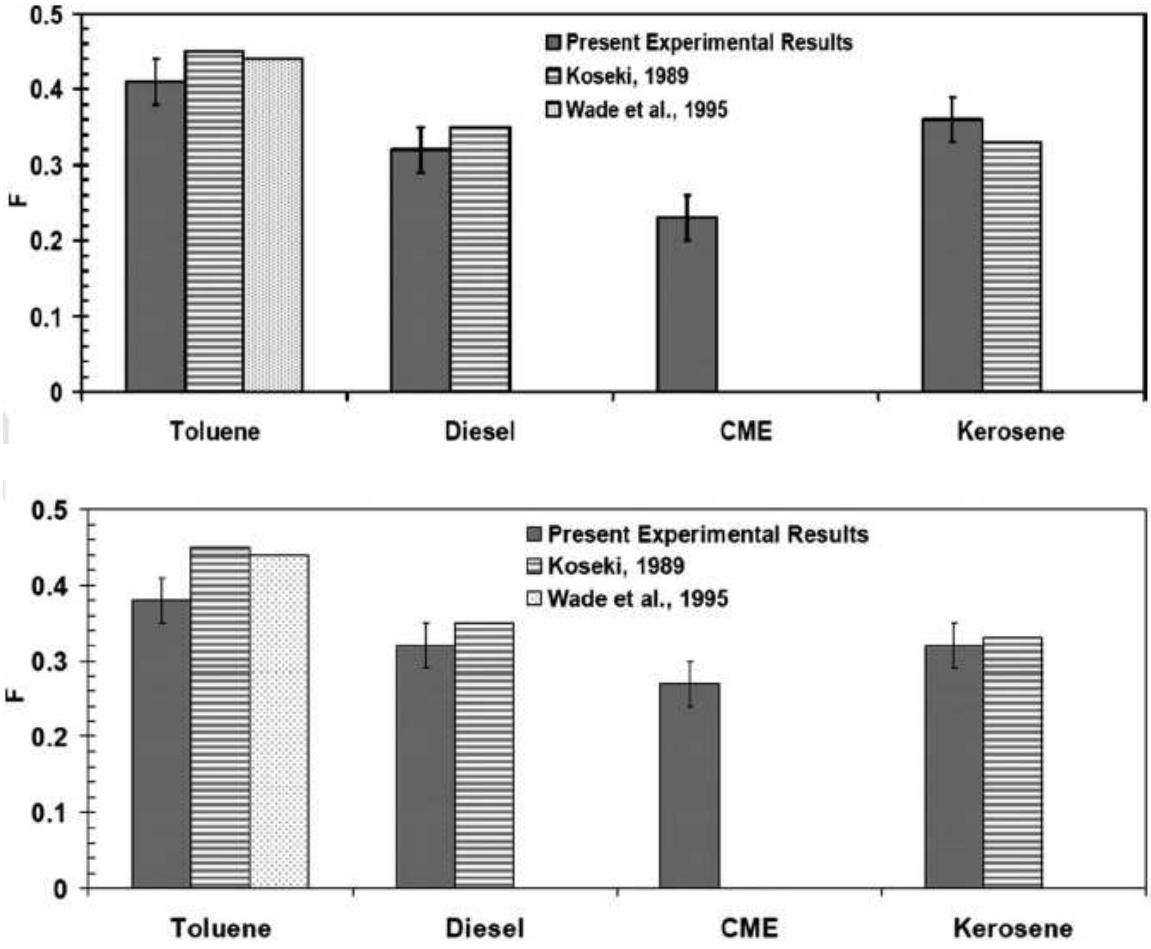

Figure 3.7 Radiative fraction of heat release for four fuels at (top) 0.82 cm^3/min and (bottom) 1.60 cm^3/min in comparison to values available in literature

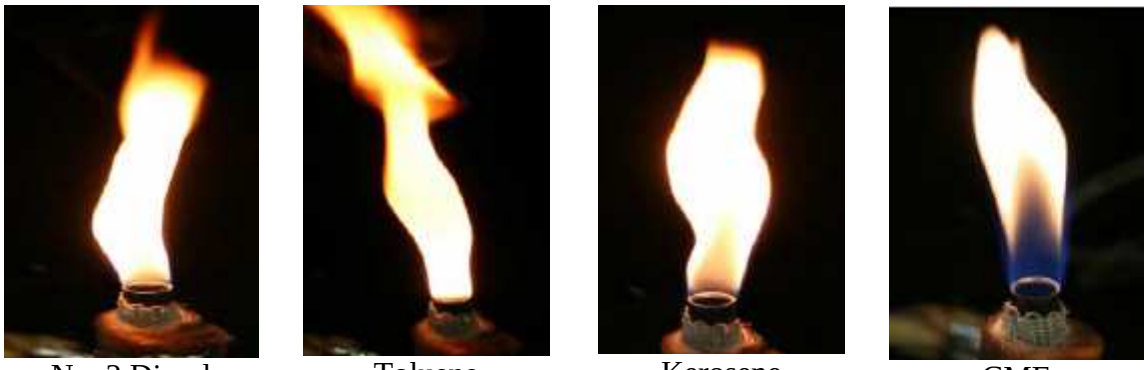

No. 2 Diesel | Toluene | Kerosene | CME

Figure 3.8 Visible flame images for tested fuels under mode 2 conditions at 0.82 cm^3/min

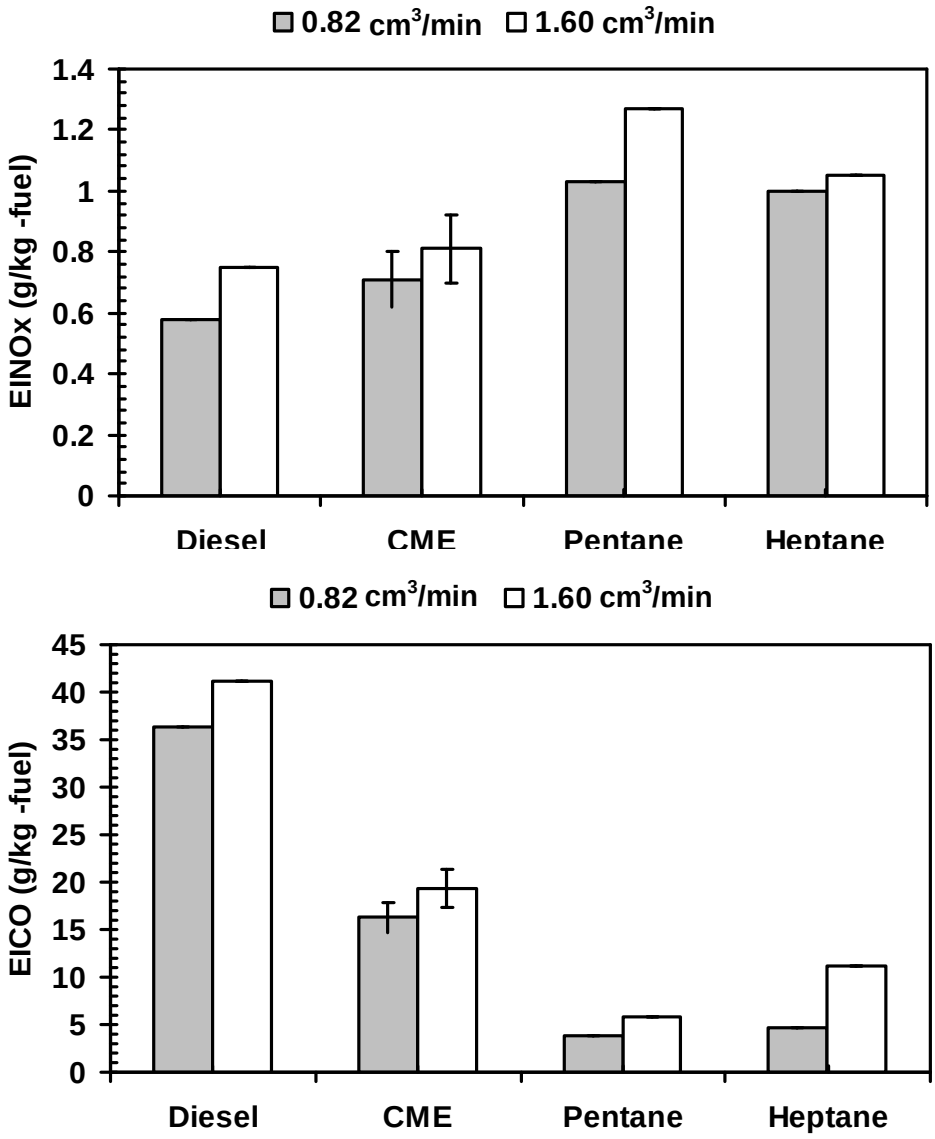

Figure 3.9 EI NO and EI CO for diesel, CME, Pentane, and Heptane

Chapter 4
Global Flame Properties

The previous chapter described a method to rapidly characterize the combustion properties of hydrocarbon and oxygenated liquid fuels. Results in Chapter 3, obtained from the burning of these fuels, demonstrated comparable trends for the pollutant emissions index of NO and CO to those available in literature for different burner and engine studies. This included the pollutant emissions of biodiesel and diesel. One particular point of interest for this study was the increase in NO observed when burning biodiesel instead of diesel fuel.

As mentioned previously (Chapter 1), the complexity of the engine studies makes the isolation and even identification of the dominant cause for NO_x increase noted with biofuels in diesel engines extremely difficult. To delineate these issues, the effects of chemical and physical variables must be separated. The technique described in the previous chapter to rapidly characterize the combustion properties of liquid fuels attributable only to the chemical structure of fuels was used. This chapter describes the global flame properties which include flame appearance, flame length, global emissions of five fuels: diesel, canola methyl ester, soy methyl ester, methyl stearate, and dodecane.

4.1 Flame Appearance and Length

4.1.1 Effect of Equivalence Ratio

The flames tested varied in color, structure, and length as ϕ was increased. At ϕ = 1.2, Fig. 4.1, all flames visually appeared blue. Two primary regions were observed, a bright blue inner cone surrounded by a second blue less luminous cone. The bright blue inner cone represented the primary gas-phase oxidation reaction zone. Remaining unburned reactants in the surrounding flame zone mixed with ambient air. The second outer cone was used to determine the average visible flame length which was 9.5 cm for diesel, 9.5 cm for soy methyl ester, 8.8 cm for canola methyl ester, 8.1 cm for dodecane, and 8 cm for methyl stearate. As the equivalence ratio was increased to ϕ = 2, Fig. 4.2, the flames became partially yellow, nearly doubling in length for all fuels. The lower portion (<6 cm) of the flames remained blue, as gas phase reactions dominated in this zone. The remaining unburned reactants including soot continued to burn downstream with ambient oxygen, emitting continuum radiation at all wavelengths, thus appearing yellow. Dodecane and diesel fuels produced flame lengths of 20.5 cm and 18.2 cm, respectively, while, the biofuels SME (17 cm), CME (16 cm), and MS (16 cm) were shorter in length. For ϕ = 3, Fig. 4.3, the flame lengths increased for diesel, SME, and CME and did not significantly vary for MS and dodecane. Diesel fuel produced the longest flame (24.5 cm) compared to dodecane (20 cm), SME (19 cm), CME (18.5 cm), and MS (14.9 cm). At ϕ = 7, the diesel flame appeared completely yellow decreasing in flame length (18 cm) reducing by 23% from the condition ϕ = 3. In contrast, the flame length increased for dodecane, (21

cm), CME (20 cm), SME (20 cm), and MS (19.3 cm). A small blue region was observed near the burner exit (<1 cm) for the biofuels and dodecane with the remaining lengths yellow, Fig. 4.4. The variation of flame length for both fuels with equivalence ratio is presented in Fig. 4.5. Uncertainties are represented in Fig. 4.5 by error bars which were calculated based on a student t distribution at a 95% confidence interval.

At ϕ = 1.2, diesel and SME flames were longer than CME by 7%, dodecane by 15%, and MS by 16%. Peak flame length values recorded for soy methyl ester and diesel at this condition implies a longer residence time over this range. Next at ϕ = 2, the longest flame was observed for dodecane which was 11% longer than the flame of diesel, 17% longer than SME flame, and 22% longer than CME and MS flames. For increasing ϕ less air was supplied, thus more air from the surroundings needed to be entrained, requiring an increase in length to effectively burn remaining fuel or particulates. At ϕ = 3, diesel produced the longest length which was 18% longer than the dodecane flame, 22% longer than the SME flame, 24% longer than the CME flame, and 40% longer than the MS flame. At the next condition, ϕ = 7, dodecane again produced the longest flame 5% longer than the SME and CME flames, 8% longer than the MS flame, and 14% longer for diesel fuel flame. The visible length for diesel flame significantly decreased, however, for all other fuels flame length increased. Between ϕ = 3 and ϕ = 7, the diesel flame decreased in length since it exceeded its maximum sooting height confirming lower soot concentration in biofuel and dodecane flames. This observation is in accordance with previous studies that showed diesel to produce

significantly more particulate matter than biodiesel fuels (McCormick et al., 2001, Graboski et al., 2003).

4.1.2 Effect of Iodine Number on Flame Length

Soy methyl ester, canola methyl ester, and methyl stearate flames possessed similar carbon chain length and energy content, but provided a wide range of iodine numbers from 0.5 to 141.6 Similarities in fuel composition resulted in comparable height and structure, as shown in Figs. 4.1 to 4.4. To investigate the effect of the chemical structure of these fuels a plot of flame length and iodine number is given in Fig. 4.6. Diesel (iodine number = 8.6) flame length values are also provided in Fig. 4.6. At $\phi = 1.2$, no significant difference was observed for the varying iodine numbers between all fuels. At $\phi = 2$, diesel produced the longest flame with no significant difference observed for the other biofuels. As the equivalence ratio was increased to 3 diesel produced the longest flame of 24.5 cm. MS with an iodine number of 0.5 produced the shortest flame of 14.9 cm. CME and SME had comparable lengths of 18.5 cm and 19 cm, respectively. At $\phi = 7$ the flame length of diesel decreased since it exceeded its maximum sooting height thus resulting in diesel producing shorter lengths than the biofuels. Also, at this condition SME (20 cm) and CME (20 cm) produced longer flames than MS (19.3 cm).

In general, there was no discernable correlation between the flame structure, length, and fuel iodine number for the tested biofuels at all conditions. Diesel, however, produced significantly longer flames at $\phi = 2$ and 3 and a shorter flame at $\phi = 7$ due to the presence of aromatics (nearly 25% by volume) in the fuel which has been shown to facilitate the production of more soot (Ladommatos et al., 1997).

4.2 Radiative Fraction

4.2.1 Effect of Equivalence Ratio

Radiation from flames depends on several factors including the total emissivity, exposed area, and flame temperature to the fourth power (Schwartz and White, 1996). Of the many gaseous combustion products emitted from the flame, primary contributors to the radiation emitted from the flame include N_2, O_2, CO_2, and H_2O which emit radiation in a banded form (Schwartz and White, 1996). For non-luminous flames such as those at $\phi = 1.2$, CO_2 and H_2O were the primary contributors to the total emitted radiation as the gaseous radiation due to N_2 and O_2 are typically ignored because of their low emission. At this condition MS (12 %) and dodecane (11%) produced the highest radiative heat fraction (F) values of all five fuels, where the three other fuels produced values of 9 %, Fig. 4.7. As the equivalence ratio increased to 2, however, a yellow luminous zone was visible. Luminous flames, as those described here, emit radiation from the above listed gases in banded form as well as from soot in continuum form. As the flame became yellow or luminous, as seen at $\phi = 2$, 3, and 7, the primary radiative losses came from the presence of solid particles (soot) within the flame. Thus the radiation emitted from the flame, quantified by the F value, was used as a quick way to indicate the amount of soot produced from the different flames. At $\phi = 2$, F values from the flames increased for all fuels. Dodecane produced the largest F value (14%) corresponding with the largest flame length (emitting area) at this condition. At $\phi = 3$, diesel produced the largest F value of 18% with all other fuels producing lower (F ~ 15 %) values not significantly different from each other. As

the equivalence ratio was increased to 7, significant changes in the flame structure and emitted radiation were observed. All flames were almost completely yellow, thus radiation losses from these flames were primarily due to the presence of soot. Diesel fuel produced the highest radiative heat fraction (32 %), followed by SME (29 %), CME (27 %), dodecane (20 %), and MS (19 %). At this condition peak soot concentrations were expected, as discussed in Chapter 3. Diesel, with a high percentage by volume of aromatics, produced the highest F values thus contained the largest amount of soot. Solid particles within the flame increased the radiative heat transfer losses to the surroundings. CME and SME produced lower F values (soot) than the diesel fuel which corresponds with engine study findings (McCormick et al. 2001, Graboski et al. 2003). Biofuels produced less soot than diesel at this condition due to the presence of the oxygen atoms in the fuel structure of the molecule which acted to suppress the formation of soot.

Typically, the principal types of reactions responsible for the fuel consumption are hydrogen atom abstractions followed by β – scission reactions of larger hydrocarbon radicals, such as olefins. The resulting H atoms from the process start the development of a pool of radicals through the reaction, $H + O_2 \rightarrow O + OH$. The presence of these radicals accelerates the fuel consumption and fuel fragment production, which can lead to large amounts of soot production such as that seen for the diesel flame. The biodiesel fuel molecule, however, contains molecularly-bonded oxygen that remains connected to the neighboring carbon atom, thus reducing precursor soot formation (Kitamura et al., 2001). Dodecane's low F-value (20%) can be attributed to the low amount of carbon (C=12)

contained in its molecular structure and soot forming precursors (aromatics) which resulted in lower amounts of soot production and in turn lower radiation losses. MS produced the lowest F value of 19%. This was thought to be due to the low iodine number and will be discussed further in the next section.

4.2.2 Effect of Iodine Number on Radiative Heat Fraction

At the conditions of ϕ = 1.2 and 2 the radiative fraction did not vary for each fuel significantly, Fig. 4.8. Since the flames were non-luminous (blue) at ϕ = 1.2 flame radiation losses were low. The flames changed to partially luminous (yellow) at ϕ = 2 where flame radiation losses were due to both banded (gaseous) and continuum (solids) radiation. Radiation increased for all fuels, however, no discernable trends were observed for the F values and iodine number of the fuels. At ϕ = 3 the diesel flame possessed the largest F value despite having a low iodine number in comparison to CME and SME. This was due to the presence of the aromatics in diesel which increased the sooting propensity to a much larger extent than the effect of the iodine number. This behavior is confirmed by comparing F values of diesel and dodecane. The F value produced by dodecane was lower because dodecane is just an alkane with a saturated chain. The biofuels, which do not contain aromatics, begin to increase with increasing in iodine number with MS (14 %) producing the lowest F value followed by CME (15 %) and SME (15 %). This same trend was also seen at the next condition where ϕ = 7. MS had the lowest F value of 19 % followed by, in ascending order, CME (27 %), SME (29 %), and diesel (32 %). Diesel, as before, did not follow with the iodine number due to other dominating soot producing chemical mechanisms. Comparison of the biofuels, however, showed increased F values with increasing iodine number. This could be due to the presence of the double bonds in the unsaturated fuels, such as SME, which are believed to facilitate the production of more soot thus resulting in higher F values (Douwel et al., 2009).

4.3 Emission Index Results

4.3.1 Effect of Equivalence Ratio on NO Emission

Emission Index of NO (EINO) for the five fuels tested at the 4 equivalence ratios are plotted in Fig. 4.9. At $\phi = 1.2$, CME produced the highest EINO of 5.6 followed by SME (5.5), diesel (5.4), dodecane (4.57), and MS (3.82). Differences between the biodiesel and diesel flames were not significant, however, were much larger than either dodecane or MS. At this condition it is expected that the Zeldovich (thermal) mechanism was dominant, hence a function of flame residence time (flame length) as seen by NO emission correlation with flame length. As the equivalence ratio was increased to 2, NO production decreased to approximately half of that from the condition of $\phi = 1.2$ with CME again having the highest EINO, 2.42, followed by SME (2.38), diesel (2.33), dodecane (2.2), and MS (1.90) in that order. At this condition the Zeldovich (thermal) mechanism was thought to accompany other formation pathways of NO which became more dominant as the equivalence ratio was increased. Beginning at this condition flame length and radiative heat fraction no longer correlated with the measured NO. Next at $\phi = 3$ the NO emissions decreased for all fuels, with dodecane producing the largest amount of NO (1.74) followed by, in descending order, CME (1.51), SME (1.44), diesel (1.38), and MS (1.28). At the two previous conditions the largest NO emissions had resulted from the combustion of the biofuels, however, dodecane produced significantly more NO than CME (13% more) or SME (17% more). It is thought that several different chemical effects were occurring at this condition. The dodecane flame visually had a larger gas

phase oxidation reaction (blue) region where temperatures were expected to be elevated and promote the formation of NO through the thermal mechanism. Diesel despite having the longest flame length produced significantly less NO than dodecane. This implies that NO production was probably due to other formation pathways along with the thermal mechanism for the diesel fuel. Despite having similar chemical composition, compounds in the diesel flame which led to the production of more soot facilitated the transfer of heat from the flame, thus lowering flame temperatures and resulting in less NO produced by the thermal mechanism. Other pathways thought to be contributing to NO formation in these flames will be described later in Chapter 5, where in-flame pollutant emissions, temperature profiles, and species concentrations are discussed. Also, for the oxygenated biofuels: CME, SME, and MS a correlation to iodine number was observed and will be discussed in the next section. These same trends continued at the next condition of $\phi = 7$, the most NO was again collected for dodecane (1.1) followed by SME (0.86), CME (0.81), MS (0.81), and diesel (0.75). At all conditions CME and SME produced more NO (3 - 15%) than diesel fuel which agrees with previous engine study findings.

4.3.2 Effect of Iodine Number on NO Emission

Figure 4.10 presents the plot of EINO for varying iodine numbers. At $\phi = 1.2$, 2, and 3 MS, with the lowest iodine number, produced the lowest amount of EINO while diesel and the two other biofuels showed significantly higher values at these conditions. At $\phi = 7$ the diesel flame produced the lowest value of EINO. As mentioned previously, the diesel flame produced large amounts of soot which were dominant over other chemical effects (iodine number) resulting in high incomplete combustion products and low amounts of EINO. It is possible that the saturated fuels participate less in the β – scission reactions of larger hydrocarbon radicals, thus resulting in less overall soot production, demonstrated by the low F value, and lower emission of NO. This correlation indicates a dependence on the chemistry of the fuel during its combustion and on the amount of soot, carbon, or unburned hydrocarbons produced.

4.3.3 Effect of Equivalence Ratio on CO Emission

Emission Index of CO (EICO) for the five fuels tested at the equivalence ratios of 1.2, 2, and 3 are plotted in Fig. 4.11. At $\phi = 1.2$, diesel produced the highest EICO of 1.89 followed by CME (1.76), SME (1.66), MS (1.43), and dodecane (1.3). As the equivalence ratio was increased to 2, CO production increased with diesel again having the highest EICO, 2.15, and did not significantly change for CME (1.76), SME (1.50), MS (1.32), and dodecane (1.2). At $\phi = 3$ the CO emissions increased for all fuels with diesel producing the largest amount of CO (6.38) followed by, in ascending order, CME (2.87), SME (2.60), MS (1.56), and dodecane (1.42). Figure 4.12 presents the EICO for $\phi = 7$, this was plotted separately since the values were much higher than at the previous conditions. At $\phi = 7$, diesel produced the largest amount of CO (41.1) followed by CME (19.36), SME (18.33), dodecane (11.31), and MS (5.35).

At each equivalence ratio the diesel fuel produced the largest amount of CO (7 – 670 % more) compared to all other fuels. At $\phi = 1.2$, EICO for all fuels were comparable and did not significantly change as the equivalence ratio was increased to 2. As the equivalence ratio was further increased large differences in CO production for the fuels were seen at $\phi = 3$ and $\phi = 7$. As the flames became more fuel rich the effect of the molecularly bonded oxygen became increasingly evident. As mentioned in section 4.2.1 of this report the biodiesel molecule contains molecularly-bonded oxygen that remains connected to the neighboring carbon atom, requiring less mixing with the ambient environment for the oxidation of CO (Kitamura et al., 2001). Diesel, however, contained soot

precursor forming compounds that required premixed and externally entrained air to oxidize formed carbon within the flame. At $\phi = 7$ the production of CO, an indication of incomplete combustion, and soot peaked for the diesel fuel producing over double the EICO than the biofuels and dodecane. This observation agrees with engine study findings which have shown similar trends for measured particulates and CO emissions when compared to CME and SME (Table 3.2). For $\phi = 1.2, 2, 3$ dodecane produced lowest value of EICO and at $\phi = 7$ produced the next to lowest. Since dodecane had the shortest carbon chain length this led to the production of less soot, demonstrated by the low radiative heat fraction at this condition, significantly lower amounts of CO, and higher concentrations of EINO compared to the other fuels. These trends indicate more complete combustion occurring for the dodecane fuel due to the low amounts of carbon in the molecular structure.

4.3.4 Effect of Iodine Number on CO Emission

Figure 4.13 presents the plot of EICO for varying iodine numbers for ϕ = 1.2, 2, and 3. At ϕ = 1.2 and 2 no significant differences were observed between the tested fuels at these two conditions. As the equivalence ratio was increased to 3 and 7 significant changes in the EICO were observed. The low iodine number fuel MS produced the lowest amount of CO compared to diesel, CME, and SME at these conditions. A strong correlation between the iodine number and EICO was also observed at the condition ϕ = 7. As discussed in section 4.3.3 of this report, it is possible that the saturated fuels participated less in the β – scission reactions of larger hydrocarbon radicals, thus resulting in less overall soot production, demonstrated by the low F value, and lower emission of NO and CO, further investigated in Chapter 5. Additionally at ϕ = 7, the diesel flame produced large amounts of soot which were dominant over other chemical effects (iodine number) resulting in high incomplete combustion products including EICO.

4.4 Chapter Conclusions

The following conclusions can be drawn regarding the global properties of hydrocarbon and biofuel flames.

- Flame length increased as the equivalence ratio was increased. The diesel fuel flame length significantly decreased between $\phi = 3$ and $\phi = 7$ since the flame exceeded the maximum sooting height.
- Radiative heat fraction values, used as an indication of the sooting tendency of the fuel, significantly increased with increasing equivalence ratio. Diesel produced the highest F value at $\phi = 2$, 3, and 7.
- EINO decreased as equivalence ratio was increased. It was observed that at the lowest equivalence ratio of 1.2 the Zeldovich mechanism was dominant and at more fuel rich equivalence ratios another NO formation mechanism was thought to significantly contribute to the NO formation.
- A correlation between iodine number and NO emission was observed for the biofuels. As iodine number increased EINO also increased at all conditions for these fuels.
- Diesel fuel combustion characteristics did not correlate with iodine number.
- At $\phi = 1.2$ and 2 no significant differences were observed between the EICO of tested fuels. At $\phi = 3$ and 7 EICO increased as equivalence ratio was increased, since CO is a product of incomplete combustion confirmed by the corresponding increasing F values (soot) measured.

- Low iodine number fuel MS was thought to participate less in the β – scission reactions of larger hydrocarbon radicals, thus resulting in less overall soot production, demonstrated by the low F value, and lower emission of NO and CO.
- At ϕ = 3 and 7 dodecane produced lower F values, higher EINO, and lower EICO indicating that the composition of diesel fuel significantly affect the measured combustion characteristics.

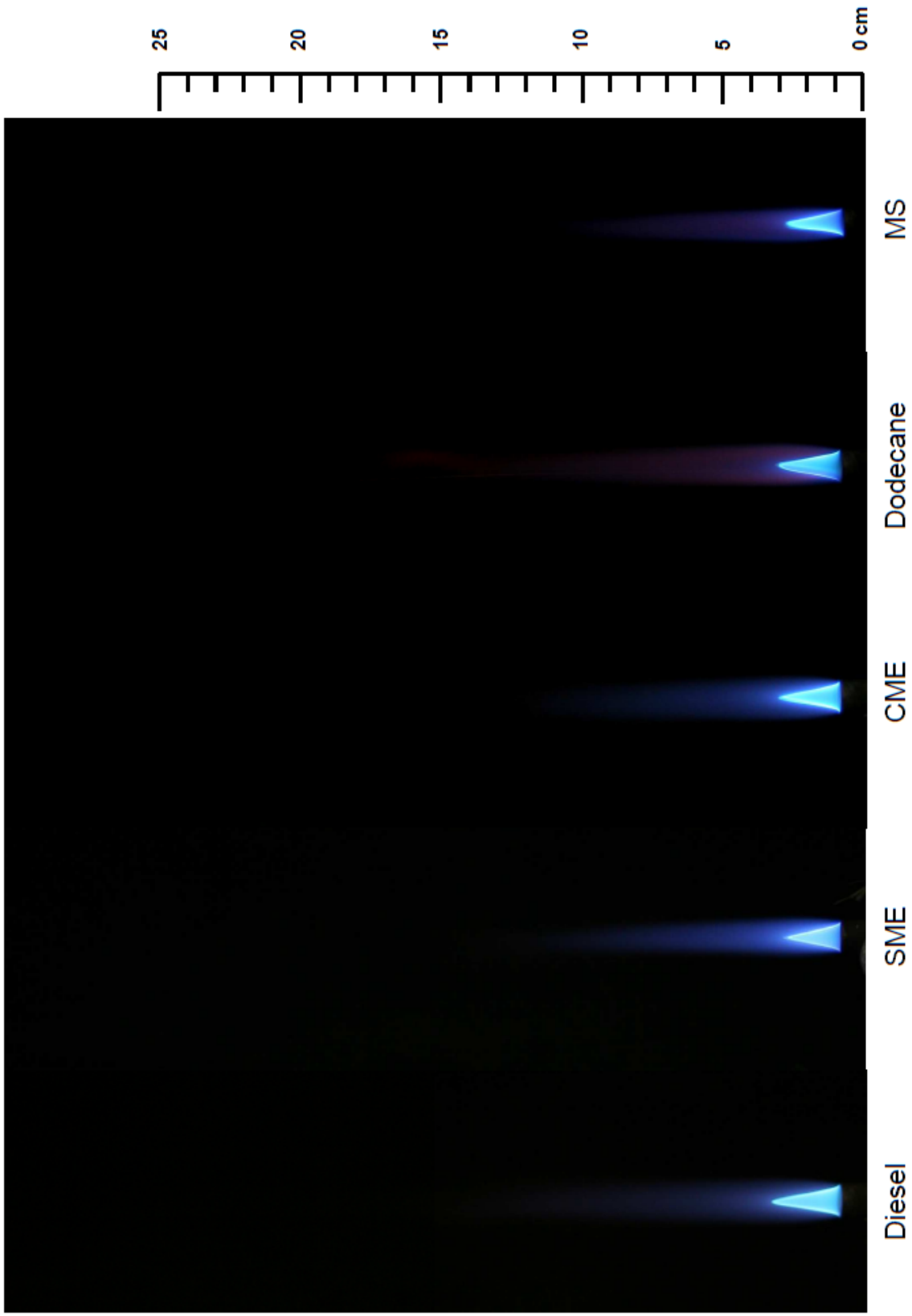

Figure 4.1 Digital photograph of all fuels tested at $\phi = 1.2$ with scale (exposure time of 1/25 seconds)

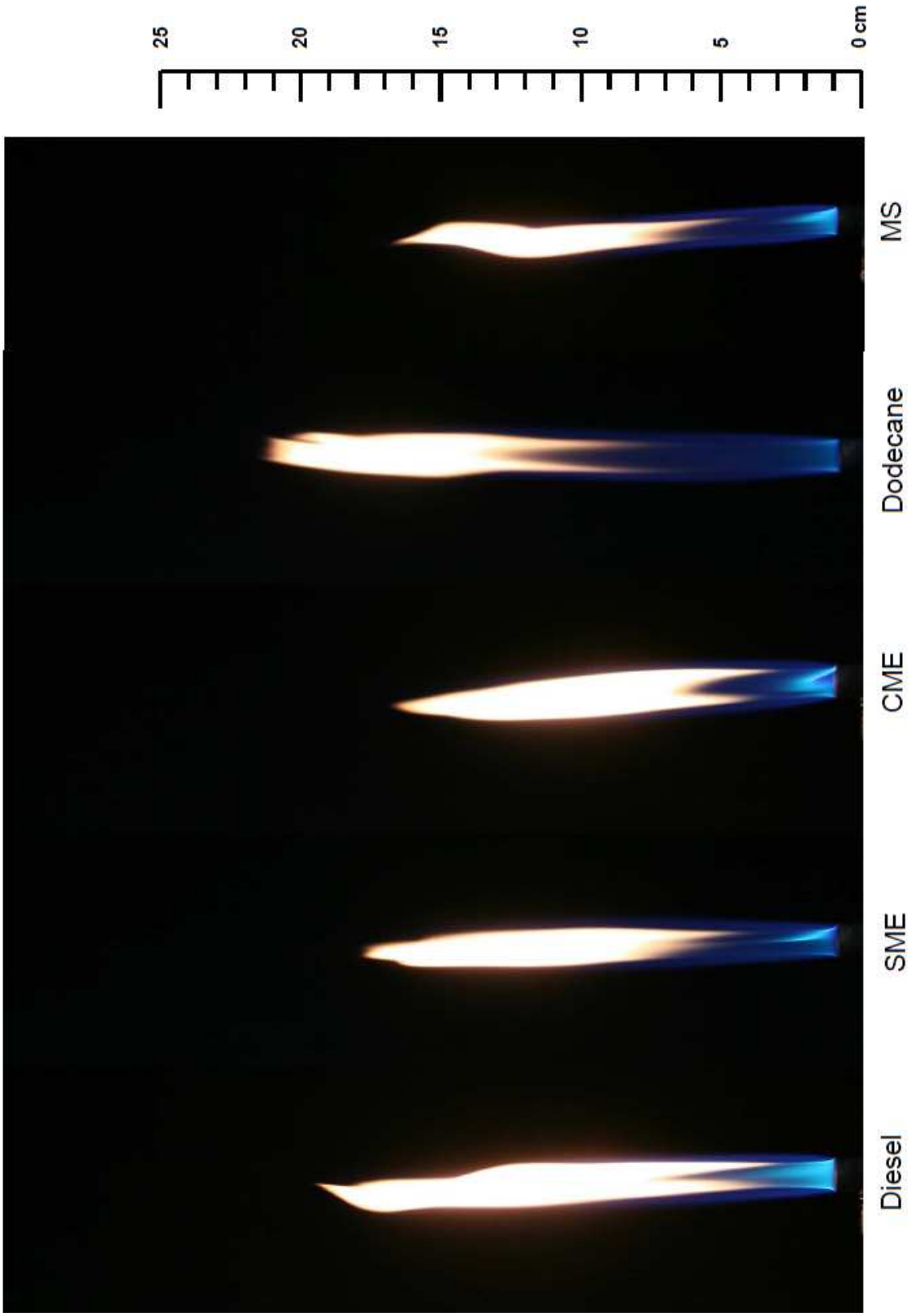

Figure 4.2 Digital photograph of all fuels tested at $\phi = 2$ with scale (exposure time of 1/25 seconds)

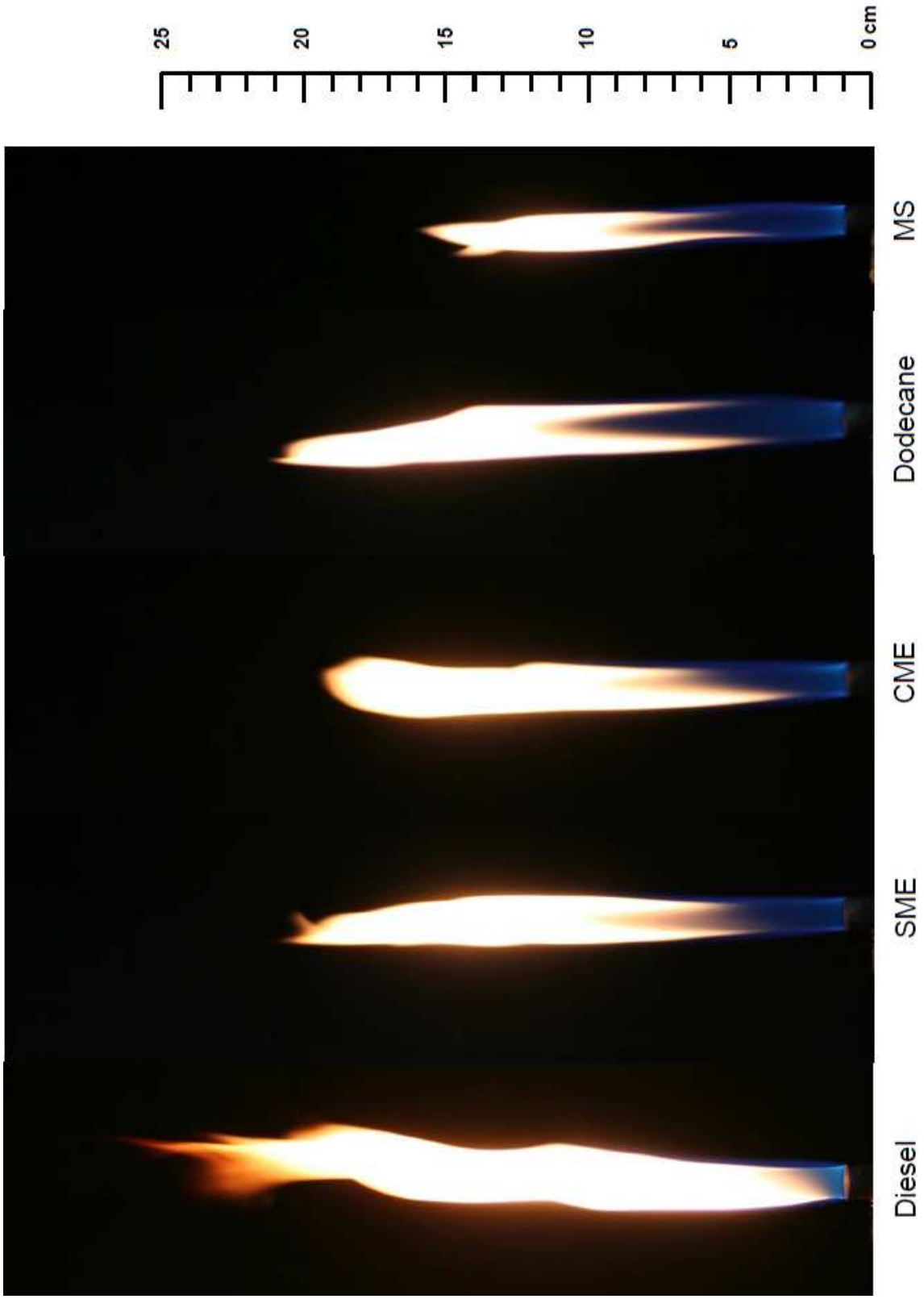

Figure 4.3 Digital photograph of all fuels tested at $\phi = 3$ with scale (exposure time of 1/25 seconds)

Figure 4.4 Digital photograph of all fuels tested at $\phi = 7$ with scale (exposure time of 1/25 seconds)

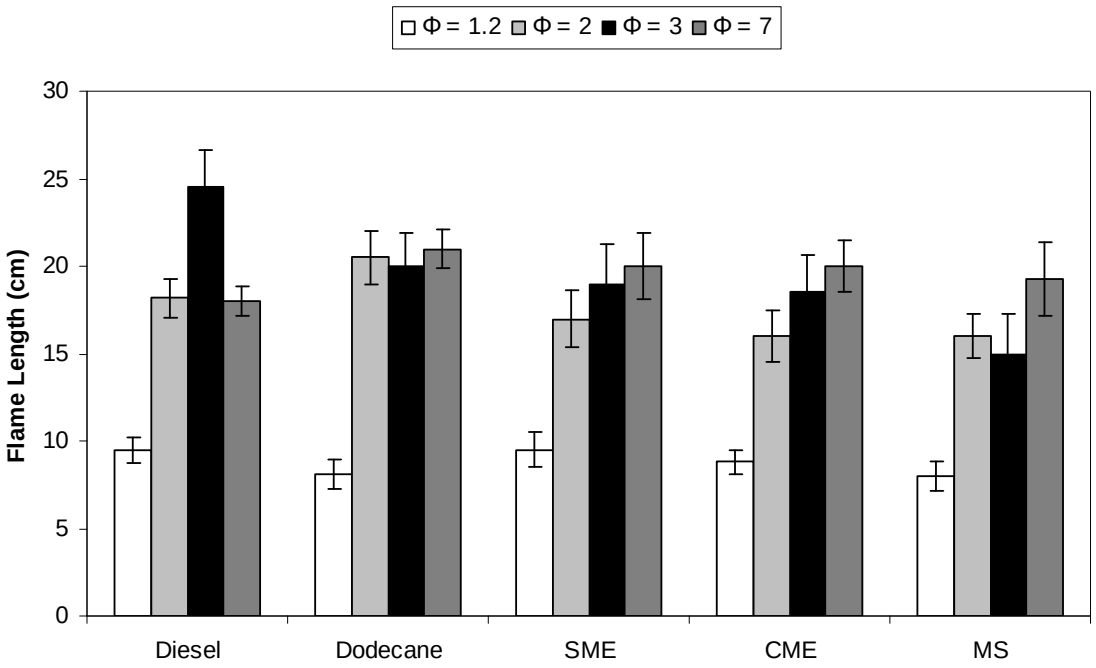

Figure 4.5 Measured visible flame length for all fuels at ϕ = 1.2, 2, 3, and 7

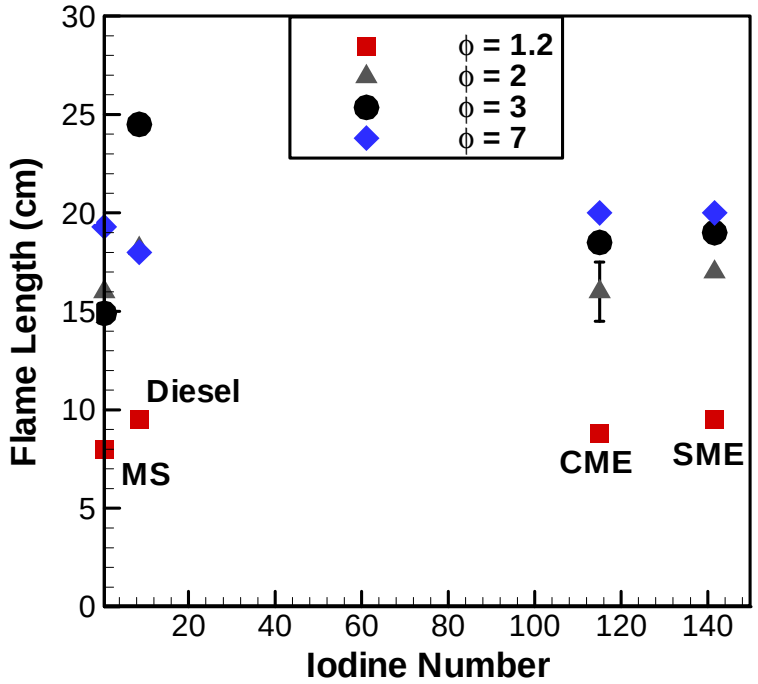

Figure 4.6 Visible flame length plotted against iodine number at ϕ = 1.2, 2, 3, and 7

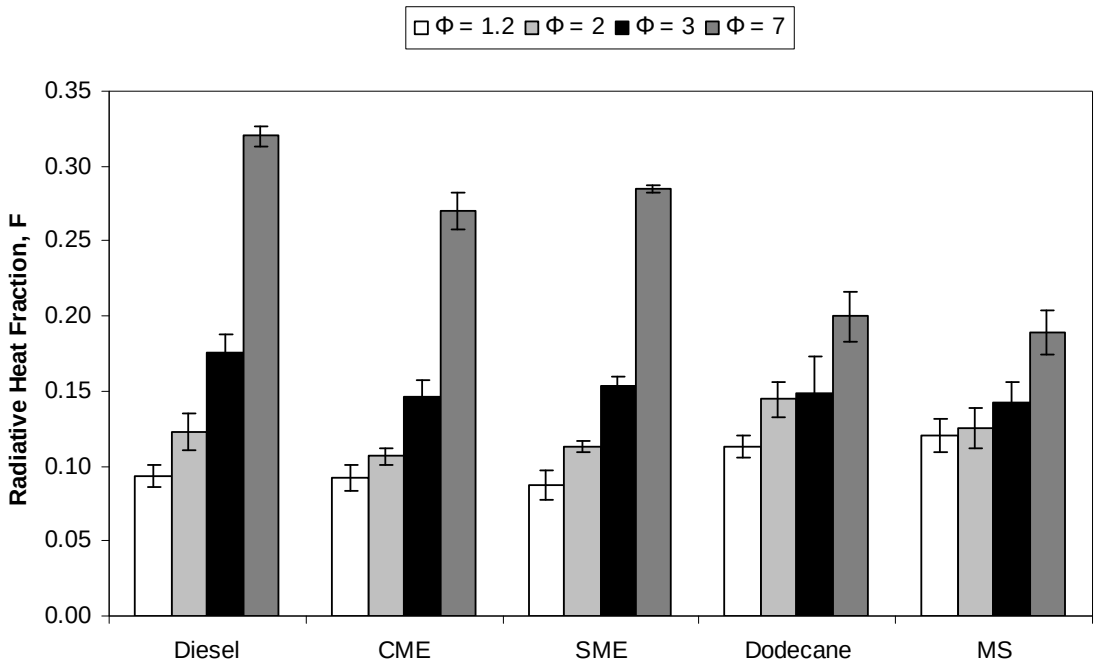

Figure 4.7 Radiative heat fraction (F) values at ϕ = 1.2, 2, 3, and 7 for all fuels tested

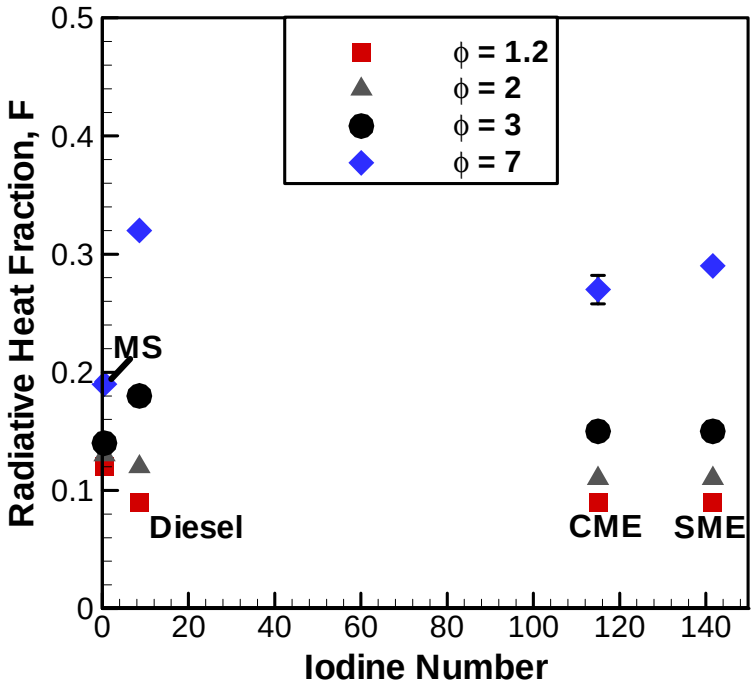

Figure 4.8 Radiative heat fraction plotted against iodine number for ϕ = 1.2, 2, 3, and 7

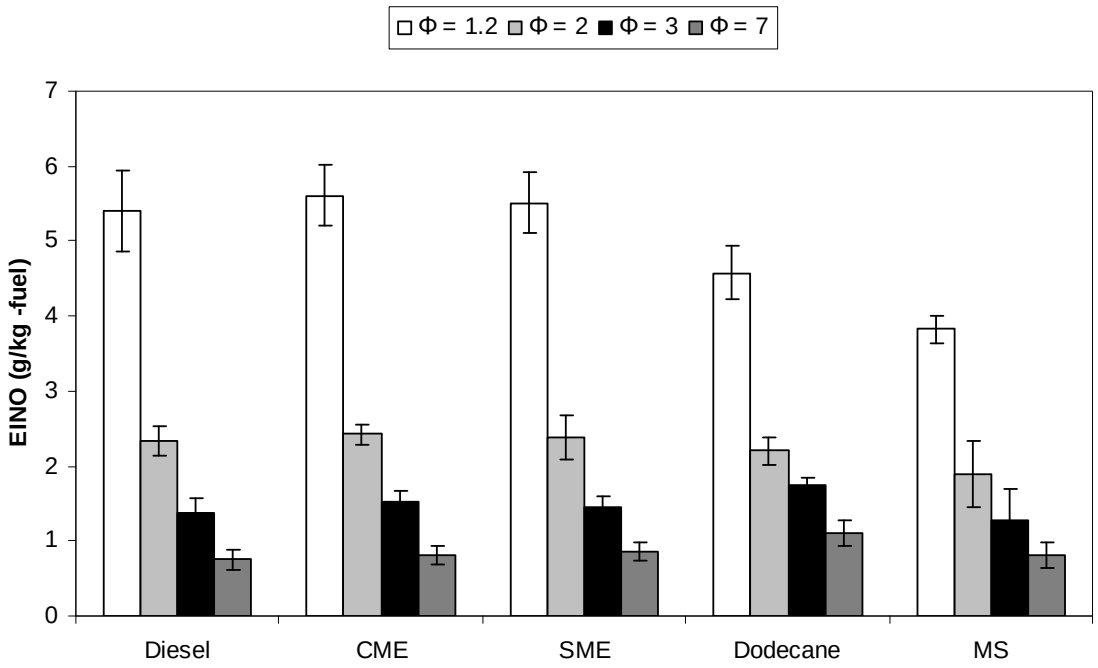

Figure 4.9 EINO for all fuels tested at ϕ = 1.2, 2, 3, and 7

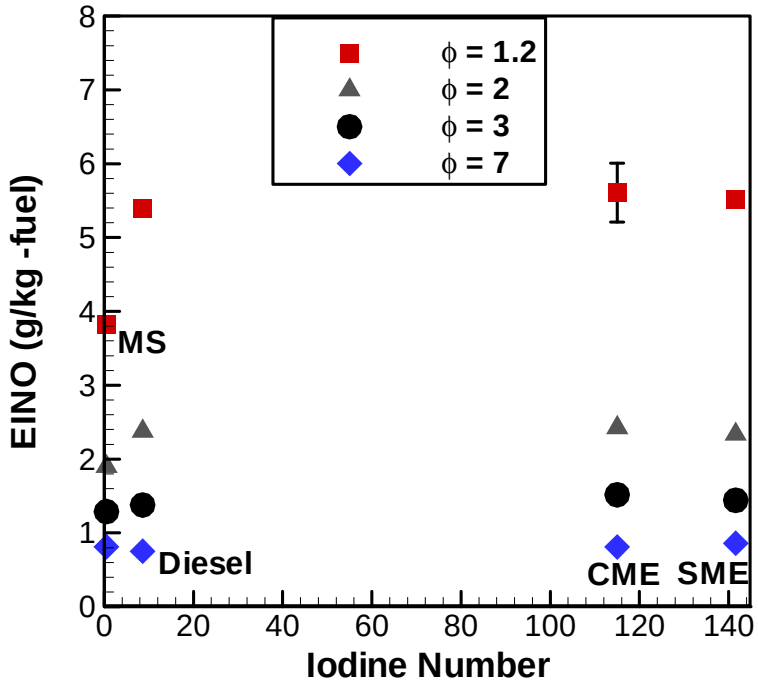

Figure 4.10 EINO plotted against iodine number for ϕ = 1.2, 2, 3, and 7

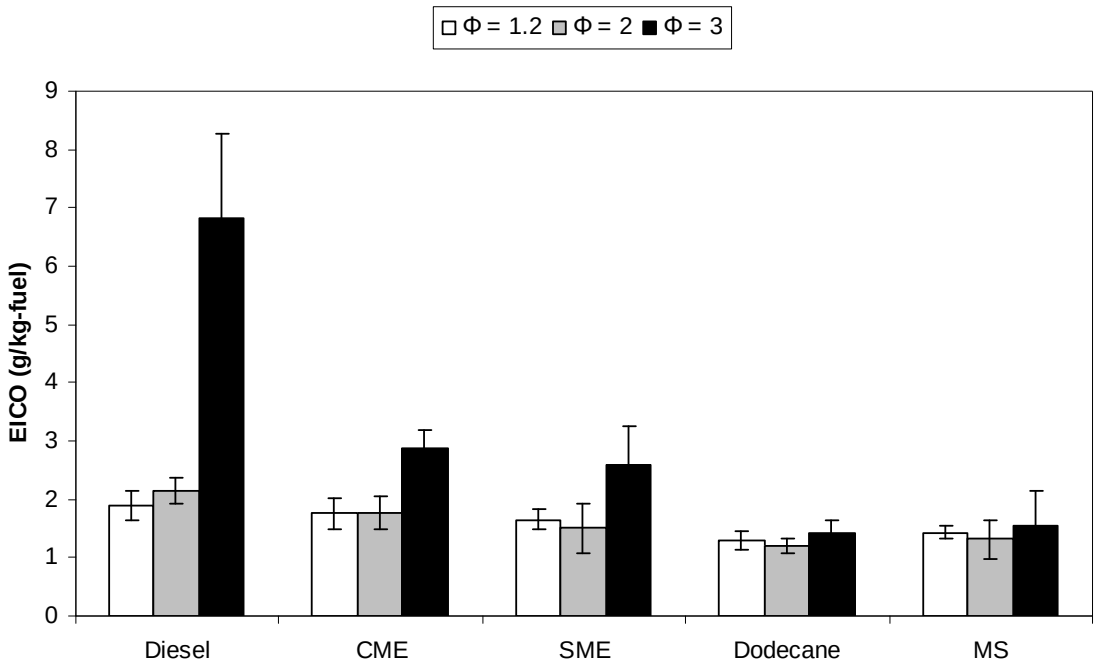

Figure 4.11 EICO for all fuels tested at ϕ = 1.2, 2, and 3

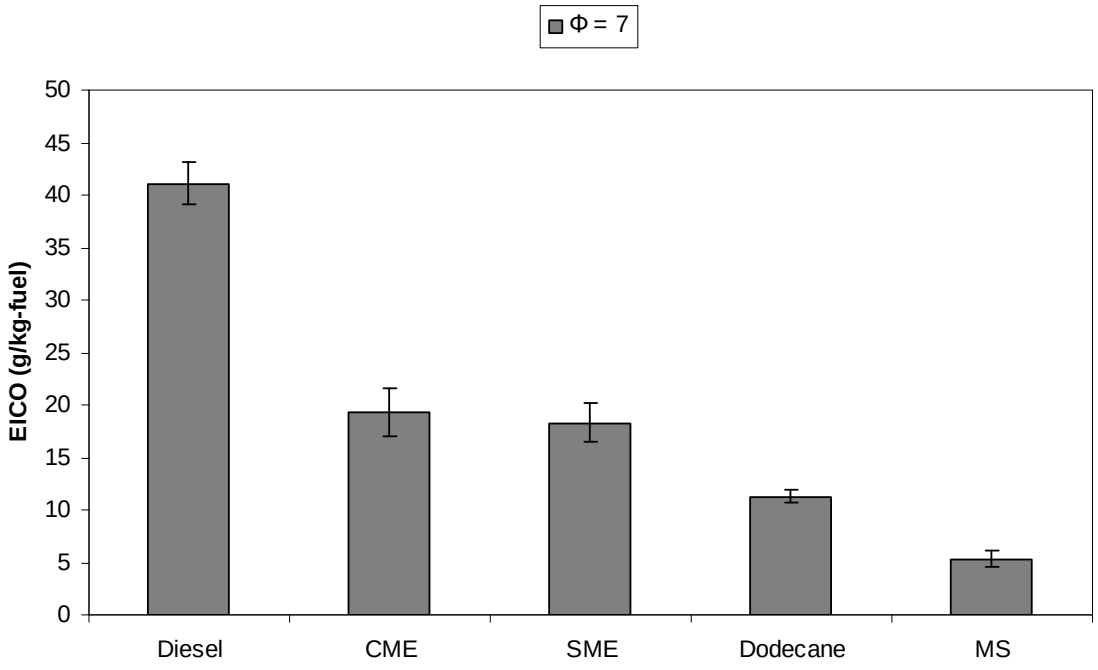

Figure 4.12 EICO for all fuels at ϕ = 7

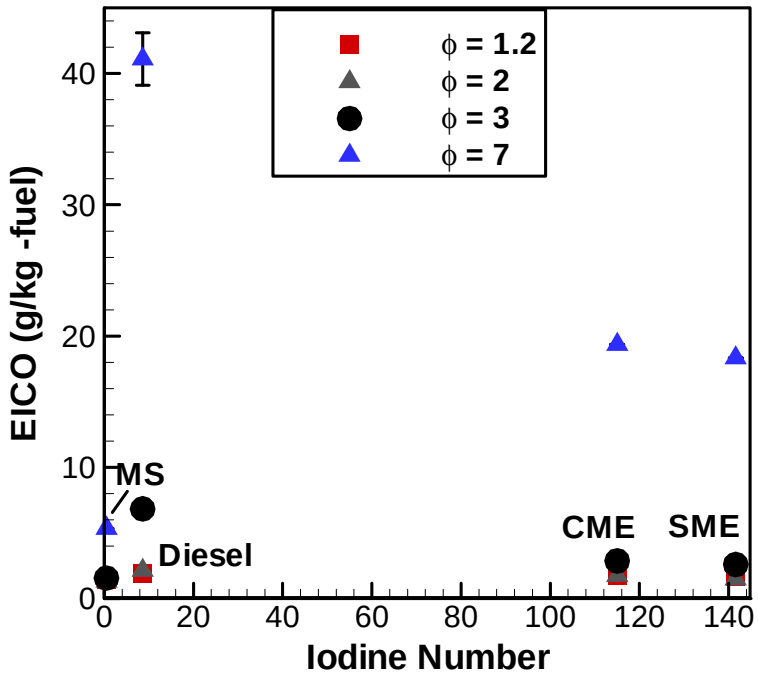

Figure 4.13 EICO plotted against iodine number for ϕ = 1.2, 2, 3, and 7

Chapter 5
Flame Structure

The effect of equivalence ratio and iodine number on the in-flame temperature profiles, pollutant species concentrations, OH and CH species concentrations, and soot volume fraction is presented in this chapter. For in-flame temperature, concentration profiles, and soot volume fraction, three axial locations downstream of the burner exit were chosen at 25% (near burner), 50% (mid-flame), and 75% (far burner) of the documented flame heights. The species concentrations of OH and CH were also presented only the near burner region of the flames. To examine the effect of equivalence ratio the same four conditions were tested as in the previous chapter at ϕ = 1.2, 2, 3, and 7. Effect of the iodine number on the above mentioned measurements was also documented for diesel, canola methyl ester, soy methyl ester, and methyl stearate fuels.

Based on the previously documented values for the global flame combustion characteristics (flame length, radiative heat fraction, etc.) in-flame concentrations were taken at selected conditions to determine the dominant mechanism of the production of NO.

5.1 Temperature Profiles

5.1.1 Effect of Equivalence Ratio on Temperature

The traverse temperature distribution corrected for radiation, conduction, and convection losses (Jha et al., 2008, Hariharan, 2004, Chinthamony, 2005) in the laminar flames of the five fuels is shown at equivalence ratios of 1.2, 2, 3, and 7 for the three flame locations, Figs. 5.1-5.20. In general, peak temperatures reached a maximum at ϕ = 1.2 and became lower as the equivalence ratios became more fuel-rich. This result was expected as maximum temperatures occur at or near stoichiometry. In the fuel rich flames, such as those at ϕ = 2, 3, and 7, less premixed air resulted in the fuel depending on mixing with the surrounding air which lowered the reaction rate of the flame, hence lowering the temperature. Comparison of the temperature profiles at ϕ = 1.2, which showed peak temperatures at the flame boundaries, with those at ϕ = 2 and 3 shows that differences in temperature distribution and structure. As the flames became more yellow and less premixed (blue) temperature profiles continue to peak along the flame edges where the equivalence ratio was expected to be stoichiometric. At these conditions flame temperatures were lowest at the flame centerline where unburned hydrocarbons and fuel fragments were expected to be at maximum concentrations. At ϕ = 7 profiles did not vary significantly as the thermocouple was traversed radially. Since the flame operated at the lowest air flow rates at ϕ = 7, it was observed that the flame moved due to small disturbances in the ambient environment. Data points recorded were averaged over the 60 second acquisition time at each radial location which included this movement of the flame and

resulted in a temperature distribution that did not significantly vary in the radial direction.

Adiabatic flame temperatures and the corresponding enthalpies of reactants are presented in Table 5.1. Adiabatic flame temperatures were calculated using computer code developed by Olikara and Borman (1975) which solved for 12 species, 7 equilibrium reactions, and atom conservation relations for C, H, N, and O. According to Table 5.1 diesel was expected to have the highest adiabatic flame temperature (2282 K) followed by dodecane (2272 K), CME (2268 K), SME (2266 K), and MS (2249 K). At ϕ = 1.2, however, the highest temperature was recorded for CME (2260 K) followed by SME (2238 K), diesel (2225 K), MS (2206 K), and dodecane (2191 K). These temperature profiles are presented in Figs. 5.1, 5.5., 5.9, 5.13, and 5.17. All peak measured temperatures occurred in the near burner region and were within experimental uncertainties, not significantly varying between each fuel. This is confirmed by similarities in appearance and structure, demonstrated by the comparable flame heights and 'blue' appearance, Fig. 4.1 and 4.6. Above the near burner region measured temperatures decreased becoming the lowest in the far burner region.

At ϕ = 2 the structure of the temperature profiles changed from the last condition. As the flames became more 'yellow', Fig. 4.2, the temperature profiles in the near and mid-flame regions reached peak values as the thermocouple was traversed into the edges of the flame boundary where it was expected that the fuel and air mixture was stoichiometric. Temperatures then decreased as the thermocouple approached the center of the flame reaching a minimum at the

flame centerline. Figure 5.3 shows the temperature profile for the diesel flame which produced the highest peak temperature of all other fuels at this condition, 1825 K. As the thermocouple was traversed through the far-burner portion of the flame a parabolic type distribution of temperature was observed reaching a peak at the centerline and decreasing along the edges of the flame boundary. Temperatures recorded in the far-burner region of the flames were lower than those recorded in the mid and near-burner portion of the flame. The other four fuels were similar in flame structure to diesel demonstrated by their temperature distributions which peaked in the near-burner or mid-flame regions along the edge of the flame. For CME, SME, MS, and dodecane peak temperatures of 1800 K (near-burner), 1798 K (near-burner), 1772 K (mid-flame), and 1705 K (near-burner) were recorded, respectfully. Comparison between diesel and the biofuels show that peak temperatures remained within experimental uncertainties. Peak dodecane flame temperature, however, was significantly lower than the diesel and biofuels. At this condition dodecane produced the highest radiative heat fraction, Fig. 4.7, of all fuels which indicates the largest heat losses to the surrounding environment in the form of radiation resulting in overall lower flame temperatures.

At $\phi = 3$ the structure of the temperature profiles were similar to those at $\phi = 2$. Significant changes in flame appearance from the previous condition were observed for the diesel fuel which became nearly completely ‘yellow’ at this condition. Profiles, however, all maintained high temperatures along the flame edges in the near burner region. In the mid-flame and far burner regions, however,

temperature distributions were parabolic in shape with peak temperatures along the flame centerline and decreasing along the flame edges. Flame temperatures were observed to peak in either the near-burner or mid-flame regions decreasing in the far-burner portion of the flame. At $\phi = 3$ the MS flame produced the highest peak temperature of 1585 K in the mid-flame region followed by dodecane (1520 K in the near-burner region), CME (1517 K in the mid-flame region), SME (1507 K in the mid-flame region), and diesel (1483 K in the near burner region). The effect of radiative heat transfer due to the presence of soot in flame was again observed at this condition. Diesel produced an F-value significantly higher than other fuels (F = 18) hence resulting in the lowest measured flame temperatures. It was also observed that MS produced a significantly higher flame temperature than the other fuels despite having been predicted to produce the lowest flame temperature by adiabatic flame temperature calculations.

At $\phi = 7$ temperature profiles were different in shape and structure than all other previous conditions in that they did not vary significantly as the thermocouple was traversed radially. Visually the flames were similar in flame height and structure and all appeared ‘yellow’ for this condition, Fig. 4.4. Peak temperatures occurred in the near burner region for all fuels, decreasing for the other two downstream flame regions. Dodecane produced the highest peak flame temperature, 1196 K, in the near burner region followed by MS (1163 K), SME (1092 K), CME (1105 K), and diesel (1057 K). MS produced a significantly higher flame temperature than SME, CME, or diesel. Referring to Fig. 4.7, it was observed that dodecane and methyl stearate produced the lowest F values; hence

the lowest amounts of soot. Heat losses from these flames appear to be directly correlated to the amount of soot that is present which can effect the pollutant emissions which will be investigated in section 5.4 of this report.

5.1.2 Effect of Iodine Number on Temperature

At ϕ = 1.2 the highest temperatures for all fuels were recorded with no significant differences observed in their temperature profiles, presented in Fig. 5.21. At the next condition of ϕ = 2 temperatures of diesel, CME, and SME were significantly higher than that of the MS fuel following with the adiabatic flame temperature calculations in Table 5.1. A shift in flame temperatures occurred at the next condition of ϕ = 3, with MS showing significantly higher temperatures than diesel, CME, and SME. This trend continued onto the next condition of ϕ = 7 which also showed MS to produce the highest temperatures.

Results demonstrated a correlation to the amount of soot present within the flame, which, as shown above, transfers heat from the flame and results in lower flame temperatures. This is confirmed by the F values presented in Chapter 4 which show MS to possess the lowest F values of diesel, CME, and SME at ϕ = 3 and 7. Figure 5.21 also shows that peak temperatures of diesel, SME, and CME vary by a maximum of 7% at ϕ = 3. This does not represent the significant temperature differences that have been used to account for significant increases in NO_x production through the Zeldovich (thermal) mechanism (Scholl and Sorenson, 1993, Wang et al., 2000, Weiss et al., 2007). Instead, since temperatures did not vary significantly at very fuel rich conditions for the diesel, CME, and SME flames it is believed that there is a dependence on the amount of available oxygen within the flame, soot, and pollutant emission production. A fuel's propensity to soot can be correlated to the chemical structure of the fuel for which the iodine number has been used. It has been shown that fuels with higher

iodine numbers produced more soot (Douwel et al., 2009) thus lower flames temperatures. Therefore, importance of soot production in these flames is further investigated in the following section.

5.2 Soot Volume Fraction

Quantification of soot level in the previously discussed flames is highly desired. Therefore, for confirmation that as radiation increased soot concentration also increased. The amount of soot has been assumed to be directly related to radiation losses from the flame (particularly for the fuel-rich equivalence ratios), which has been expressed as the radiative fraction of heat released (F-values). This section will compare the values obtained from the radiation to the soot volume fraction measurements to validate this assumption. Additionally, it was desired to observe the behavior of the formation of soot axially and radially through the flame. This will provide insight into regions where the soot might affect other properties such as pollutant emissions and radical concentrations.

Plots of soot volume fraction at the same axial and radial positions as the temperature measurements are given in Figs. 5.22 – 5.41. In these figures soot volume fraction is presented as a fraction of the maximum value (normalized), $f_v/f_{v,max}$, where the maximum value occurred for diesel fuel at $\phi = 7$ with a value of 2.14 ppmv. This was done since the extinction coefficient (k_λ), which depended on the refractive index of soot, was unavailable for the biofuels. For this reason, it has been assumed that k_λ was constant for both the hydrocarbon and oxygenated fuels. Rather than providing a directly quantitative value, since k_λ for biofuels unknown, soot concentration of these fuels were presented as relative values for a quick and general comparison. If needed, more conventional values can be assigned to the data in Figs. 5.22-5.41 from the maximum soot volume fraction for diesel fuel at $\phi = 7$ provided.

5.2.1 Effect of Equivalence Ratio on Soot Volume Fraction

In general, it was observed that as the equivalence ratio was increased the peak soot volume fraction measurements also increased. This was expected in an environment where less air has been supplied, such as those in this study. In very fuel rich environments hydrocarbon radicals cannot oxidize fully. Low oxygen concentrations result in the formation of precursor species, such as polycyclic aromatic hydrocarbons, which form ring structures that react with hydrocarbons within the flame to form small particles. These small particles then begin to agglomerate and grow which typically occur in the regions located in the near (25 % of flame length) to the mid flame (50 % of flame length) regions. The particles (soot) continue to pass through the flame into the far burner region (75 % of the flame length) downstream of the injector exit. Above this portion of the flame, concentrations of soot decrease downstream until oxidized at the flame tip. If the flame, however, has exceeded its smoke point, soot will not oxidize before reaching the flame tip resulting in a flame that releases black smoke or soot.

At $\phi = 1.2$ profiles for all fuels were similar in structure and soot distribution. Soot radial profiles across these flames were relatively low with 5.68% of the maximum value of soot volume fraction recorded for dodecane, 5.38% for MS, 4.6% for CME, 4.23% for SME, and 3.4% for diesel. At this condition, the largest amount of air was supplied, resulting in the oxidation of hydrocarbon species that lead to the production of soot. Low amounts of soot recorded at this condition were confirmed by the ‘blue’ appearance of the flame and low F-values recorded which indicate low amounts of soot, and primary radiaition losses in banded form.

Recorded F-values for MS, dodecane, and all other fuels were 12%, 11%, and 9% respectively. The maximum soot volume fraction values listed follow with the F-values from these flames despite emitting low radiative heat losses.

At $\phi = 2$ diesel had a peak soot concentration of 9.74% of the maximum value followed by 7.69% for SME, 6.3% for CME, 5.48% for MS, and 5.12% for dodecane. At this condition, the profiles in the near burner region showed that higher values occurred along the edges of the flame boundary and decreased along the flame centerline. As soot was produced along the centerline the particles radially convected outward, replaced by newly formed soot, to the flame boundary where they could be oxidized. Above this portion of the flame, the profiles became parabolic in shape reaching a peak along the centerline monotonically decreasing along the edges of the flame. Peak soot volume fraction measurements were recorded in the far burner region of these flames. Diesel produced peak soot volume fraction as soot precursors, such as aromatics, composed nearly 25% of the fuel composition. The biofuel values for soot volume fraction were less than that of diesel, with SME producing the highest amount of soot of the biofuels followed by CME and MS. This trend was attributed to the chemical structure of the fuel and will be discussed later. Dodecane produced the lowest amount of soot as it did not contain soot precursor species found in the diesel fuel. At this condition, dodecane produced the highest F value followed by MS, diesel, SME, and CME.

At $\phi = 3$ diesel again had a peak soot concentration of 36.1% of the maximum value followed by 9.81% for SME, 9.02% for CME, 6.79% for MS, and 6.78% for dodecane. At this condition the diesel flame produced significantly more soot than the other fuels. It was also observed that the F-value recorded for the diesel fuel was highest followed by SME, CME, dodecane, and lowest value obtained for MS. At $\phi = 3$ the radiative heat loss correlated well with peak measured soot volume fraction. Peak soot volume fraction values occurred for the diesel flame in the mid-flame region and in the far burner region for all other fuels. The fuel structure of the biofuels acted to suppress the formation of soot by preventing the development of a pool of radicals by the reaction $H + O_2 \rightarrow O + OH$. This was accomplished through the molecularly-bonded oxygen that remained connected to the neighboring carbon atom, thus reducing precursor soot formation (Kitamura et al., 2001). The low amount of amount of soot in the dodecane flame could be attributed to the low amount of carbons in the molecular structure (Chapter 4) which required less oxygen to react with unburned hydrocarbons. Dodecane also does not contain double bonds which have been shown to promote the formation of soot as discussed in the previous section. At $\phi = 7$ the diesel flame produced the peak soot concentration for which all other values were normalized. Diesel was followed by a production of 50.5% of the full scale value for CME, 39.1% for SME, 24% for dodecane, and 14% for MS. Diesel fuel produced the highest radiative heat fraction (32 %), followed by SME (29 %), CME (27 %), dodecane (20 %), and MS (19 %).

In general, the radiative fraction values and peak soot volume fraction measurements correlated well. F values provided a good ‘quick’ approximation for the amount of soot for these flames. The method selected to compare the soot volume fraction and F-values, however, lead to some discrepancies. The peak soot volume fraction was selected as a representative of the total soot in the flame. This did not account for flames which had regions of peak soot volume fraction followed by a drop in soot in the other two measured portions of the flame. An example of this can be seen in Fig. 5.29 (CME at $\phi = 7$) and Fig. 5.33 (SME at $\phi = 7$), CME peaks in the mid-flame region with soot volume fraction measurements significantly lower in the near and far burner regions. This is in comparison to the SME soot volume fraction profiles which are seen in Fig. 5.33 which do not significantly vary in the three portions of the flame. The F-value accounts for the additional soot demonstrated by the higher value recorded for the SME flame. Also, it was also observed that biofuels produced lower peak soot volume fraction values and lower radiative heat fraction values than the diesel fuel which corresponds with engine study findings.

5.2.2 Effect of Iodine Number on Soot Volume Fraction

At fuel equivalence ratios of 1.2 and 2 no significant differences for soot volume fraction, as it varied with iodine number were observed. As the equivalence ratio was increased to very rich conditions such as those at 3 and 7 differences were apparent between the fuels. At $\phi = 3$, it was observed that diesel produced substantially more soot than the corresponding biofuels. As mentioned before, this was attributed to the soot precursors, such as aromatics, found in diesel which composed nearly 25% of the fuel composition. For biofuels at $\phi = 3$ SME produced the highest amount of soot followed by CME and MS. Therefore, for the biofuels, as the iodine number increased the amount of soot also increased at $\phi = 3$. At $\phi = 7$, diesel produced significantly more soot than the other biofuels. MS produced the lowest peak soot volume fraction followed by SME and CME which produced the highest. This was in contrast to the F values which showed SME to produce more soot based on the global measurement of radiation from the flame. From these data it can be seen that the unsaturated fuels which contain double bonds, such as SME and CME, facilitate the production of more soot which has been shown in previous studies (Douwel et al., 2009). This correlation, therefore, can affect other combustion products such as formed radical species. The next section describes the concentrations of intermediate radicals and their relation to soot and pollutant formation potential.

5.3 Intermediate Species Concentrations

Planar Laser Induced Fluorescence (PLIF) has been used extensively to determine the relative population densities of intermediate radicals within a combustion test medium (Baird and Gollahalli 2006, Haudiquert 1997, Kirby and Hanson 2000, Love et al. 2006). For PLIF measurements, a wavelength-controlled narrowband light source (laser) was used to excite molecules of a desired species (OH and CH) to a higher energy level. The incident photons absorbed at each point are re-emitted with a modified spectral distribution. The re-emitted photons, a form of molecular scattering and radiation termed fluorescence, are of interest for PLIF measurements. By capturing emitted fluorescence a non-intrusive method for measurement of various flow field properties, such as species concentration, with high temporal (5-20 ns) and spatial resolution (0.1mm – 1 mm) can be accomplished.

5.3.1 OH Radical Distributions

As previously mentioned (Chapter 2), the laser was tuned to the corresponding excitation wavelength of OH (283.5 nm). At this wavelength, OH was pumped at the Q_1 (6) transition in the OH $A^2\Sigma \leftarrow X^2\Pi$ system of the (1,0) band and the fluorescence from the (1,1) band was collected. PLIF images were captured from the injector exit to 5 cm above the burner; above this location recorded values were negligible. Because of the limited field of view of the ICCD camera composite images of the flames were overlapped and used. Images are presented as normalized signal intensities providing a qualitative representation and can be found in Figs. 5.43-5.46.

OH radicals have been used as indicators of the reaction zone of a flame, NO formation regions through the Zeldovich (thermal) mechanism seen in Eqs. (5.1-5.3), and locations of soot oxidation. Various authors have documented the presence of OH and NO though the PLIF and LIF techniques in diesel engines (Nakagawa et al., 1997, Fayoux et al., 2004, Demory et al., 2006). These engine studies, introduce several variables simultaneously, such as high pressure and temperature, which affect the various measured parameters both chemically and physically. For this study, a laminar flame was used in the present study to eliminate physical variables, attributing changes to fuel chemistry alone. PLIF was qualitatively used to determine relative concentrations of OH. The maximum intensity detected by the ICCD camera, occurring for diesel fuel at $\phi = 1.2$, was used to normalize all other detected values. OH images are presented for five liquid fuels: No. 2 diesel, canola methyl ester (CME), soy methyl ester (SME), dodecane, and methyl stearate (MS).

$$O + N_2 \leftrightarrow NO + N \quad (5.1)$$

$$N + O_2 \leftrightarrow NO + O \quad (5.2)$$

$$N + OH \leftrightarrow NO + H \quad (5.3)$$

At $\phi = 1.2$, Fig. 5.43, distributions of OH radicals for all fuels were greatest within the flame reaction zone. This location can be described as the primary gas phase oxidation region and area of interest. In this region diesel demonstrated the

highest concentrations followed by SME, CME, dodecane, and MS in that order. From Fig. 5.43 it can be seen that diesel produced up to 40 % more OH than either SME or CME, 50% more than dodecane, and 60% more than MS. At this condition, diesel was supplied with the largest amount of externally supplied oxygen (13.5 LPM), followed by dodecane (12.4 LPM), CME (12.37 LPM) and SME (12.37 LPM), and MS (12 LPM). Although all fuels were premixed at different air flow rates, they varied by <10% from fuel to fuel. This fails to account for the significant differences observed in the OH concentrations (up to 60%), thus, fuel chemistry was used to describe the cause for these differences. The kinetic model for diesel and oxygenated fuel combustion shown by Kitamura et al. (2001) was used to account for this. According to this model, the principal types of reactions responsible for the fuel consumption are hydrogen atom abstractions followed by β – scission reactions of larger hydrocarbon radicals, such as olefins. The resulting H atoms from the process start the development of a pool of radicals through the reaction, $H + O_2 \rightarrow O + OH$. The presence of these radicals accelerates the fuel consumption and fuel fragment production, which can lead to large amounts of soot production for the diesel flame. The biofuel molecules, however, contain molecularly-bonded oxygen that remains connected to the neighboring carbon atom, thus reducing precursor soot formation and lower flame height. Dodecane fails to develop the pool of radicals equal to those for the diesel fuel demonstrated by the lower OH radicals detected. Since dodecane is a straight-chain single component fuel and lacks double bonds, it became less likely to participate in reactions which promoted the formation of the hydroxyl radical.

At ϕ =2, Fig. 5.44, peak intensities were observed to be up to 60% lower than at ϕ =1.2, therefore, the intensity scale was modified. This was done to enhance the OH radical image for analysis. For this condition SME produced the highest amount of OH followed by MS, CME, diesel, and dodecane. SME intensities were 8-10% higher than that of MS, 10-12% higher for CME, 12-16% higher for diesel, and 20% or more for dodecane. The major concentration of OH was seen up to 1 cm above the burner. Above this location, low amounts of OH were documented. Differences between these fuels were attributed to the molecularily bonded oxygen within the fuel. At ϕ =1.2, the reaction step described by Kitamura et al. (2001) was used to describe the formation of the pool of radicals. However, at ϕ =2 this effect was no longer dominant since OH radicals were lower for diesel and dodecane compared to the biofuel flames, thus the effect of fuel/air premixing near the injector exit was smaller than the molecularily bonded oxygen in the biofuels. As the flames became more fuel rich, more oxygen was required to produce the OH radical. For this reason, the diesel and dodecane flames showed near uniform distributions in the captured region. For CME, SME, and MS internally supplied oxygen, found in the molecular structure, coupled with entrained air resulted in larger OH concentrations. Downstream of this location (<1.5 cm above the burner), mixing and entrainment with ambient air overtook the effect of the molecular oxygen, as seen by the similar concentrations of OH for all fuels. At ϕ = 3 and 7, the population of OH radicals dropped significantly for all fuels, between 4 and 8% of the full scale value, due to OH depleting

oxidation reactions. Therefore, no significant differences were observed between the OH concentration fields of the flames at $\phi = 3$ and 7.

5.3.2 CH Radical Distributions

For CH radical measurements the laser was tuned to the corresponding excitation wavelength of 431 nm. At this wavelength, CH PLIF was done using the transition of (0,0) band near 431 nm of the $A^2\Delta \leftarrow X^2\Pi$ system. PLIF images were captured from the injector exit to 6 cm above the burner; corresponding to the OH PLIF measurements. As before, due to the limited field of view of the ICCD camera composite images of the flames were overlapped and used. Images are presented as normalized signal intensities providing a qualitative representation and can be found in Figs. 5.47-5.50.

Since CH radicals are intermediately linked with the formation of NO through the Fenimore (prompt) mechanism, see Eqs. (5.4-5.6), CH PLIF was qualitatively used to determine relative concentrations of CH. The maximum intensity detected by the ICCD camera, occurring for SME fuel at $\phi = 7$, was used to normalize all other detected values. CH images are presented for five liquid fuels: No. 2 diesel, canola methyl ester (CME), soy methyl ester (SME), dodecane, and methyl stearate (MS).

$$CH + N_2 \leftrightarrow HCN + N \quad (5.4)$$

$$C_2 + N_2 \leftrightarrow 2\,CN \quad (5.5)$$

$$C + N_2 \leftrightarrow CN + N \quad (5.6)$$

At ϕ = 1.2, Fig. 5.47, distributions of CH radicals for all fuels were greatest within the flame reaction zone. CH radicals have been used to determine the location of the reaction in a flame, as opposed to OH radicals which typically are used as the location of where the reaction had just occurred. Experimental results presented show that the OH and CH concentration regions were similar in size and distribution. Results found in this region were similar to those found in the previous section of the report where diesel demonstrated the highest concentrations followed by SME, CME, dodecane, and MS. From Fig. 5.47 it can be seen that diesel produced up to 30 % more CH than either SME or CME, and 50% more than dodecane or MS.

At ϕ = 2, Fig. 5.48, the detected amount of CH radicals dramatically decreased. The levels of CH were found to be less than 20% of the peak concentration value for all fuels. For ϕ = 2 values for OH were also significantly lower than at ϕ = 1.2. A transition occurred, from high amounts of OH and CH at ϕ = 1.2 to this condition where concentrations dropped so that neither was dominant. The visible flame images show the lower portions of the flames, where these measurements were taken, to be ‘blue’ with the remaining flame length downstream of the injector exit ‘yellow’. Since less oxygen was supplied more oxygen was required through entrainment for the production of OH as can be seen by the lower concentrations. The formation, however, of other soot producing compounds such as polycyclic aromatic hydrocarbons were reduced since sufficient oxygen was supplied to suppress their formation demonstrated by the low soot volume

fraction. Therefore, at $\phi = 2$ there seems to be a transitional point in the formation of soot, CH, and hydroxyl radicals.

As the equivalence ratio was increased to 3, Fig. 5.49, significantly more CH was detected at 4-5 cm above the injector exit. From the visible flame images of the biofuels and dodecane this region corresponded with the boundary of the gas phase oxidation regions of these flames and the 'yellow' soot containing regions. Near the injector exit where oxidation reactions were expected low concentrations of CH were detected, similar to results from $\phi = 2$. Downstream of this location the amount of pyrolyzed hydrocarbons and soot increased with CH reaching peak approximately 4-5 cm above the burner. Values above this region decreased, followed by a steep increase in the detection of CH due to the presence of significant amounts of soot which emitted radiation at all wavelengths saturating the readings from the ICCD camera. CME produced the highest peak CH concentrations with the largest detected region followed by SME, diesel, dodecane, and methyl stearate. The region of detection for the CME flame extended from the base of the acquired image to 5 cm above the burner. SME and diesel CH radicals peaked along this region while dodecane and MS fuels did not demonstrate this behavior. This region seems to be the location of significant reactions for CME, SME, and diesel which possibly accounts for the formation of NO as will be discussed later in section 5.4.

At $\phi = 7$, Fig. 5.50, significant CH concentrations were again detected at 4-5 cm above the injector exit. Visible flame images of the all fuels appeared yellow with the biofuels blue very near the injector exit (<1 cm). Highest to lowest peak

values of CH were recorded for SME, CME, diesel, MS, and dodecane at 4-5 cm above the burner. SME produced peak concentrations of all fuels at any condition in a pocket 3-4 cm above the injector and 1 cm across in the radial direction. Diesel and MS also produced this small pocket of CH, existing at 4-5 cm above the burner exit and reaching a peak along the centerline of the flame. CME produced a similar distribution to that at $\phi = 3$ with CH detected in the near burner region extending to the pocket of radicals observed for the other fuels. Dodecane produced the lowest amount of radicals and was the only fuel that did not produce a high concentration of CH or distribution comparable to the other fuels. Above this region of measurement values of CH increased significantly again due to the presence of significant amounts of soot resulting in the saturation of the readings from the ICCD camera.

5.4 In-Flame Species Concentration Profiles

Radial concentration profiles of NO, CO, CO_2, and O_2 at the same axial locations as temperature and soot volume fraction are presented in Figs. 5.51-5.130. Experimental uncertainties were also calculated using Student's t-distribution at a 95% confidence interval and are presented in the appropriate figures as error bars. Several radial points were repeated during the measurements for each axial location. The largest uncertainty was selected for each pollutant emission at each condition and used as a representative for the overall uncertainty.

5.4.1 Nitric Oxide (NO)

Concentration profiles of NO are presented in Figs. 5.51 – 5.70 for all fuels at equivalence ratios of 1.2, 2, 3, and 7. At ϕ = 1.2 all fuels demonstrated similar distributions of NO, with peaks occurring along the flame boundary where the primary region of gas-phase oxidations reactions took place. Peak NO concentrations, occurring in the far-burner region, were highest for SME (447 ppm), CME (430 ppm), diesel (400 ppm), MS (335), and dodecane (315 ppm) in that order. In the region near the injector exit distributions of OH (Fig. 5.43) were highest for all fuels indicating regions of primary oxidizing reactions which corresponded with peak flame temperatures ($\approx$ 2200 K) at this condition. An increase in NO was observed at farther locations downstream of the injector exit which can be attributed to the effects of an increase in cumulative residence time. Based on these results the dominant formation of NO at this condition can be attributed to the thermal (Zeldovich) mechanism.

Next, at $\phi = 2$, the relationship between residence time (flame length), flame temperature, OH radical distribution, and NO concentrations was significantly different from data obtained at $\phi = 1.2$. At $\phi = 2$ NO production did not follow with temperature, OH, or CH distributions. Flame temperatures of the biofuels and diesel were similar with dodecane producing the lowest flame temperatures due to radiative heat losses. Also, low concentrations of OH and CH were recorded in the near burner region where peak NO concentrations were as follows: SME (404 ppm), diesel (380 ppm), CME (298 ppm), MS (123 ppm), and dodecane (88 ppm). Since primary NO formation was observed in the near burner region of these flames, the relatively longer residence time needed by the thermal mechanism was not achieved. These findings indicate that a transition was occurring and the thermal mechanism was no longer dominant.

At $\phi = 3$, NO concentrations in the near burner region and along the centerline increased significantly dropping to much lower values at the mid and far burner locations in the flame. In this region SME produced the highest peak NO (569 ppm) followed by CME (564 ppm), diesel (324 ppm), MS (225 ppm), and dodecane (107 ppm). As at the previous condition of $\phi = 2$, measured values of NO did not correlate with the peak measured temperatures, OH concentrations, or residence time for the fuels. Additionally, CH radical concentration significantly increased with the amount of NO, with SME and CME producing the largest concentrations of CH followed by diesel, dodecane, and MS. CH radicals found in this portion of the flame peaked along the centerline of the flame where peak fuel, fuel fragments, and soot was expected. This was also observed for the very fuel

rich equivalence ratio of 7. At $\phi = 7$ in the near-burner region, NO concentration significantly increased in the near burner region and centerline of the flame reaching peak values of 1166 ppm for SME, 1067 ppm for CME, 470 ppm for diesel, 414 ppm for MS, and 106 ppm for dodecane. CH radicals peak values for SME and CME along the centerline of the flame corresponded with peak NO measurements. This was followed by descending amounts of CH radicals measured for diesel, MS, and dodecane. These data which include increased NO near the injector exit, high CH radical concentrations, and low (<1800 K) flame temperatures imply dominance of NO formation through the prompt mechanism.

Engine studies have attributed NO formation to the Zeldovich mechanism (Scholl and Sorenson, 1993, Wang et al., 2000) when comparing biodiesel to diesel fuel emissions. NO formation through the Zeldovich mechanism has been described by the reactions in Eqs. (5.1-3). In cases where there are small concentrations of oxygen, N atoms have been shown to react with atoms other than oxygen or hydroxyls. At rich equivalence ratios, such as those encountered in the non- premixed flame combustion in diesel engines and those in this study can not account for the very high concentrations of NO observed in the near burner region. An alternative mechanism suggested by Fenimore (1970) and Iverach (1972) is shown in Eqs. (5.4-6).

As mentioned before, the formation of nitric oxide by the prompt mechanism, seen in Eqs. (5.4-6), is connected to the degradation of hydrocarbons. Along the centerline position where peak concentration of fuel pyrolysis fragments and soot was expected, NO concentrations peaked. Nitrogen atoms generated by the

reactions $C + N_2 \leftrightarrow CN + N$ and $CH + N_2 \leftrightarrow HCN + N$ reacted with oxygen radicals to form NO. For the biofuels the atomically bonded oxygen which did not remain connected to the neighboring carbon atom accelerated the conversion of N demonstrated by the higher amount of NO measured compared to diesel and dodecane.

It was also observed that peak NO concentrations increased with iodine number, Fig. 5.71, particularly at equivalence ratios of 3 and 7. This corresponded with previous findings in engine exhaust studies that have shown this same trend (McCormick et al., 2001). Therefore, this phenomenon is certainly dependent on the chemical structure of the fuel. The double bonds present in unsaturated fuels, such as SME, facilitate the production of more soot (Douwel et al., 2009) ultimately resulting in the production of more NO. Higher iodine numbers indicate the number of carbon-carbon pi bonds which are more likely to break than C-C or C-H bonds leading to high radical formation thus more CH. This coupled with the presence of the oxygen in the fuel accelerated the formation of NO. All fuels produced peak NO concentrations at the same axial location, $0.25F_L$, and at the centerline location raidially. Above this NO concentrations sharply decreased. At very rich equivalence ratios it has been shown that NO can be recycled to HCN inhibiting its production (Turns, 2000).

5.4.2 Carbon Monoxide (CO)

Carbon monoxide is a colorless, odorless, poisonous gas that can cause severe harm and even death (Pulkrabek, 2004). Carbon monoxide (CO) is a significant species in the combustion of rich mixtures such as those in the present study and typically represents the incomplete combustion product of pyrolyzed fuel components. Concentration profiles of CO are presented in Figs. 5.72 – 5.91 for all fuels at equivalence ratios of 1.2, 2, 3, and 7. In general, all fuels demonstrated similar distributions of CO in the radial and axial profiles of the flames. Low values were recorded until reaching the flame boundary increasing up to ≈ 6% along the flame centerline. Peak values were achieved for all fuels and conditions in the near burner region of the flames decreasing at the mid-flame and far burner locations as CO was oxidized to CO_2.

At ϕ = 1.2 all fuels demonstrated similar distributions of CO concentration, with peaks occurring along the fuel-rich flame centerline. At approximately 6-7 mm from the center of the burner, where the flame boundary was visually defined, CO concentration values began to increase from zero and continued to increase to the flame centerline where the peak values occurred. Quantities of CO are listed here in descending order with MS producing the highest value of 6.03 % followed by 5.81% for diesel, 5.44 % for CME, 5.2% for dodecane, and 5.15% for SME. Similar results were obtained at ϕ = 2 and 3. Flames increased in thickness thus the CO concentrations began to increase at locations farther from the flame centerline, e.g., 10-14 mm from the center of the burner. Peak CO concentrations again occurred in the near burner regions decreasing at

downstream locations. At $\phi = 2$ diesel (6.05 %) produced the largest amount of CO followed by dodecane (5.98 %), SME (5.9 %), CME (5.87 %), and MS (5.77 %). At $\phi = 3$ SME (6.03 %) and MS (6.03 %) both had the highest amount of CO and was practically the same as that produced by CME (6.02 %), dodecane (6.02 %), and diesel (5.79 %). Although values of the in-flame concentrations were comparable for these fuels at $\phi = 2$ and 3, the global emissions of EICO showed a significant increase for all fuels at $\phi = 3$, particularly for diesel. At $\phi = 7$ dodecane (5.98 %) showed the largest amount of CO with MS (5.83 %) showing the next highest followed by SME (5.62), CME (5.56 %), and diesel (5.48 %). Profiles were similar to those at the lower equivalence ratios, decreasing as the probe was moved further downstream of the injector exit. It was observed, however, that dodecane and MS produced the highest quantities of CO at this condition. This does not correspond to the measured EICO values in the previous chapter. Diesel at $\phi = 7$ produced very high values of EICO and other fuels showed a significant increase from $\phi = 3$, Fig. 4.12, with MS and dodecane producing the lowest values of EICO. This could be due to the presence of soot in the far burner region of diesel, CME, and SME flames which continued to oxidize above this region and form CO. Diesel which produced significantly more EICO than these fuels was also found to produce up to 50% more soot than CME and SME and up to 80% more soot than dodecane or MS at the same condition.

5.4.3 Carbon Dioxide (CO_2)

Carbon dioxide, a product of complete combustion, indicates the oxidation of fuel fragments and CO within the flame. Recently, emphasis has been placed on reducing CO_2 emissions and on 'carbon-neutral' technologies. For this reason and to obtain a better understanding of the combustion characteristics of these flames, carbon dioxide measurements are presented in this section of the report. Concentration profiles of CO_2 from this study are presented in Figs. 5.92 – 5.111 for the five fuels at equivalence ratios of 1.2, 2, 3, and 7. For the tested fuels, CO_2 production was directly affected by fuel equivalence ratio and flame temperatures, remaining higher for the lowest equivalence ratio of 1.2 and decreasing for the subsequent conditions.

At ϕ = 1.2 fuels demonstrated a 'double-hump' structure near the injector exit with peak values obtained along the flame reaction zone boundary while decreasing toward the flame centerline. Profiles above this region became flatter in the mid and far-burner regions. No significant differences were observed in the peak CO_2 concentrations for all fuels at this condition with diesel (14.7 %) and CME (14.7 %) showing the highest value followed by SME (14.4 %), MS (14.2 %), and dodecane (13.9 %).

As the equivalence ratio was increased to 2 and less oxygen was supplied, peak concentrations of CO_2 dropped. The flames maintained similar structure to that at ϕ = 1.2 with peaks along the flame boundary, decreasing as the probe traversed near the centerline. MS produced the highest peak value of CO_2 (12.5 %), other fuels produced 12.1 %, 11.6%, 11.3%, and 10.6 for SME, dodecane,

CME, and diesel, respectfully. At $\phi = 3$ peak concentrations dropped with MS producing 11.5%, 10.8% for SME, 10.3% for CME, 10 % for diesel, and 9.5 % for dodecane. At the next condition of $\phi = 7$, peak concentrations dropped again with SME producing 11.1%, 10.4% for dodecane, 9.9% for CME, 9.8 % for MS, and 8.4 % for diesel.

Profiles of CO_2 for $\phi = 1.2$, 2, 3, and 7 corresponded with the measured temperature profiles from these flames, (Figs. 5.1-5.20), typically reaching a maximum value in regions of peak temperature. It was also observed that the biofuels produced more CO_2 above $\phi = 2$ than diesel fuel. As the biofuel was burned, some of the carbon oxygen bonds seen in the molecular structure remained connected allowing for faster oxidation of CO to CO_2 (Kitamura et al., 2001).

Although the biofuel flames produced more CO_2, they have been considered as essentially 'carbon neutral' fuels. Since these fuels derived from organic vegetation the carbon dioxide captured by the plant (e.g., soy) was used to convert the gas into glucose through photosynthesis. Glucose in the plants could then be converted to sugars, starches, proteins, and oils within the plant itself. The oils derived from the plant were then transesterified and used in this study as a biofuel thus resulting in a carbon dioxide balance.

5.4.4 Oxygen (O_2)

Varying amounts of oxygen were found within the present flames depending on the equivalence ratio of the flame. Oxygen concentrations at the same locations as the other emissions are presented in Figs. 5.112-5.131. Uncertainties based on the Student's t-distribution at a 95% confidence interval presented as error bars cannot been seen for most conditions due to their small size. At the lowest equivalence ratio of 1.2 all flames began with the local atmospheric oxygen percentage outside of the flames. As the probe approached the flame boundary, the O_2 concentration values began to decrease to zero as the probe entered the reaction region which occurred at approximately 6 mm from the burner centerline. It was observed that as the probe moved further downstream to the mid-flame and far burner regions more oxygen was present. This effect is least at this condition as the amount of air supplied was highest requiring less air entrainment from the surroundings. At $\phi = 2$ up to 4% oxygen was measured in the far burner region along the centerline of the diesel, SME, and CME flames indicating the entrainment of more air in order to oxidize fuel fragments, soot, and CO. Dodecane showed the highest amount of O_2 in the far-burner region up to 8%. Next at $\phi = 3$, oxygen concentrations remained about zero in the near burner region for all fuels and increased in the mid flame regions to 5% for the diesel fuel. As the probe traversed across the far burner region near the centerline, the O_2 concentration values rose to 14%, 7%, 5%, 4%, and 1% for diesel, CME, SME dodecane, and MS. For $\phi = 7$, more oxygen was detected in all regions of the flames for all fuels. Oxygen concentrations dropped to about zero in the near

burner region at much closer locations to the centerline (2-4 mm).This was due to the low flow rate which allowed for air in the surrounding quiescent environment only to diffuse and mix with the very fuel rich vapor-air mixture.

5.5 Liquid and Vapor Biofuel Flames

The results of this study showed that vapor flames of CME and SME biodiesel produced higher quantities of NO compared to conventional petroleum diesel fuel. This was true for both the measured global and in-flame species concentration measurements. The most recent diesel spray flame model by Flynn et al. (1999) predicts the spray inside the cylinder of an engine as a vapor plume burning at very fuel rich equivalence ratios from 4 to 8. As mentioned several times in this report, diesel engine studies have shown that NO is higher for biodiesel compared to diesel engines. This was also observed by Barajas (2009); the author studied the combustion of biodiesel and Jet-A fuels using porous media burners. The porous media vaporized the liquid spray flames through radiative heat feedback and resulted in higher values of EINO.

Other authors, however, have shown that liquid spray flames of biodiesels have produced lower values of EINO compared petroleum based diesel. Erazo (2008) investigated the combustion of liquid spray flames of biodiesel and diesel fuel at various equivalence ratios and atomization properties. The author observed that EINO was significantly lower than in petroleum diesel flames. Habib (2008) used neat biodiesel and blends in a SR-30 small scale gas turbine. Results showed that increasing amounts of biodiesel in the blends decreased NO concentrations.

These studies show the effect of fluid mechanics (droplet evaporation) on the resulting emissions. This is noted here as an observation to others. Further investigation in this, however, is beyond the scope of this study.

5.6 Chapter Conclusions

The following conclusions are drawn regarding the in-flame properties of hydrocarbon and biofuel flames.

Flame Temperature:

- Flame temperatures at ϕ = 1.2 and 2 were similar for all fuels. At ϕ = 3 and 7 fuels with higher soot concentrations transferred heat away from the flame resulting in lower measured flame temperatures.

Soot Volume Fraction:

- The fuel structure of the biofuels acted to suppress the formation of soot by preventing the development of a pool of radicals
- The radiative fraction values used in the previous chapter to predict the amount of soot in the flame was in agreement with soot volume fraction measurements. Thus, F values provided a good 'quick' indication of the amount of soot for these flames.

Radical Distributions and Emission Concentrations:

- NO concentrations at ϕ = 1.2 increased with flame length, were produced in high temperatures ($\approx$ 2200 K), and were present in regions of significant OH concentrations therefore was attributable to the thermal mechanism.

- At fuel rich conditions NO concentrations no longer correlated with flame length, temperature, and were present in regions of significant CH concentrations therefore attributable to the prompt mechanism.
- Iodine number was a parameter that primarily affected only the biofuel emissions, as trends were clearly observed which corresponded with engine study findings.

Table 5.1 Adiabatic flame temperature of all fuels at stoichiometry

Fuel	MS	Dodecane	Diesel	CME	SME
Adiabatic Flame Temperature at Stoichiometry (K)	**2249**	**2272**	**2282**	**2268**	**2266**
Enthalpy of Reactants (kJ/kmol – fuel)	**-927267**	**-318563**	**-256037**	**-760220**	**-771217**

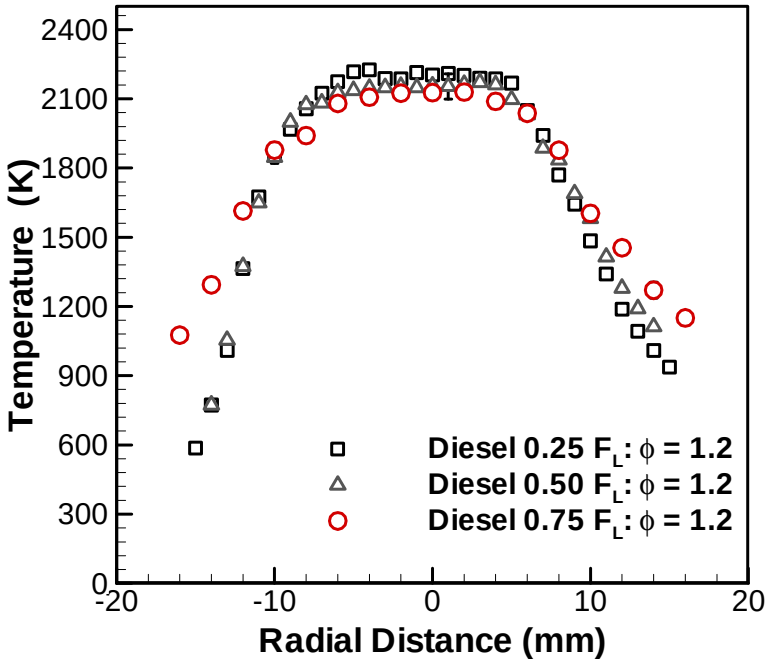

Figure 5.1 Temperature profiles of diesel at ϕ =1.2

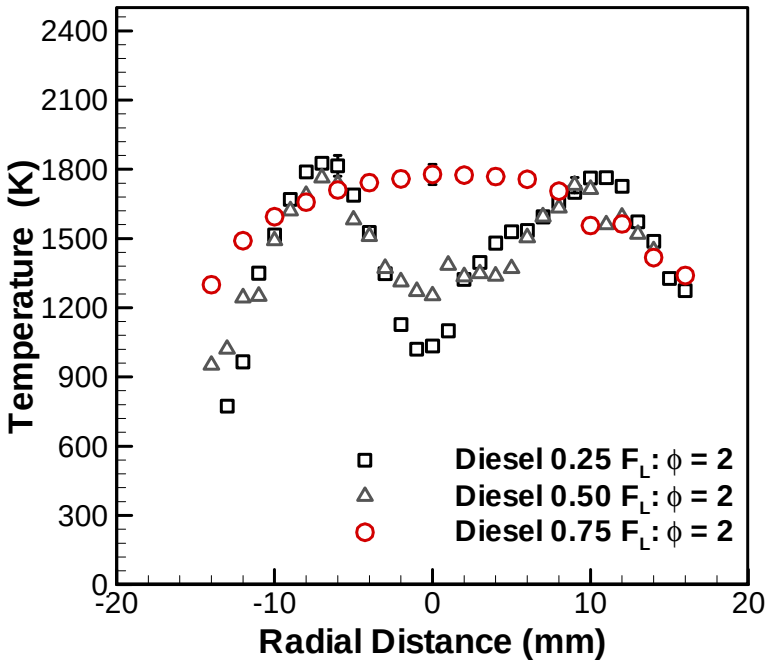

Figure 5.2 Temperature profiles of diesel at ϕ =2

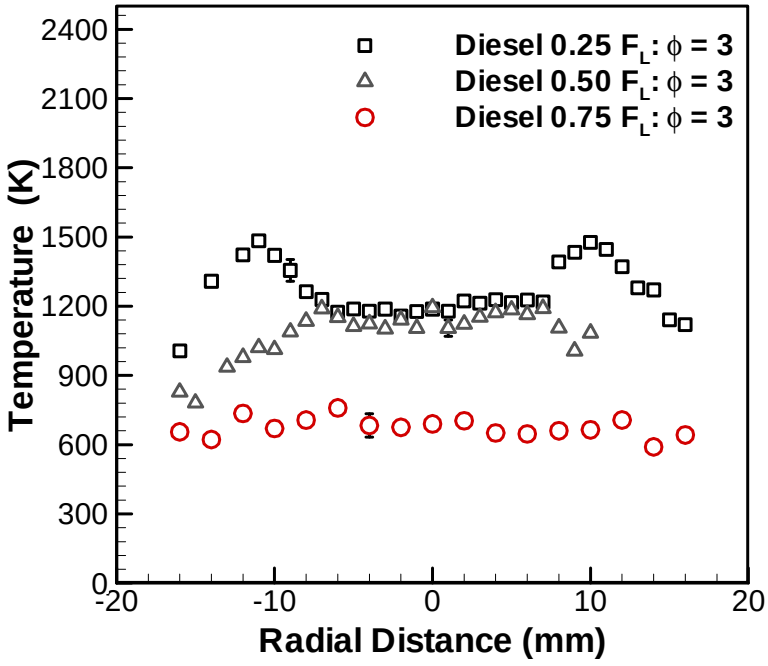

Figure 5.3 Temperature profiles of diesel at ϕ =3

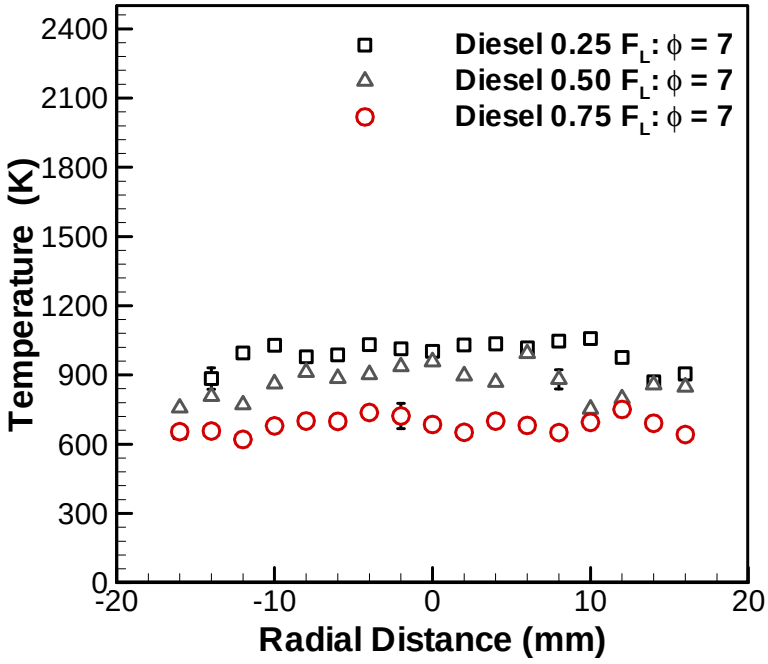

Figure 5.4 Temperature profiles of diesel at ϕ =7

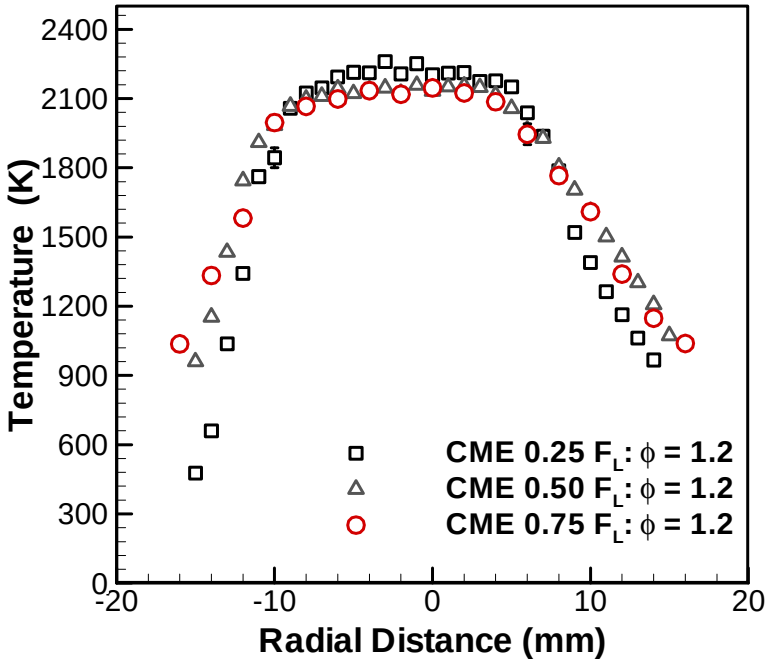

Figure 5.5 Temperature profiles of CME at ϕ =1.2

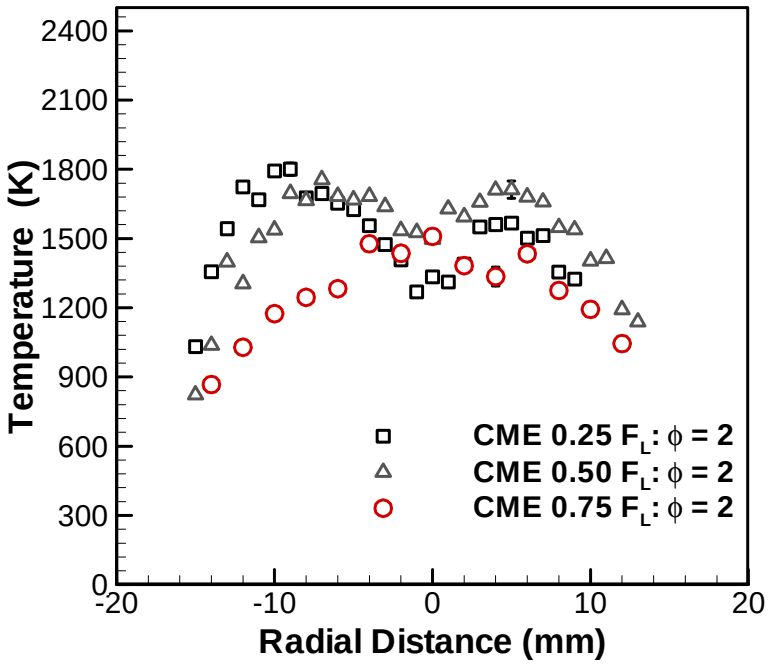

Figure 5.6 Temperature profiles of CME at ϕ =2

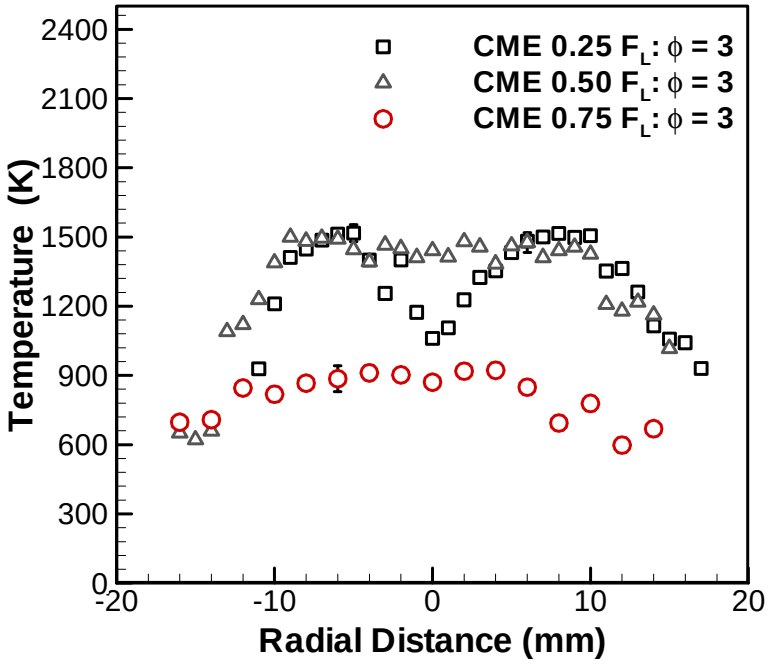

Figure 5.7 Temperature profiles of CME at ϕ =3

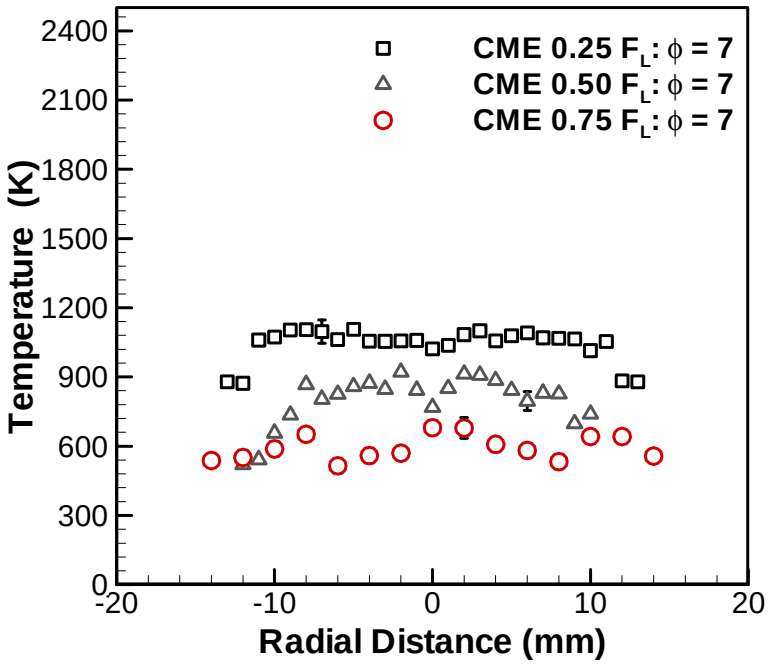

Figure 5.8 Temperature profiles of CME at ϕ =7

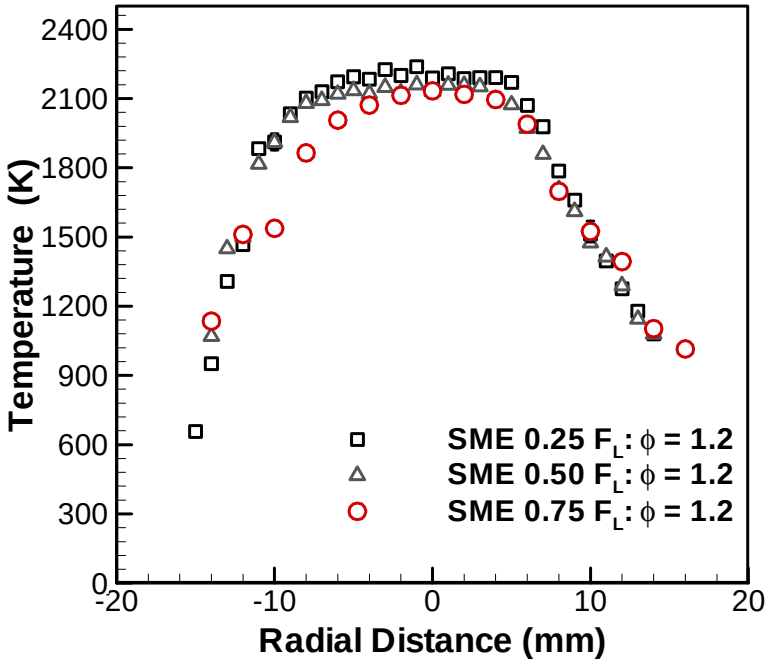

Figure 5.9 Temperature profiles of SME at ϕ =1.2

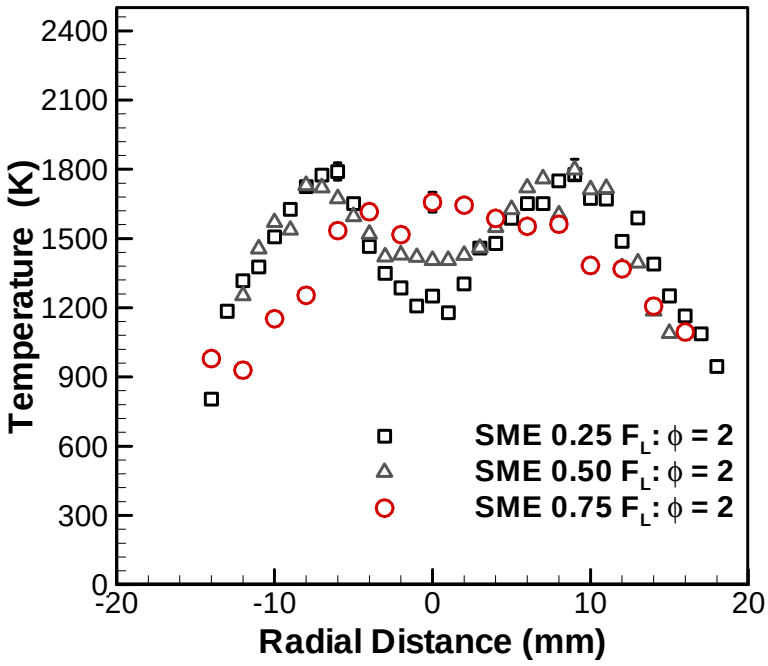

Figure 5.10 Temperature profiles of SME at ϕ =2

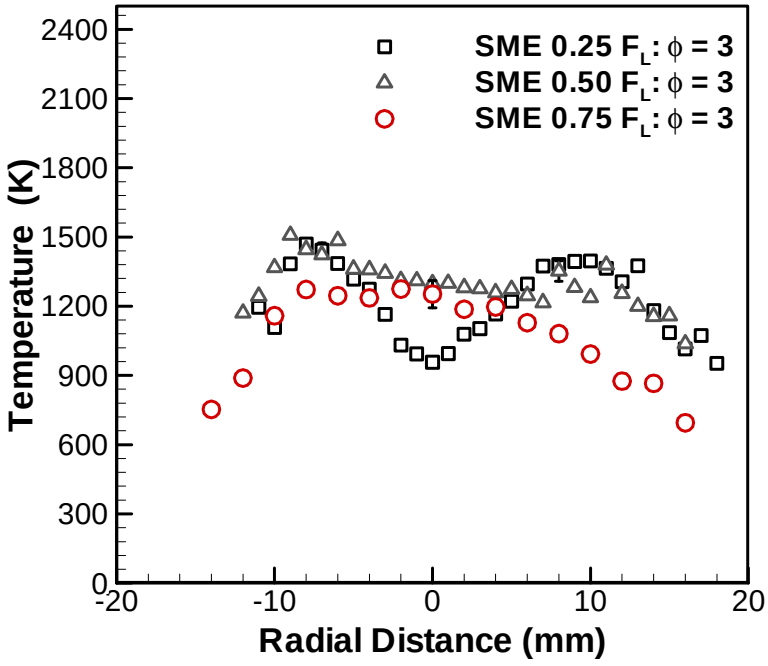

Figure 5.11 Temperature profiles of SME at ϕ =3

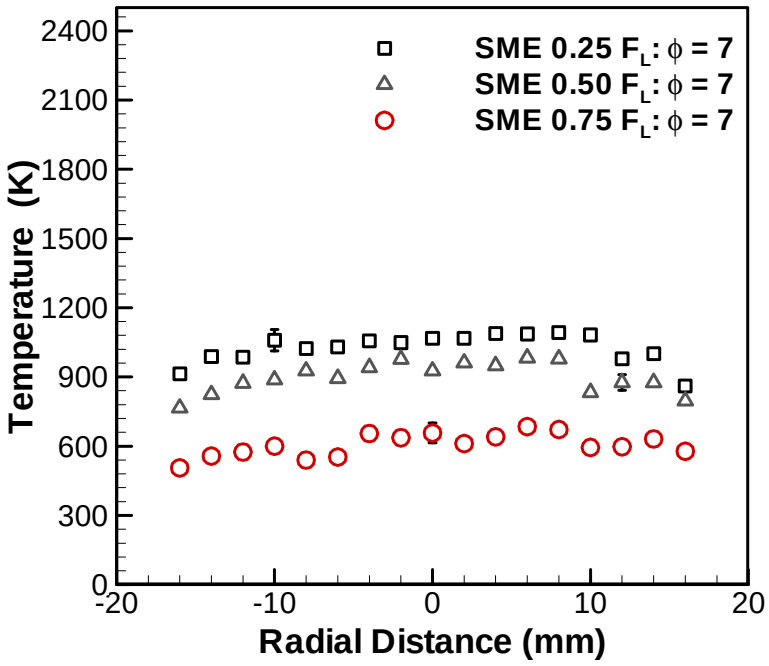

Figure 5.12 Temperature profiles of SME at ϕ =7

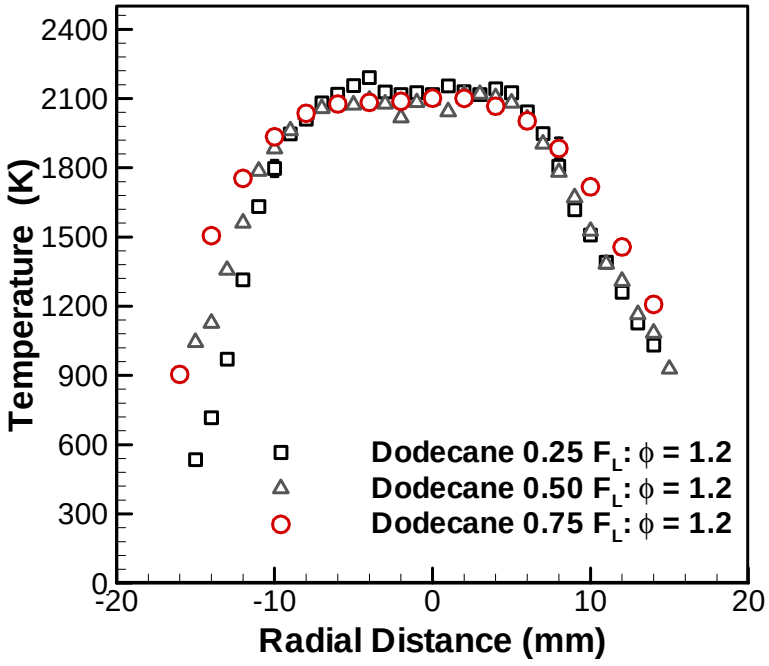

Figure 5.13 Temperature profiles of dodecane at ϕ =1.2

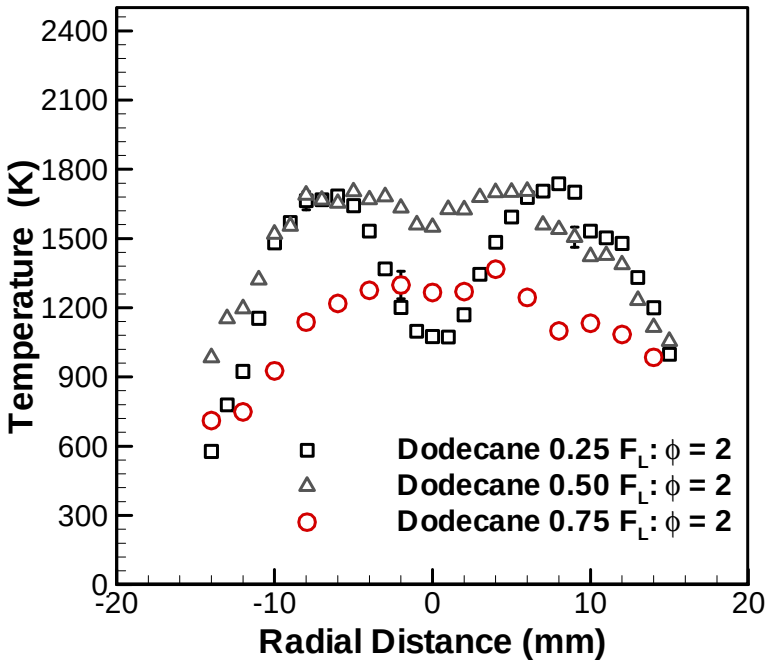

Figure 5.14 Temperature profiles of dodecane at ϕ =2

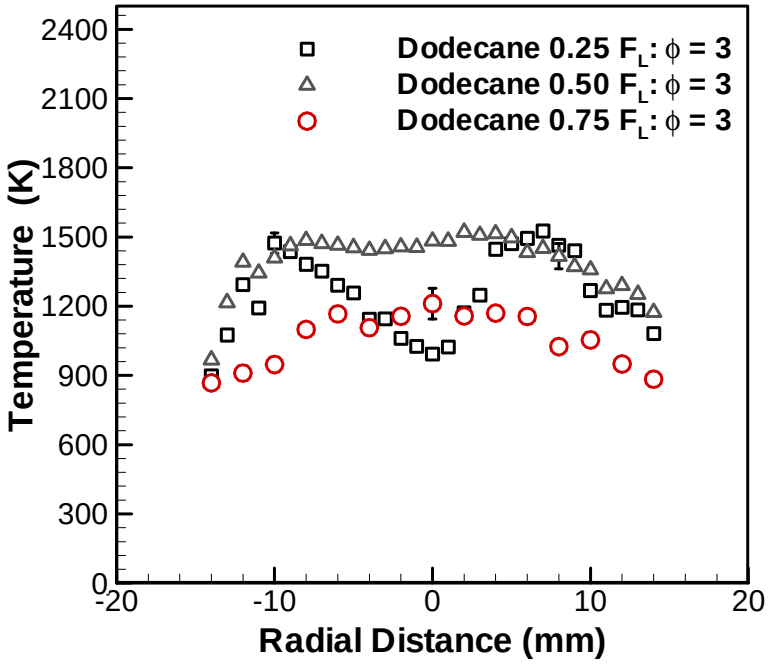

Figure 5.15 Temperature profiles of dodecane at ϕ =3

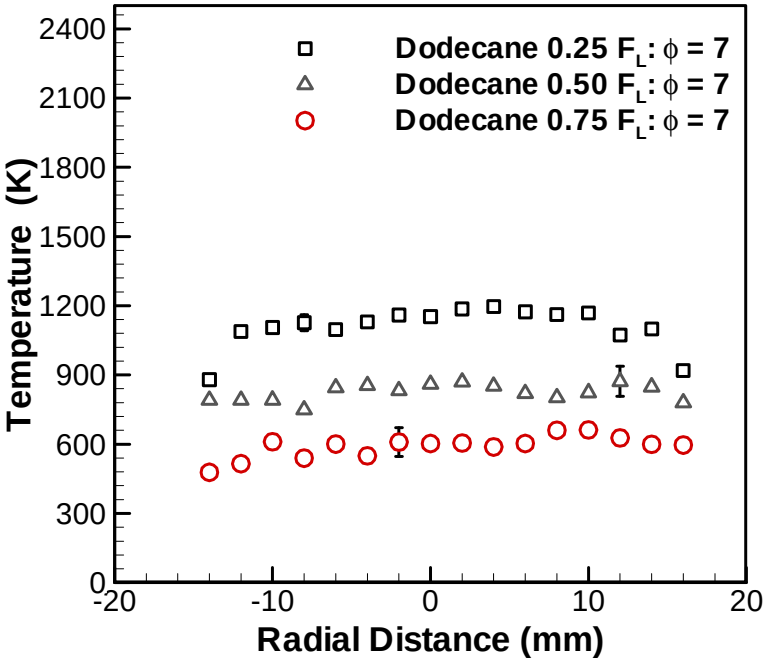

Figure 5.16 Temperature profiles of dodecane at ϕ =7

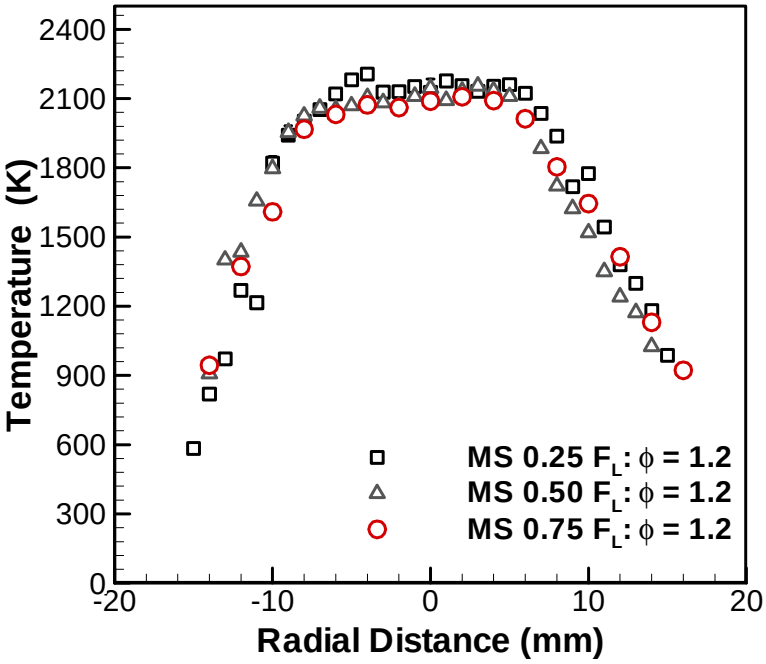

Figure 5.17 Temperature profiles of methyl stearate at ϕ =1.2

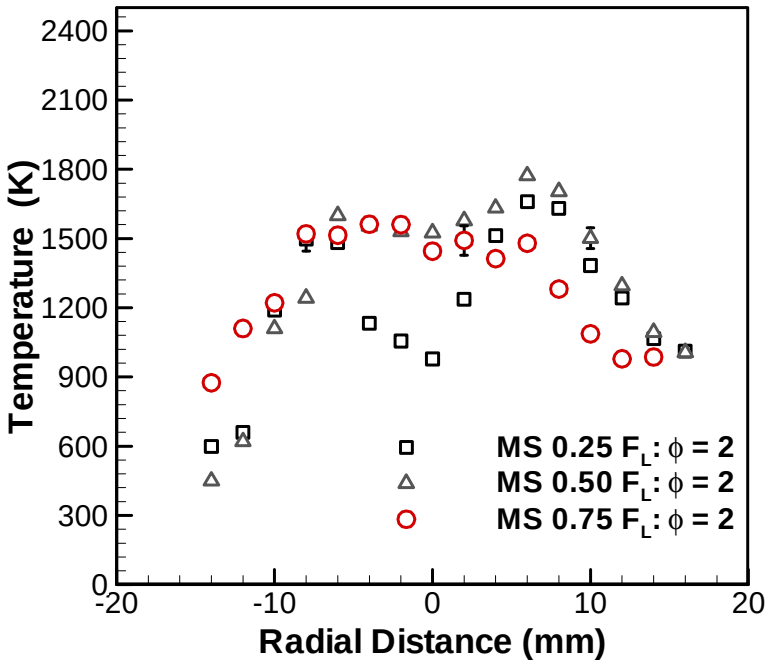

Figure 5.18 Temperature profiles of methyl stearate at ϕ =2

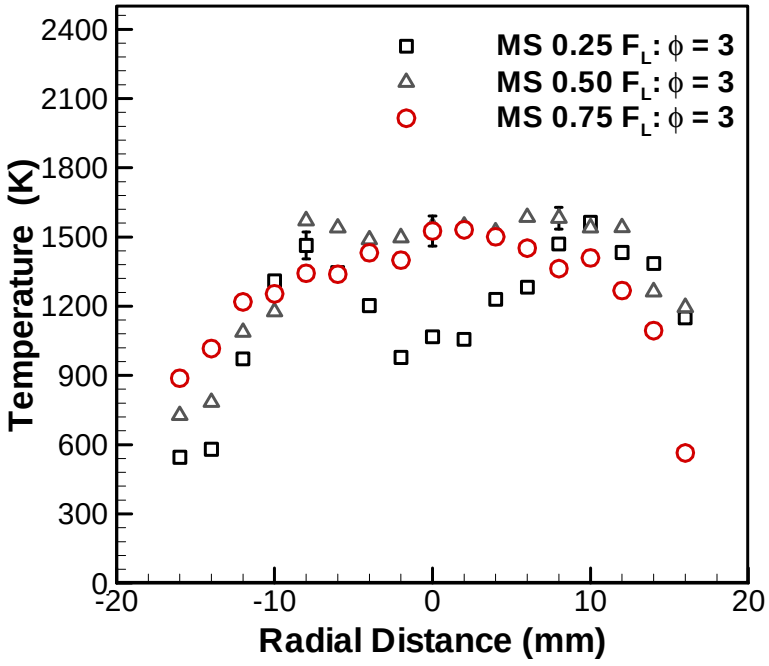

Figure 5.19 Temperature profiles of methyl stearate at ϕ =3

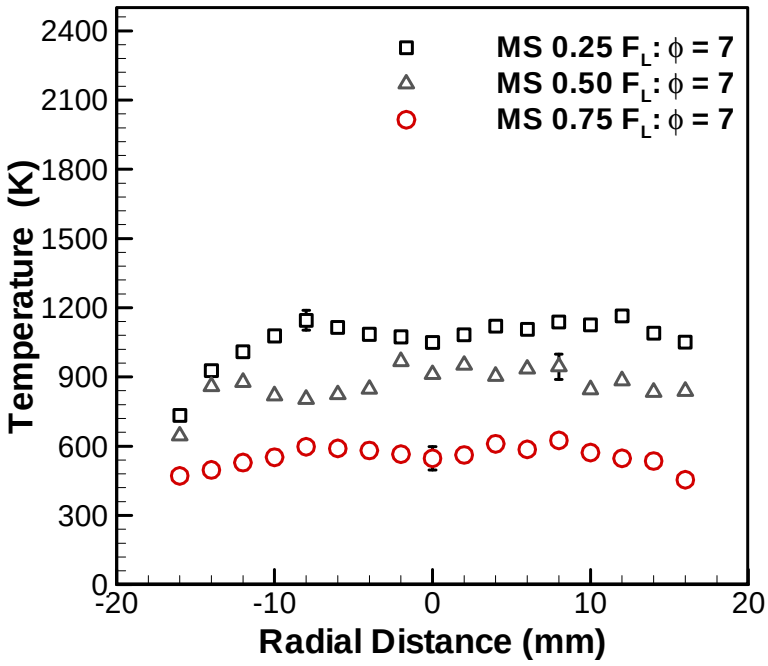

Figure 5.20 Temperature profiles of methyl stearate at ϕ =7

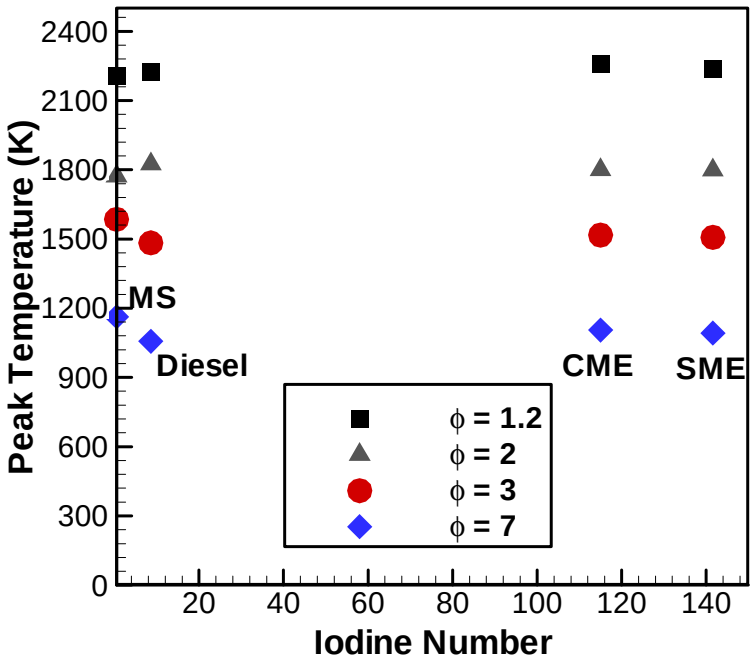

Figure 5.21 Peak temperatures at ϕ =1.2, 2, 3, and 7 plotted against Iodine Number

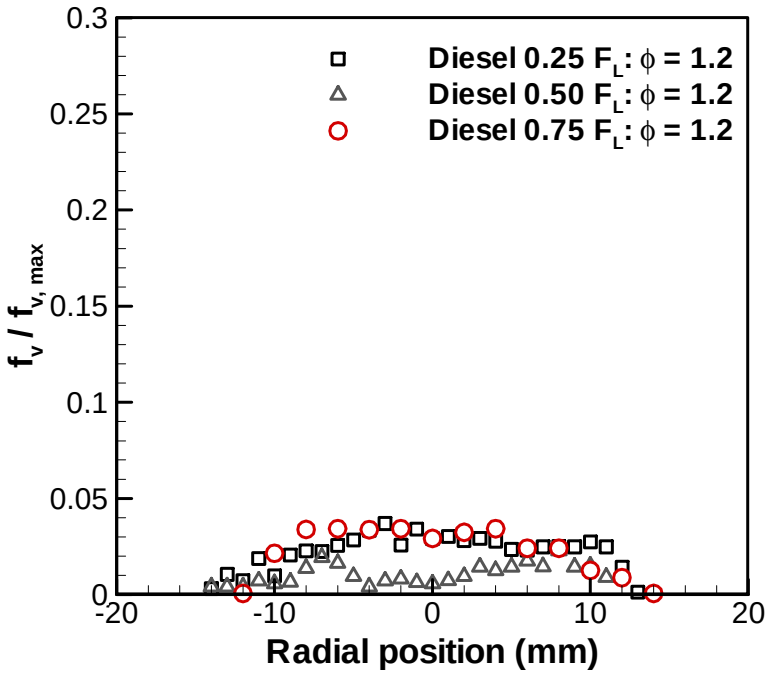

Figure 5.22 Diesel soot volume fraction profiles at ϕ =1.2

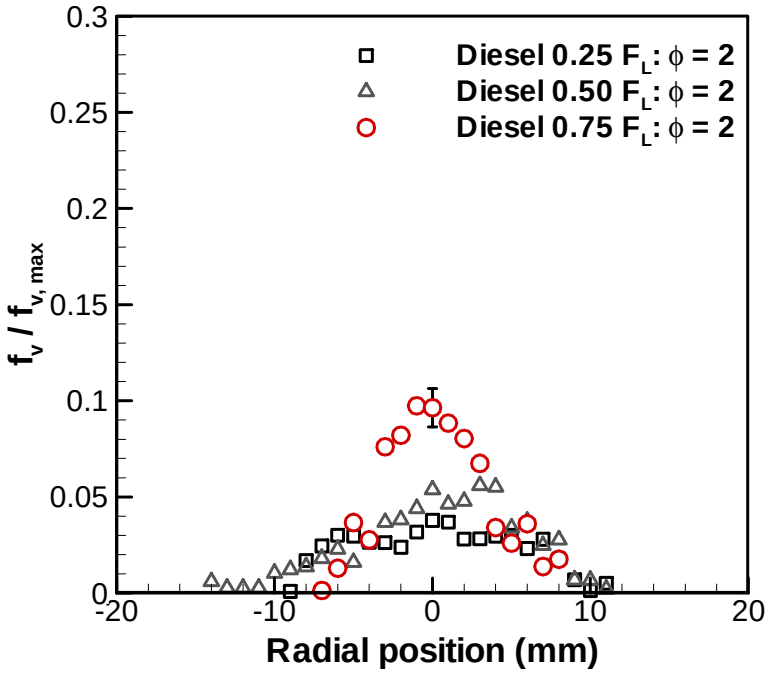

Figure 5.23 Diesel soot volume fraction profiles at ϕ =2

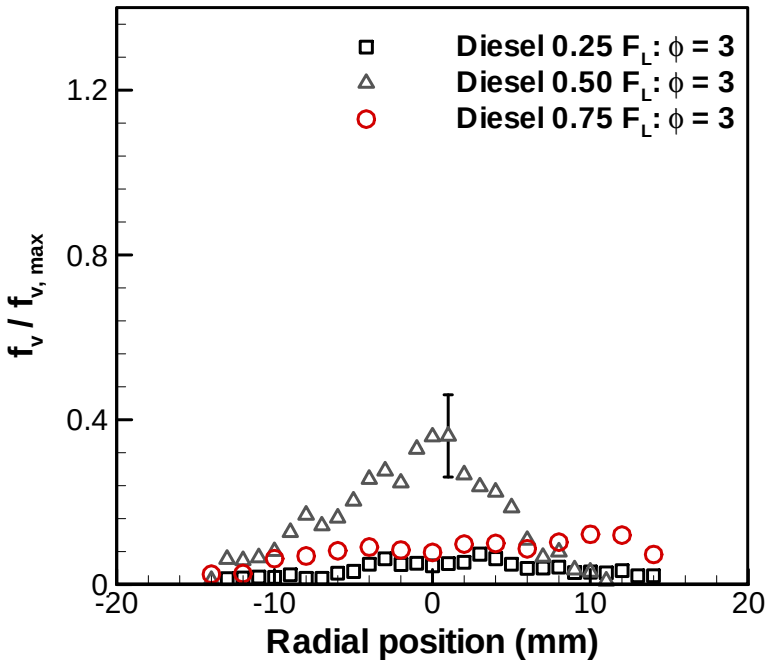

Figure 5.24 Diesel soot volume fraction profiles at ϕ =3

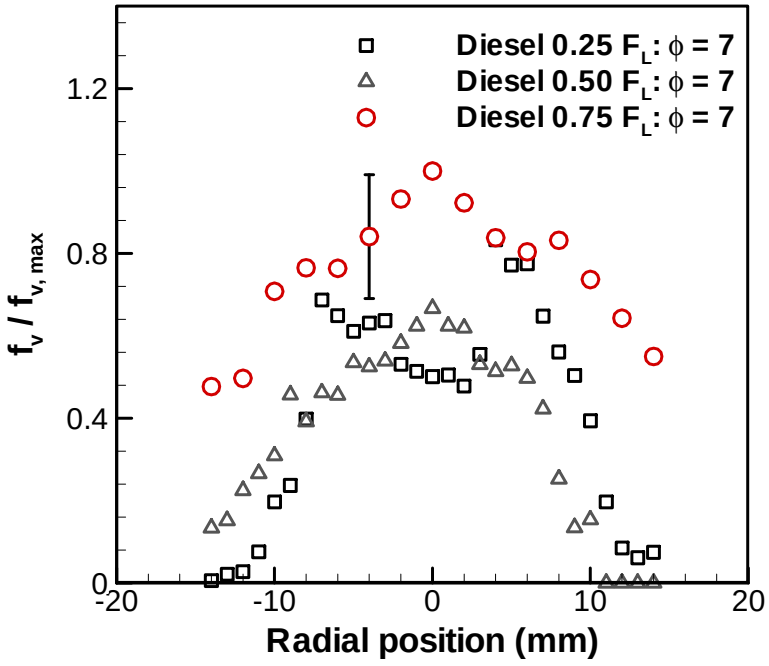

Figure 5.25 Diesel soot volume fraction profiles at ϕ =7

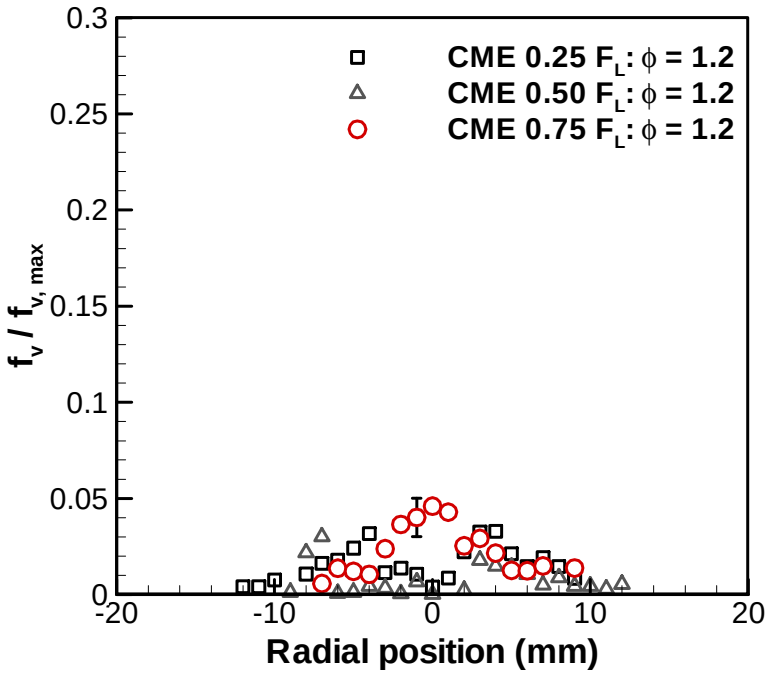

Figure 5.26 CME soot volume fraction profiles at ϕ =1.2

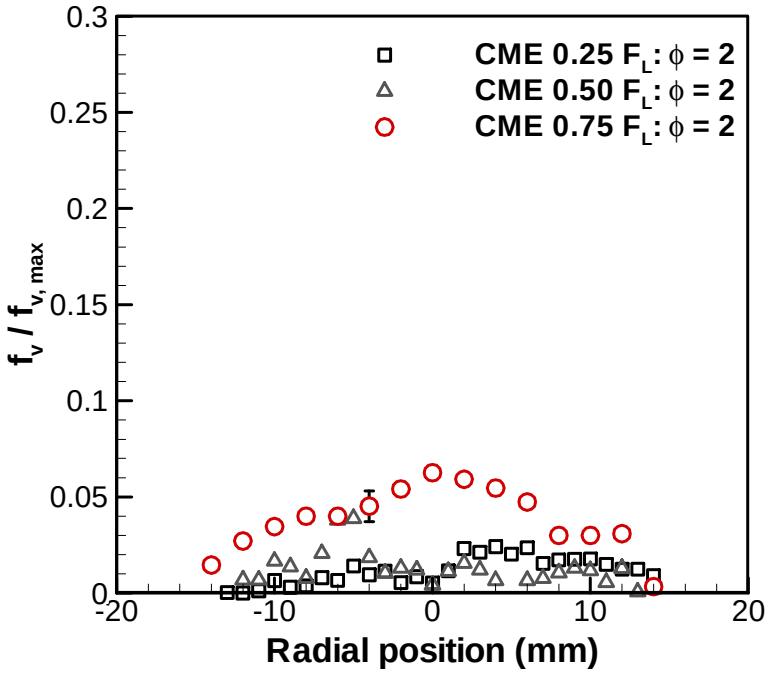

Figure 5.27 CME soot volume fraction profiles at ϕ =2

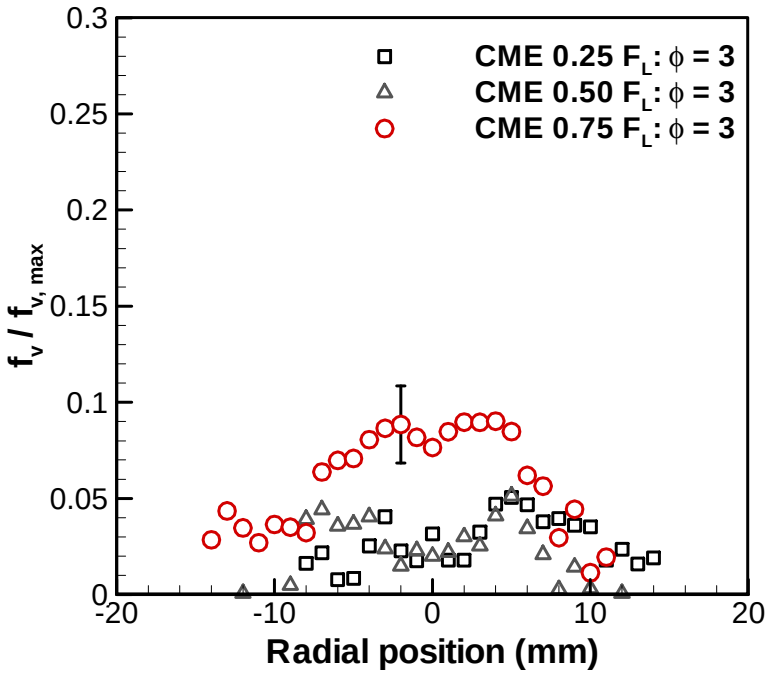

Figure 5.28 CME soot volume fraction profiles at ϕ =3

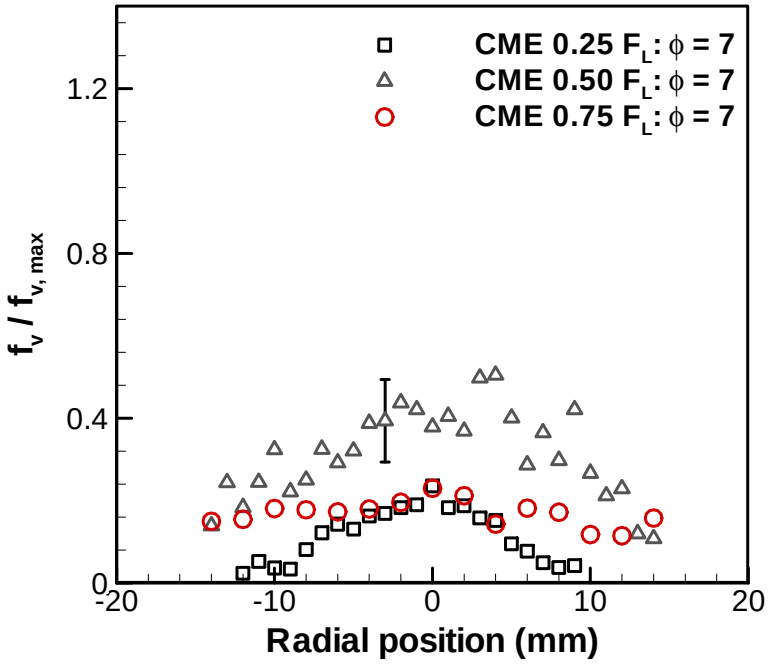

Figure 5.29 CME soot volume fraction profiles at ϕ =7

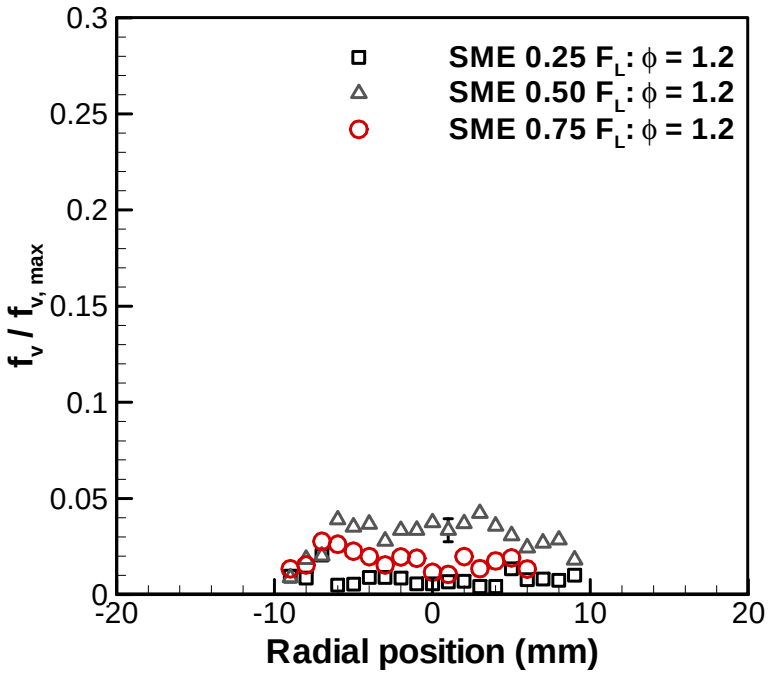

Figure 5.30 SME soot volume fraction profiles at ϕ =1.2

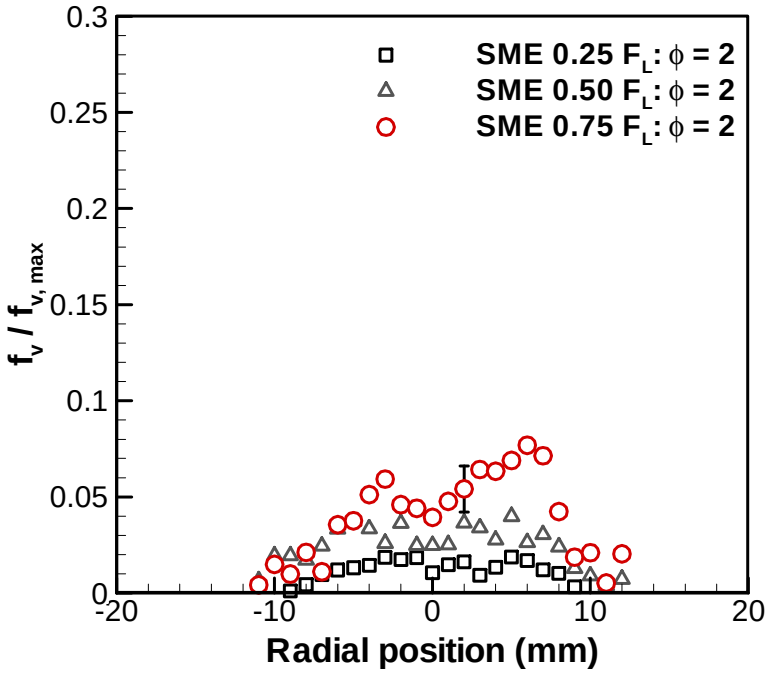

Figure 5.31 SME soot volume fraction profiles at ϕ =2

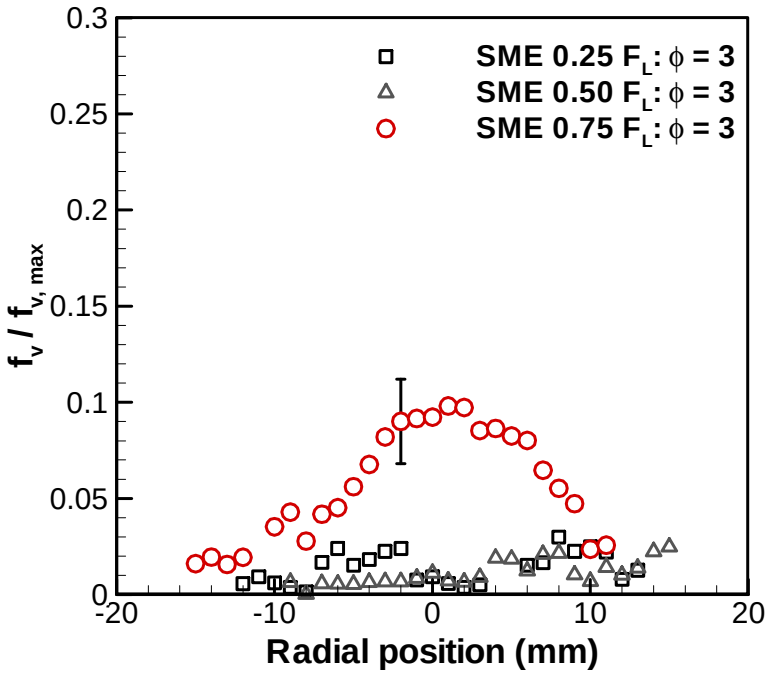

Figure 5.32 SME soot volume fraction profiles at ϕ =3

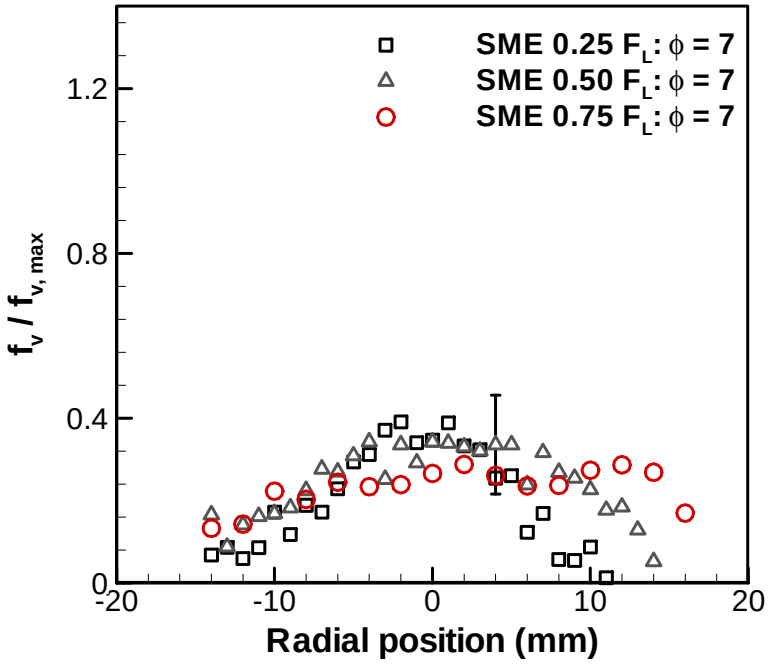

Figure 5.33 SME soot volume fraction profiles at ϕ =7

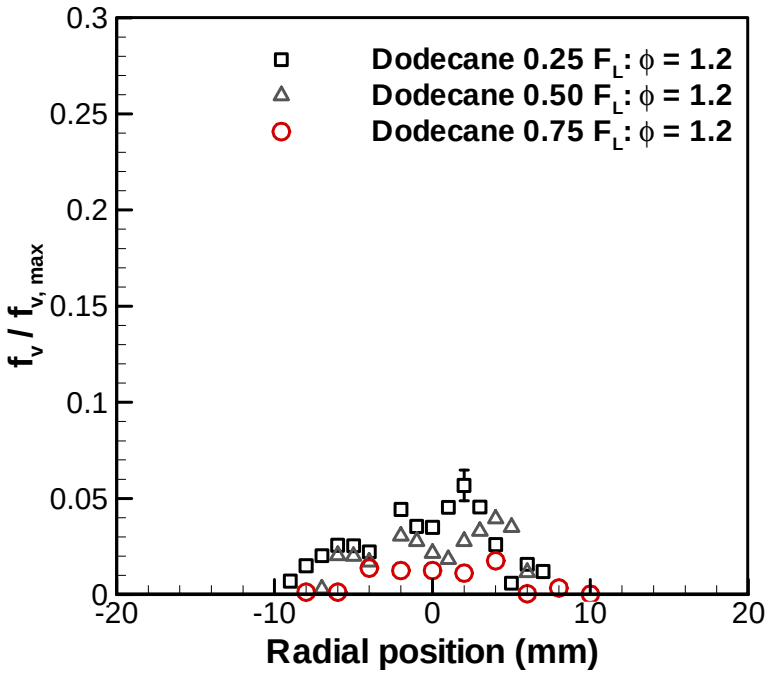

Figure 5.34 Dodecane soot volume fraction profiles at ϕ =1.2

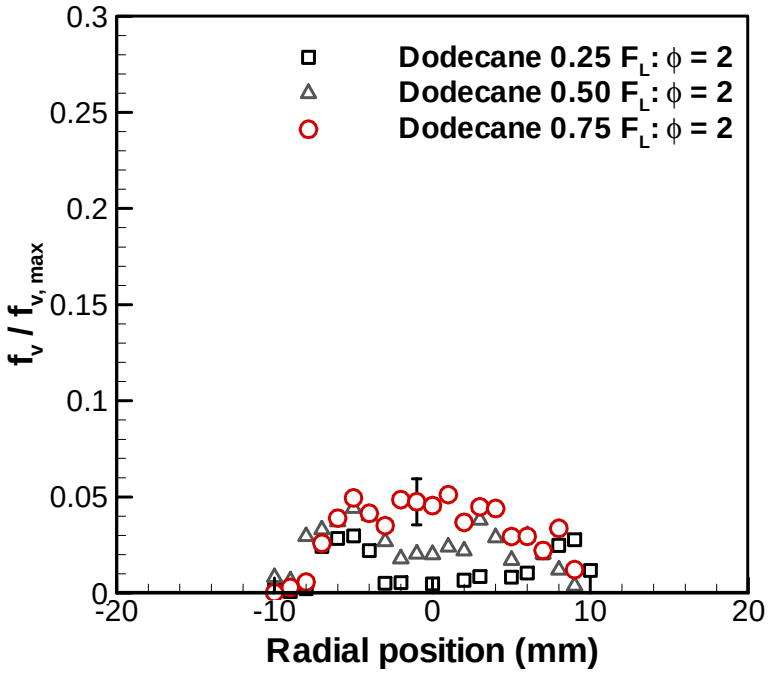

Figure 5.35 Dodecane soot volume fraction profiles at ϕ =2

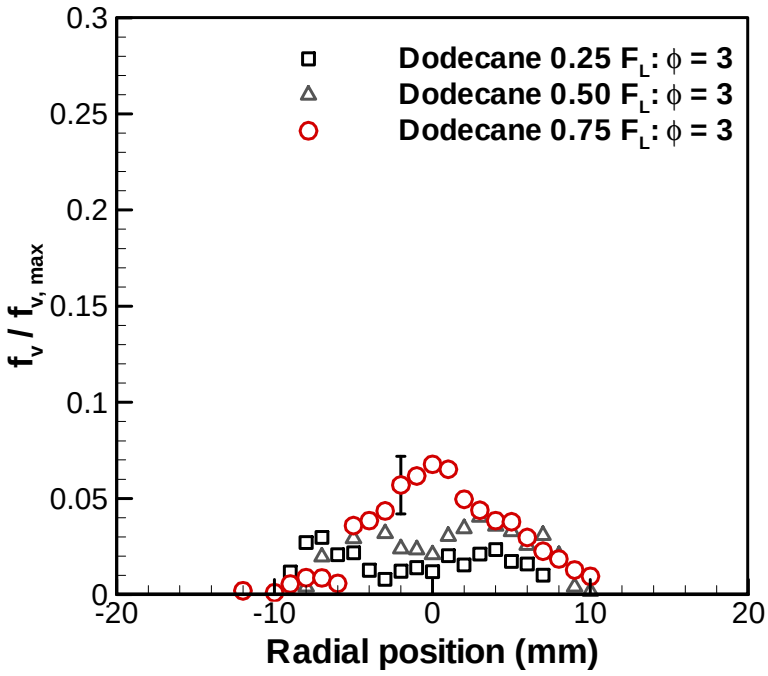

Figure 5.36 Dodecane soot volume fraction profiles at ϕ =3

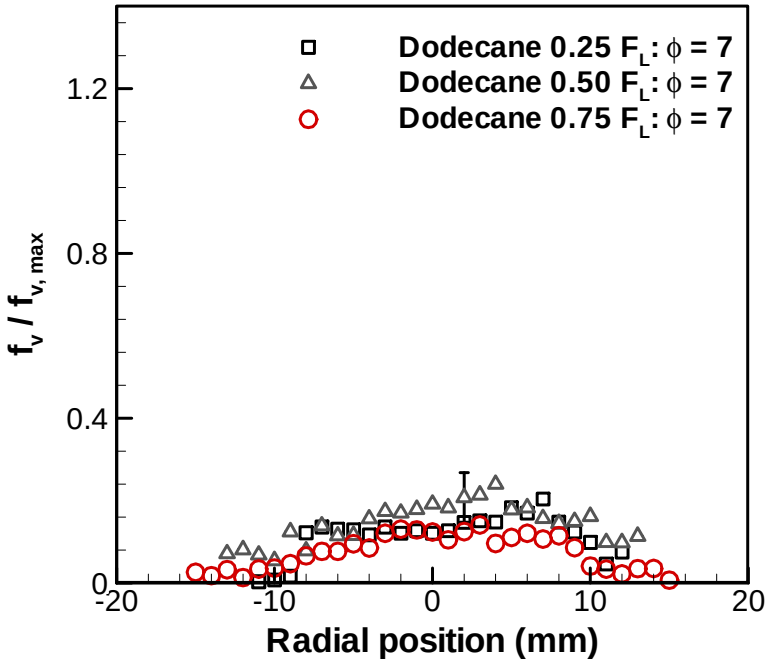

Figure 5.37 Dodecane soot volume fraction profiles at ϕ =7

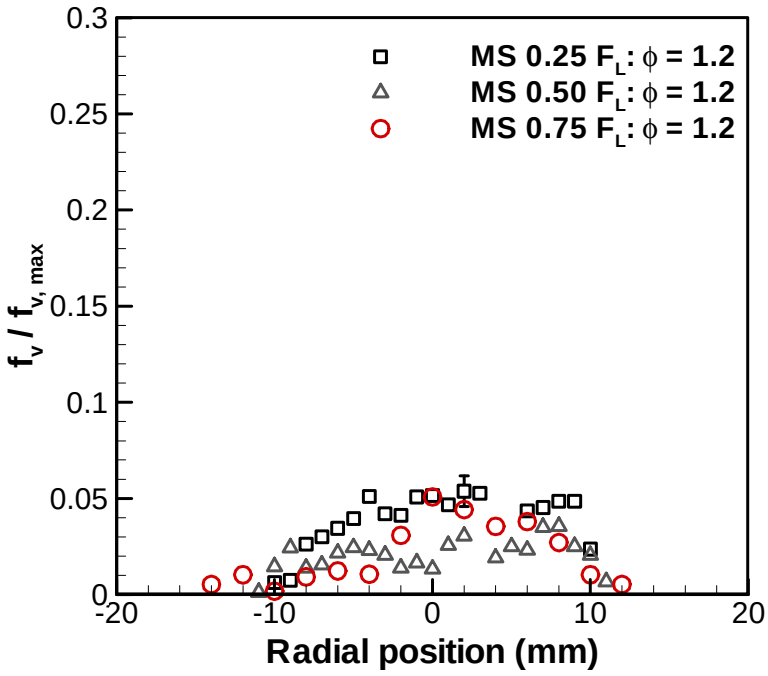

Figure 5.38 Methyl stearate soot volume fraction profiles at ϕ =1.2

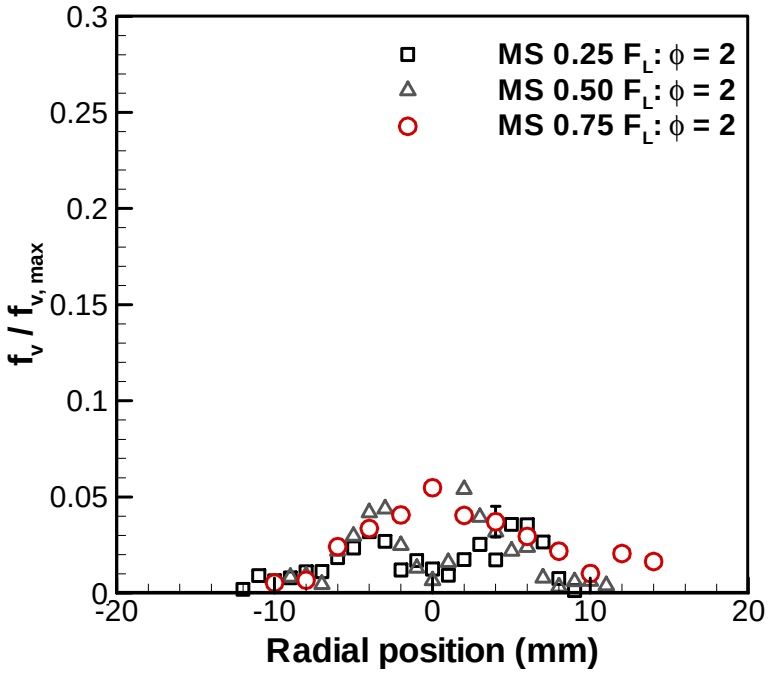

Figure 5.39 Methyl stearate soot volume fraction profiles at ϕ =2

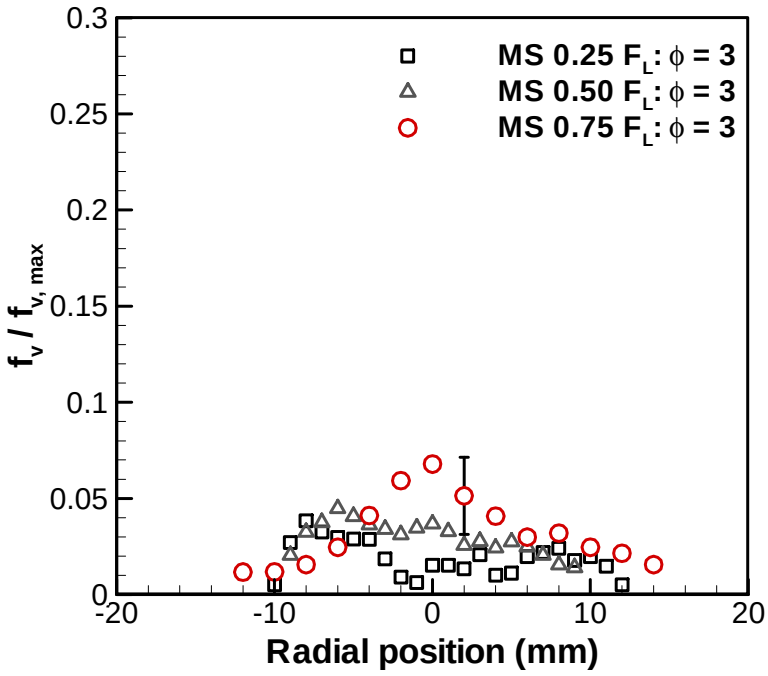

Figure 5.40 Methyl stearate soot volume fraction profiles at ϕ =3

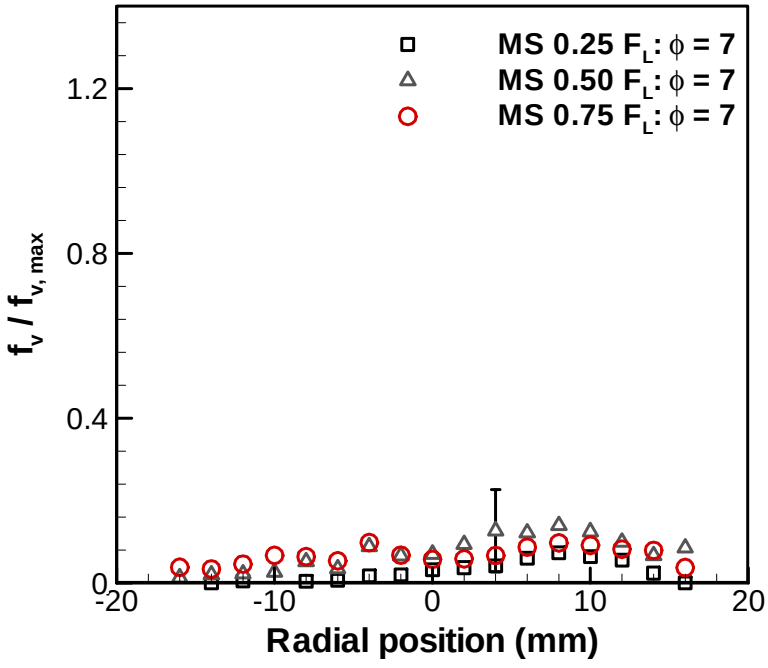

Figure 5.41 Methyl stearate soot volume fraction profiles at ϕ =7

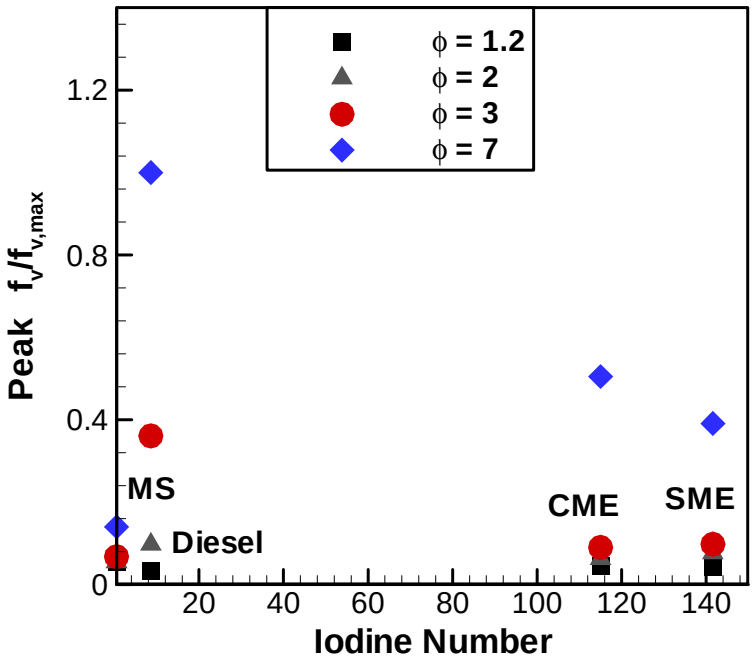

Figure 5.42 Peak $f_v/f_{v,max}$ at ϕ =1.2, 2, 3, and 7 plotted against Iodine Number

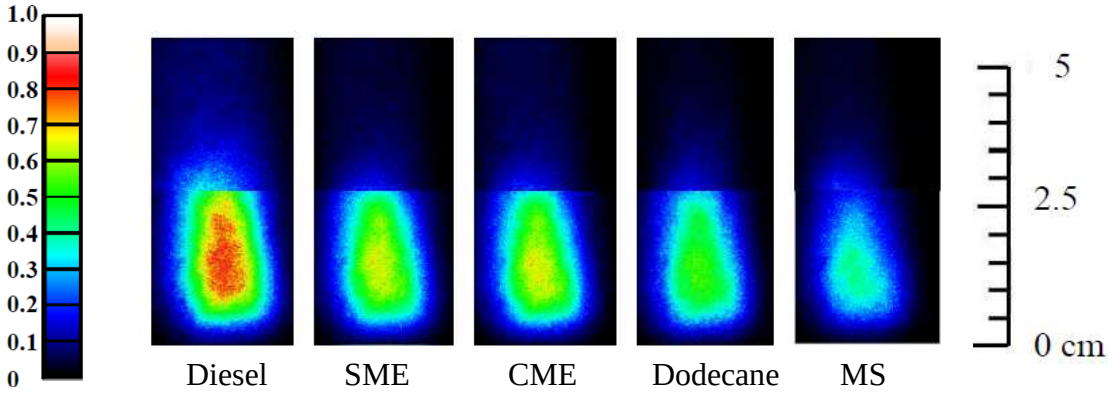

Figure 5.43 OH PLIF images of all fuels at ϕ =1.2

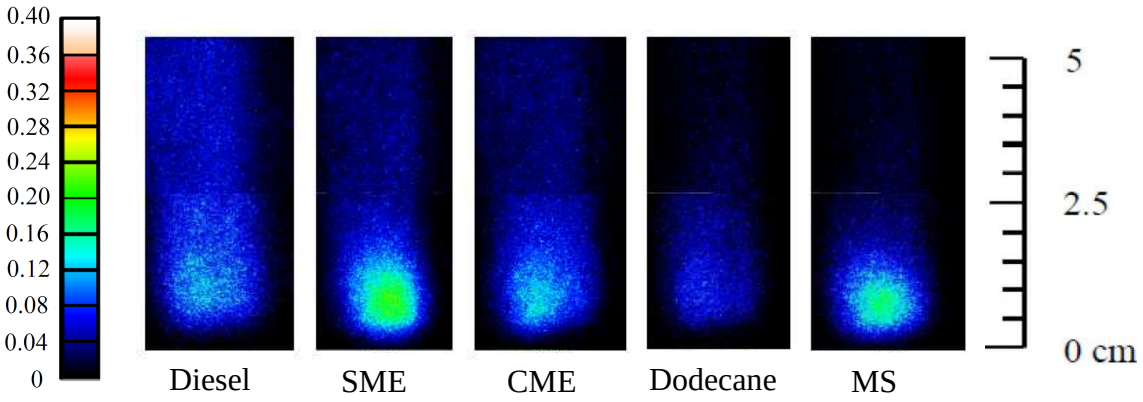

Figure 5.44 OH PLIF images of all fuels at ϕ =2

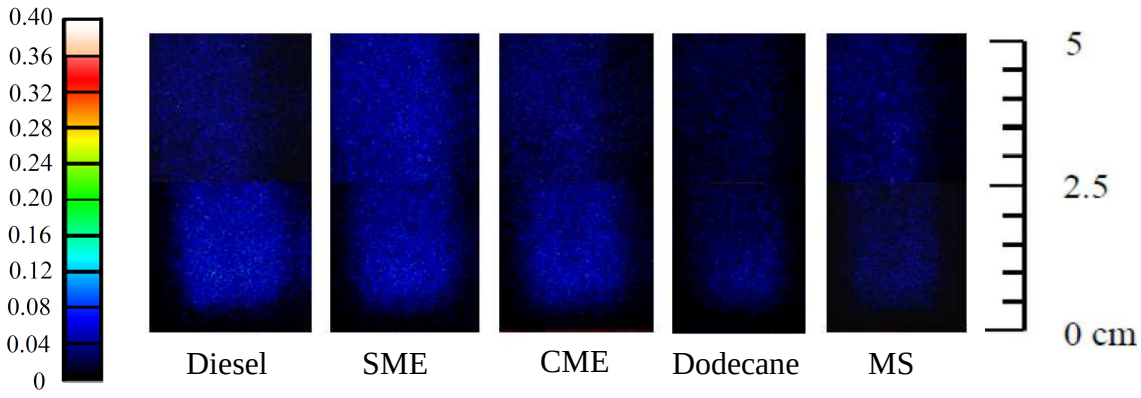

Figure 5.45 OH PLIF images of all fuels at ϕ =3

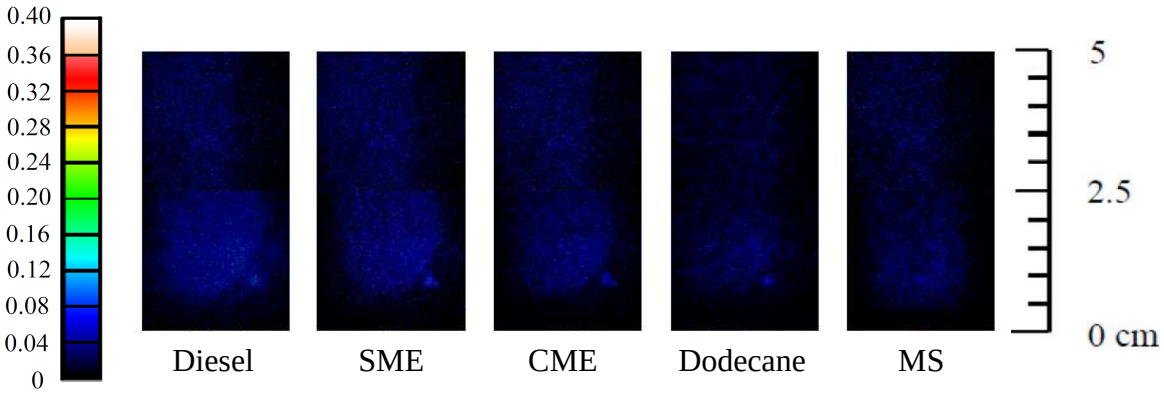

Figure 5.46 OH PLIF images of all fuels at ϕ =7

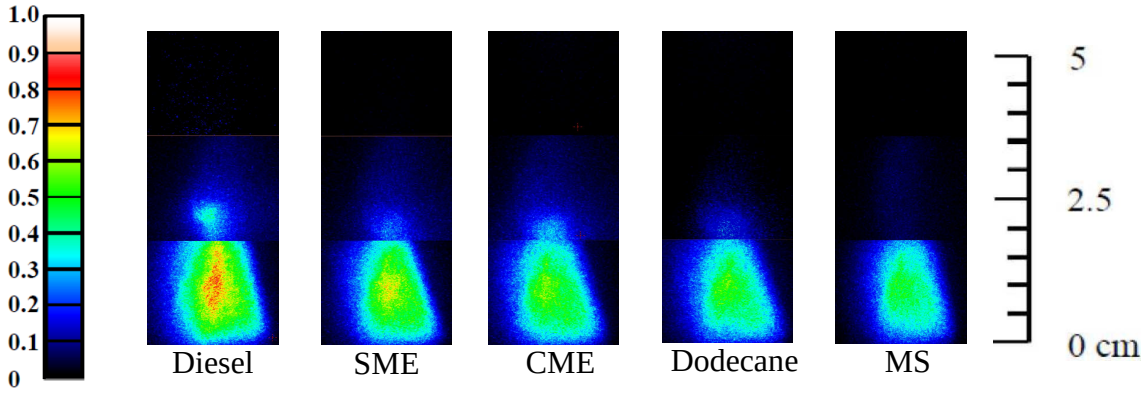

Figure 5.47 CH PLIF images of all fuels at ϕ =1.2

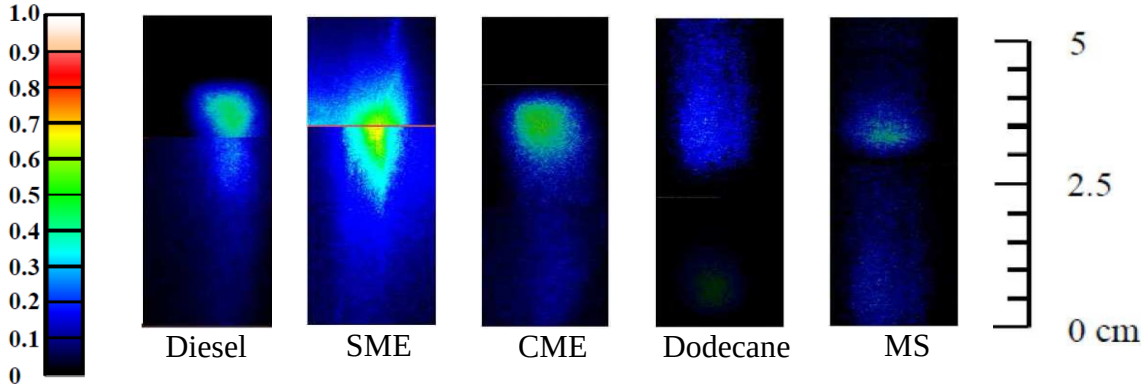

Figure 5.48 CH PLIF images of all fuels at ϕ =2

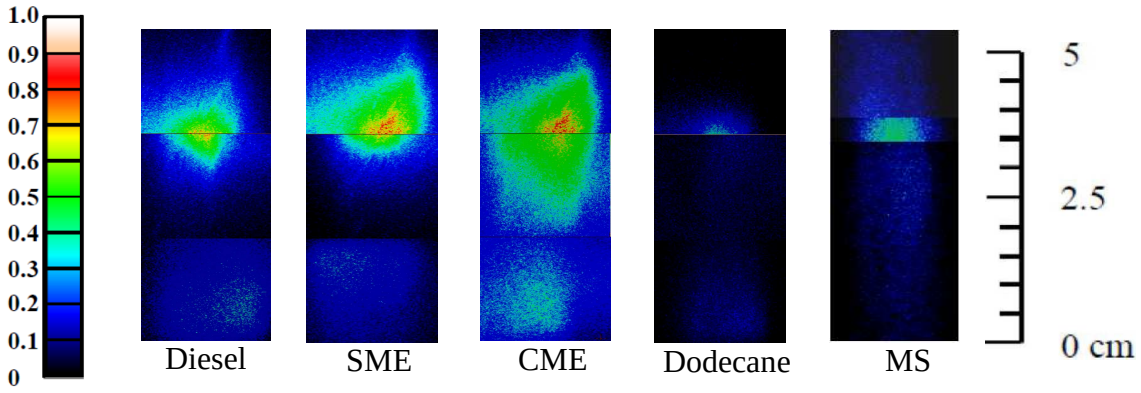

Figure 5.49 CH PLIF images of all fuels at ϕ =3

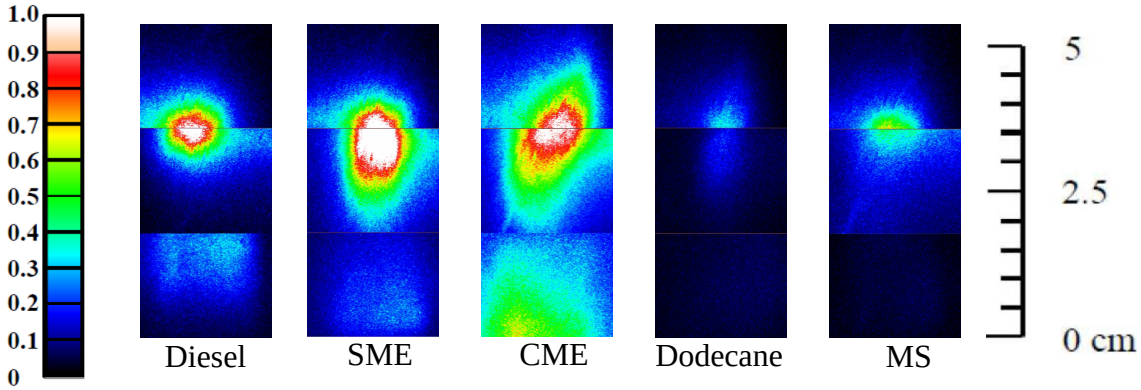

Figure 5.50 CH PLIF images of all fuels at ϕ =7

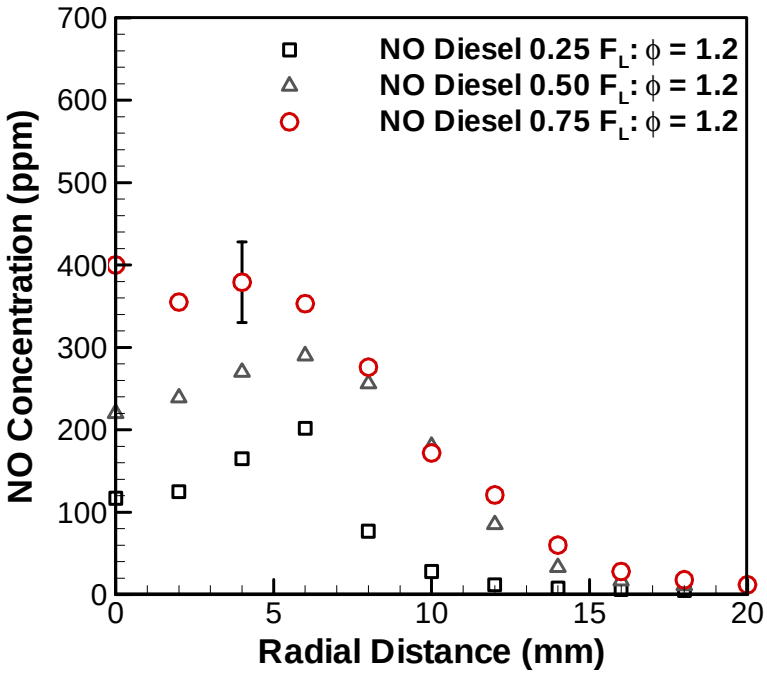

Figure 5.51 Diesel NO concentration profiles at ϕ =1.2

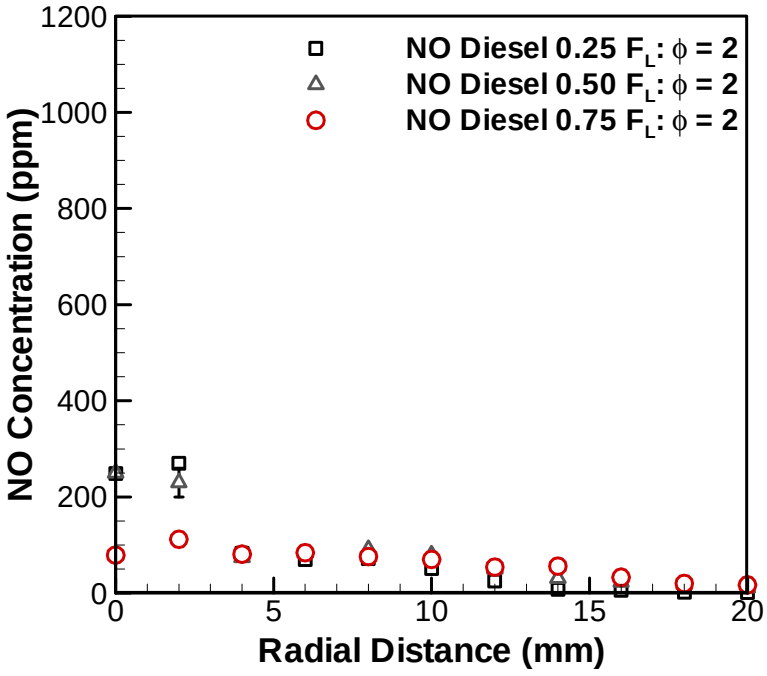

Figure 5.52 Diesel NO concentration profiles at ϕ =2

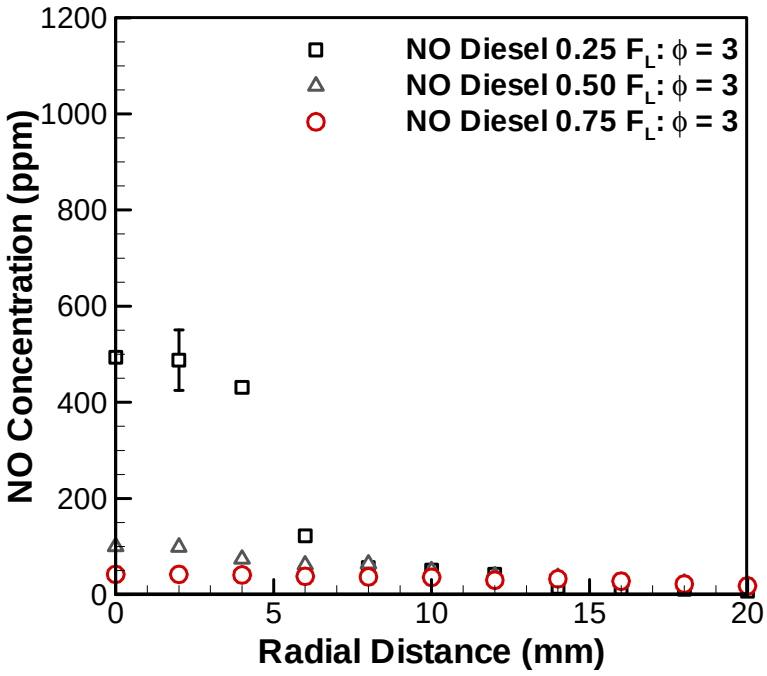

Figure 5.53 Diesel NO concentration profiles at ϕ =3

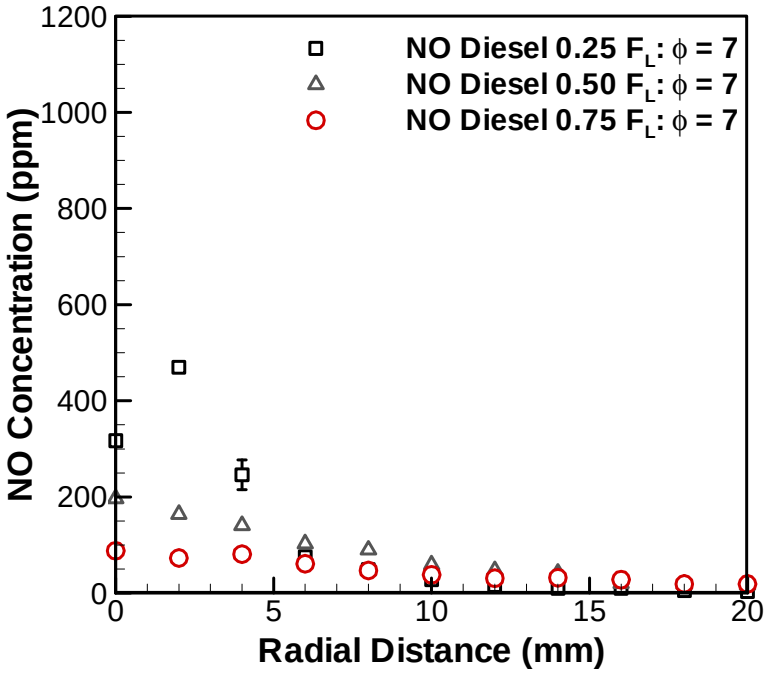

Figure 5.54 Diesel NO concentration profiles at ϕ =7

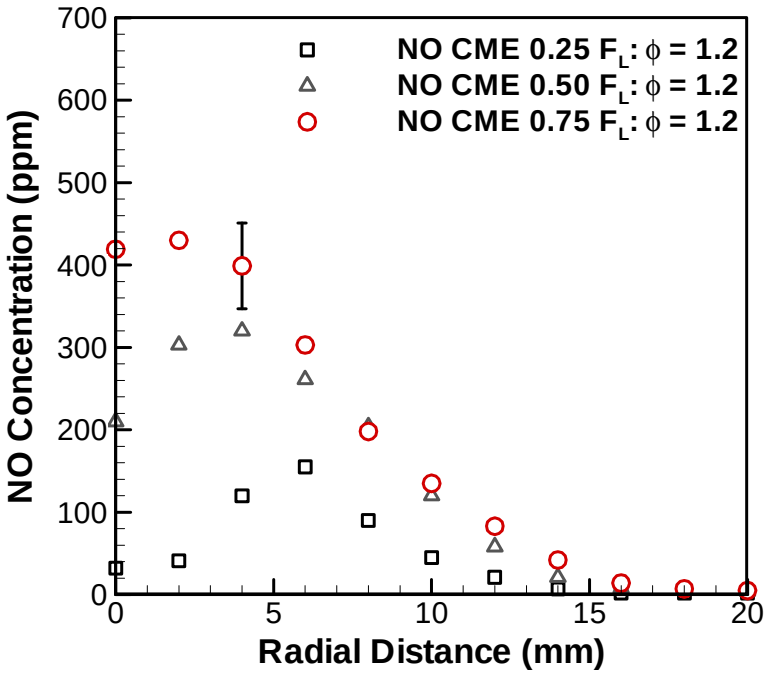

Figure 5.55 CME NO concentration profiles at ϕ =1.2

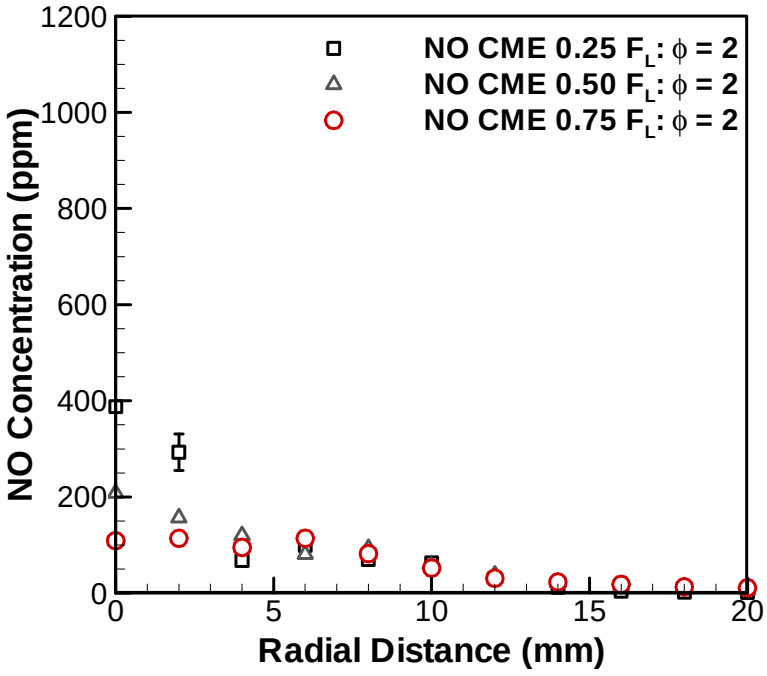

Figure 5.56 CME NO concentration profiles at ϕ =2

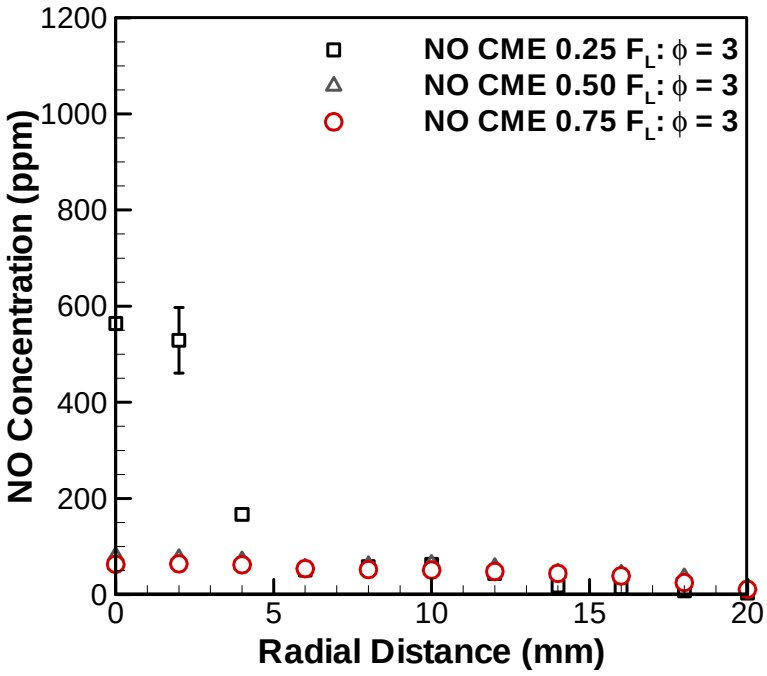

Figure 5.57 CME NO concentration profiles at ϕ =3

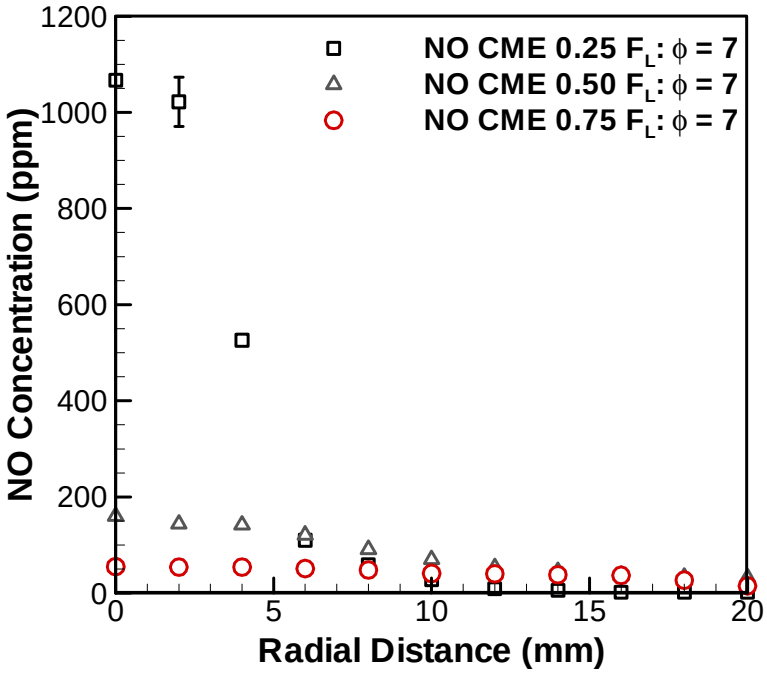

Figure 5.58 CME NO concentration profiles at ϕ =7

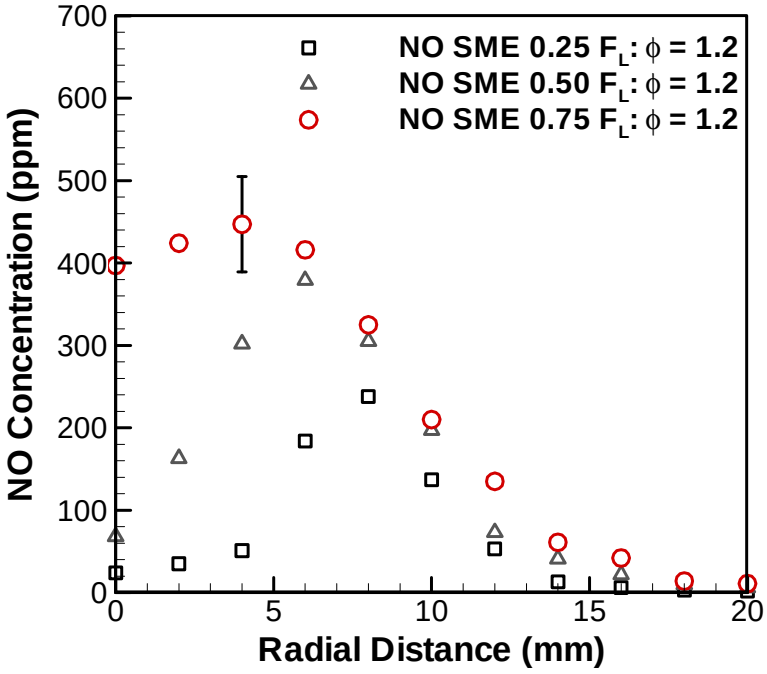

Figure 5.59 SME NO concentration profiles at ϕ =1.2

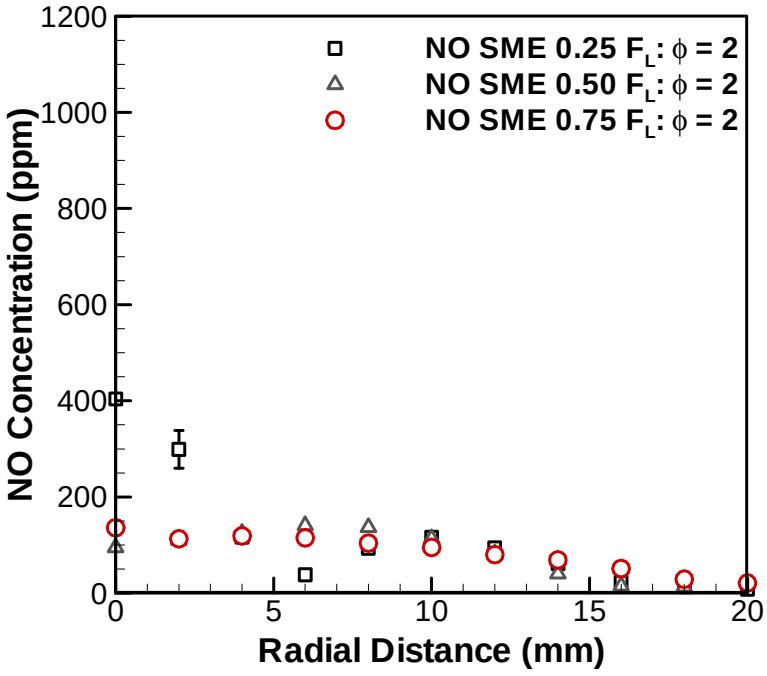

Figure 5.60 SME NO concentration profiles at ϕ =2

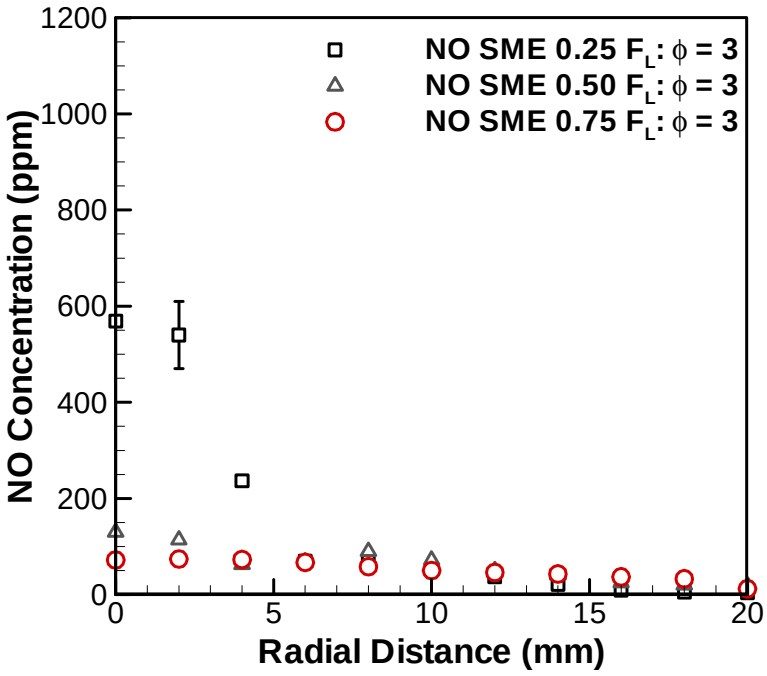

Figure 5.61 SME NO concentration profiles at ϕ =3

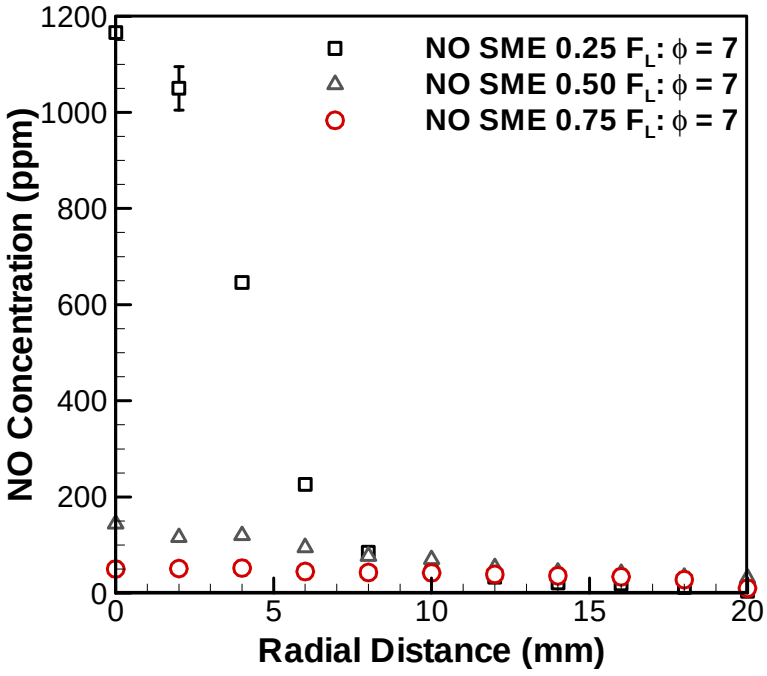

Figure 5.62 SME NO concentration profiles at ϕ =7

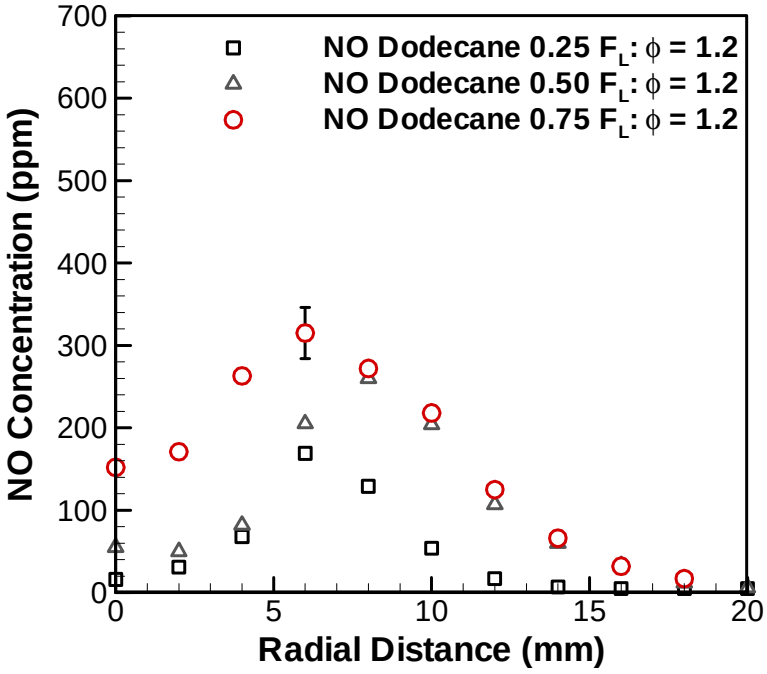

Figure 5.63 Dodecane NO concentration profiles at ϕ =1.2

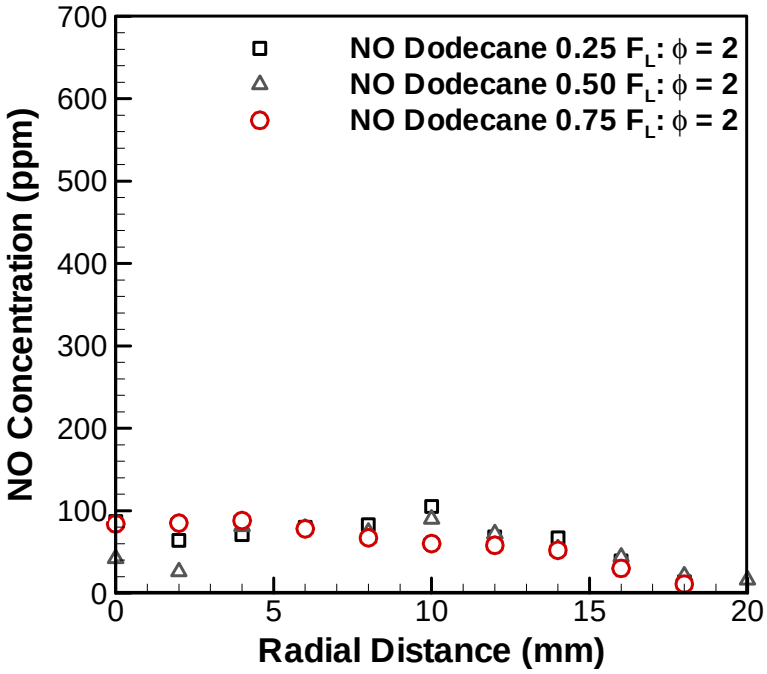

Figure 5.64 Dodecane NO concentration profiles at ϕ =2

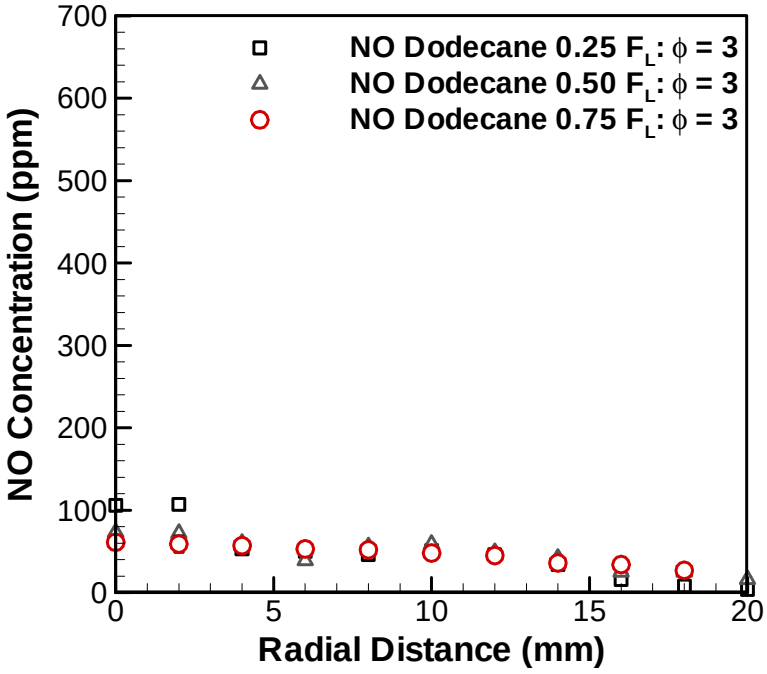

Figure 5.65 Dodecane NO concentration profiles at ϕ =3

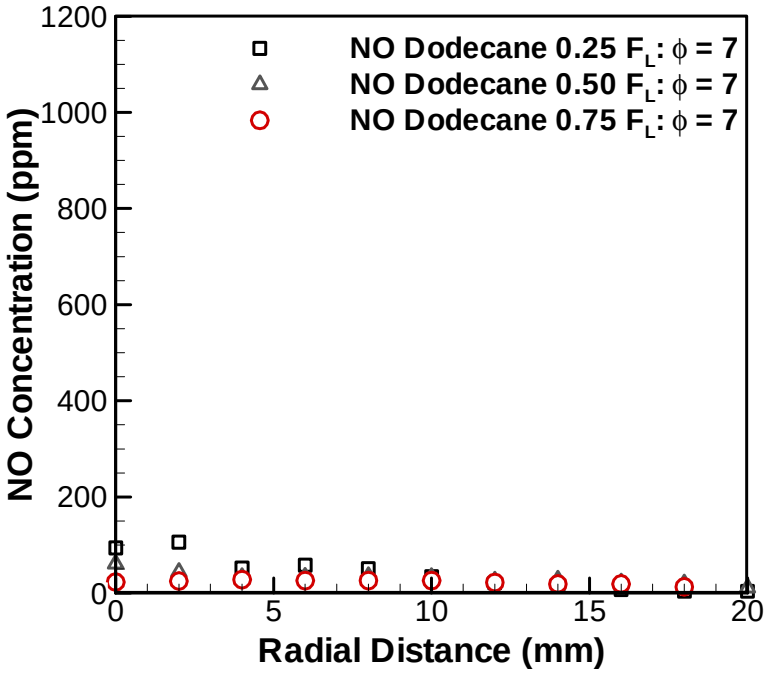

Figure 5.66 Dodecane NO concentration profiles at ϕ =7

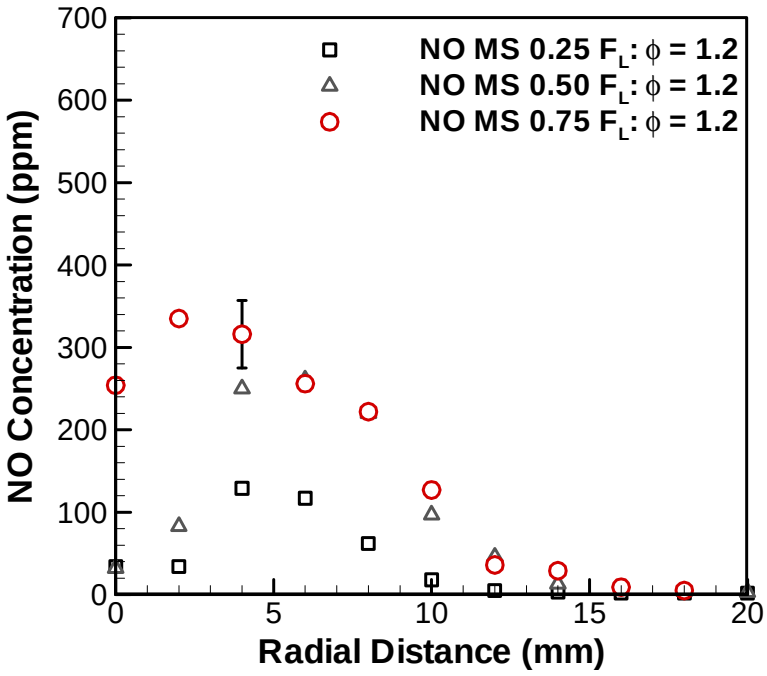

Figure 5.67 Methyl stearate NO concentration profiles at ϕ =1.2

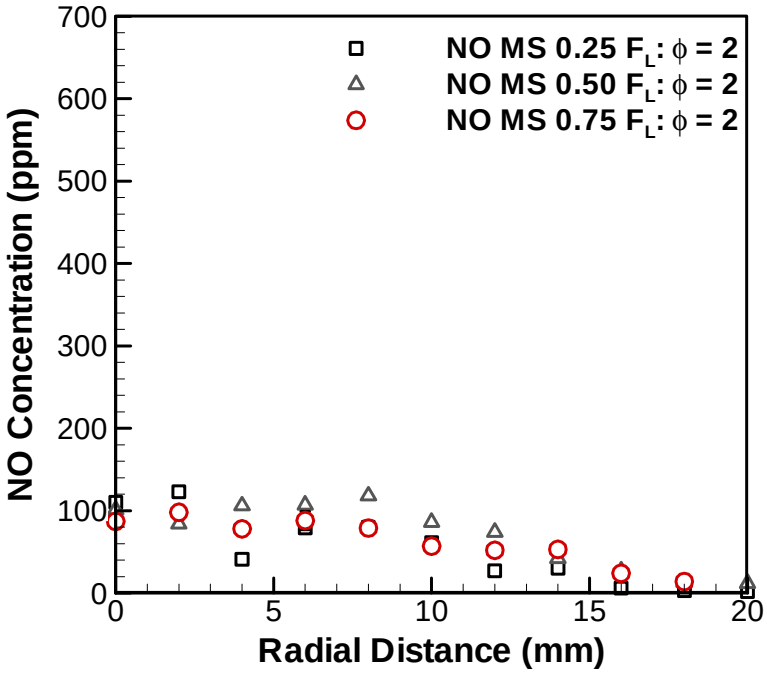

Figure 5.68 Methyl stearate NO concentration profiles at ϕ =2

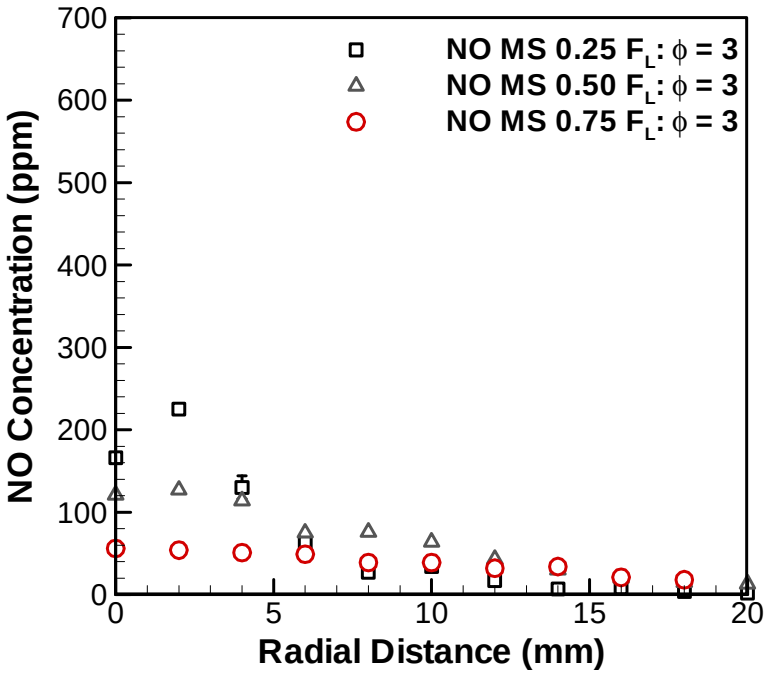

Figure 5.69 Methyl stearate NO concentration profiles at ϕ =3

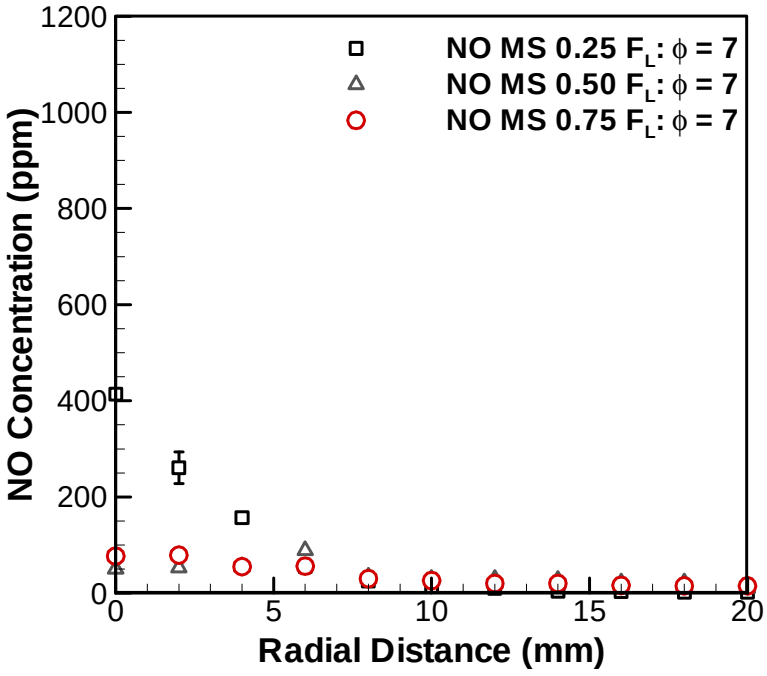

Figure 5.70 Methyl stearate NO concentration profiles at ϕ =7

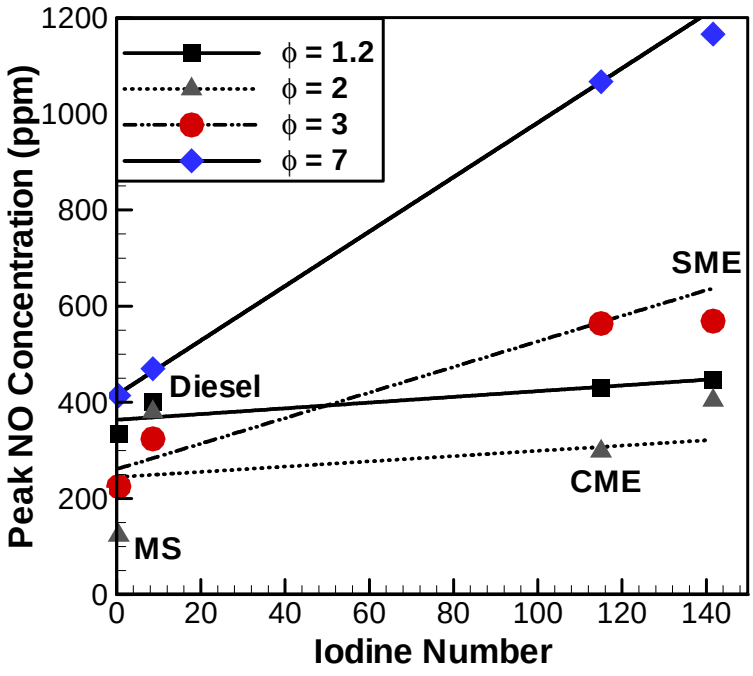

Figure 5.71 Peak NO concentrations versus Iodine Number at all conditions

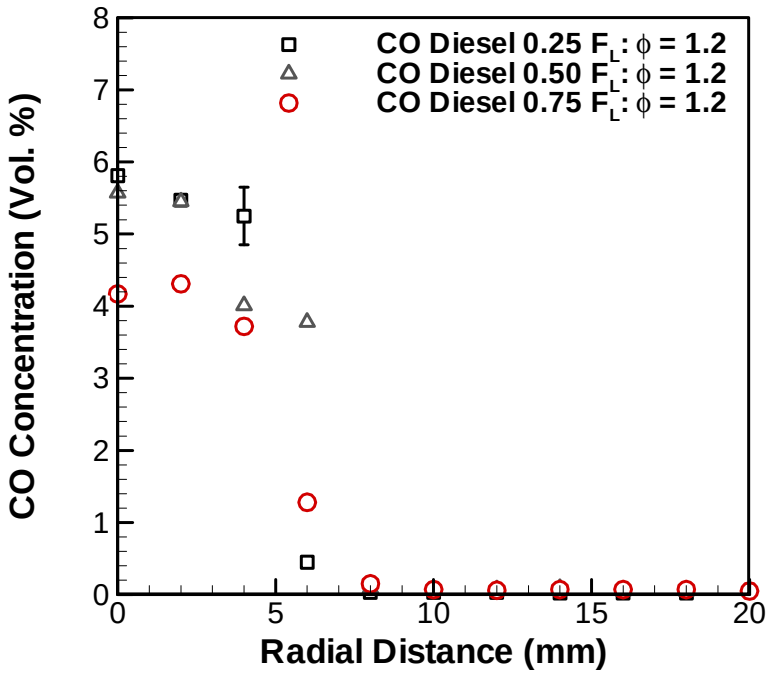

Figure 5.72 Diesel CO concentrations at ϕ =1.2 for three axial locations

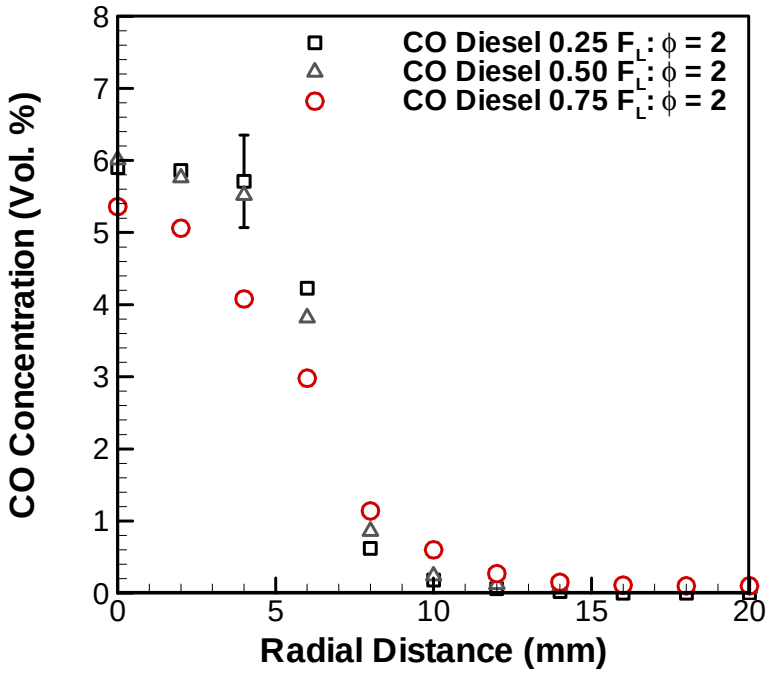

Figure 5.73 Diesel CO concentrations at ϕ =2 for three axial locations

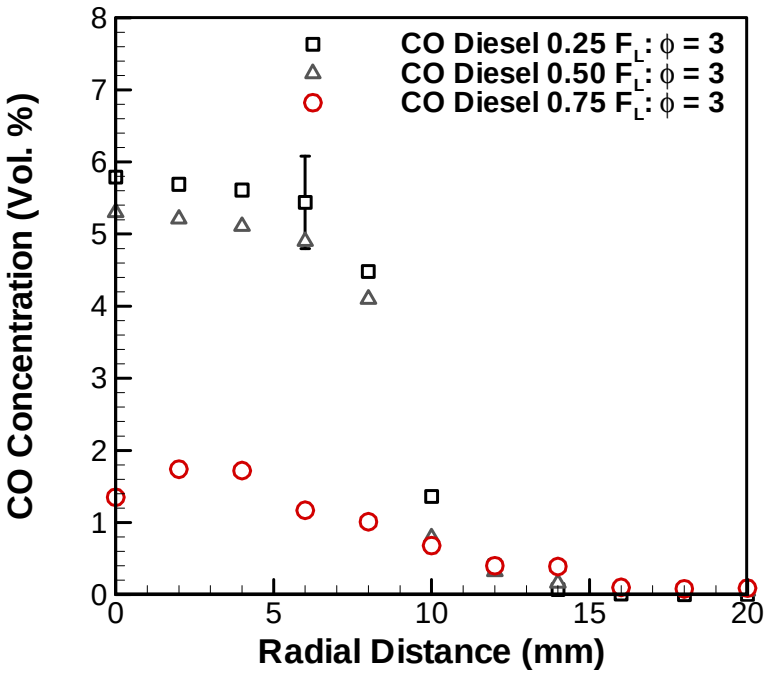

Figure 5.74 Diesel CO concentrations at ϕ =3 for three axial locations

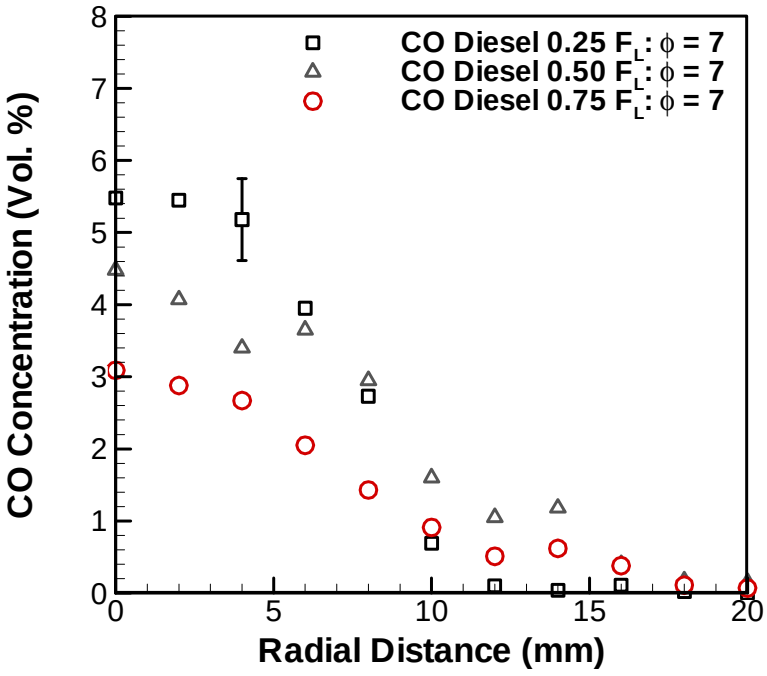

Figure 5.75 Diesel CO concentrations at ϕ =7 for three axial locations

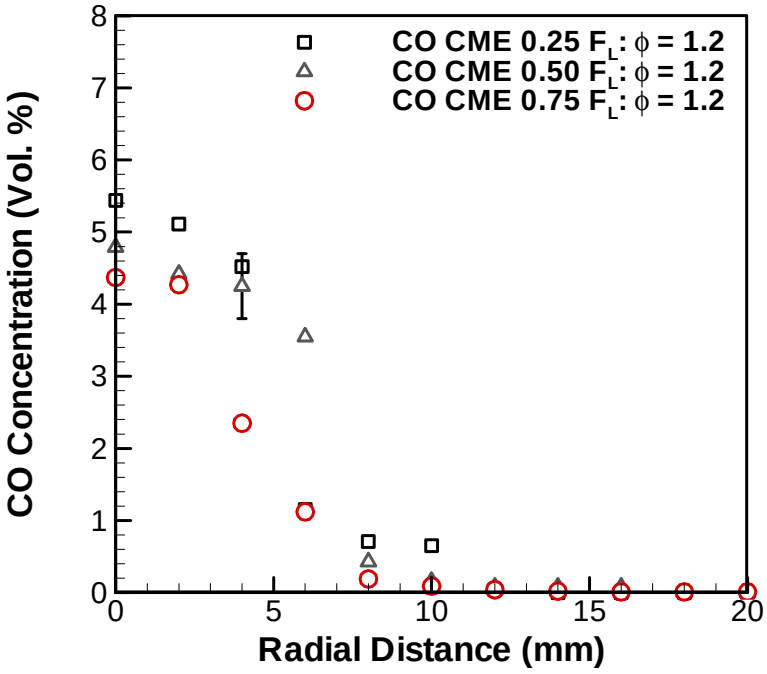

Figure 5.76 CME CO concentrations at ϕ =1.2 for three axial locations

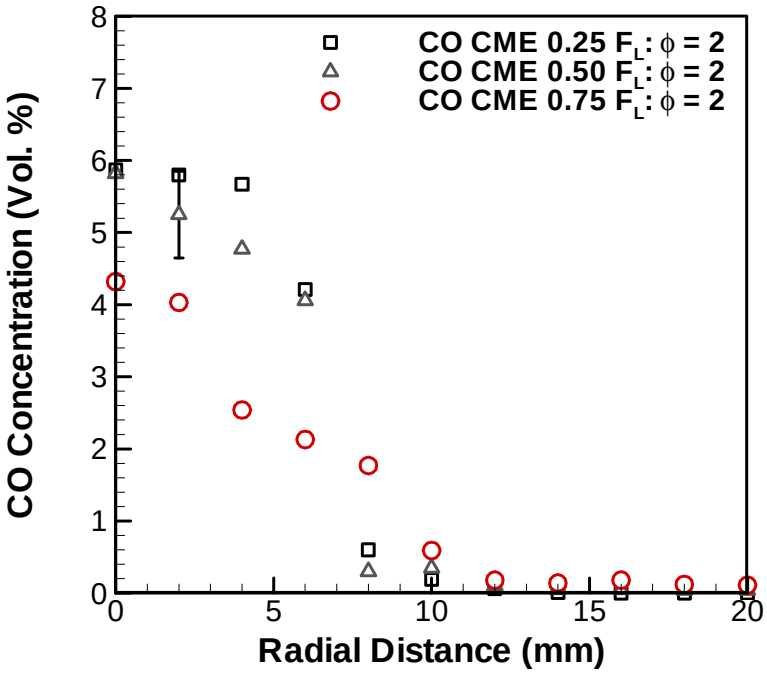

Figure 5.77 CME CO concentrations at ϕ =2 for three axial locations

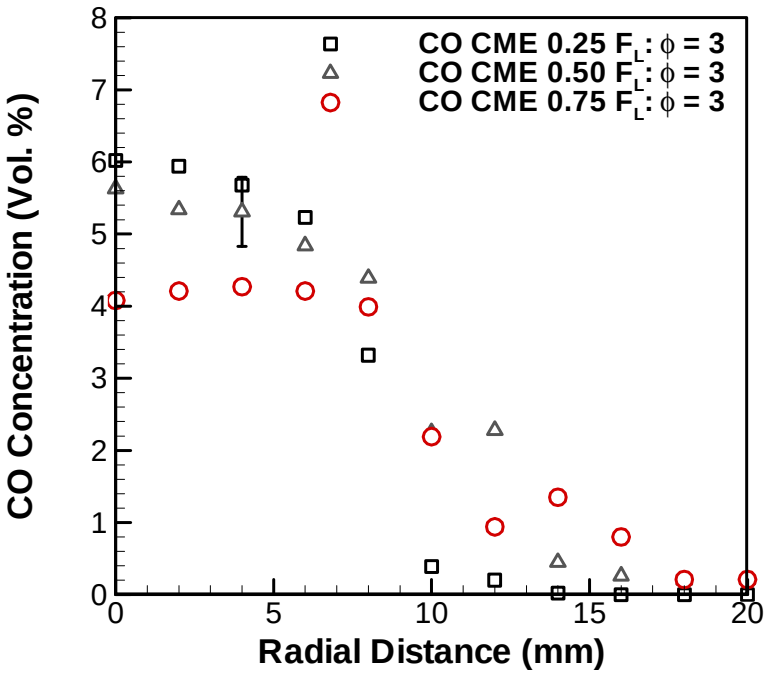

Figure 5.78 CME CO concentrations at ϕ =3 for three axial locations

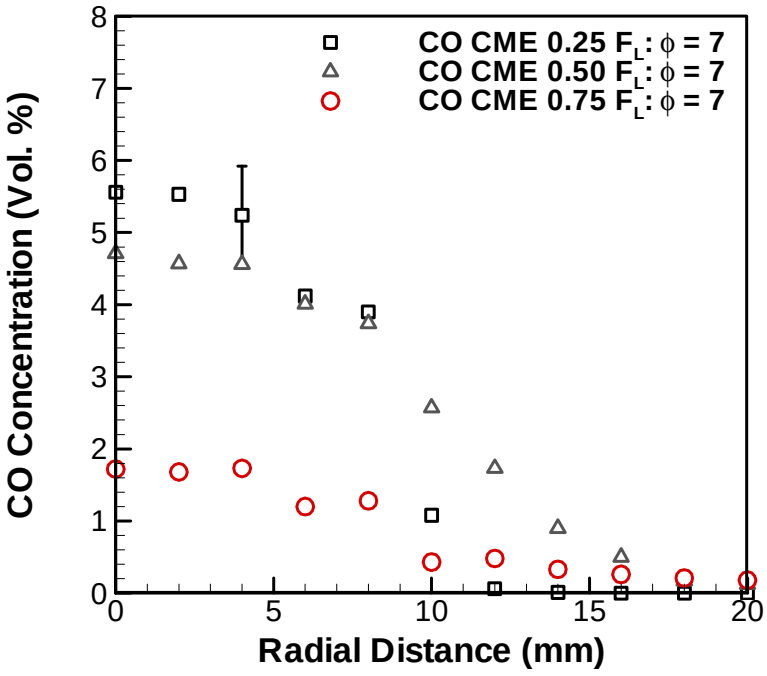

Figure 5.79 CME CO concentrations at ϕ =7 for three axial locations

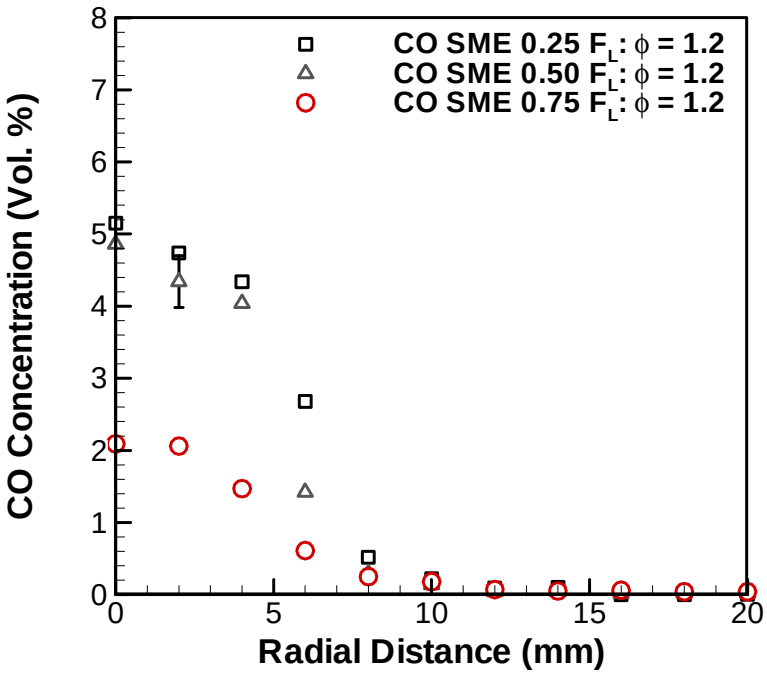

Figure 5.80 SME CO concentrations at ϕ =1.2 for three axial locations

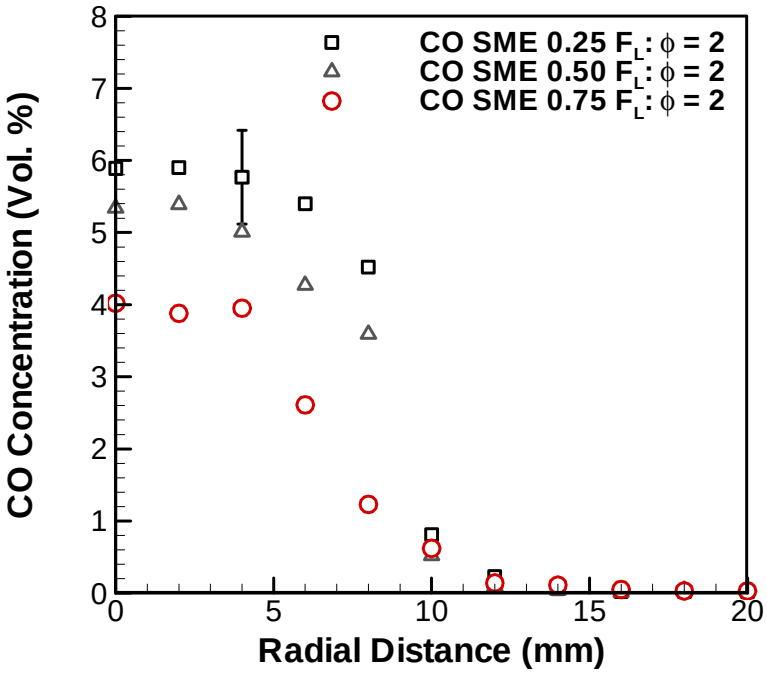

Figure 5.81 SME CO concentrations at ϕ =2 for three axial locations

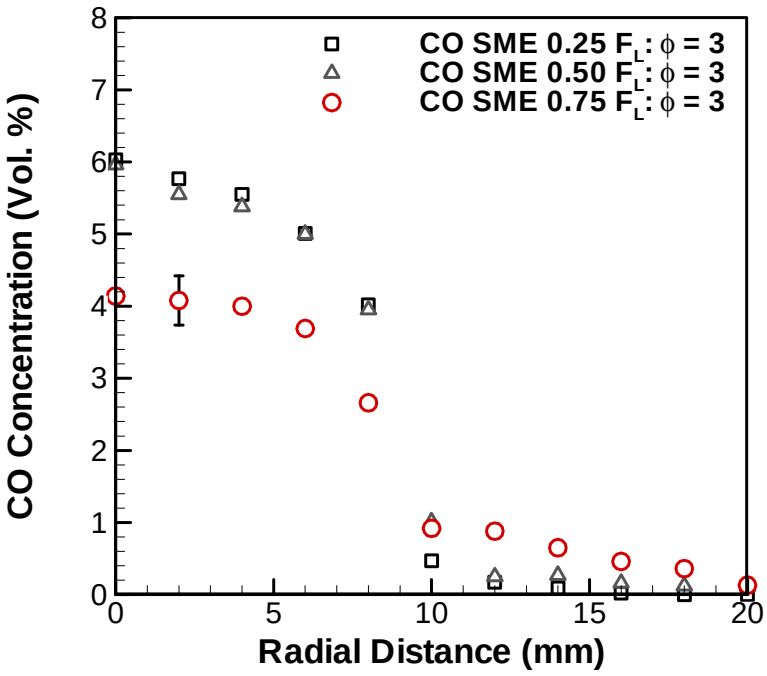

Figure 5.82 SME CO concentrations at ϕ =3 for three axial locations

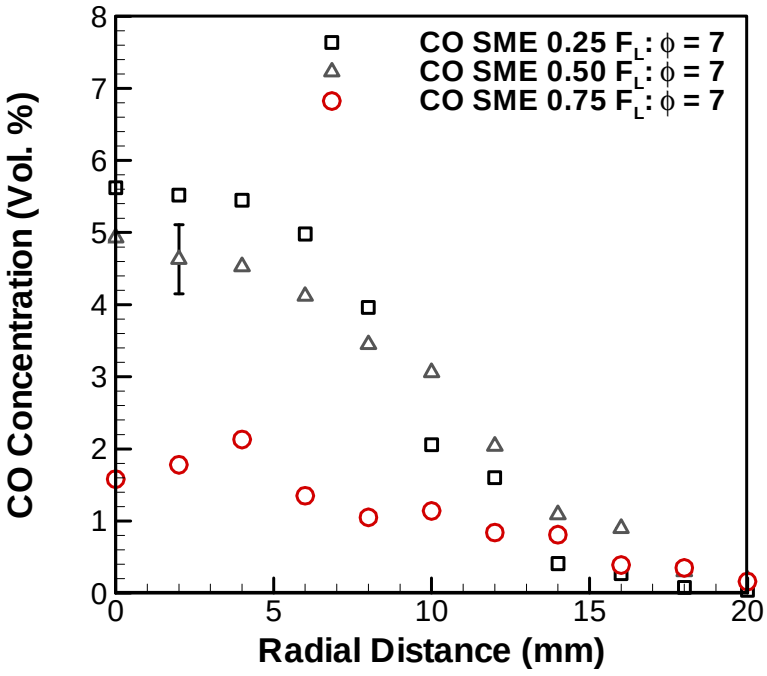

Figure 5.83 SME CO concentrations at ϕ =7 for three axial locations

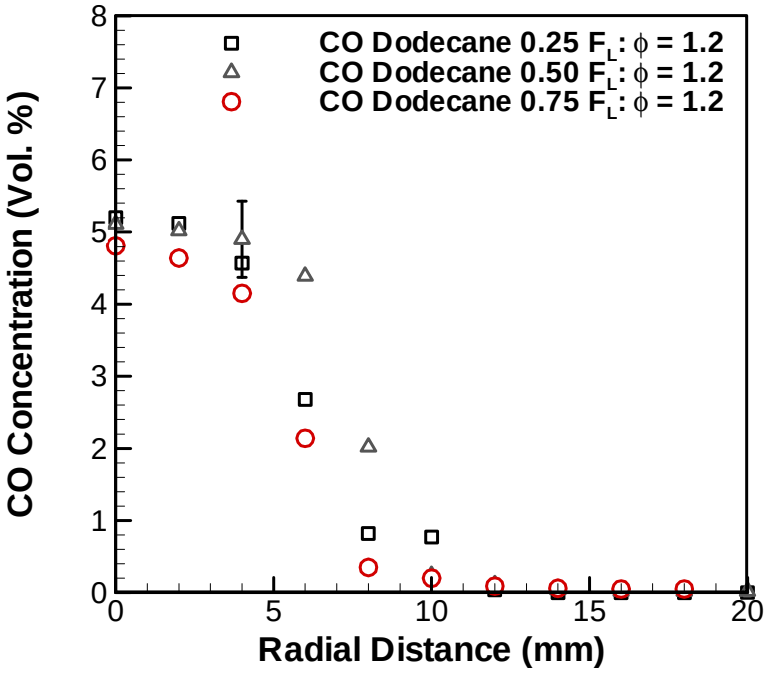

Figure 5.84 Dodecane CO concentrations at ϕ =1.2 for three axial locations

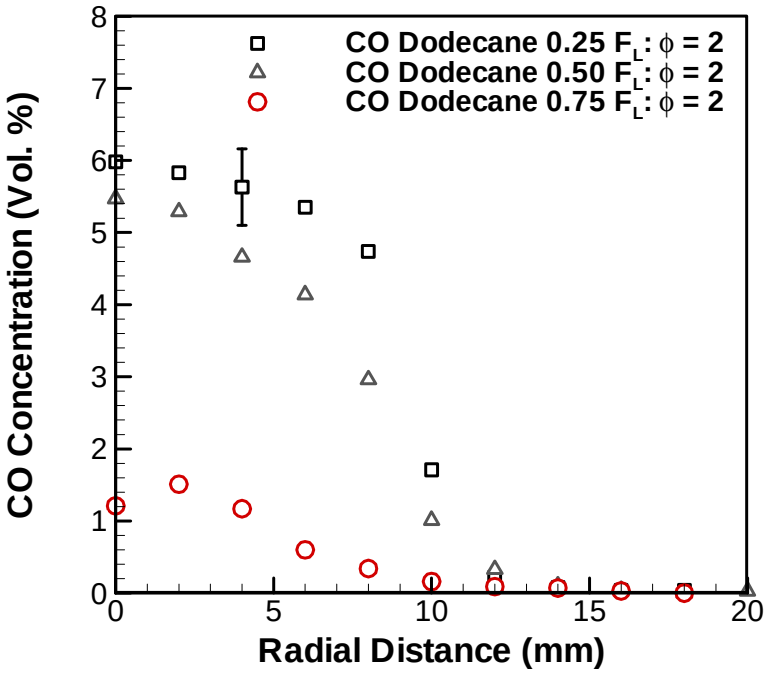

Figure 5.85 Dodecane CO concentrations at ϕ =2 for three axial locations

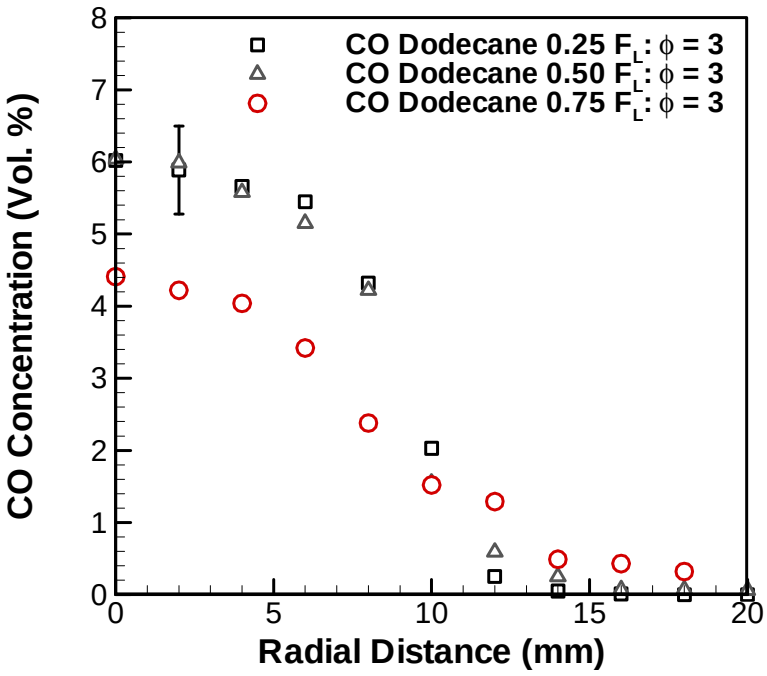

Figure 5.86 Dodecane CO concentrations at ϕ =3 for three axial locations

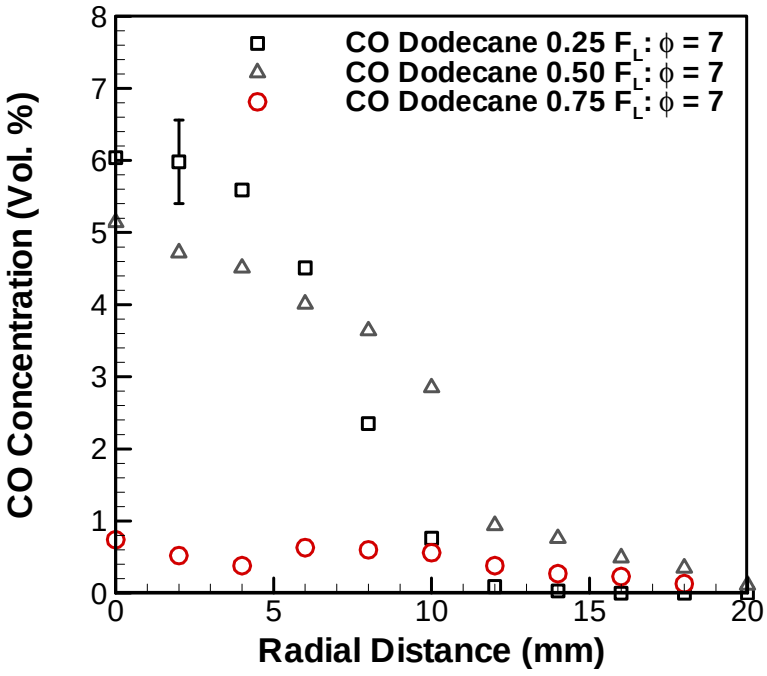

Figure 5.87 Dodecane CO concentrations at ϕ =7 for three axial locations

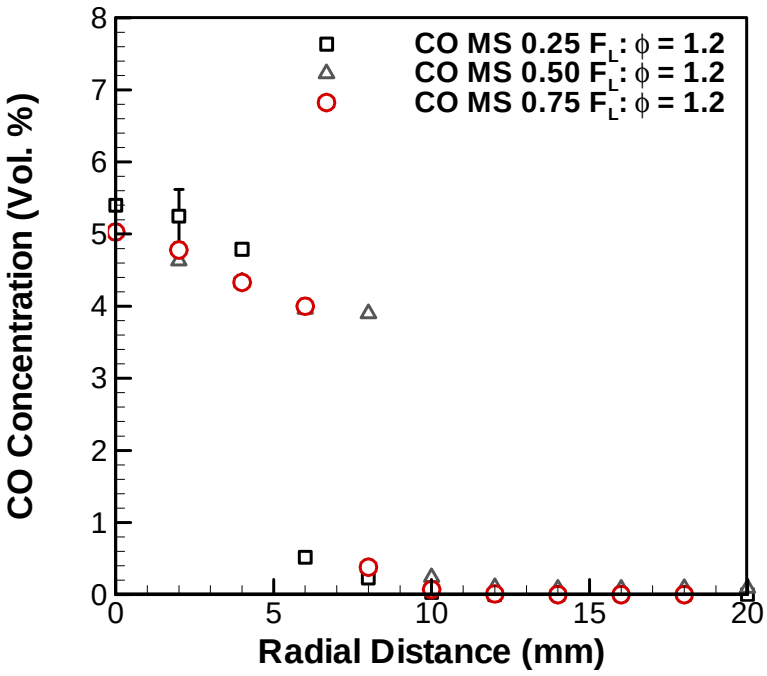

Figure 5.88 Methyl stearate CO concentrations at ϕ =1.2 for three axial locations

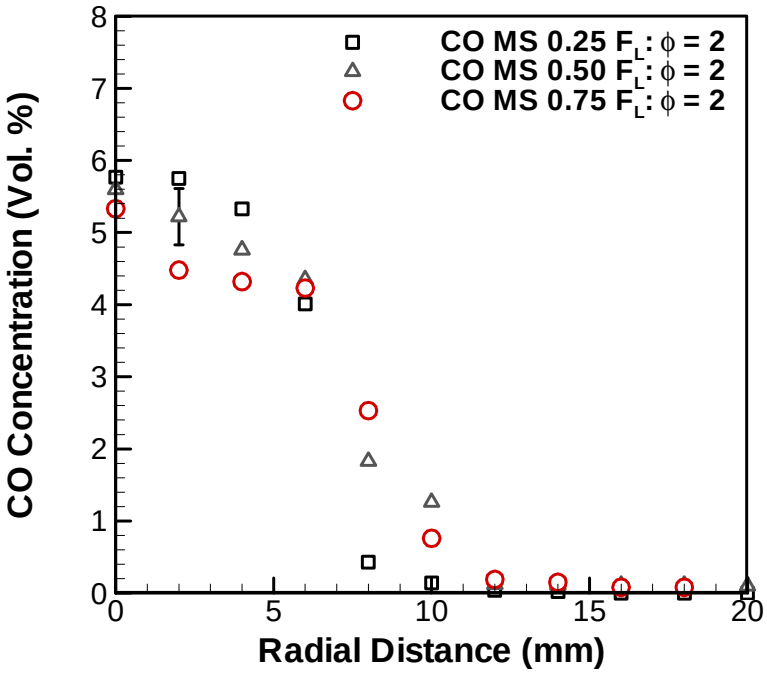

Figure 5.89 Methyl stearate CO concentrations at ϕ =2 for three axial locations

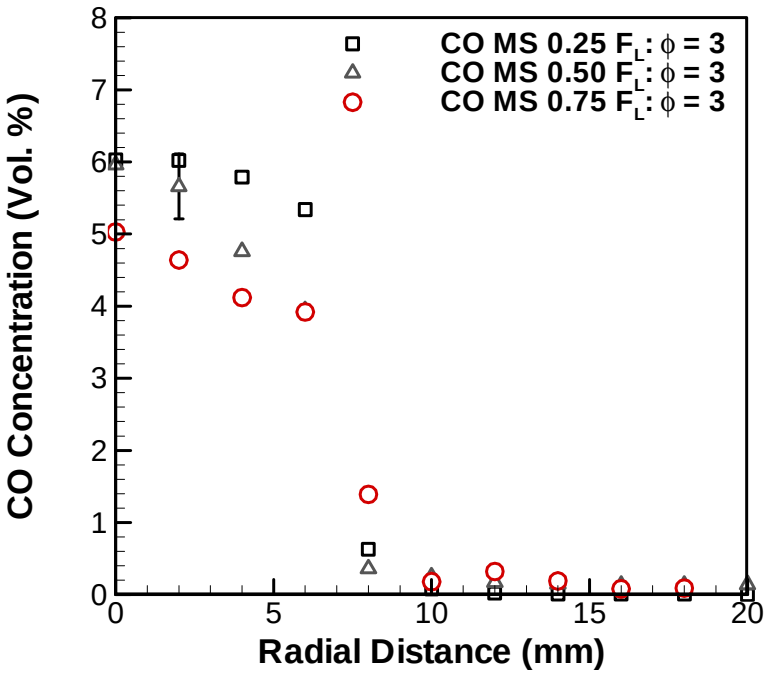

Figure 5.90 Methyl stearate CO concentrations at ϕ =3 for three axial locations

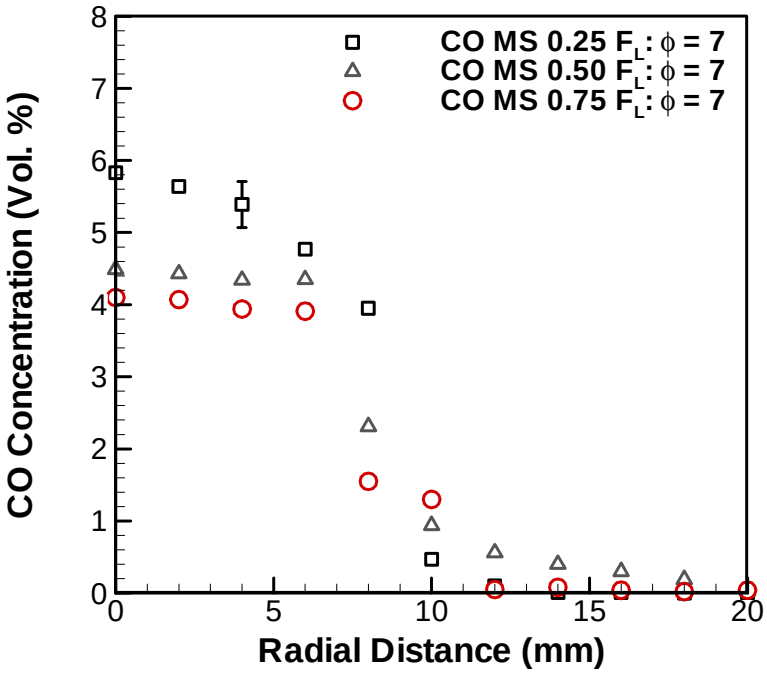

Figure 5.91 Methyl stearate CO concentrations at ϕ =7 for three axial locations

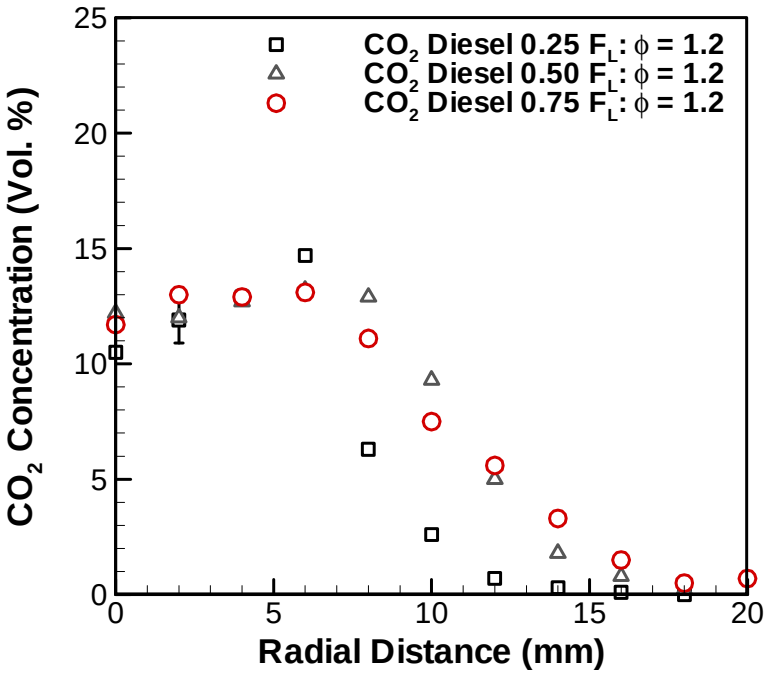

Figure 5.92 Diesel CO_2 concentrations at ϕ =1.2 for three axial locations

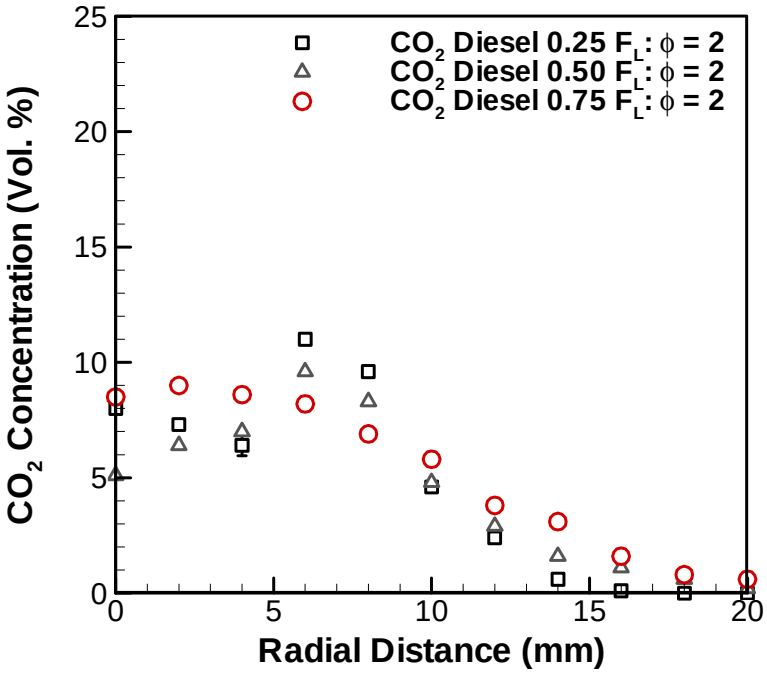

Figure 5.93 Diesel CO_2 concentrations at ϕ =2 for three axial locations

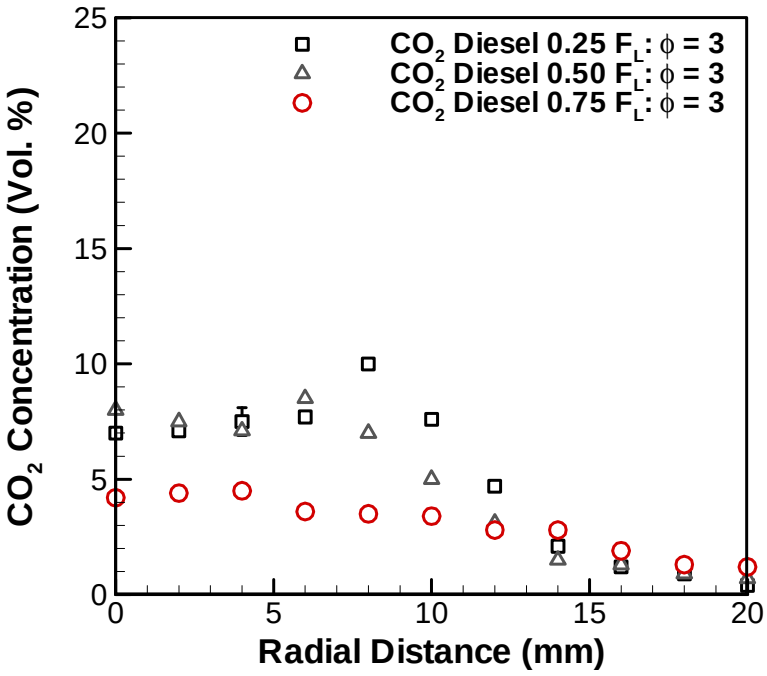

Figure 5.94 Diesel CO_2 concentrations at ϕ =3 for three axial locations

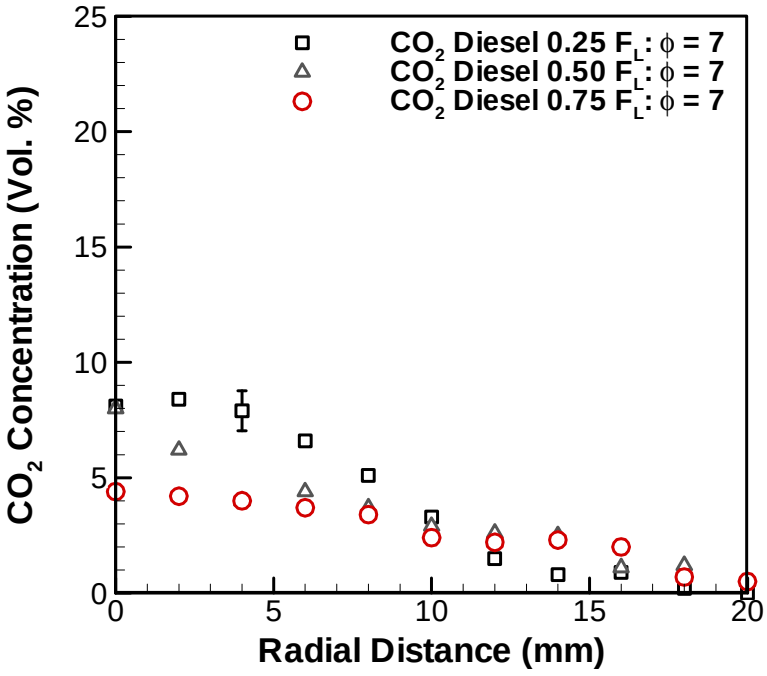

Figure 5.95 Diesel CO_2 concentrations at ϕ =7 for three axial locations

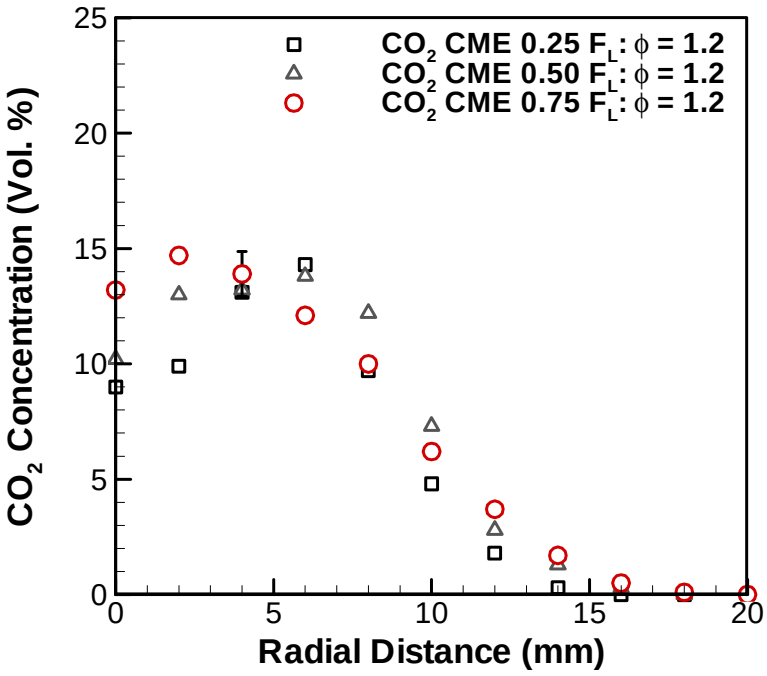

Figure 5.96 CME CO_2 concentrations at ϕ =1.2 for three axial locations

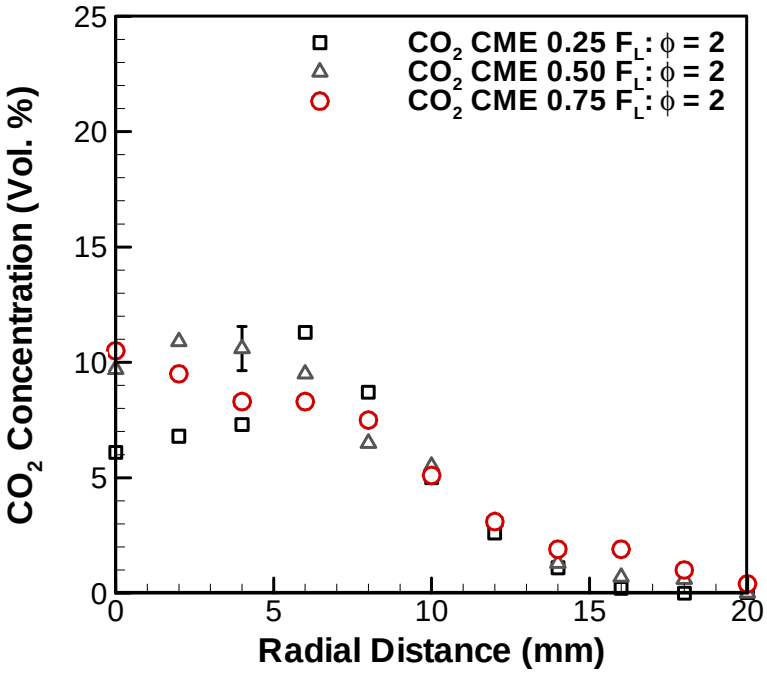

Figure 5.97 CME CO_2 concentrations at ϕ =2 for three axial locations

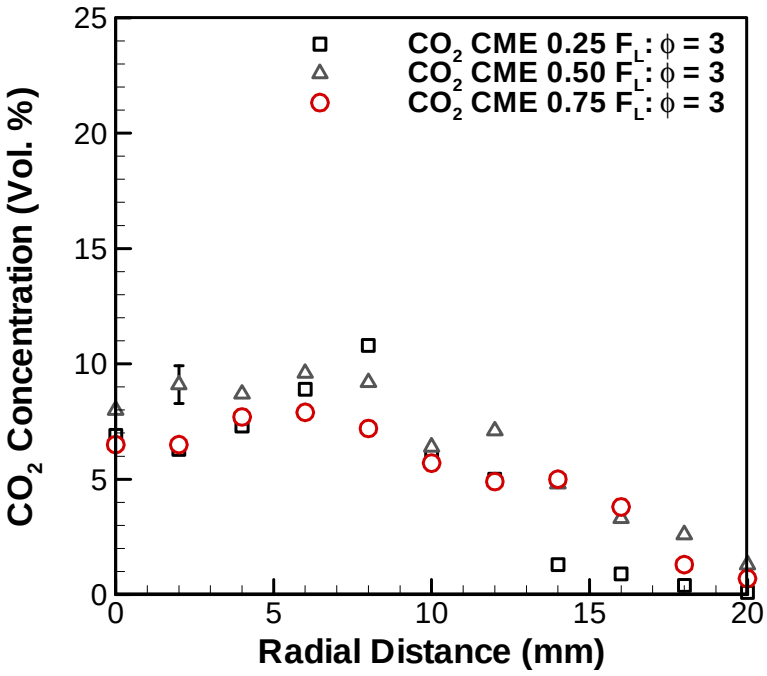

Figure 5.98 CME CO_2 concentrations at ϕ =3 for three axial locations

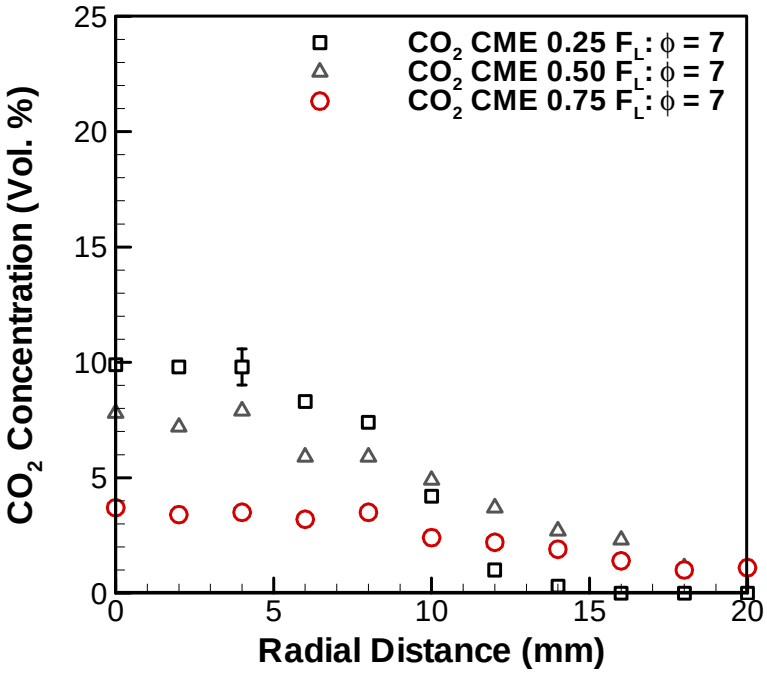

Figure 5.99 CME CO_2 concentrations at ϕ =7 for three axial locations

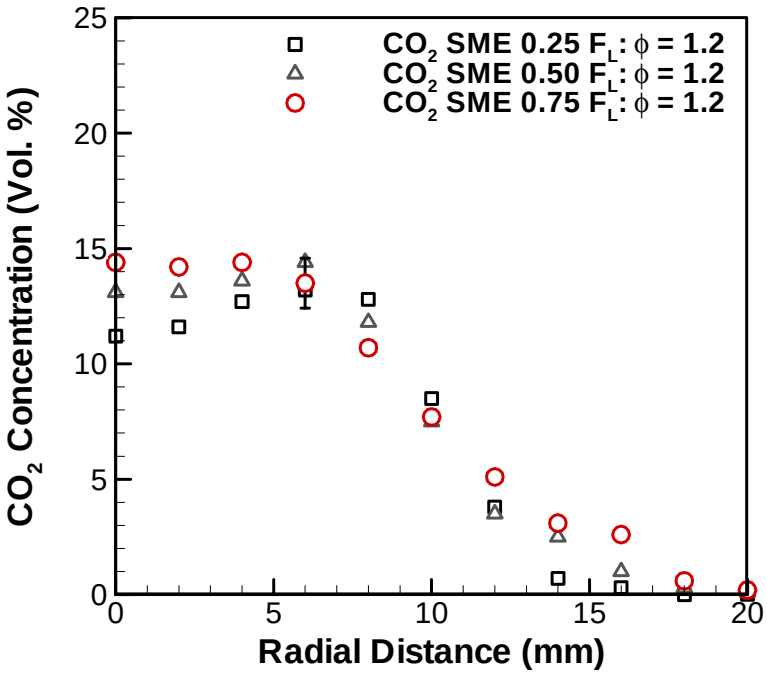

Figure 5.100 SME CO_2 concentrations at ϕ =1.2 for three axial locations

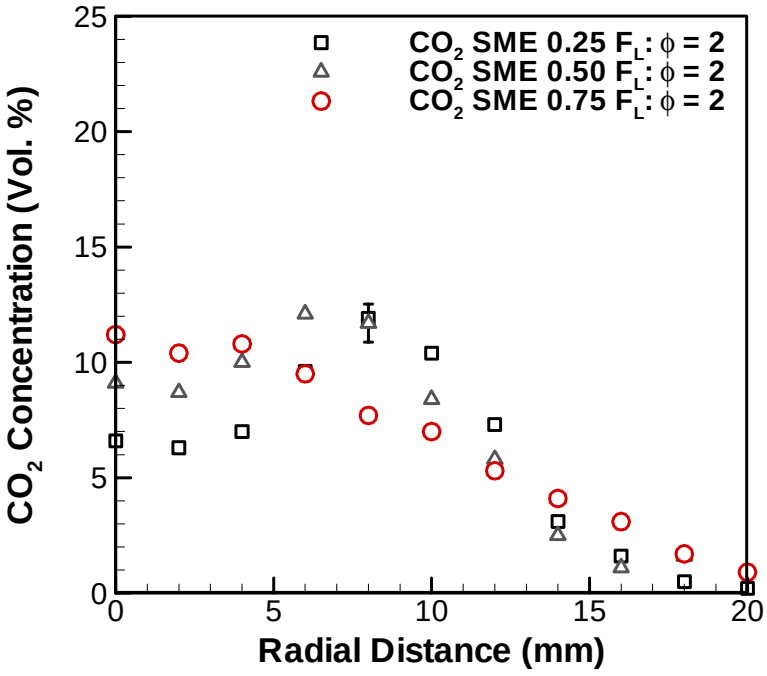

Figure 5.101 SME CO_2 concentrations at ϕ =2 for three axial locations

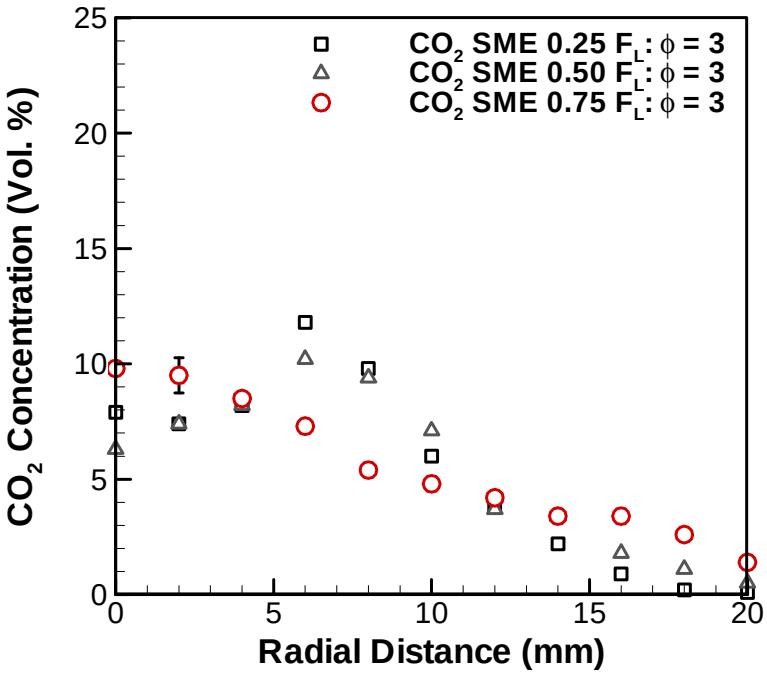

Figure 5.102 SME CO_2 concentrations at ϕ =3 for three axial locations

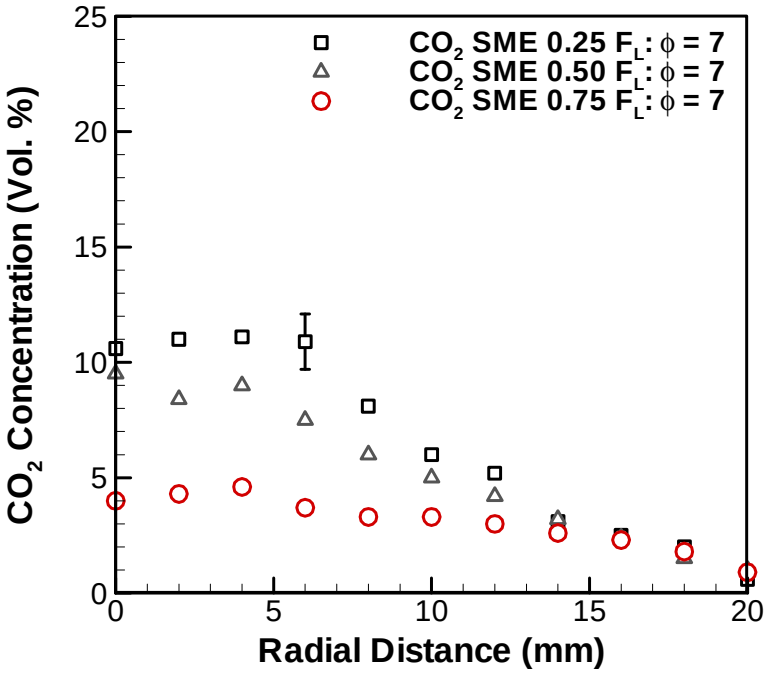

Figure 5.103 SME CO_2 concentrations at ϕ =7 for three axial locations

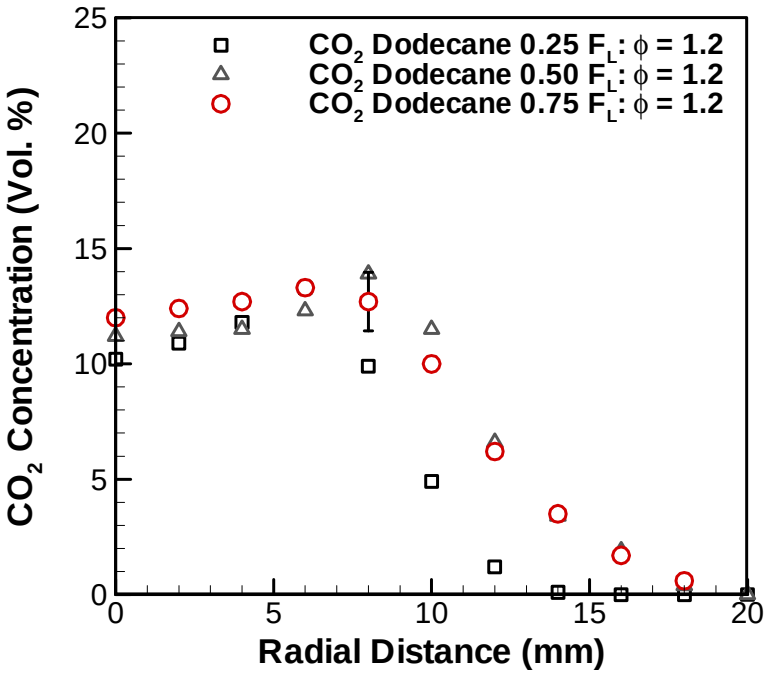

Figure 5.104 Dodecane CO_2 concentrations at ϕ =1.2 for three axial locations

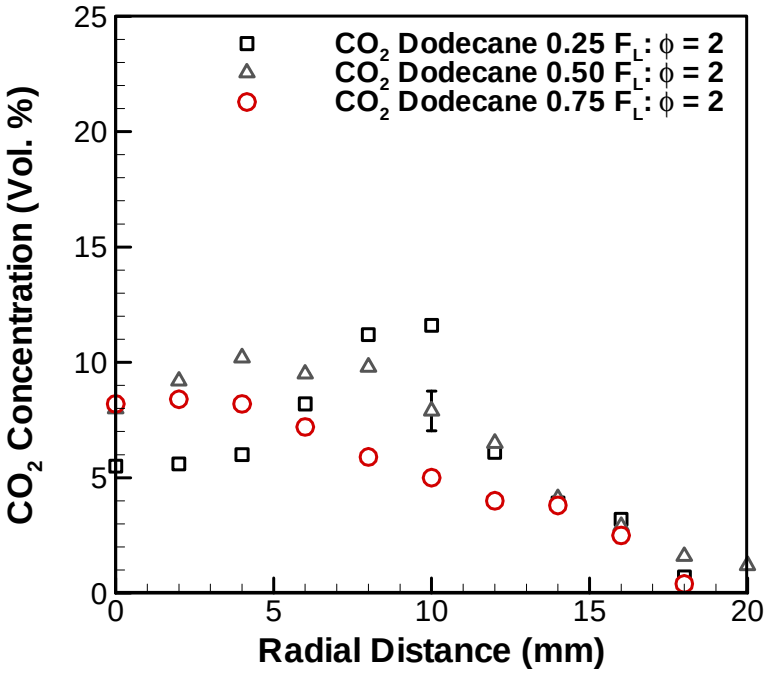

Figure 5.105 Dodecane CO_2 concentrations at ϕ =2 for three axial locations

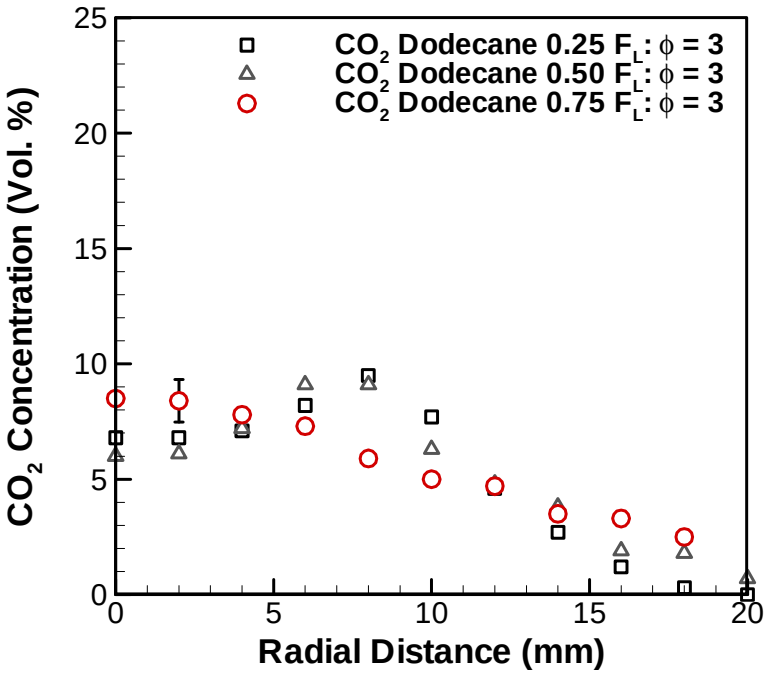

Figure 5.106 Dodecane CO_2 concentrations at ϕ =3 for three axial locations

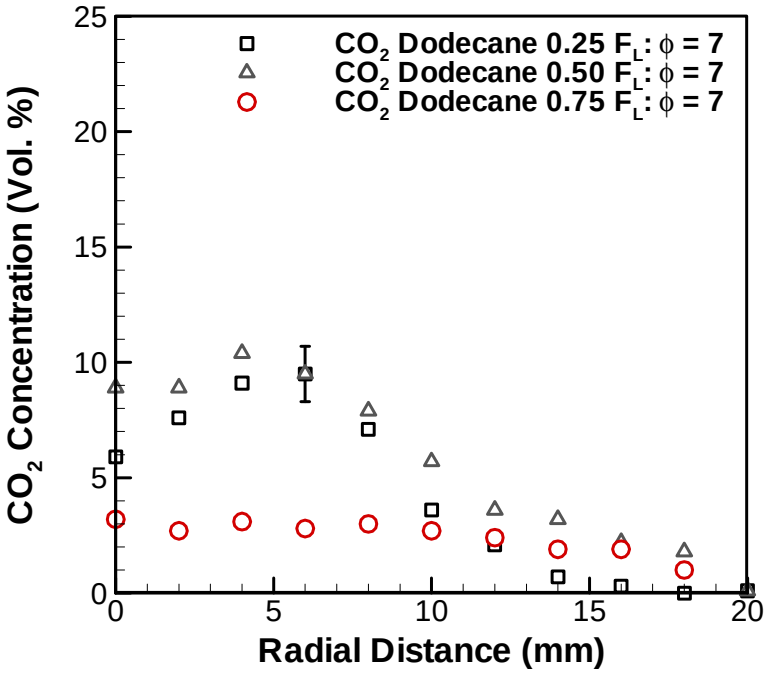

Figure 5.107 Dodecane CO_2 concentrations at ϕ =7 for three axial locations

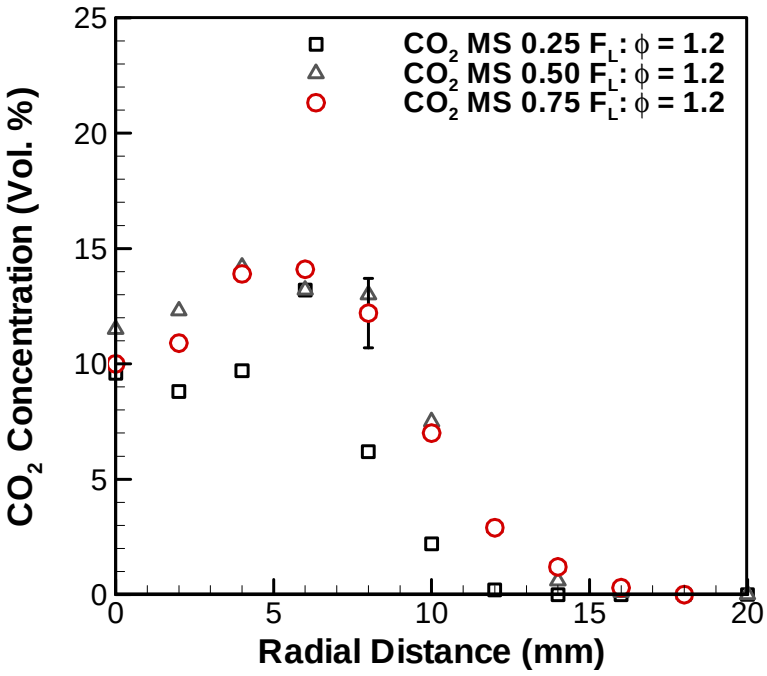

Figure 5.108 Methyl stearate CO_2 concentrations at ϕ =1.2 for three axial locations

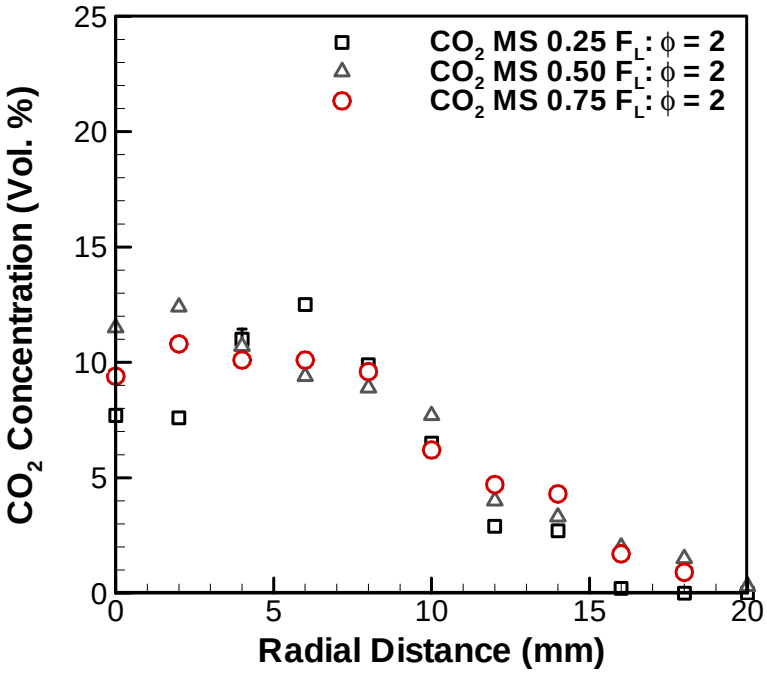

Figure 5.109 Methyl stearate CO_2 concentrations at ϕ =2 for three axial locations

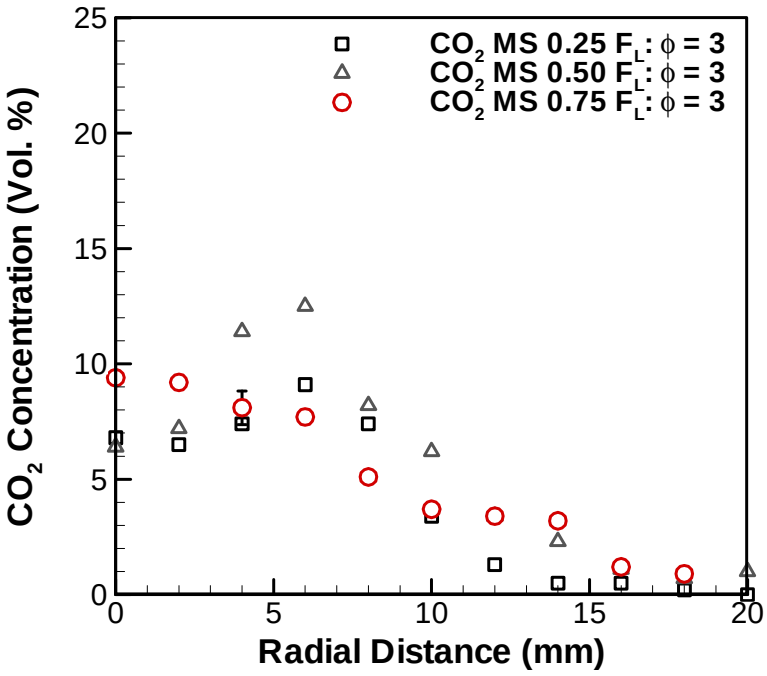

Figure 5.110 Methyl stearate CO_2 concentrations at ϕ =3 for three axial locations

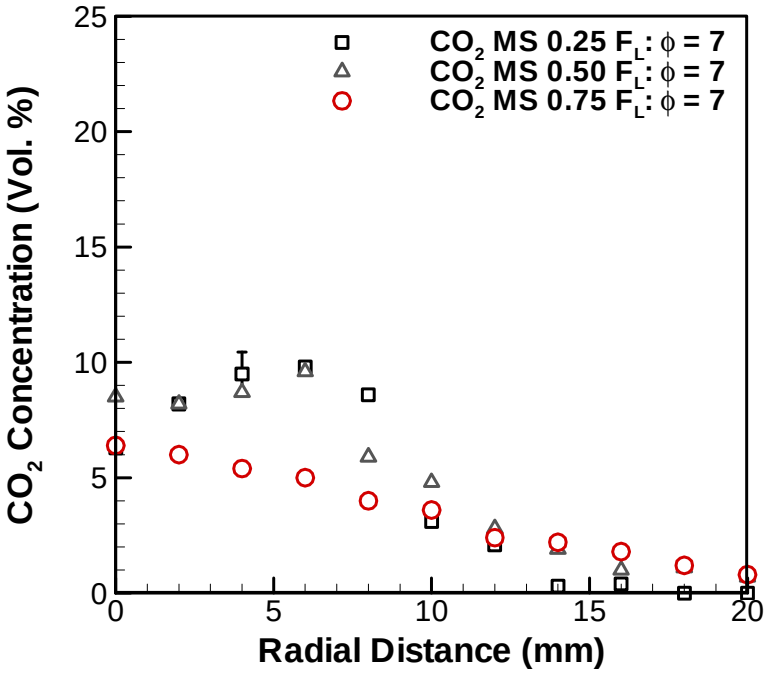

Figure 5.111 Methyl stearate CO_2 concentrations at ϕ =7 for three axial locations

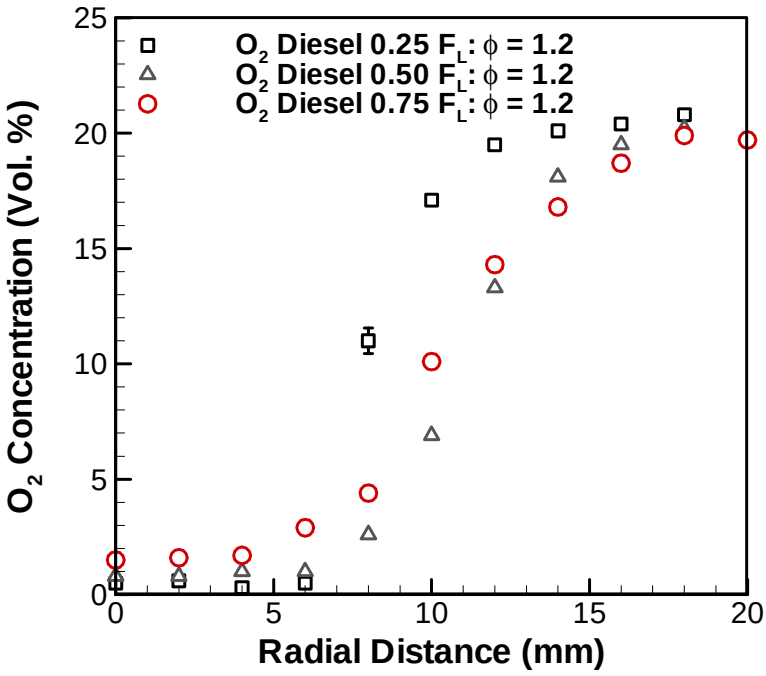

Figure 5.112 Diesel O_2 concentrations at ϕ =1.2 for three axial locations

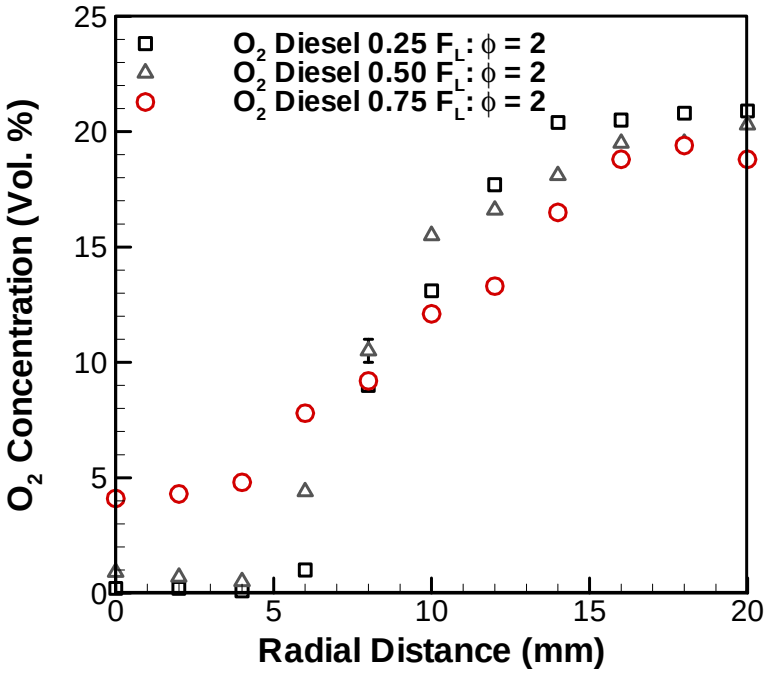

Figure 5.113 Diesel O_2 concentrations at ϕ =2 for three axial locations

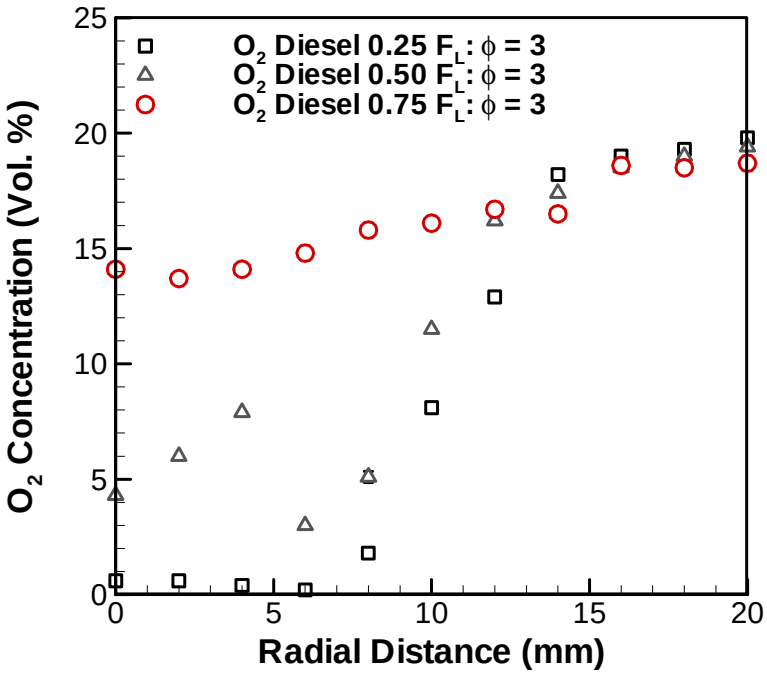

Figure 5.114 Diesel O_2 concentrations at ϕ =3 for three axial locations

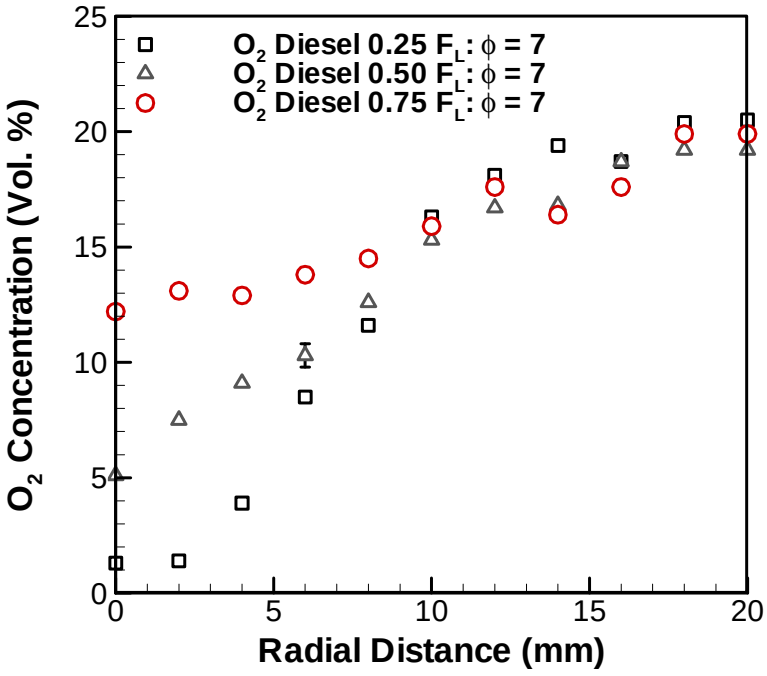

Figure 5.115 Diesel O_2 concentrations at ϕ =7 for three axial locations

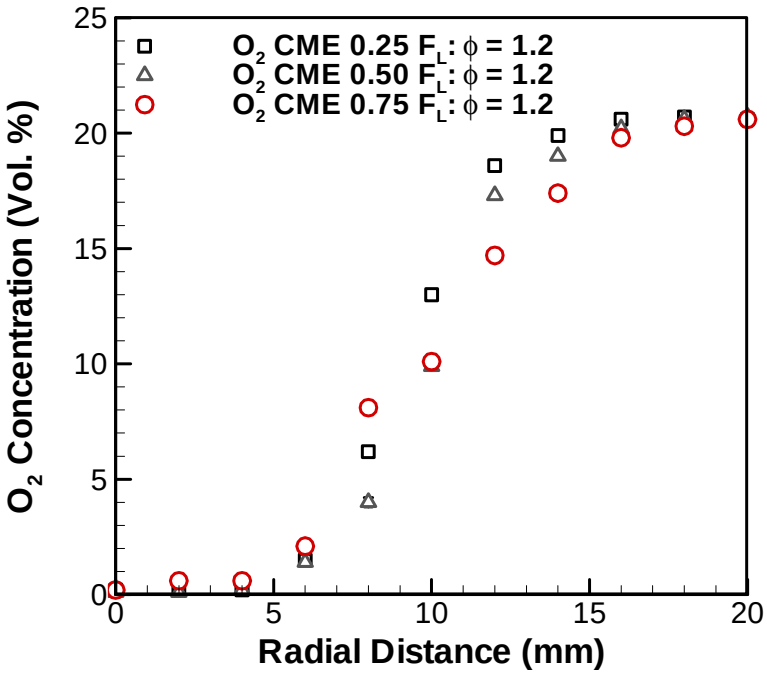

Figure 5.116 CME O_2 concentrations at ϕ =1.2 for three axial locations

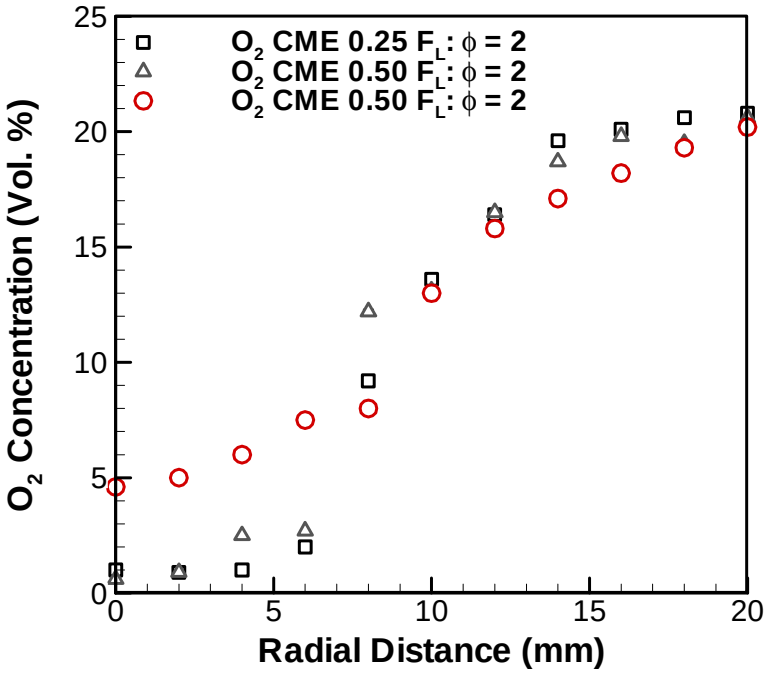

Figure 5.117 CME O_2 concentrations at ϕ =2 for three axial locations

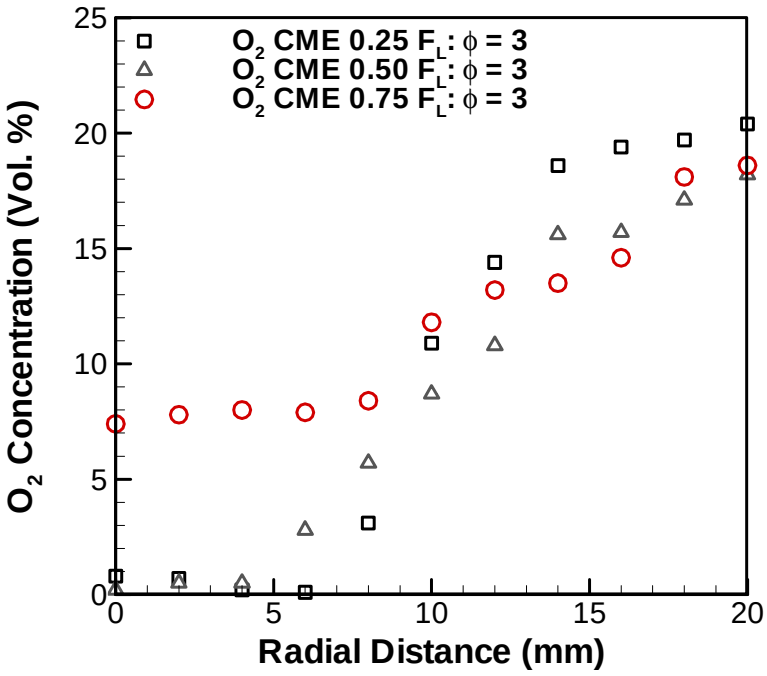

Figure 5.118 CME O_2 concentrations at ϕ =3 for three axial locations

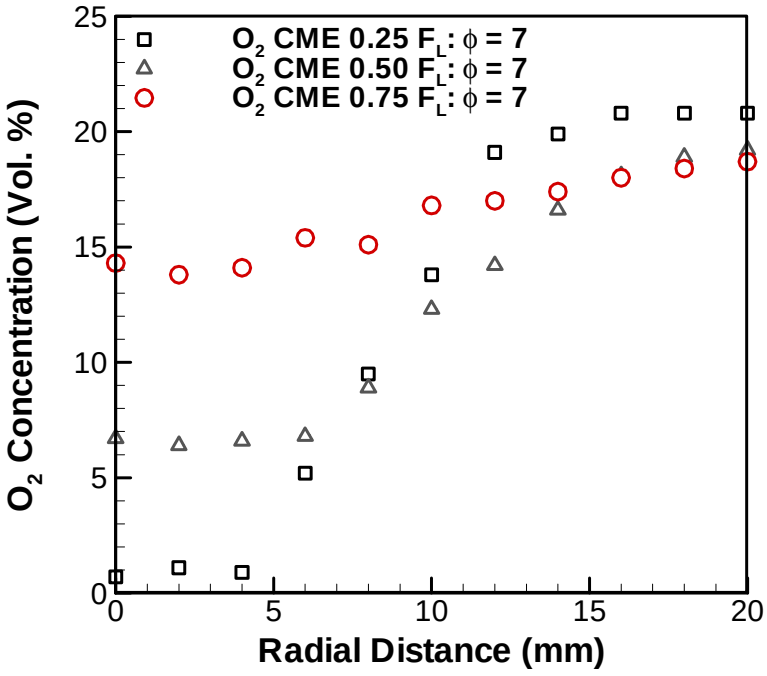

Figure 5.119 CME O_2 concentrations at ϕ =7 for three axial locations

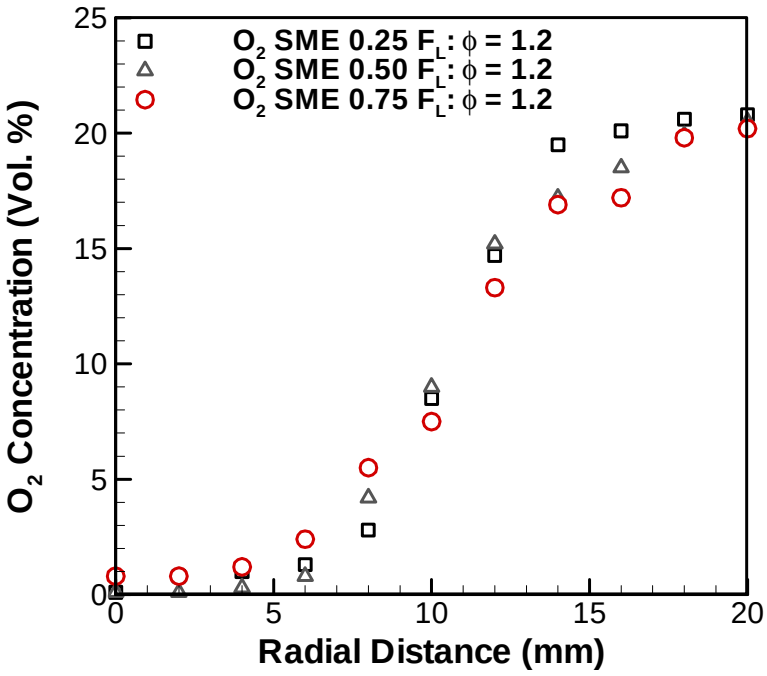

Figure 5.120 SME O_2 concentrations at ϕ =1.2 for three axial locations

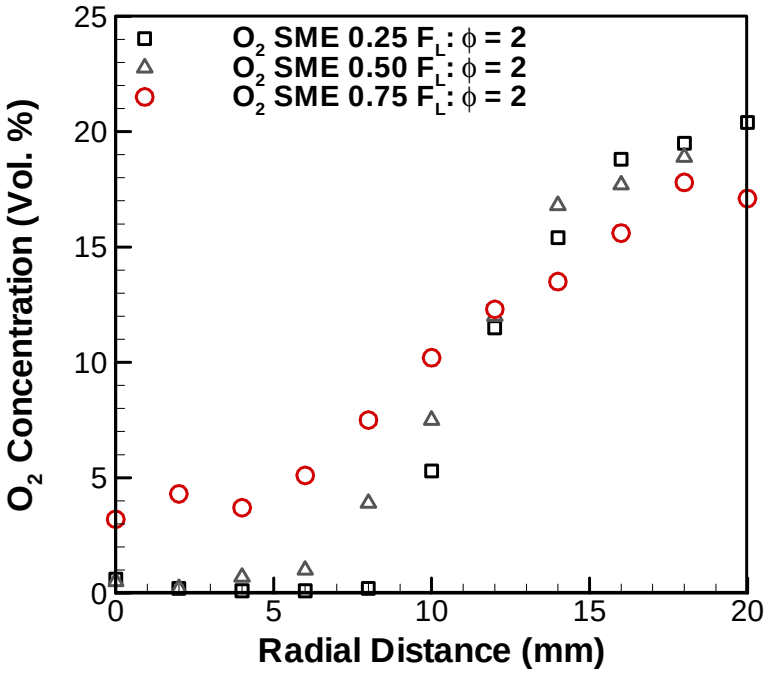

Figure 5.121 SME O_2 concentrations at ϕ =2 for three axial locations

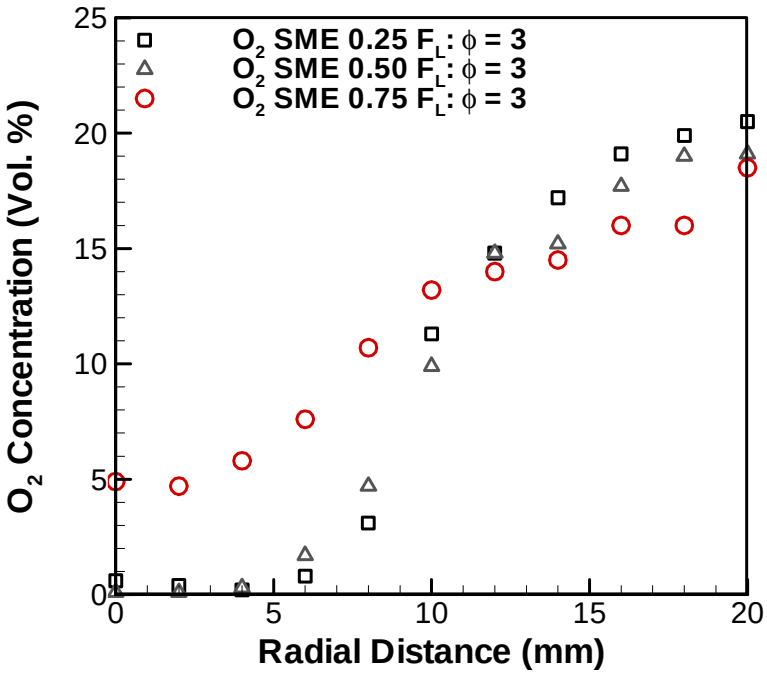

Figure 5.122 SME O_2 concentrations at ϕ =3 for three axial locations

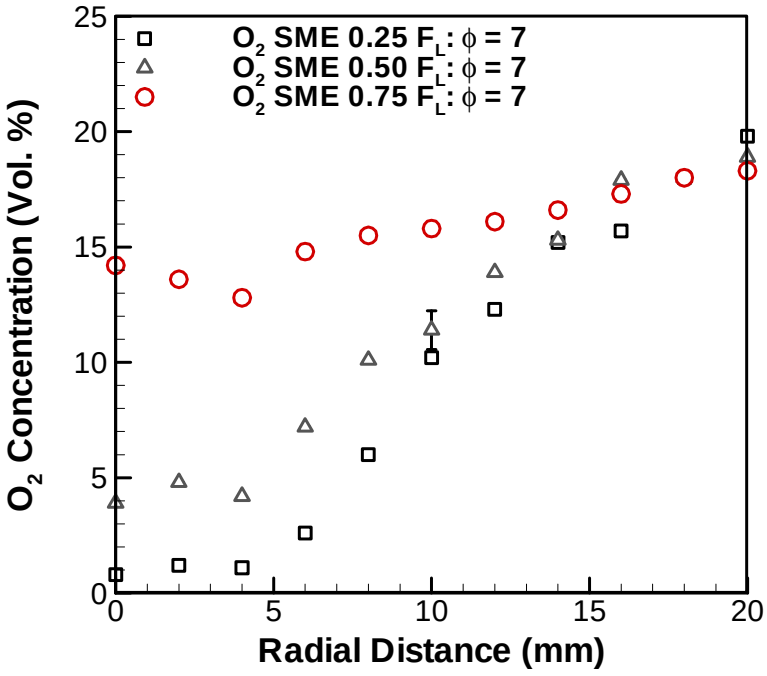

Figure 5.123 SME O_2 concentrations at ϕ =7 for three axial locations

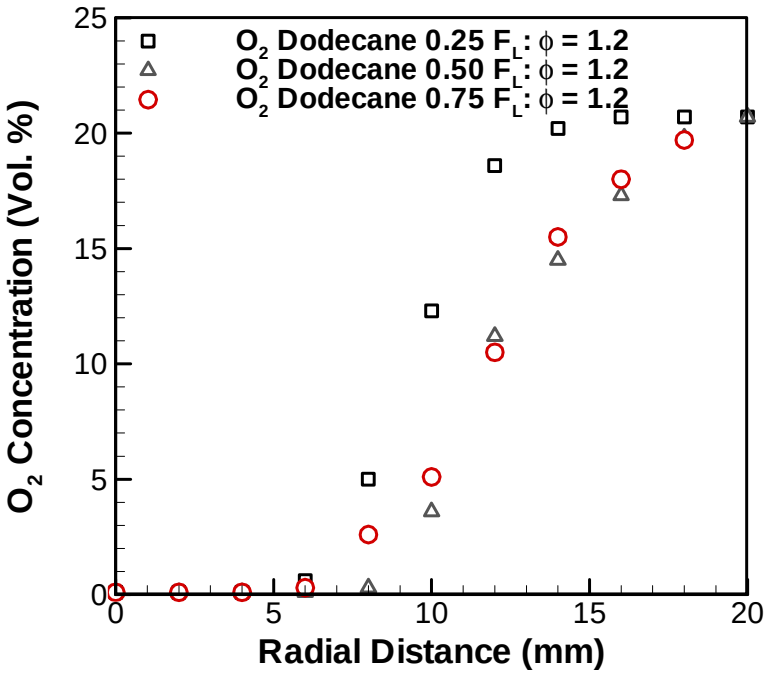

Figure 5.124 Dodecane O_2 concentrations at ϕ =1.2 for three axial locations

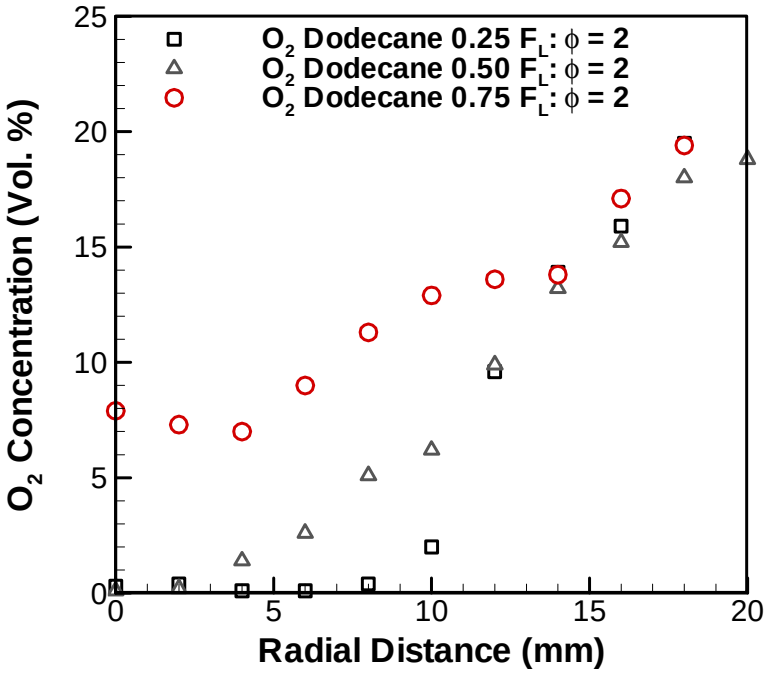

Figure 5.125 Dodecane O_2 concentrations at ϕ =2 for three axial locations

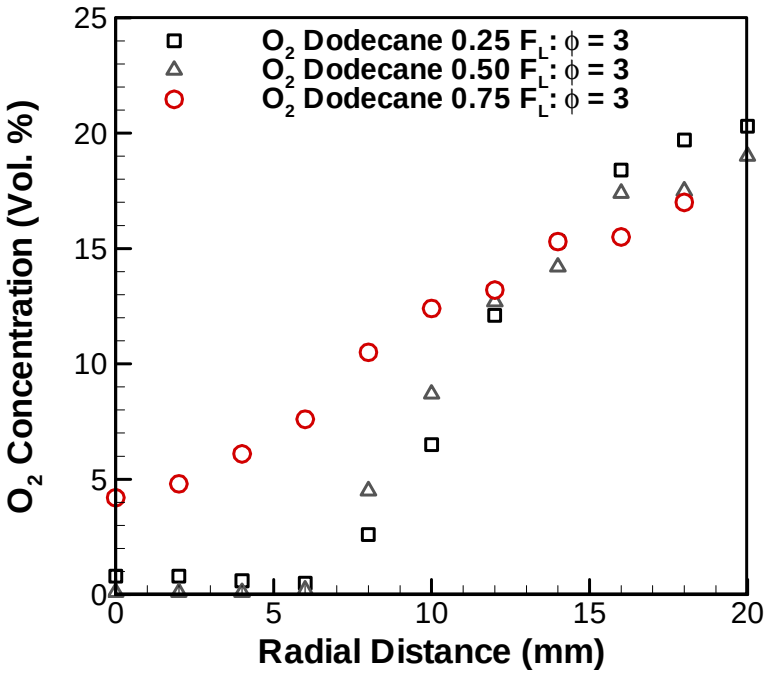

Figure 5.126 Dodecane O_2 concentrations at ϕ =3 for three axial locations

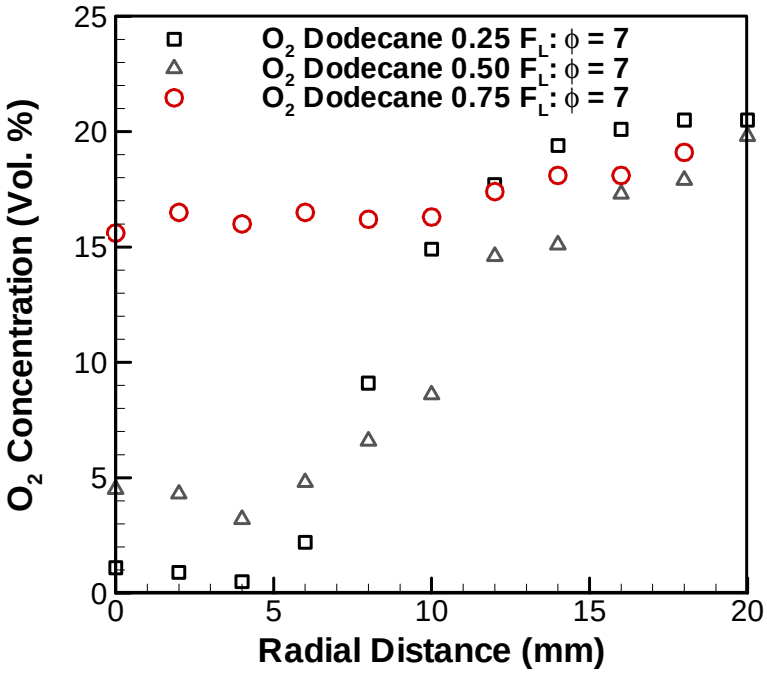

Figure 5.127 Dodecane O_2 concentrations at ϕ =7 for three axial locations

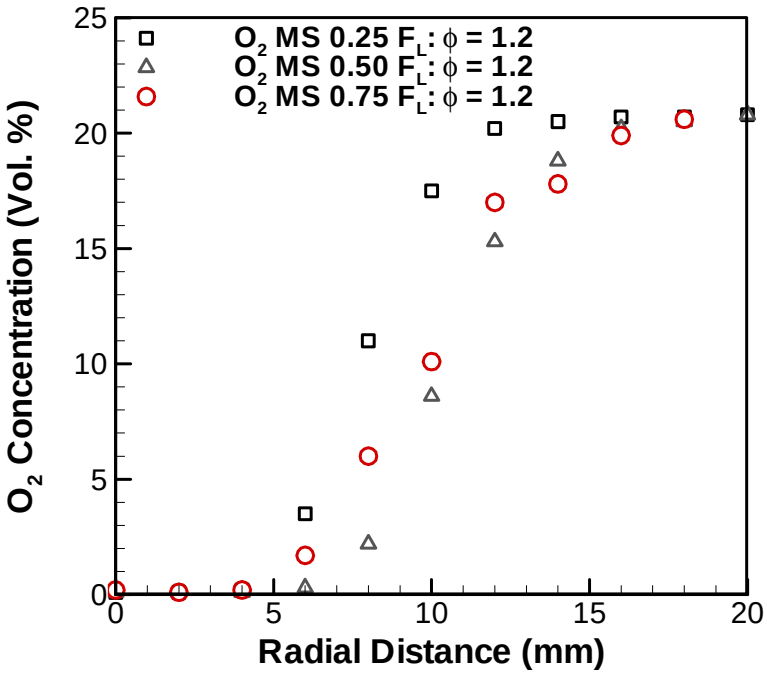

Figure 5.128 Methyl stearate O_2 concentrations at ϕ =1.2 for three axial locations

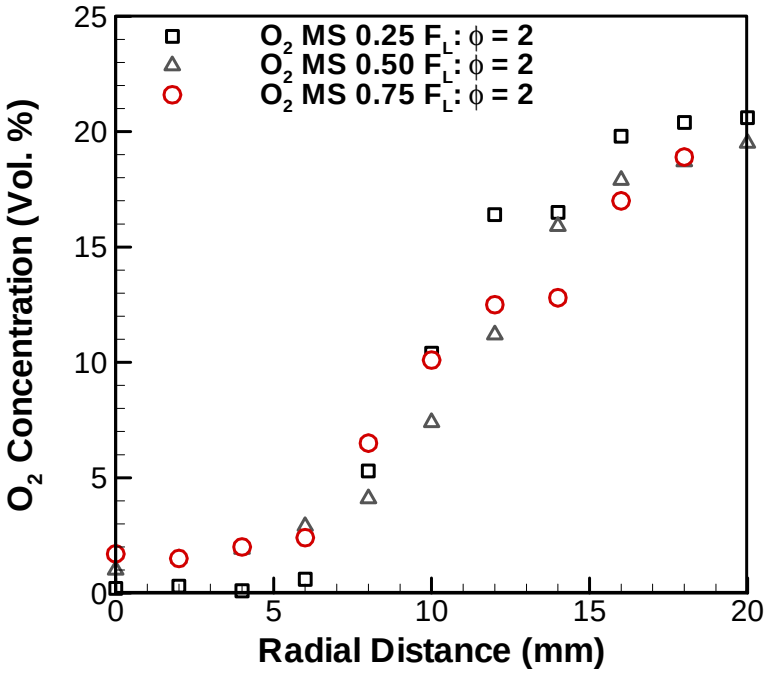

Figure 5.129 Methyl stearate O_2 concentrations at ϕ =2 for three axial locations

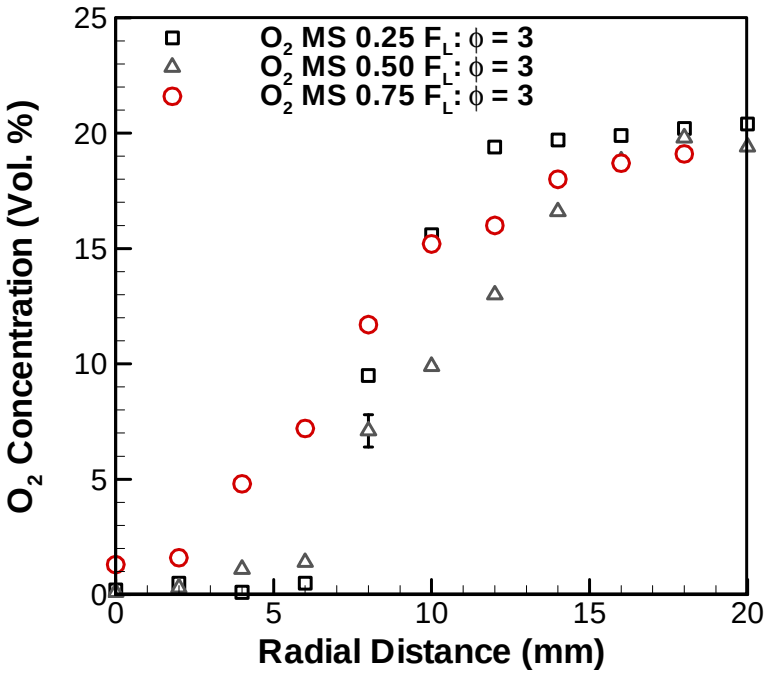

Figure 5.130 Methyl stearate O_2 concentrations at ϕ =3 for three axial locations

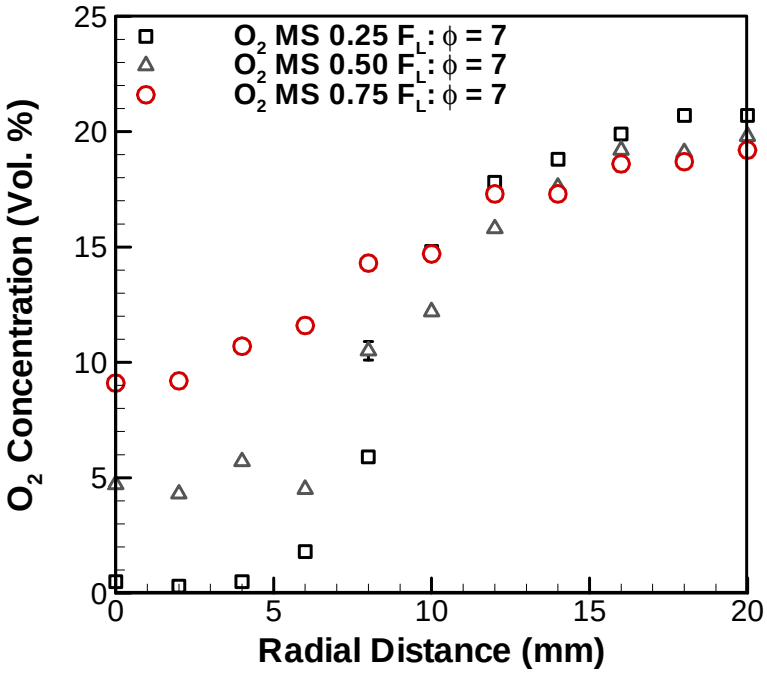

Figure 5.131 Methyl stearate O_2 concentrations at ϕ =7 for three axial locations

Chapter 6
Computational Results

Temperature, CO, CO_2, O_2, and NO concentrations were modeled for laminar premixed flames of dodecane and one oxygenated biofuel, methyl butanoate. Computational fluid dynamics software FLUENT version 6.3.26 and chemical kinetics software CHEMKIN version 4.1 were used and the results are presented in this chapter. A heated laminar fuel vapor/air jet from an axisymmetric burner was modeled. The dimensions of the modeled burner were the same as the dimensions of the burner used for the experimental portion (9.5 mm ID, 12.7 mm OD). The fuel-air mixture was initially set at an equivalence ratio of 1.2 at the burner exit. Local fuel/air mixtures calculated from the non-reacting jet were then used to determine the temperature and concentrations of CO, CO_2, O_2, and NO at each point using the CHEMKIN software package with equilibrium and non-equilibrium combustion models.

The purpose of the developed models was to establish a predictive method by which the combustion properties of diesel (n-dodecane) and biodiesel (methyl butanoate) fuels burning in a laminar flame could be documented at a fuel rich equivalence ratio. The initial equivalence ratio of 1.2 was chosen since the largest global NO was measured at that equivalence ratio in the experimental portion of the dissertation. Experimental measurements showed that NO production was primarily due to the Zeldovich mechanism at this same equivalence ratio of 1.2. This is in contrast to higher equivalence ratios tested (2 to 7) which showed that

NO production was due to the Fenimore mechanism and is discussed later in this chapter.

6.1 Governing Equations

6.1.1 Model Assumptions

Modeling the injection of a heated fuel and air jet requires the energy, momentum, and mass conservation equations to be solved. Additionally, modeling the combustion of these mixtures requires specific thermodynamic and kinetic mechanism equations as well. Therefore, to simplify the complexities involved in obtaining the solution of these equations, the following assumptions were made:

1. The computational domain is assumed to be symmetric about the injector axis.
2. Heat transfer from the heated fuel-air jet and burner tip was neglected. The radiative losses from the flame in the combustion model were also neglected.
3. Single component fuels, methyl butanoate ($C_5H_{10}O_2$) for biodiesel and n-dodecane for diesel, were assumed to avoid multi-component effects.
4. The fuel and air mixture jet was injected above the boiling point of both fuels and assumed to be completely in vapor form.

6.1.2 Continuity and Momentum Equations

FLUENT software package was used for solving of the laminar flow field, the 2-D axisymmetric conservation and momentum equations. The continuity equation is expressed in Eq. (6.1). Equation (6.2) presents the momentum equation where $\rho\vec{g}$ is the gravitational body force in the x direction, $\vec{\upsilon}$ the velocity, $\bar{\bar{\tau}}$ is the stress tensor given in Eq. (6.2a), μ the dynamic viscosity, and P the static pressure.

$$\nabla \cdot (\rho\vec{\upsilon}) = 0 \tag{6.1}$$

$$\nabla \cdot (\rho\vec{\upsilon}\vec{\upsilon}) = -\nabla P + \nabla \cdot (\bar{\bar{\tau}}) + \rho\vec{g} \tag{6.2}$$

$$\bar{\bar{\tau}} = \mu\left(\nabla\vec{\upsilon} + \nabla\vec{\upsilon}^{T}\right) \tag{6.2a}$$

6.1.3 Energy Equation

Flows in this study also involved heat transfer thus required additional equations for energy conservation. Equation (6.3) shows the energy equation used for this purpose where the dissipation due to viscosity was assumed small.

$$\frac{\partial}{\partial x_i}\left[u_i(\rho E + P)\right] = \frac{\partial}{\partial x_j}\left(k\frac{\partial T}{\partial x_j}\right) \tag{6.3}$$

Here k is the thermal conductivity, T is the temperature, and E is defined in Eq. (6.3a) as:

$$E = h - \frac{P}{\rho} + \frac{\upsilon^2}{2} \tag{6.3a}$$

Values used in the numerical model for dodecane and methyl butanoate are presented in Table 6.1 (Baroncini et al., 1981, Gilliland, 1934).

6.1.4 Species Transport Equation

Further, since flows in this study involved species mixing the species conservation equation was also solved, Eq. (6.4) and Eq. (6.4a).

$$\nabla \cdot \left(\rho \vec{\upsilon} Y_i\right) = -\nabla \cdot \vec{J}_i \tag{6.4}$$

$$\vec{J}_i = -\sum_{j=1}^{N_o - 1} \rho D_{ij} \nabla Y_j \tag{6.4a}$$

Where D_{ij} is the binary mass diffusion coefficient in the mixture, N_o is the number of chemical species, and Y_i is the mass fraction of species i.

6.1.5 Equilibrium Calculations

Equilibrium calculations were used to determine species concentrations of CO, CO_2, NO, O_2, and flame temperature. These values were calculated based on the minimization of Gibb's free energy and thermodynamic properties of the fuel used. The equation used for Gibb's function of a system is:

$$G = \sum_{k=1}^{K} \overline{g}_k N_k \tag{6.5}$$

where $\overline{g}_k$ is the partial molar Gibb's function, N_k the number of moles of species k in the system, and K the total number of species. The equilibrium solution is given by the distribution of N_k that minimized the system Gibb's function.

6.1.6 Non-Equilibrium Calculations

To account for residence time and for the history of fuel, non-equilibrium calculations were made. Equilibrium calculations, typically, greatly over predict NO concentrations, as will be discussed in later sections. Thus, by accounting for the residence time the determination of NO concentration is more accurate. Results from this model were obtained with the use of a perfectly stirred reactor network based on a predefined model in the CHEMKIN database which simulated the formation of NO in a methane-air flame. The model did not consider transport processes and hence results are based on the chemical kinetics, residence time and composition of the gas mixtures (CHEMKIN, 2006). Residence times and velocities for these reactors were based on results from the non-reactive heated fuel/air jet numerical simulations seen in Figs. 6.4-6.

Thermodynamic and gas phase mechanisms provided by Dooley et al. (2008) and Westbrook et al. (2009) resulted in the predictions of species and intermediate products. To solve Eqs. 6.6-9 CHEMKIN was used. Equation (6.6) shows the forward rate constant which was assumed to have the following Arrhenius temperature dependence,

$$k_{fi} = A_i T^{B_i} \exp\left(\frac{-E_i}{RT}\right) \tag{6.6}$$

where A_i is the pre-exponential factor, B_i is the temperature exponent, R the universal gas constant, T the gas temperature, and E_i the activation energy. The constants A_i, B_i and E_i are provided by Dooley et al. (2008) and Westbrook et al. (2009) in the gas phase kinetics package for each reaction. The reverse rate

constant (k_{ri}) was related to the forward rate and constants (K_i) by the relation shown in Eq. (6.7).

$$k_{ri} = \frac{k_{fi}}{K_i} \tag{6.7}$$

The constant K_i can be determined by the relationships in Eqs. (6.8, 9):

$$K_i = K_{pi}\left(\frac{P_{atm}}{RT}\right)^{\sum_{k=1}^{K}\upsilon_{ki}} \tag{6.8}$$

$$K_{pi} = \exp\left(\frac{\Delta S_i^o}{R} - \frac{\Delta H_i^o}{RT}\right) \tag{6.9}$$

Where υ_{ki} is the difference between the stoichiometric coefficients of the forward reaction $\upsilon_{ki}^{'}$ and the reverse reaction $\upsilon_{ki}^{"}$ in $\sum_{k=1}^{K}\upsilon_{ki}^{'}\chi_k \Leftrightarrow \sum_{k=1}^{K}\upsilon_{ki}^{"}\chi_k$ and χ_k is the chemical symbol for k^{th} species.

It became necessary also to establish further criteria (Fig. 6.7) to account for the time history of the gas. For this Eq. 6.10 was used:

$$\frac{dY_k^{(n)}}{dt} = \frac{1}{\dot{m}_o \tau_R}\sum_{i=1}^{M}\dot{m}_i\left(Y_{i,k} - Y_k\right) + \frac{W_k\dot{\omega}_k^{(n)}}{\rho^{(n)}} \tag{6.10}$$

Where $\dot{m}_o$ is the mass through-flow rate, and $\dot{m}_i$ is the mass flow rate of the i^{th} inlet, Y is the mass fraction of the species, ρ is the mass density, W_k is the molecular weight of the k^{th} species, $\dot{\omega}_k$ is the molar rate of production of the k^{th} species by gas phase chemical reaction per unit volume, and τ_R is given by Eq. 6.11 as:

$$\tau_R = \frac{\rho V}{\dot{m}_o} \tag{6.11}$$

6.2 Reaction Models

The combustion of methane (CH_4) which contains only one carbon atom involves 325 elementary reactions and 53 species (GRI-Mech 3.0). For comparison biodiesel is composed of several fatty acid methyl esters that typically range in carbon chain length from 15 to 21. This implies that a full kinetic model for a biodiesel fuel will be large and computationally taxing. To the author's knowledge, there is currently no complete kinetic model for the combustion of oxygenated biofuels of carbon chain length 15-21. However, without chemical kinetic models, accurate predictions of temperatures, intermediate radicals, and pollutant concentrations cannot be achieved. To resolve this problem some authors have used surrogate fuels which are significantly smaller in length and hence modest in computational requirements. Authors such as Fisher et al. (2000), Weiss et al. (2006), and Dooley et al. (2008) have developed and made available the chemical kinetic models for a surrogate fuel methyl butanoate ($C_5H_{10}O_2$). Methyl butanoate contains the same essential chemical structure features such as the $RC(=O)OCH_3$ or $RC(=O)OC_2H_5$ (where R is an alkyl or alkenyl radical) hence possessing similar kinetic properties of the oxidation of the methyl ester as a biodiesel fuel (Metcalfe et al., 2007, Herbinet et al., 2008). The kinetic model by Dooley et al. (2008) will be used in the numerical portion of this dissertation; the model consists of 275 species and 1545 reactions to simulate the biofuel combustion.

This mechanism reduces the need for a large computational facility, time, and has been validated as an appropriate surrogate for biodiesel. The mechanism in

CHEMKIN compatible format can be found at the Combustion Chemistry Centre website in the following link: http://c3.nuigalway.ie/biofuels.html.

Diesel fuel is also composed of various saturated and unsaturated molecules; see Table 1.1 on page 27. Diesel typically has a carbon chain length range much larger than biofuels, ranging from 10-22 of which nearly 25% are aromatics. A few authors have used various n-alkane and n-alkane/aromatic mixtures as diesel surrogates. Fuels such as n-hepatne, n-dodecane, n-hexadecane, and mixtures of these with toluene (see Table 3.1) have all been used to simulate the combustion of diesel (Kitamura et al., 2001, Farell et al., 2007, Westbrook et al., 2009). Normal dodecane has been shown to have similar thermo-physical and transport properties to that of diesel (Farell et al., 2007). It has been used previously and found to be a satisfactory surrogate for diesel according to a review by Farell et al. (2007). Also, since experimental data in this dissertation were obtained for n-dodecane, the predictive mechanism would provide a direct comparison. Hence, the kinetic model provided by Westbrook et al. (2009) was used; the model consists of 5030 reactions and 1282 total species for the combustion of n-dodecane. The mechanism and thermodynamics files in compatible CHEMKIN format can be found at the Lawrence Livermore National Laboratory website in the following link: https://www-pls.llnl.gov/?url=science_and_technology-chemistry-combustion-c8c16_n_alkanes.

6.3 Grid Development

A schematic diagram of the computational domain with boundary conditions and coordinate system can be seen in Fig. 6.1. Boundary conditions and dimensions are also given in this figure. The grid extended to 2 m in the axial direction and 0.05 m in the radial direction. This included the burner section (0.00475 m radial and 0.475 m axial distance) which had an initial section prior to the outlet that was sufficiently long for fully developed flow to occur (50 diameters). The axisymmetric computational domain was aligned along the center of the burner. The grid was initially assigned a very coarse mesh of 3 cells/cm radially and 3 cells/cm axially to reduce the initial computational time of the solution. After the solution was obtained, the grid was refined and tested again. Refinement was done primarily along the center of the flame where gradients were large. This process was repeated twice. Results of the grid refinement procedure are given in Fig. 6.2 a-c. Temperature profiles are also shown at the three axial locations for the different grid variations, Figs. 6.3 a-c. The largest difference occurred between the original grid and the first adapted grid. The location and magnitude of the peak temperature increased as the grid was refined at all three axial locations. With an increased number of grid cells, the magnitude and position of peak radial temperature was within 7.5%, thus the solution was reasonably grid independent.

Other considerations during the grid development process included: 1) effect of boundary layer development along the fuel tube and 2) heat transfer between the burner tip and flame. In the present model a no-slip boundary condition was

imposed on the outer wall of the burner to account for the effect of boundary layer. Heat transfer between the burner and flame, however, was neglected as were the beveled sharp edges at the burner exit due to the complexity of the heat transfer problem involved (Choudhuri, 2000).

6.4 Results

The in species mole fractions and temperature contours of heated non-reactive dodecane/air and methyl butanoate/air jets predicted with for the equilibrium model are shown in Figs. 6.4-6. Although the jet was simulated for the entire grid only the region of interest is presented in these figures, approximately 15 cm above the injector exit. The results from the equilibrium model for temperature and CO, CO_2, O_2, and NO concentrations are also shown in Figs. 6.7-16. In general, the equilibrium model successfully predicted the concentration of the combustion products and temperature with the exception of NO. Temperature, carbon monoxide, CO_2, and O_2 concentrations showed trends that were in agreement with experimental data for both fuels. However, the nitric oxide concentration predicted by the equilibrium model did not correspond with experimental results for both fuels. For a more accurate prediction of NO, which has a chemical time scale much larger than other flame species; the chemical state, age, and history of the gas mixture must also be accounted for (CHEMKIN, 2006). Therefore, both the equilibrium and non-equilibrium results are presented in this section.

6.4.1 Dodecane Equilibrium Model

The predicted carbon monoxide concentrations in the n-dodecane flame are shown at the same three locations downstream of the burner as the experimental portion of this dissertation in Fig. 6.8. The concentration profiles become wider further downstream of the injector and increased from 5.73% to 5.85% and 5.87% in the near (x = 0.02375 m), mid (x = 0.0475 m), and far (x = 0.07125 m) burner locations, respectively. These locations downstream of the burner were based on the flame lengths of diesel fuel at the same condition. For the near and mid portions of the flame, the model predicted the behavior of the fuel jet and the species concentrations near the jet centerline well. Very small amounts of intermediate compounds, including HOCHO, OCHO, CH_2O, H_2O_2, HO_2, and HCO on the order of 10^{-6} to 10^{-8} moles, were also predicted along the centerline at the region where CO decreased. To determine if the numerically modeled amounts were feasible, a carbon-carbon balance was performed in locations of the peak CO and CO_2 production and was found to be in agreement with values obtained from the equilibrium code developed by Olikara and Bormann (1975). The predicted values of CO were larger than measured quantities. Experimental CO_2 concentrations increase in the far-burner region which was not found in the modeled results since residence time, and soot combustion history was not accounted in the model. Overall, it was found that the model predicted the correct peak values of CO within 10% in the near burner region to 20% in the far burner region despite not accounting for the time history of gas.

Carbon dioxide concentration width increased in the radial direction downstream of the injector exit. Although the model predicted somewhat lower values than experimental data, computed values followed the trend of CO_2 concentration well. Peak values predicted by the numerical model varied little in the axial direction at the near, mid and far burner locations with values of 10.9%, 11.1%, and 11.2%, respectively. The model did not account for residence time and soot history and hence resulted in a lower prediction of peak values compared to experimentally obtained data. It was also seen that peak temperatures occurred at the same places as peaks in CO_2 concentrations at all three axial locations. This corresponded with the expected maximum heat release rates as CO oxidized to CO_2 (Turns, 2000). Predicted flame temperatures were higher by 10 to 17% compared those measured up to 6 to 8 cm from the center of the flame in the radial direction. Outside of this region, the predicted flame temperatures decreased to the point of becoming lower than the measured values. Again, this was due to the effects of radiative losses particularly due to soot combustion from the flame which were not accounted for in the numerical model. The heat released from the flame resulted in the thermocouple measuring higher temperatures compared to those predicted. As the thermocouple approached the flame, it was exposed to the radiative heat release from the flame, thus resulting in higher measured temperatures outside of the primary and secondary reaction zones.

The predicted values of NO concentration in these flames did not correlate well with experimentally measured data as seen in Fig. 6.12. In the vicinity of the flame centerline ($\leq$0.004 m) in the near-burner and mid-flame locations, the

predicted values agreed well with experimental data. At greater radial distances from the flame centerline (0.006 m≤ r), where the equivalence ratio approached stoichiometry, temperatures and CO_2 peaked, and NO concentrations greatly increased to 2400 ppm for n-dodecane. This was because NO had a much larger characteristic chemical time scale than other pollutants and required a time history in order to correctly predict its values. Therefore, based on the comparison with experimental data the current model was not suitable for prediction of NO and will be done with the use of non-equilibrium model developed and shown in Fig. 6.18.

6.4.2 Biodiesel Equilibrium Model

Results for the carbon monoxide concentrations arising from the biodiesel combustion, using the equilibrium model are shown in Fig. 6.13. The radial width of the profiles increased in the mid and far burner regions becoming more parabolic in shape at these locations. Peak CO concentration values in the near (x = 0.02375 m), mid (x = 0.0475 m), and far (x = 0.07125 m) burner locations were 5.43%, 5.42%, and 5.42% respectively. For the near and mid portions of the flame the model predicted the behavior of the fuel jet and concentrations well for all locations. Experimental data for SME was used for comparison. Far-burner calculations, however, resulted in overprediction of the amount of CO a maximum of 25%, as was the case with n-dodecane. A carbon-carbon balance was also performed for the biodiesel (methyl butanoate) in locations of the peak CO and CO_2 production and found to be in agreement with values obtained from the equilibrium code developed by Olikara and Bormann (1975). For CO concentrations, the largest differences between experimental values and predictions were 15% in the near-burner region and 20% in the mid and far-burner sections.

Carbon dioxide concentration profile peaks were lower in the near-burner region, 12.9%, increasing in the mid and far burner locations to 13.7%. Temperature profiles were observed to begin to decline after regions of peak CO_2 concentrations at all three axial locations. Also, as with n-dodecane the predicted flame temperatures were higher than the measured temperatures up to 6 to 8 cm from the center of the flame in the radial direction. Outside of this region

experimentally measured temperatures were higher than those predicted by the model. This was attributed again to the effect of radiative losses from the flame which the thermocouple detected resulting in higher measured temperatures outside of the primary and secondary reaction zones.

The nitric oxide concentration calculations in these flames did not correlate well with experimentally measured data as can be seen in Fig. 6.17. Similar behavior was observed for biodiesel as with n-dodecane. Near the flame centerline ($r \leq 0.004$ m) in the near-burner axial location, the predicted values corresponded well with experimental data. At greater radial distances from the flame centerline ($0.006 \text{ m} \leq r$), where the equivalence ratio approached stoichiometry and CO_2 peaked, the magnitudes of NO concentrations were much larger than experimentally obtained data (1650 ppm). Therefore, for biodiesel also the current model was also not suitable for prediction of NO and will be done with the use of non-equilibrium model which is shown in the next section of this report.

6.4.3 Non- Equilibrium Model

Results obtained from the equilibrium model were found to be in reasonable agreement with experimental data for CO, CO_2, O_2 concentrations and temperature. The model, however, significantly overpredicted the amount of NO produced in the actual combustion of the two fuels. Results obtained from use of the non-equilibrium model showed the NO concentrations to be far below its equilibrium value.

Figure 6.18 and Fig. 6.19 show the NO concentration for biodiesel and dodecane at the same three axial locations downstream of the injector as presented before in Figs. 6.11 and 6.16. At x = 0.02375 m, the results peaked at a value of 231ppm for biodiesel and 206ppm for dodecane compared to the experimental peaks of 155ppm and 169ppm, respectively. Similarly, peak values obtained at the mid (x = 0.0475 m) and far burner (0.07125 m) locations for the numerical model of biodiesel were 356ppm and 465ppm, compared to biodiesel values of 320 ppm and 430 ppm for the experimentally obtained data and 242 ppm and 328 ppm for dodecane compared to 260ppm and 315ppm at the same corresponding experimental locations of dodecane. Also, since prompt NO formation was characterized by the presence of CH, as seen in Chapter 5 of this dissertation, a plot of predicted CH mole fraction plotted against the axial location is given in Fig. 6.20. Using this plot, dominant regions of NO formation by the prompt mechanism can be determined by locating regions of peak CH production.

Overall, measurements were in much better agreement with the results of the non-equilibrium model than those predicted with the equilibrium model for both

fuels. Nitric oxide concentration profiles showed peaks near the flame boundaries where local equivalence ratios were near unity and where the previous model greatly over predicted concentrations. At further locations downstream, the profiles became more parabolic and increased from 231ppm in the near burner region, 356ppm in the mid flame region, and 465ppm in the far burner location. The temperature peaks corresponded to the peaks in NO concentrations, implying a strong influence of NO formation by the thermal mechanism. This agrees with experimentally obtained data that showed the same trend at the initial equivalence ratio of 1.2 (Love et al., 2009).

Nitric oxide production for biodiesel was predicted to be higher than those for n-dodecane at every location. Experimental values showed the same trend with the exception in the near burner region where data were within experimental uncertainties. Temperature data for experimental and the numerical model showed that n-dodecane and biodiesel produced comparable values and were within temperatures (above 1800K) required for the formation of NO by the Zeldovich mechanism. Additionally, both the numerical and experimental results showed that NO concentrations increased downstream of the burner indicating a dependence on residence time, thus the primary formation mechanism at this condition was attributed to the Zeldovich mechanism.

In conformity with the initial objectives of the chapter predictive models have been established for the combustion of diesel (n-dodecane) and biodiesel (methyl butanoate) laminar flames at a fuel rich equivalence ratio of 1.2. The results obtained from an equivalence ratio of 1.2, however, are in contrast to those at

higher equivalence ratios from 2 to 7 which showed that NO production was due to the Fenimore mechanism. From Fig. 6.20, CH mole fraction was found to reach a maximum for both fuels in the near-burner region. In this same region the biofuel showed higher predicted mole fraction of CH than n-dodecane. This value subsequently dropped for both fuels further downstream. Based on this prediction and experimental data at this condition, it is expected that at as the mixture becomes more fuel rich (higher equivalence ratios) the amount of CH, particularly in the near burner region, would grow in magnitude. This coupled with lower temperatures, based on experimental results, would favor the formation of NO through the Fenimore mechanism.

In this chapter since the predictive models corresponded well with experimental data it can be assumed that radiative losses due to the presence of soot were small. The more fuel rich equivalence ratios are not presented in the chapter as soot formation is expected to significantly affect temperatures through radiative losses at these conditions. Soot formation, soot concentration, and their effect on the radiative losses were not accounted for in the present model and could significantly effect overall NO production at higher equivalence ratios.

6.5 Chapter Summary and Conclusions

The following was obtained regarding the numerical simulation of biofuel and hydrocarbon and flames.

- Numerical models for the combustion of laminar flames of biodiesel and n-dodecane were successfully developed using FLUENT and CHEMKIN software packages.
- Equilibrium model predicted peak values of CO, CO_2, O_2, and temperature within 20% of experimentally obtained data.
- Equilibrium model did not correctly predict the amount of NO and therefore a non-equilibrium model was used.
- Non-equilibrium model predicted NO concentrations reasonably well for both fuels.
- Data obtained from numerical models showed that at an equivalence ratio of 1.2 the NO formation mechanism was primarily due to the Zeldovich mechanism and secondarily due to the prompt mechanism.

Table 6.1 Material Properties for fuel mixture with air

	Biodiesel (Methyl Butanoate)	n-dodecane
Inlet A/F Ratio by Mass	10.36	12.45
Thermal Conductivity (W/m-K)[1,2]	0.0831	0.106
Viscosity (kg/m-s)[2,3]	3.05e-05	3.25e-05
Mass Diffusivity (m^2/s)[4]	2.51e-5	2.88e-05
Density (kg/m^3)	Incompressible Ideal Gas	Incompressible Ideal Gas
Cp (J/kg-K)	Mixing-Law	Mixing-Law

[1]Baroncini et al., (1981),[2]Kanury (1975), [3]Maxwell (1950), [4]Gilliland (1934)

Table 6.2 Under - Relaxation Parameters

Pressure	0.3
Density	1
Body Forces	1
Momentum	0.7
$C_{12}H_{26}$ or Biodiesel	0.8
O_2	0.8
Energy	0.9

Table 6.3 Discretization Methods

Pressure	Standard
Momentum	First Order Upwind
$C_{12}H_{26}$ or Biodiesel	First Order Upwind
O_2	First Order Upwind
Energy	First Order Upwind

Table 6.4 Boundary Conditions

Outflow Boundaries	
Pressure Outlet	
Gauge Pressure (Pa)	0
Backflow Total Temperature (K)	300
Backflow Direction Specification Method	Normal to Boundary
Species Mass Fractions	Biodiesel and $C_{12}H_{26}$ = 0 O_2 = 0.23 N_2= 0.77
Inlet	
Velocity Inlet	
Velocity Specification Method	Magnitude, Normal to Boundary
Reference Frame	Absolute
Velocity Magnitude (m/s)	7.21 for $C_{12}H_{26}$ and 7.17 for Biodiesel
Temperature (K)	700
Species Mass Fractions	$C_{12}H_{26}$ = 0.074 O_2 = 0.216 N_2= 0.71 For Biodiesel Biodiesel = 0.0874 O_2 = 0.213 N_2 = 0.699
Burner Top and Side	
Wall	
Wall Motion	Stationary
Shear Condition	No Slip
Heat Flux (W/m^2)	0
Heat Generation (W/m^3)	0
Species	Zero Diffusive Flux
Symmetry	
Axis	

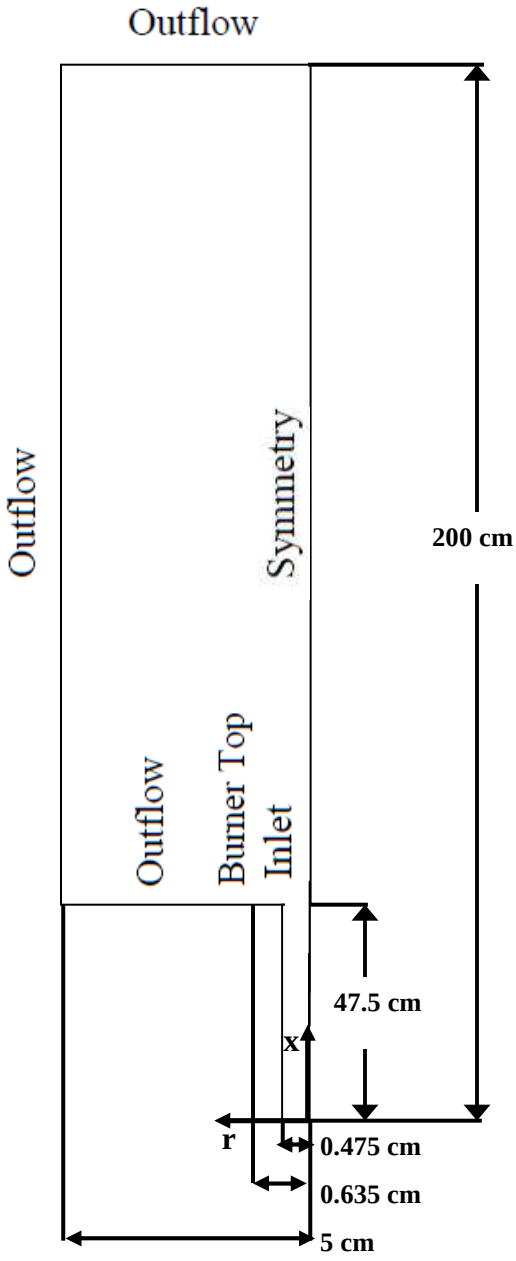

Figure 6.1 Schematic drawing of the computational domain

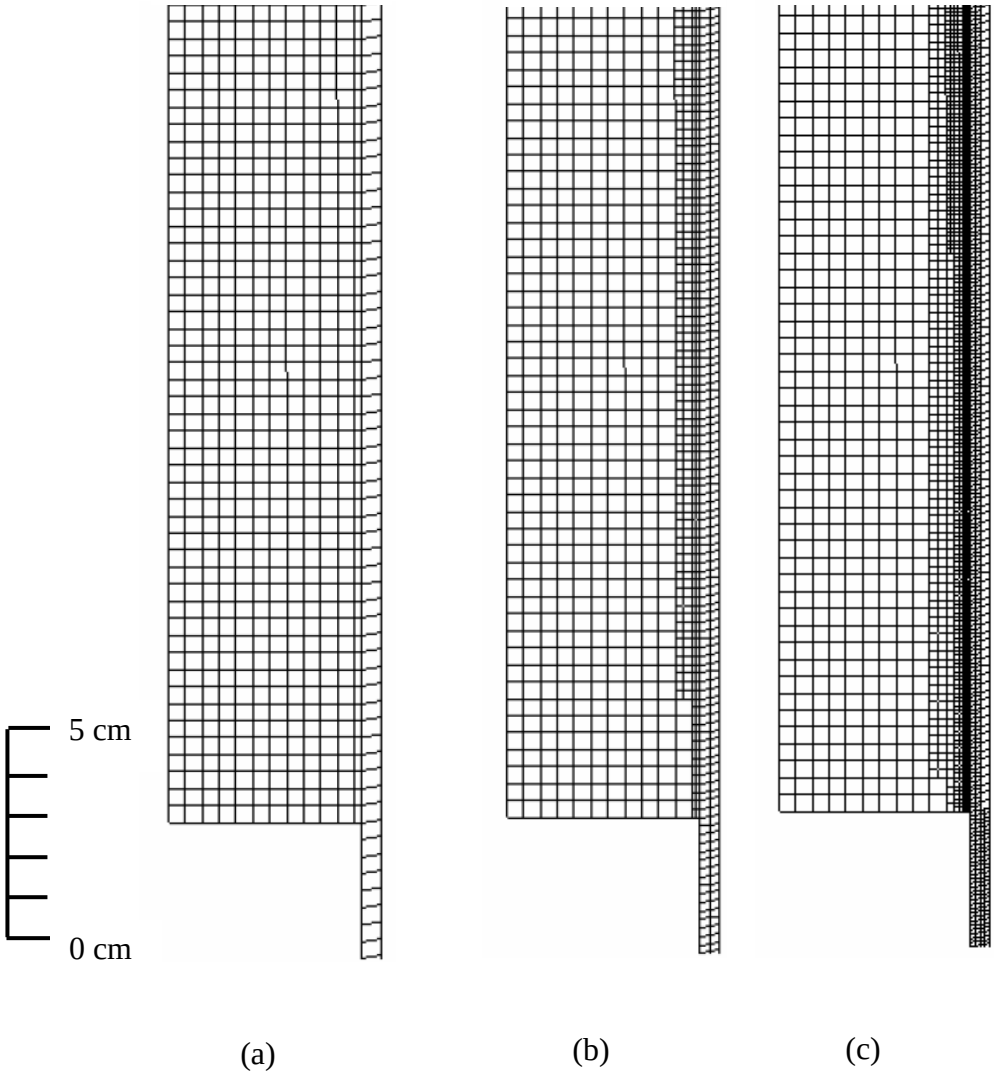

Figure 6.2 Variation of grid sensitivity for (a) original grid (6619 cells, 7252 nodes, 13870 faces), (b) adaptation 1 (10996 cells, 12258 nodes, 23253 faces), and (c) adaptation 2 (35137 cells, 37689 nodes, 72825 faces)

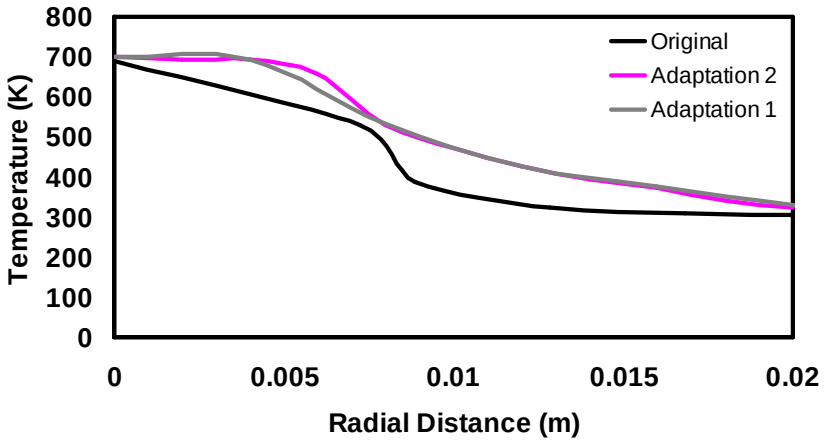

(a)

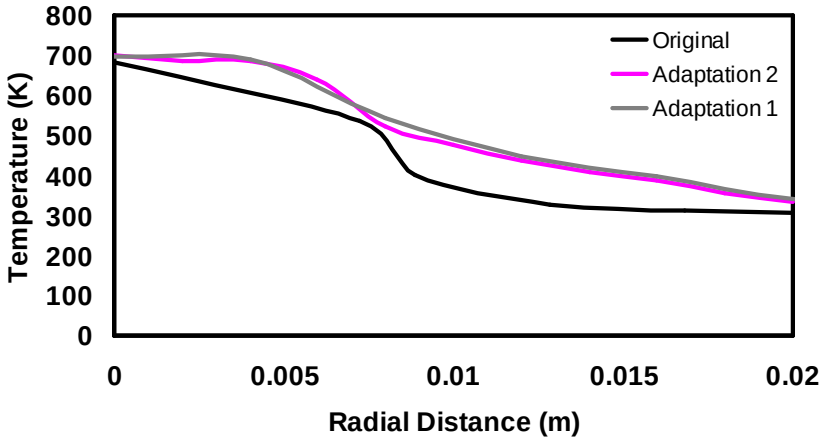

(b)

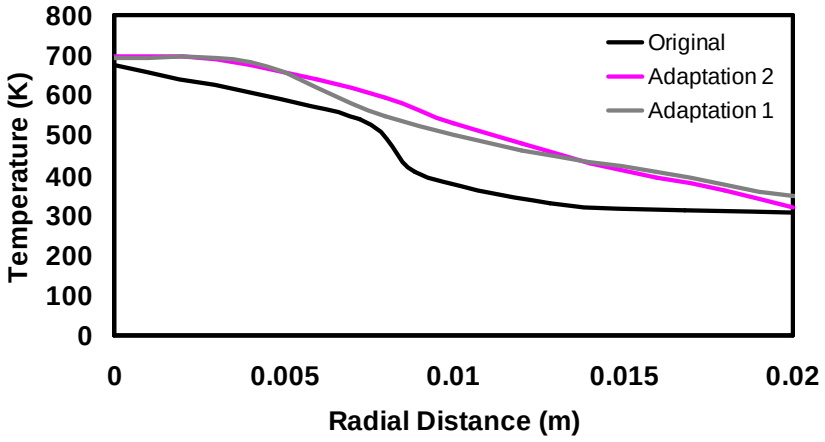

(c)

Figure 6.3 Temperature variation with grid size for the (a) near the burner at x = 0.024 m, (b) at x = 0.048 m, and (c) far from the burner at x = 0.071 m for n-dodecane/air

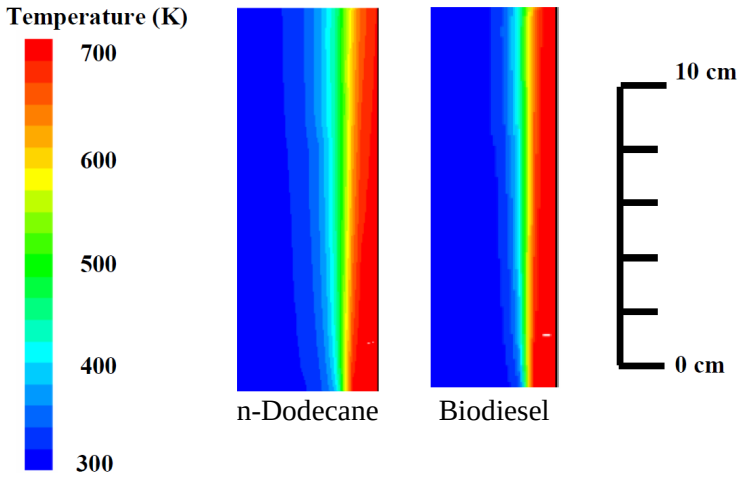

Figure 6.4 Temperature distributions for n-dodecane and biodiesel heated fuel/air jets in region of interest up to 15 cm above injector exit

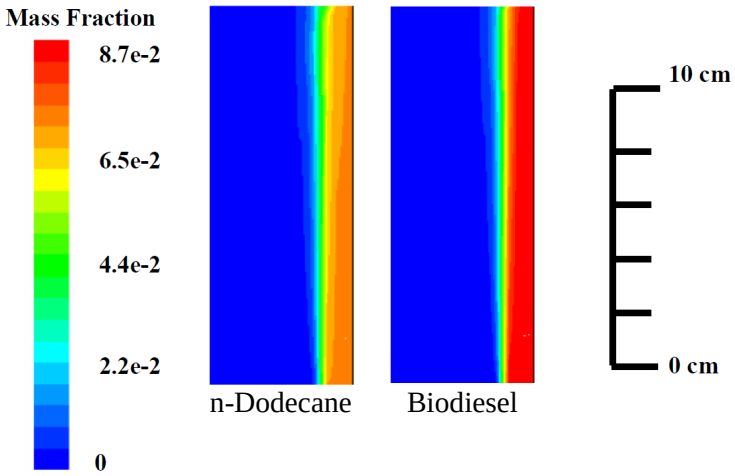

Figure 6.5 Mass fraction of n-dodecane and biodiesel in heated fuel/air jets in region of interest up to 15 cm above injector exit

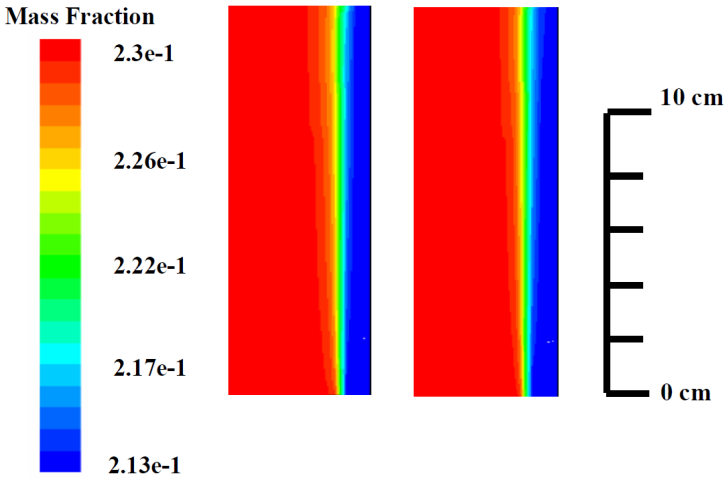

Figure 6.6 Mass fraction of O_2 in n-dodecane and biodiesel in heated fuel/air jets in region of interest up to 15 cm above injector exit

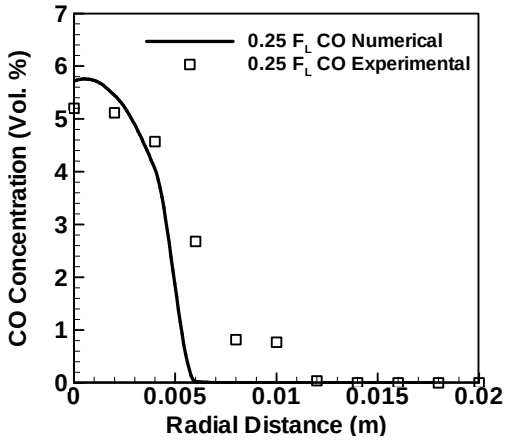

(a)

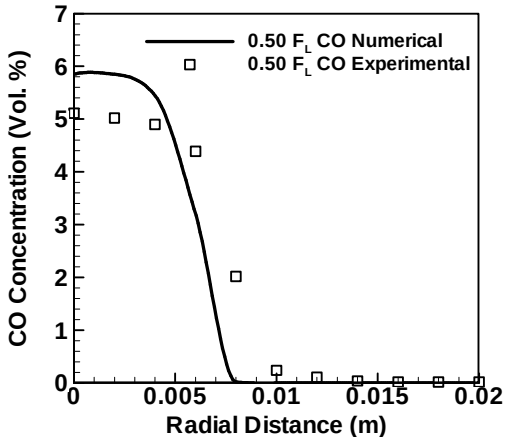

(b)

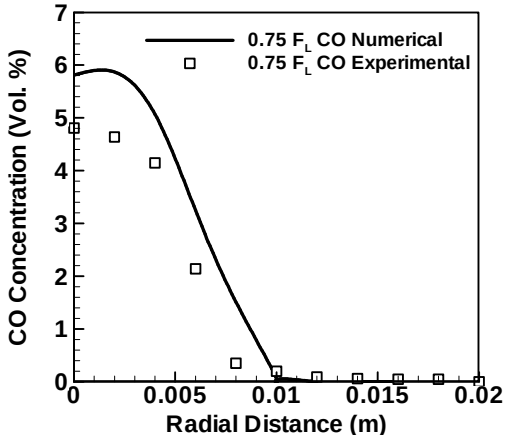

(c)

Figure 6.7 Carbon Monoxide concentration profiles for n – dodecane at (a) x = 0.02375 m, (b) x = 0.0475 m, and (c) 0.07125 m for equilibrium model

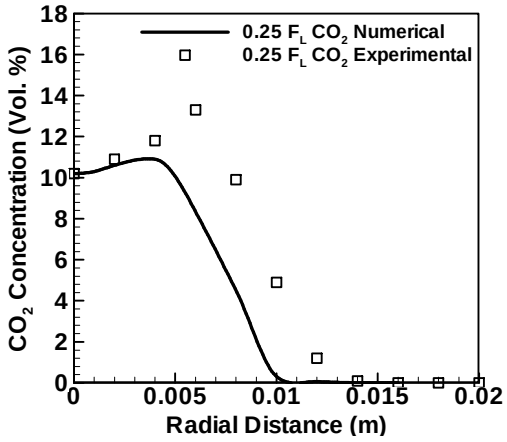

(a)

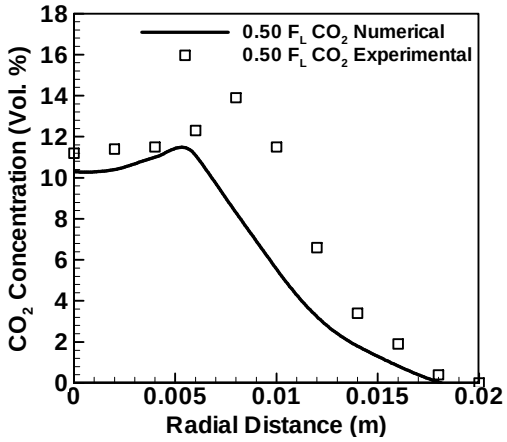

(b)

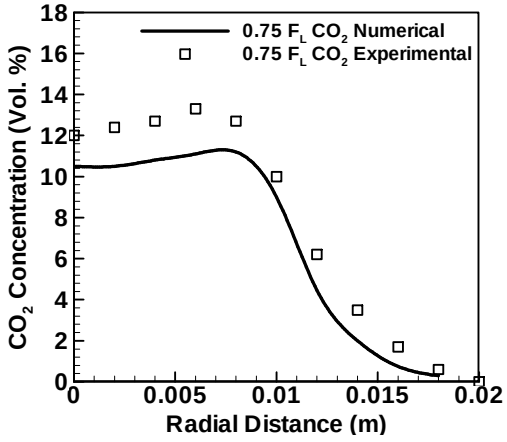

(c)

Figure 6.8 Carbon Dioxide concentration profiles for n – dodecane at (a) x = 0.02375 m, (b) x = 0.0475 m, and (c) 0.07125 m for equilibrium model

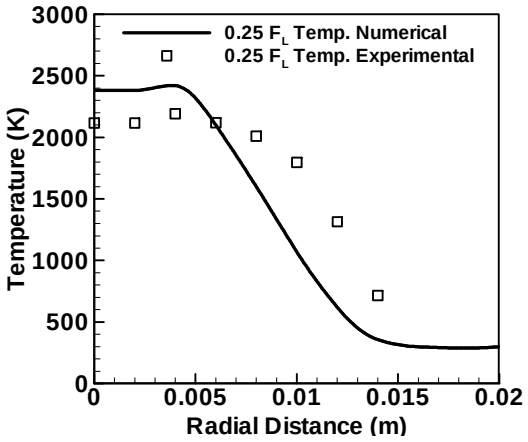

(a)

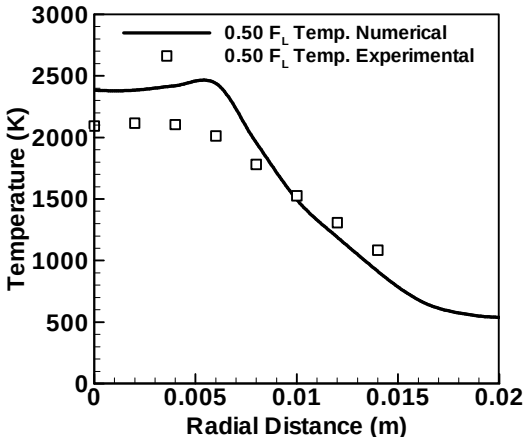

(b)

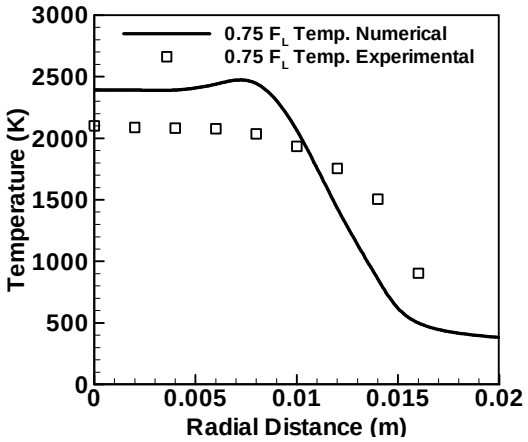

(c)

Figure 6.9 Temperature profiles for n – dodecane at (a) x = 0.02375 m, (b) x = 0.0475 m, and (c) 0.07125 m for equilibrium model

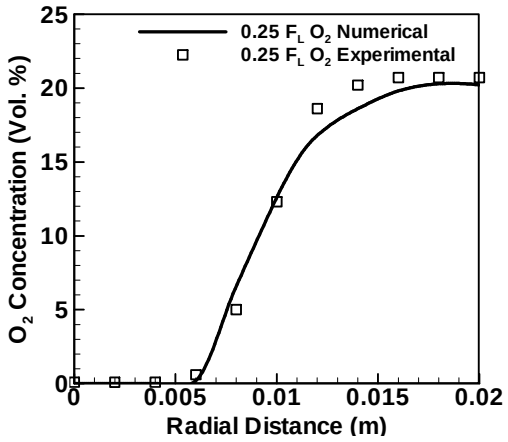

(a)

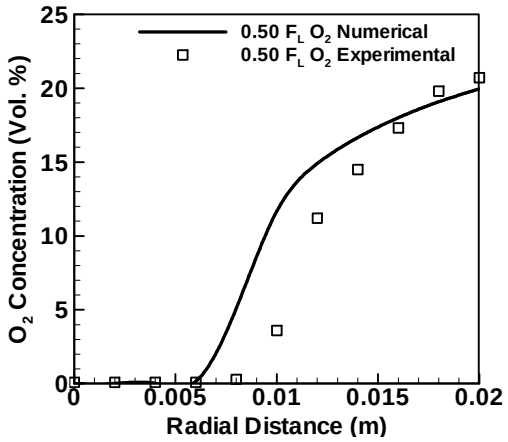

(b)

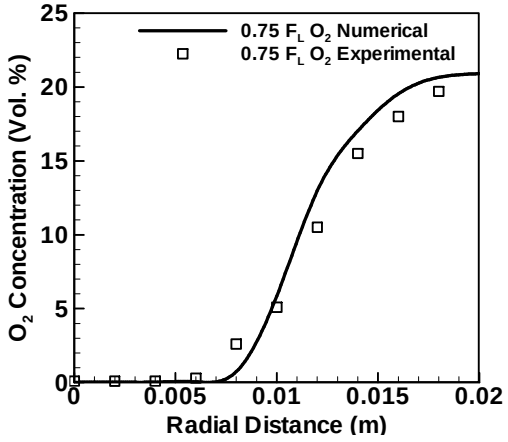

(c)

Figure 6.10 Oxygen concentration profiles for n – dodecane at (a) x = 0.02375 m, (b) x = 0.0475 m, and (c) 0.07125 m for equilibrium model

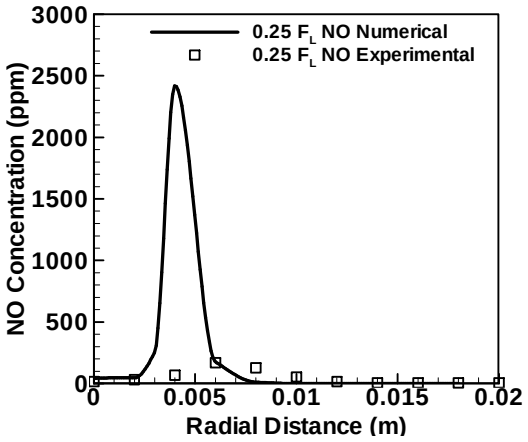

(a)

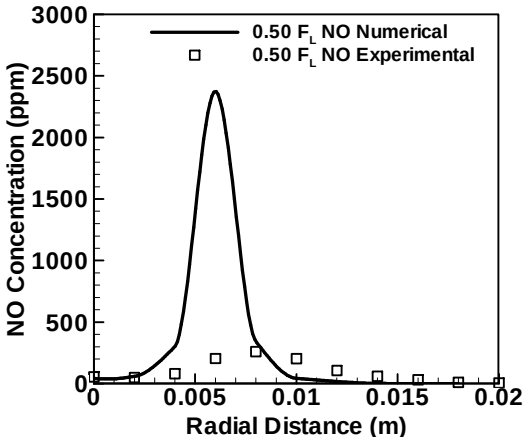

(b)

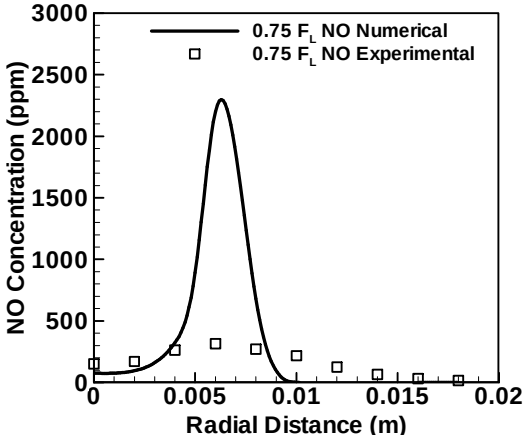

(c)

Figure 6.11 NO concentration profiles for n – dodecane at (a) x = 0.02375 m, (b) x = 0.0475 m, and (c) 0.07125 m for equilibrium model

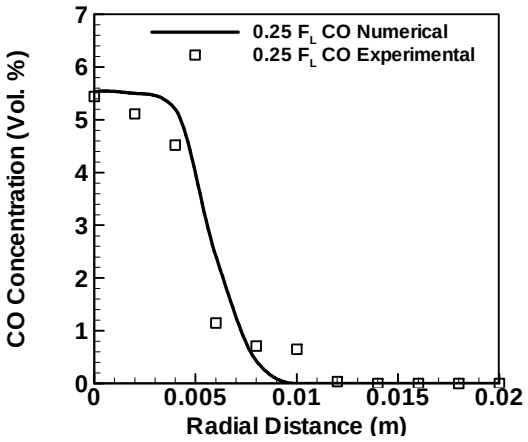

(a)

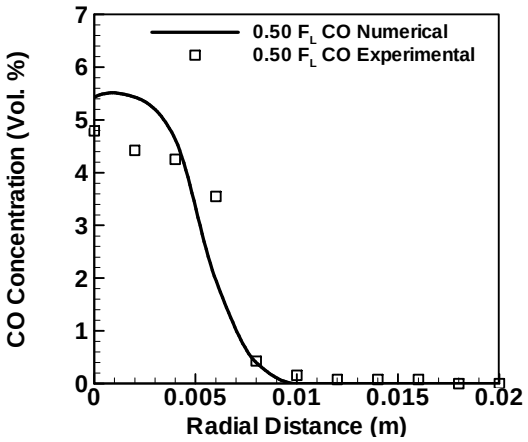

(b)

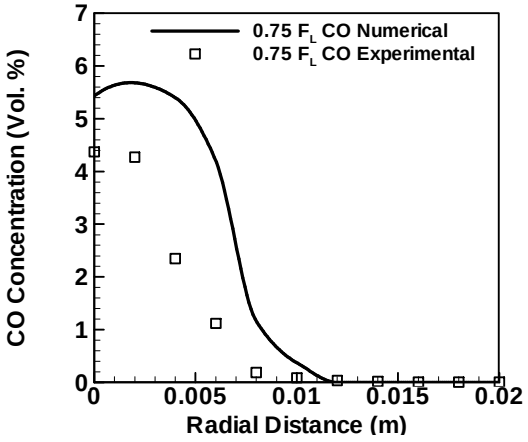

(c)

Figure 6.12 Carbon Monoxide concentration profiles for biodiesel at (a) x = 0.02375 m, (b) x = 0.0475 m, and (c) 0.07125 m for equilibrium model

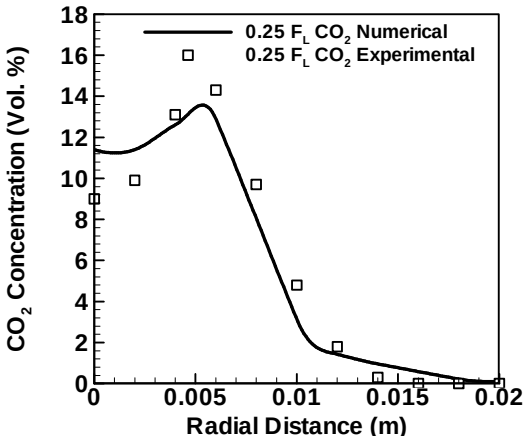

(a)

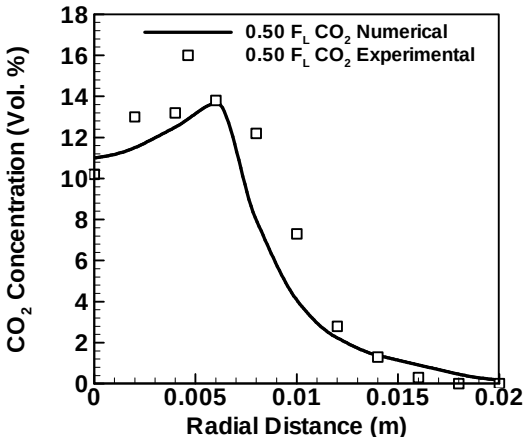

(b)

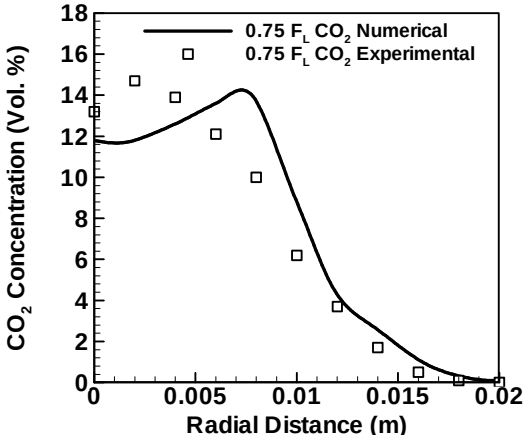

(c)

Figure 6.13 Carbon Dioxide concentration profiles for biodiesel at (a) x = 0.02375 m, (b) x = 0.0475 m, and (c) 0.07125 m for equilibrium model

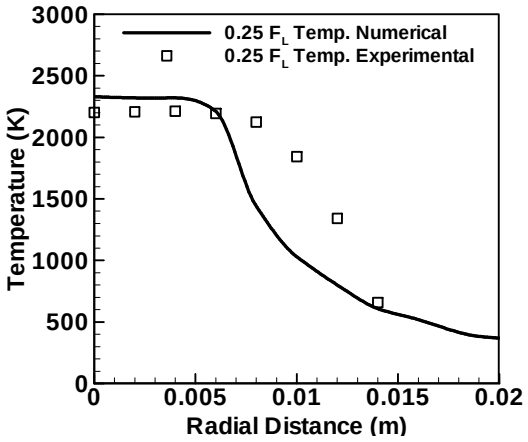

(a)

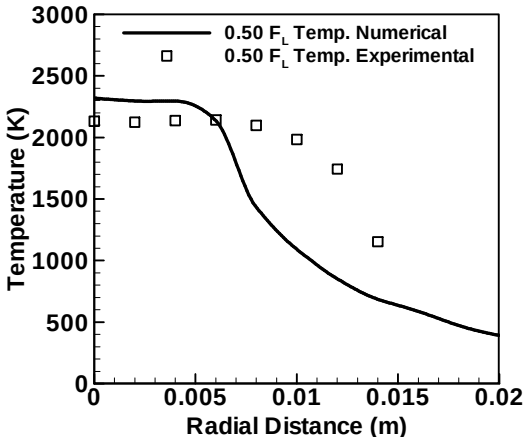

(b)

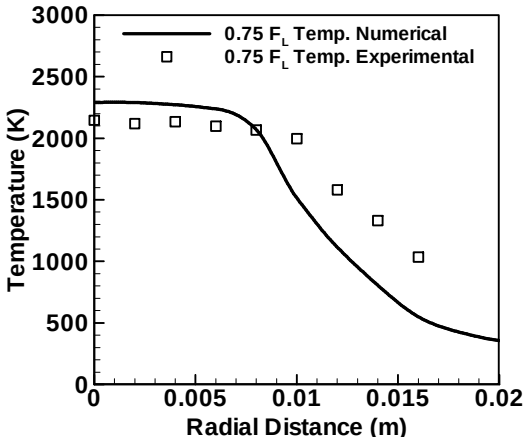

(c)

Figure 6.14 Temperature profiles for biodiesel at (a) x = 0.02375 m, (b) x = 0.0475 m, and (c) 0.07125 m for equilibrium model

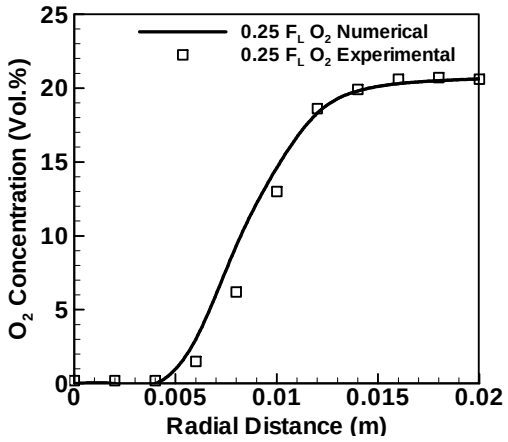

(a)

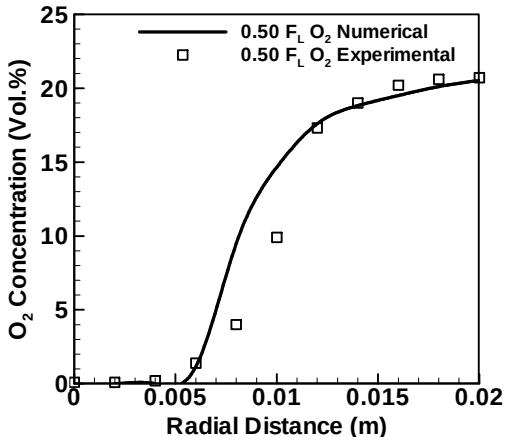

(b)

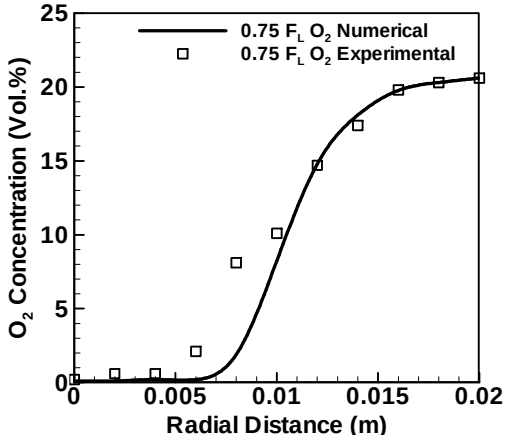

(c)

Figure 6.15 Oxygen concentration profiles for biodiesel at (a) x = 0.02375 m, (b) x = 0.0475 m, and (c) 0.07125 m for equilibrium model

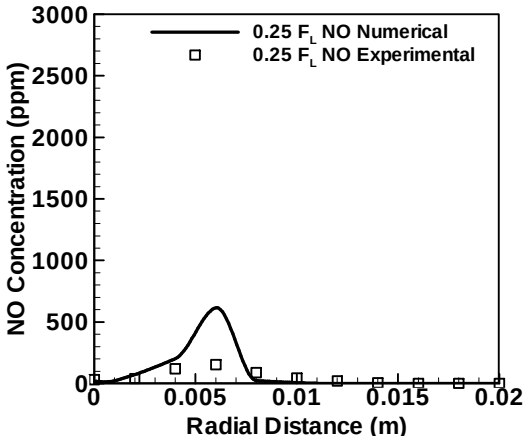

(a)

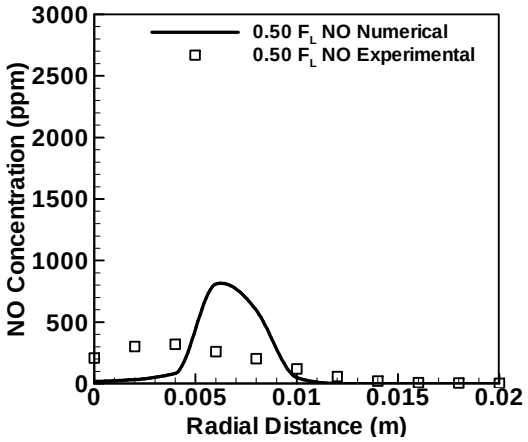

(b)

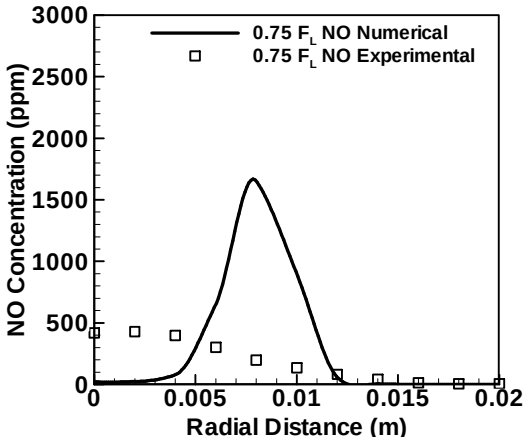

(c)

Figure 6.16 NO concentration profiles for biodiesel at (a) x = 0.02375 m, (b) x = 0.0475 m, and (c) 0.07125 m for equilibrium model

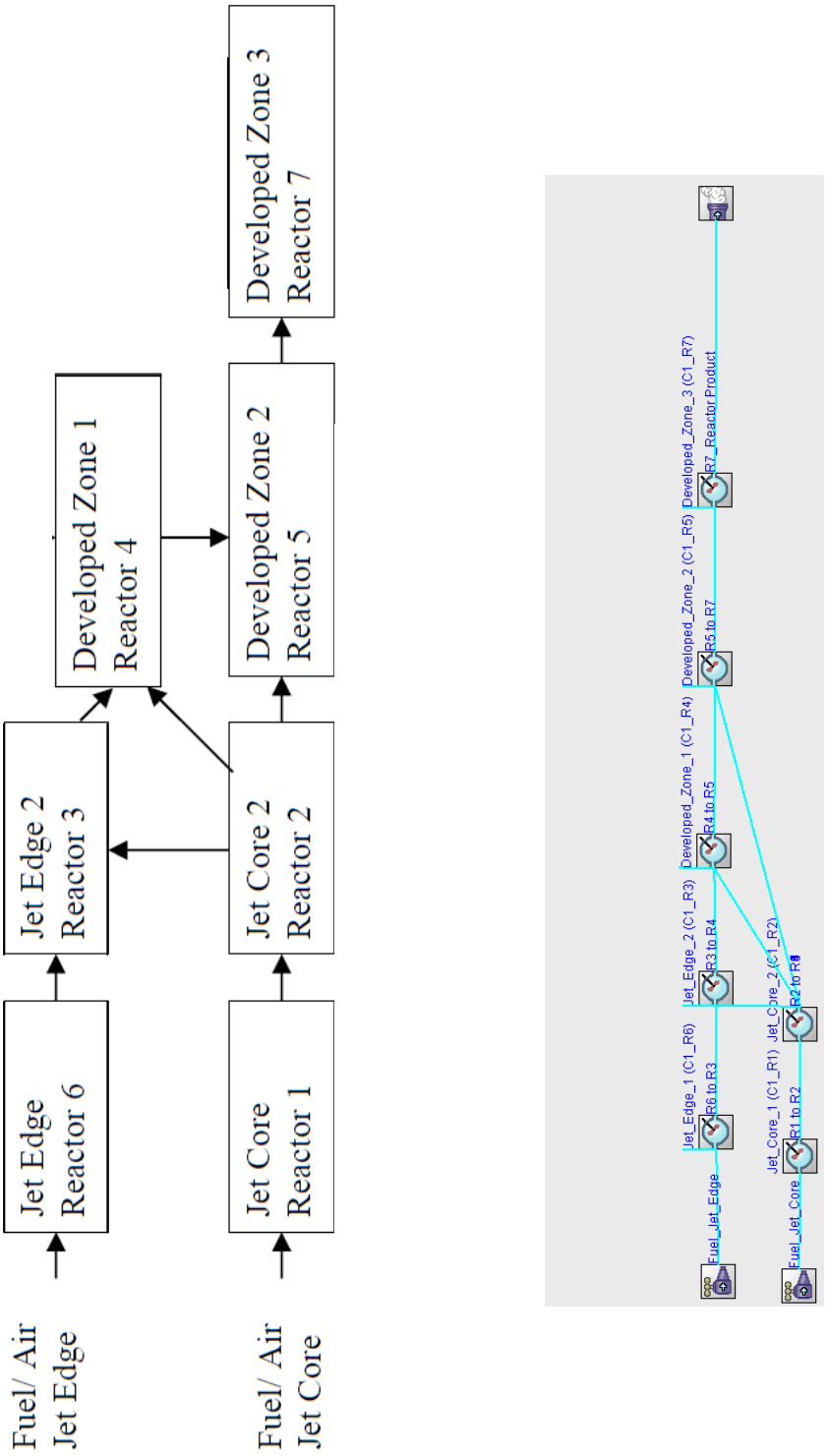

Figure 6.17 Jet reactor network schematic diagram and actual model in CHEMKIN used for non-equilibrium model

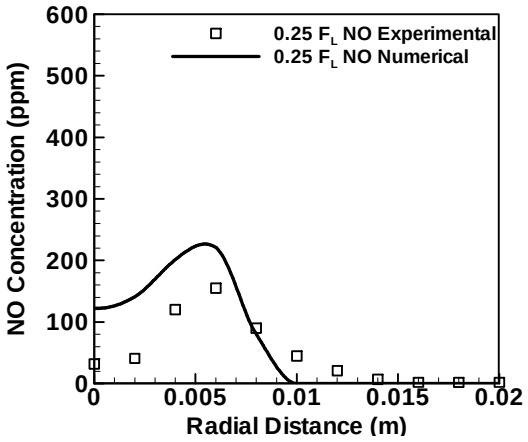

(a)

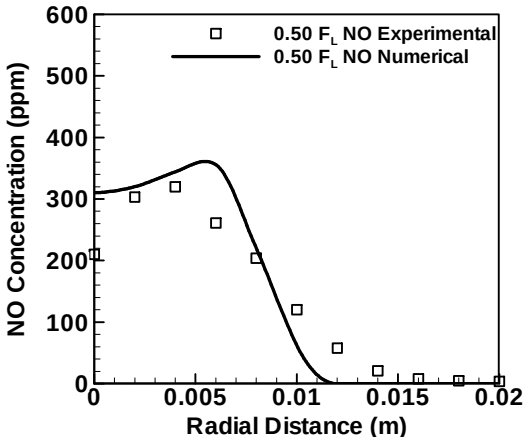

(b)

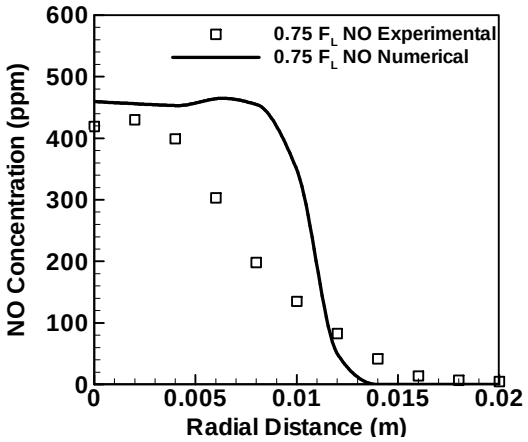

(c)

Figure 6.18 NO concentration profiles using non-equilibrium model for biodiesel at (a) x = 0.02375 m, (b) x = 0.0475 m, and (c) 0.07125 m

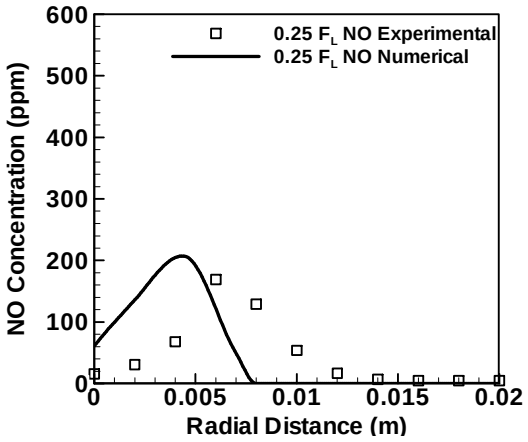

(a)

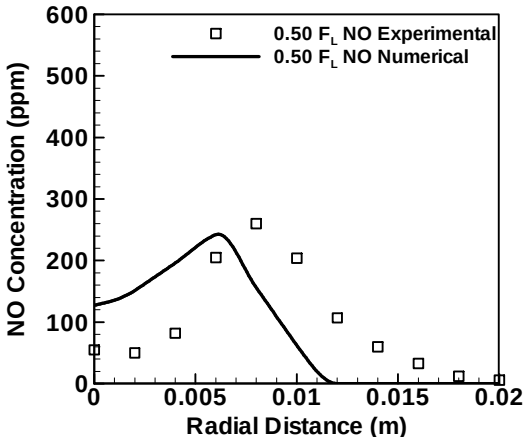

(b)

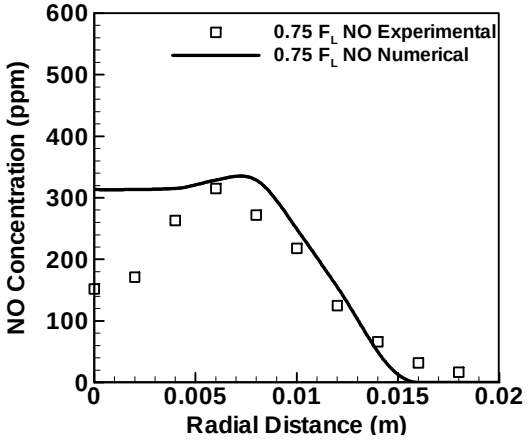

(c)

Figure 6.19 NO concentration profiles using non-equilibrium model for n-dodecane at (a) x = 0.02375 m, (b) x = 0.0475 m, and (c) 0.07125 m

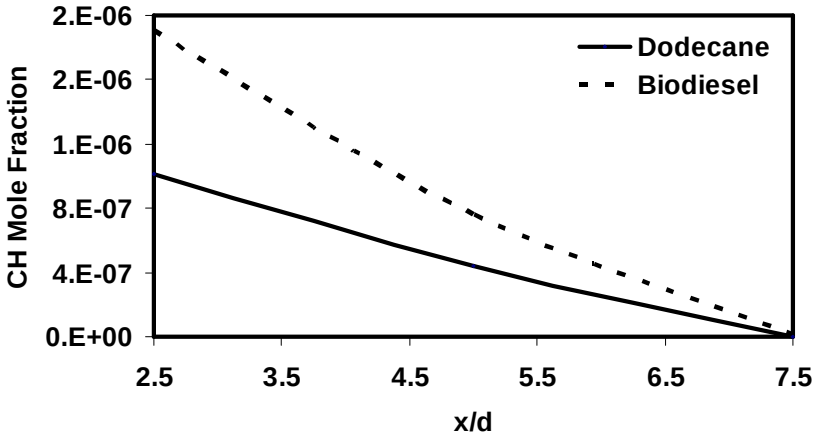

Figure 6.20 Predicted mole fraction of CH for both fuels at (a) x = 0.02375 m, (b) x = 0.0475 m, and (c) 0.07125 m

Chapter 7
Summary and Conclusions

7.1 Summary of Results

Increased energy consumption in the United States has led to a push for the development of new bio-derived fuels. This study was motivated by the need to test these fuels and provide quick feedback to fuel developers on the combustion characteristics. Therefore this dissertation presented 1) a technique to characterize the combustion properties of liquid fuels based on the chemistry of the fuel alone and 2) an investigation on the cause for NO_x increase for biodiesel when compared to conventional diesel in internal combustion engines.

For the first part of the study the development of a method for the rapid characterization of combustion properties, such as emission index and flame radiation, that required only small amounts of a liquid fuel was presented. The technique provided a way of comparing existing and new fuels such as biodiesel. Burner conditions were selected to make flame properties sensitive primarily to fuel chemistry. The technique was validated through a comparison of measured radiative heat release fraction and pollutant (NO and CO) emission indices of several fuels in laminar flames available in literature. It was seen that the relative changes compared well with the values documented during engine testing and other combustion configurations.

After establishing the validity of the technique, the second part of the dissertation used this same experimental setup and investigated the cause for the increase in NO_x produced in compression ignition engines by biodiesel when

compared to diesel. For this purpose the equivalence ratio and iodine number were varied and their effect on the formation of NO_x studied for the four different fuels: canola methyl ester, soy methyl ester, diesel, and normal dodecane fuels. Measurements of intermediate species, flame temperatures, soot volume fraction, and global emissions were done to determine the cause. Results indicated that at the most fuel rich conditions, similar to operating conditions found in a compression ignition engine, the Fenimore mechanism was responsible.

7.1.1 Development of Experimental Technique

In order to characterize liquid fuels on a chemical basis alone the following criteria needed to be met: 1) laminar flow needed to be maintained in order to avoid the effects of flow parameters, 2) Fuel needed to be pre-vaporized to avoid the atomization and vaporization effects, and 3) The appropriate burner needed to be selected.

The final version of the experimental technique included the use of a tubular burner (yielding repeatable results and easy to manufacture), temperature controlled heating tapes (to pre-vaporize the fuel), syringe pump (for steady liquid fuel flow supply), and an external ignition source (to avoid pyrolysis effects when burning with other fuels). Findings showed that petroleum-derived diesel produced a higher radiative heat fraction than biodiesel. The biodiesel flames also had lower emission index of CO and higher emission index of NO compared to those of the diesel flame. Overall, the present technique was determined to be valid tool in the determination of NO and CO emission potentials of new fuels and could obtain quick feedback to fuel developers, since the entire experiment was completed within twenty minutes per fuel. Moreover, the relative ease with which the current setup was operated and the small amounts of fuel used made the present method a valuable predictive tool of fuel combustion characteristics.

7.1.2 Primary Mechanism of Formation of NO

During the experimental development process global flame results showed that NO emission was higher in flames of biodiesel compared to diesel. In general, previous research onto why this occurred had been a topic based on the assumption that temperatures were higher in diesel engines that ran on biodiesel, therefore, resulting in more NO through the Zeldovich mechanism. In the case of engine studies, however, the problem had not been decoupled into chemical and physical mechanisms involved in the combustion of diesel/biodiesel thus the direct cause not isolated. Since the developed experimental setup described in this dissertation obtained results based on the chemistry of the fuel alone, isolating the primary formation mechanism was possible with the current technique.

Initially global measurements from the flame were taken at one set of air and fuel flow rates, and later expanded to include various amounts of air flow rates corresponding to different equivalence ratios. Differences in the amount of NO produced varied as the amount of air supplied to the flame changed. However, it was observed that the biodiesel fuel produced more NO than diesel at all conditions. In flame pollutant species concentrations were taken to observe locations of peak pollutant concentration. At the lowest equivalence ratio tested of 1.2, more NO was observed at the location furthest from the burner indicating that residence time was a primary factor in the development of the pollutant. At higher equivalence ratios, peak NO was found very near the burner exit indicating the dominance of another mechanism. Further tests were needed to identify the

dominant mechanism in these flames, therefore, intermediate radicals associated with each mechanism were captured and temperature distributions recorded.

Temperature distributions showed that for most conditions differences between flames of CME, SME, and diesel were not significant and therefore the amount of NO produced not necessarily due to higher temperatures. This was later confirmed by observing the intermediate radical populations (CH, OH) which showed that OH concentrations, a primary contributor to NO formation by the Zeldovich mechanism, were greatest at the lowest equivalence ratio of 1.2 for all fuels. This was also in agreement with the numerical model for these fuels which predicted similar results. Additionally, CH concentrations, a primary contributor to NO formation by the prompt mechanism, were found to increase from the equivalence ratio of 2 to 7 and were found to be higher in fuels with higher iodine numbers such as SME and CME. This correlated with more NO emission being produced for the higher iodine number fuels in areas of high CH radical concentration. This indicated the dominance of NO formation through the prompt mechanism for both diesel and biodiesel fuels at the fuel rich conditions from 2 to 7.

7.2 Conclusions

From the present study the following conclusions can be made:

- Currently a simple and quick method to compare the particulate and pollutant emissions for different liquid fuels (e.g. diesel/biodiesel), particularly when the liquids are available in small quantities does not exist.
- The developed technique in this dissertation addresses the above deficiency. It allows a comparison of pollutant emission potential of hydrocarbon and biofuels, that can be assessed quickly (20 min), with small amounts of fuel (50 ml).
- This technique can assist fuel researchers in the development of new fuels. Since bench scale experiments yield small amounts of fuel they cannot be run in an engine which requires fuel on the order of liters. Additionally, this technique can provide quick feedback on the combustion properties of the fuel thus allowing the developers opportunity to modify the molecular structure and produce improved products.
- This burner technique successfully predicts the sooting tendency and emission potential of different fuels for diesel engine applications. This was validated by comparing results obtained from this technique to those in literature on diesel engine combustion. As has been observed in diesel engines, global and in-flame NO pollutant species concentrations were found to be higher for CME and SME biodiesel compared to diesel fuel while using the developed experimental setup.

- The study showed that at lower equivalence ratios NO production was primarily due to the Zeldovich mechanism for both diesel and biodiesel.
- A numerical model simulating the combustion of these fuels also showed that NO production was primarily due to the Zeldovich mechanism at the lowest equivalence ratio (1.2).
- At higher equivalence ratios (2 to 7), similar to those predicted to exist in diesel engines; NO production was primarily due to the Fenimore mechanism for both diesel and biodiesel. At these equivalence ratios it was observed that biodiesel produced significantly more NO than diesel for the in-flame and global emissions.
- NO pollutant was observed to correlate with iodine number. Fuels with lower iodine number values (diesel and methyl stearate) produced less NO while fuels with higher iodine numbers (SME and CME) produced the highest. The double bonds present in unsaturated fuels, such as SME, facilitated the production of more CH radical concentrations. Hence this led to the production of more NO by the Fenimore mechanism.

7.3 Practical Implications

The technique and experimental setup described in this dissertation were applied to the testing of the combustion characteristics of several petroleum based fuels and biodiesel. Currently many fuels are compared using different engines running at different load settings. Since most combustors incorporate factors such as: high pressure, droplet evaporation, turbulence, and injection timing into the combustion process this can significantly effect engine outputs (emissions, particulate matter, performance) and makes it difficult to compare outputs of different engines. Burning fuel vapor in a controlled laminar flame environment as described in this study removes most physical variables that are encountered in more complex combustors. Use of this technique would lead to a more uniform comparison of the combustion characteristics of fuels attributable to their chemical structure and result in production of better fuels and methods to control their contribution to environmental pollution.

7.4 Recommendations for Further Study

This dissertation could be extended to investigate the following:

Experimental Work:

1. As described in chapter 5 section 5 of this dissertation, it would be desirable to investigate the effect of droplet versus fuel vapor combustion and its effect on the production of NO_x for diesel and biodiesel.

2. The primary focus of this dissertation was on the application of petroleum based and biofuels to internal combustion engines. As the use and application of biofuels grows and it is used in more combustors such as gas turbines (Habib, 2008) combustion properties at these conditions are also required. Thus a study investigating the combustion of these fuels at lower (less than stoichiometric) equivalence ratios would further improve the understanding of these fuels.

3. The types of fuels tested could also be expanded to include gasoline/ethanol, biodiesel/ethanol, or biodiesel/methanol flames as ethanol and gasoline also represent a large population of the automotive industry in the US.

4. This study investigated the effect of iodine number on the NO pollutant. The range of iodine numbers could be extended in the future to better see the correlation between the two properties.

Numerical Work:

1. The current model neglected effects of soot formation and radiative losses from the flame. Numerical simulations can be performed on the estimation of soot precursors, soot concentrations, and the effect of radiative losses for biofuel flames for fuel rich and non-premixed flames.

References

Adams, J., Cassarino, C., Lindstrom, J., Spangler, L., Binder, M., and Holcomb, F., 2004, "Canola Oil Fuel Cell Demonstration Volume I – Literature Review of Current Reformer Technologies," **US Army Corps of Engineers**, ERDC/CERL SR-04-24, pg. 9.

Agency for Toxic Substances and Disease Registry (ATSDR), 1995, "Toxicological Profile for Fuel Oils," **U.S. Department of Health and Human Services**, Public Health Service.

Annamalai, K., and Puri, I., 2007, **Combustion Science and Engineering**, CRC Series in Computational Mechanics and Applied Analysis, CRC Press, New York, New York, pg. 988.

Baird, B., and Gollahalli, S., 2006, "Effects of Temperature and Hydroxyl Radical Concentration Distribution on Emissions of Partially Premixed Flames from Elliptical Burners," **ASME Turbo Expo**, Barcelona, Spain, GT2006-90065.

Barajas, P., 2009, **Combustion Characteristics of Biodiesel Fuel with Porous Media Burners**, Master's Thesis, University of Oklahoma, Norman, Oklahoma.

Baroncini, C., Filippo, P., Latini, G., and Pacetti, M., 1981, "Organic Liquid Thermal Conductivity: A Prediction Method in the Reduced Temperature Range 0.3 to 0.8," **International Journal of Thermophysics**, Vol. 2(1), pp. 21-38.

Bryce, D., Ladommatos, N., and Zhao, H., 2000, "Quantitative Investigation of Soot Distribution by Laser-Induced Incandescence," **Applied Optics**, Vol. 39(27), pp. 5012-5022.

Chevron Products Company, 1998, "Diesel Fuels Technical Review," **Report No. FTR-2**.

Chinthamony, S., 2005, **Structure of Gas Jet Diffusion Flames from an Elliptic Burner in an Elliptic Co-Flow**, Master's Thesis, University of Oklahoma, Norman, Oklahoma.

Choudhuri, A., 2000, **An Experimental and Numerical Investigation on Hydrogen-Hydrocarbon Composite Fuel Combustion**, Ph. D. Dissertation, University of Oklahoma, Norman, Oklahoma.

Demory, R., Crua, C., Gold, M., and Heikal, M., 2006, "Measuring and Processing In-Cylinder Distributions of NO and OH Obtained by Laser – Induced Fluorescence in a Diesel Rapid Compression Machine," **13th International Symposium on Applications of Laser Techniques to Fluid Mechanics**, Lisbon, Portugal, Paper No. 1092, pp.1-12.

Dooley, S., Curran, H.J., and Simmie, J.M., 2008, "Autoignition Measurements and a Validated Kinetic Model for the Biodiesel Surrogate, Methyl Butanoate," **Combustion and Flame**, Vol. 153, pp. 2-32.

Dorado, M., Ballesteros, E., Arnal, J., Gomez, J., and Lopez, F., 2003, "Exhaust Emissions from a Diesel Engine Fueled with Transesterfied Waste Olive Oil," **Fuel**, Vol. 82, pp. 1311-1315.

Douwel, R., Donkerbroek, A., Vliet, A., Boot, M., Somers, L., Baert, R., Dam, N., and Meulen, J., 2009, "Soot and Chemiluminescence in Diesel Combustion of Bio-derived, Oxygenated and Reference Fuels," **Proceedings of the Combustion Institute**, Vol. 32, The Combustion Institute, PA, pp. 1-17.

Durbin, T., Collins, J., Norbeck, J., and Smith, M., 2000, "Effects of Biodiesel, Biodiesel Blends, and a Synthetic Diesel on Emissions from Light Heavy-Duty Diesel Vehicles," **Environmental Science and Technology**, Vol. 34 (3), pp. 349-355.

Erazo, J., 2008, **Effects of Droplet Size and Fuel Iodine Number on Biodiesel Spray Flames**, Master's Thesis, University of Oklahoma, Norman, Oklahoma.

Farrell, J., Cernansky, N., Dryer, F., Friend, D., Hergart, C., Law, C., McDavid, R., Mueller, C., Patel, A., and Pitsch, H., "Development of an Experimental Database and Kinetic Models for Surrogate Diesel Fuels," **SAE Paper 2007-01-0201**, pp. 1-27.

Fayoux, A., Dupre, S., Scouflaire, P., Houille, S., Pajot, O., and Rolon, J., 2004, "OH and HCHO LIF Measurements in a HCCI Engine," **12th International Symposium of Applications of Laser Techniques**, Portugal, pp. 1-11.

Fenimore, C.P., 1970, "Formation of Nitric Oxide in Premixed Hydrocarbon Flames," **Thirteenth Symposium on Combustion**, The Combustion Institute, PA, pp. 373-380.

Fernando, S., Hall, C., and Jha, S., 2006, "NO_x Reduction from Biodiesel Fuels," **Energy and Fuels**, Vol. 20, pp. 376-382.

Fisher, E.M., Pitz, W.J., Curran, H.J., and Westbrook, C.K., 2000, "Detailed Chemical Kinetic Mechanisms for Combustion of Oxygenated Fuels," **Proceedings of the Combustion Institute**, Vol. 28, The Combustion Institute, PA, pp. 1579-1586.

Flynn, P., Durrett, R., Hunter, G., Loye, A., Akinyemi, O., Dec, J., and Westbrook, C., 1999, "Diesel Combustion: An Integrated View Combining Laser Diagnostics, Chemical Kinetics, and Empirical Validation," **SAE Paper 1999-01-0509**, pp. 1-14.

Gilliland, E.R., 1934, "Diffusion Coefficients in Gaseous Systems," **Journal of Industrial and Engineering Chemistry**, Vol. 26(6), pp. 681-685.

Graboski, M., McCormick, R., and Alleman, T., 2003, "The Effect of Biodiesel Composition on Engine Emissions from a DDC Series 60 Diesel Engine," **National Renewable Energy Laboratory**, Technical Report NREL/SR-510-31461.

Habib, Z., **Effects of Biodiesel on the Performance and Emissions Characteristics of a Small Scale Gas Turbine**, Master's Thesis, University of Oklahoma, Norman, Oklahoma.

Haruiharan, P., **An Experimental Study on Elliptic Turbulent Partially Premixed Propane / Hydrogen / Air Flames with and without Co-Flow Air**, Master's Thesis, University of Oklahoma, Norman, OK.

Haudiquert M., Cessou, A., Stepowski, D., and Coppalle, A., 1997, "OH and Soot Concentration Measurements in a High-Temperature Laminar Diffusion Flame," **Combustion and Flame**, Vol. 111, pp. 338-349.

Herbinet, O., Pitz, W., and Westbrook, C., 2008, "Detailed Chemical Kinetic Oxidation Mechanism for a Biodiesel Surrogate," **Combustion and Flame**, Vol. 154, pp. 507-528.

Hura, H., and Glassman, I., 1987, "Fuel Oxygen Effects on Soot Formation in Counterflow Diffusion Flames," **Combustion Science and Technology**, Vol. 53, pp. 1-21.

Iverach, D., Basden, K., and N. Kirov, 1972, "Formation of Nitric Oxide in Fuel Lean and Fuel Rich Flames," **Fourteenth Symposium on Combustion:** The Combustion Institute, Pittsburgh, PA, pp. 77-84.

Jassma, D., and Borman, G., 1980, "Measurements of Oxides of Nitrogen Produced by Liquid Fuel Diffusion Flames," **Combustion Science and Technology**, Vol. 22, pp. 131-141.

Jha, S.K., Fernando, S., and Filip To, S.D., 2008, “Flame Temperature Analysis of Biodiesel Blends and Components,” **Fuel**, Vol. 87, pp. 1982-1988.

Kanury, A., 1975, **Introduction to Combustion Phenomena**, Volume 2, Combustion Science and Technology Book Series, Gordon and Breach Science Publishers, Langhorne, Pennsylvania, pp. 54, 130.

Kirby, B., and Hanson, R., 2000, “Imaging of CO, CO_2 Using Infrared Planar Laser-Induced Fluorescence,” **Proceedings of the Combustion Institute**, Vol. 28, The Combustion Institute, PA, pp. 253-259.

Kitamura, T., Ito, T., Senda, J., and Fujimoto, H., 2001, “Detailed Chemical Kinetic Modeling of Diesel Spray Combustion with Oxygenated Fuels,” **SAE Paper 2001-1262**, pp.1-20.

Koseki, H., 1989, “Combustion Properties of Large Liquid Pool Fires,” **Fire Technology**, Vol. 25(3), pp. 241-255.

Krisnangkura, K., 1991, “Estimation of Heat of Combustion of Triglycerides and Fatty Acid Methyl Esters,” **Journal of the American Oil Chemists Society**, Vol. 68 (1), pp. 56-58.

Ladommatos, N., Rubenstein, P., Harrison, K., Xiao, Z., and Zhao, H., 1997, “The Effect of Aromatic Hydrocarbons on Soot Formation in Laminar Diffusion Flames and in a Diesel Engine,” **Journal of the Institute of Energy**, Vol. 70, pp. 84-94.

Lang, X., Dalai, A., Bakhshi, N., Reaney, M., and Hertz, P., 2001, “Preparation and Characterization of Bio-Diesels from Various Bio-Oils,” **Bioresource Technology**, Vol. 80, pp. 53-62.

Lin C., and Lin, H., 2007, “Engine Performance and Emission Characteristics of Three-Phase Emulsion of Biodiesel Produced by Preoxidation,” **Fuel Processing Technology**, Vol. 88, pp. 35-41.

Love, N., Periasamy, C., Gollahalli, S.R., and Choudhuri, A., 2006, "Laminar Burning Velocity Measurements of Synthetic Gas Premixed Flames Near Extinction Conditions," **4th International Energy Conversion Engineering Conference and Exhibit**, San Diego, CA, AIAA-2006-4122.

Love, N., Parthasarathy, R.N., and Gollahalli, S.R., 2007, “A Method for the Rapid Characterization of Combustion Properties of Liquid Fuels Using a Tubular Burner,” **ASME International Mechanical Engineering Congress and Exposition,** Seattle, WA, IMECE2007-42112.

Love, N., Parthasarathy, R.N., and Gollahalli, S.R., 2009, "Effects of Equivalence Ratio on Temperature and OH Radical Concentration in Laminar Premixed Biofuel and Diesel Vapor Flames,"**47th AIAA Aerospace Sciences Meeting and Exhibit,** Orlando, FL, AIAA-2009-829.

Love, N., Parthasarathy, R., and Gollahalli, S., 2009, "Rapid Characterization of Radiation and Pollutant Emissions of Biodiesel and Hydrocarbon Liquid Fuels," **Journal of Energy Resources Technology**, Vol. 131, pp. 012202-1 – 012202-9.

Ma, M., and Hanna, A., 1999, "Biodiesel Production: A Review," **Bioresource Technology**, Vol. 70, pp. 1-15.

Maxwell, J.B., 1950, **Data Book on Hydrocarbons Application to Process Engineering**, 9th Printing, Robert E. Krieger Publishing Company, Malabar, FL, pg. 175.

McCormick, R., Graboski, M., Alleman, T., and Herring, A., 2001, "Impact of Biodiesel Source Material and Chemical Structure on Emissions of Criteria Pollutants from a Heavy-Duty Engine," **Environmental Science and Technology**, Vol. 35, pp. 1742-1747.

McEnally, C., and Pfefferle, L., 2007, "Improved Sooting Tendency Measurements for Aromatic Hydrocarbons and Their Implications for Naphthalene Formation Pathways," **Combustion and Flame**, Vol. 148, pp. 210-222.

Metcalfe, W., Dooley S., Curran, H., Simmie, J., El-Nahas, A., and Navarro, M., 2007, "Experimental and Modeling Study of $C_5H_{10}O_2$ Ethyl and Methyl Esters," **Journal of Physical Chemistry**, Vol. 111, pp. 4001-4014.

Nakagawa, H., Endo, H., Deguchi Y., Noda, M., Oikawa, H., and Shimada, T., 1997, "NO Measurement in Diesel Spray Flame Using Laser Induced Fluorescence," **SAE Paper 970874**, pp.1349-1358.

Olikara, C., and Borman, G.L., 1975, "A Computer Program for Calculating Properties of Equilibrium Combustion Products with Some Applications to I.C. Engines," **SAE Paper 750468**.

Perez, C., Walton, S., and Wooldridge, M., 2007, "An Experimental Investigation of the Effects of Functional Group Structure on Particulate Matter and NO Emissions of Oxygenated Hydrocarbons," **2007 ASME International Mechanical Engineering Congress and Exposition**, Seattle, WA, IMECE2007-41947.

Pickett, L., and Siebers, D., 2004, "Soot in Diesel Fuel Jets: Effects of Ambient Temperature, Ambient Density and Injection Pressure," **Combustion and Flame**, Vol. 138, pp. 114-135.

Pinto, A., Guarieiro, L., Renzende, M., Ribeiro, N., Torres, E., Lopes, W., Pereira, P., and Andrade, A., 2005, "Biodiesel: An Overview," **Journal of Brazilian Chemical Society**, Vol. 16 **(**6B), pp. 1313-1330.

Pulkrabek, W., 2004, **Engineering Fundamentals of the Internal Combustion Engine**, 2nd Edition, Pearson Prentice-Hall, Upper Saddle River, New Jersey.

Santana, R., Do P., Santikunaporn, M., Alvarez, W., Taylor, J., Sughrue, E., and Resasco, D., 2006, "Evaluation of Different Reaction Strategies for the Improvement of Cetane Number in Diesel Fuels," **Fuel**, Vol. 85, pp. 643-656.

Scholl, K., and Sorenson, S., 1993, "Combustion of Soybean Oil Methyl Ester in a Direct Injection Diesel Engine," **SAE Paper 930936**, pp. 221-223.

Schwartz, R., and White, J., 1996, "Flare Radiation Prediction: A Critical Review," American Institute of Chemical Engineers, **30th Annual Loss Prevention Symposium**, American Institute of Chemical Engineers, Paper No. 12a.

Seiser, R., Pitsch, H., Seshadri, K., Pitz, W., and Curran, H., "Extinction and Autoignition of n-Heptane in Counterflow Configuration," **Proceedings of the Combustion Institute**, Vol. 28, The Combustion Institute, PA, pp. 2029-2037.

Strong, C., Erickson, C., and Shukla, D., 2004, "Evaluation of Bio-Diesel Fuel: Literature Review," **Montana Department of Transportation Report FHWA/MT-04-001/8117-20**, Montana State University.

Turns, S., 2000, **An Introduction to Combustion: Concepts and Applications**, 2nd Edition, McGraw-Hill Inc., New York, New York.

US Department of Energy, 2009, "2008 Annual Energy Review," **DOE/EIA-0384(2008)**.

US Environmental Protection Agency, 2002, "A Comprehensive Analysis of Biodiesel Impacts on Exhaust Emissions," Air and Radiation, **Technical Report EPA420-P-02-001**.

Wade, R.A., Sivathanu, Y. R., and Gore, J.P., 1995, "Soot Volume Fraction and Temperature Properties of High Liquid Loading Spray Flames," **Proceedings Combustion Fundamentals and Applications**, Combustion Institute/ Central and Western States, Mexican National Section, pp. 791-796.

Wang, W.C., Lyons, D.W., Clark, N.N., and Gautam, M., 2000, "Emissions from Nine Heavy Trucks Fueled by Diesel and Biodiesel Blend Without Engine Modification," **Environmental Science and Technology**, Vol. 34, pp. 933-939.

Wang, Y., Holley, A., Andac, M., Egolfopoulos, F., and Tsotsis, T., 2007, "Studies of Combustion Characteristics of Biofuels in Premixed and Non-Premixed Flames," **5th US Combustion Meeting**, Paper No. A18, San Diego, CA.

Weiss, G., Chen, J., and Buchholz, B., 2007, "A Numerical Investigation Into the Anomalous Slight NO_x Increase When Burning Biodiesel: A New Old Theory," **Fuel Processing Technology**, Vol. 88(7), pp. 659-667.

Westbrook, C., Pitz, W., and Curran, H., 2006, "Chemical Kientic Model Study of the Effects of Oxygenated Hydrocarbons on Soot Emissions from Diesel Engines," **Journal of Physical Chemistry**, Vol. 110, pp. 6912-6922.

Westbrook, C., Pitz, W., Herbinet, O., Curran, H., and Silke, E., 2009, "A Comprehensive Detailed Chemical Kinetic Reaction Mechanism for Combustion of n-Alkane Hydrocarbons from n-Octane to n-Hexadecane," **Combustion and Flame**, Vol. 156, pp.181-199.

Yagi, S., and Iino, H., 1962, "Radiation from Soot Particles in Luminous Flames," **Eighth International Symposium on Combustion**, The Combustion Institute, PA, pp. 288-293.

Appendix A
Estimated Uncertainties

Precision (random) and bias (fixed) errors were calculated and presented in the figures of this report as error bars. The precision error was statistically determined based on the sample size and standard deviation of the data points. Bias error was also found based on the calibration error or least count of the instrument used, typically 0.1 – 1% of the full scale value. The overall uncertainty (ω) can be expressed mathematically as:

$$\omega = \sqrt{P^2 + B^2}$$

where P is the precision and B the bias error of the measurements. The precision error was calculated based on the following:

$$P = t_{\alpha/2} \frac{S_x}{\sqrt{n}}$$

where S_x represents the standard deviation of the data points, n is the number of data points, and $t_{\alpha/2}$ the student's t-distribution value for a 95% confidence interval. Typical $t_{\alpha/2}$ values are presented below.

n =	υ =	$t_{\alpha/2}$ for a 95% confidence interval
3	2	4.303
4	3	3.182
5	4	2.776
6	5	2.571
7	6	2.447
8	7	2.365
9	8	2.306

Precision errors were much larger than corresponding bias errors and accounted for most of the uncertainty in the present study. For this reason the measurements were repeated 5 to 9 times and instruments calibrated before use each day. For some cases where multiple uncertainties were present, as in the calculation of the Emission Index, the errors were propagated. Below is a sample of how the error was propagated for the Emission Index of NO.

$$\delta EI_{NO} = \sqrt{\left(\frac{\partial EI_{NO}}{\partial \chi_{NO}}\delta\chi_{NO}\right)^2 + \left(\frac{\partial EI_{NO}}{\partial \chi_{CO}}\delta\chi_{CO}\right)^2 + \left(\frac{\partial EI_{NO}}{\partial \chi_{CO_2}}\delta\chi_{CO_2}\right)^2}$$

where;

$$EI_{NO} = \left(\frac{\chi_{NO}}{\chi_{CO} + \chi_{CO_2}}\right)\left(\frac{N \cdot MW_{NO}}{MW_f}\right)$$

$$\frac{\partial EI_{NO}}{\partial \chi_{NO}} = \left(\frac{1}{\chi_{CO} + \chi_{CO_2}}\right)\left(\frac{N \cdot MW_{NO}}{MW_f}\right)$$

$$\frac{\partial EI_{NO}}{\partial \chi_{CO}} = -\left(\frac{\chi_{NO}}{(\chi_{CO} + \chi_{CO_2})^2}\right)\left(\frac{N \cdot MW_{NO}}{MW_f}\right)$$

$$\frac{\partial EI_{NO}}{\partial \chi_{CO_2}} = -\left(\frac{\chi_{NO}}{(\chi_{CO} + \chi_{CO_2})^2}\right)\left(\frac{N \cdot MW_{NO}}{MW_f}\right)$$

$\delta\chi_{NO}$ = Overall uncertainty (ω) associated with the NO measurements

$\delta\chi_{CO}$ = Overall uncertainty (ω) associated with the CO measurements

$\delta\chi_{CO_2}$ = Overall uncertainty (ω) associated with the CO_2 measurements

The uncertainty associated with the Emission Index of NO is then expressed as:

$$EI_{NO} \pm \delta EI_{NO}$$

Appendix B
Soot Concentration

The volumetric soot concentration measurement was done with the use of the relationship from the application of Beer's Law and Mie's theory as seen in a paper by Yagi and Iino (1962) for a propane-air flame. This relationship has been used by various authors including Bryce et al. (2000) who studied the soot distributions in a diesel-air flame and combustion in a diesel engine. Pickett and Siebers (2004) also used this relationship for a constant volume, high pressure and temperature, constant volume combustion of a diesel fuel jet flame.

$$f_v = \frac{-\ln\left(\frac{I_o}{I_s}\right)\cdot\lambda}{k_\lambda \cdot \delta}$$

where;

I_s = Incident laser intensity

I_o = Attenuated laser intensity

k_λ = Spectral extinction coefficient based on the refractive indices of the soot

λ = He:Ne laser wavelength

δ = Flame thickness

Using the equation for soot volume fraction for diesel fuel at $\phi = 7$ along the centerline.

I_s = 3.88 mW

I_o = 2.65 mW

δ = 2.72 cm

λ = 633 nm

k_λ = 4.16

$$f_v = -\ln\left(\frac{2.65}{3.88}\right)\cdot\frac{633 \text{ x } 10^{-9}}{4.16\cdot 0.027} = 2.14 \text{ E} - 6$$

Appendix C
Reynolds Number Approximation

The mixture flow rates were kept so as to maintain laminar flow hence a low Reynold's number (Re) at the exit of the injector. Densities and viscosities for the vaporized fuel and air mixture were calculated with data from Maxwell (1968) and the equations shown below from Kanury (1975).

$$\mu_{mixture} = \sum_{i=1}^{n} \frac{\chi_i \mu_i}{\sum_{j=1}^{n} \chi_j \Omega_{ij}}$$

$$\Omega_{ij} = \frac{1}{\sqrt{8}} \left(1 + \frac{MW_i}{MW_j}\right)^{-1/2} \left[1 + \left(\frac{\mu_i}{\mu_j}\right)^{1/2} \left(\frac{MW_j}{MW_i}\right)^{1/4}\right]^2$$

where;

χ	=	mole fraction
$\mu_{mixture}$	=	dynamic viscosity
MW	=	molecular weight

For dodecane and air at the preheat temperature of 700K at $\phi = 7$

	Dodecane	Air
MW	170	28.85
Density (kg/m^3)	3.02	0.49
μ ($N\text{-}s/m^2$)	1.09×10^{-5}	$3.39\ 10^{-5}$

Ω_{ij}		i =1	i =2
		Dodecane	Air
j = 1	Dodecane	1	4.59
j = 2	Air	0.25	1

From the stoichiometric balance:

$$C_{12}H_{26} + 18.5\left(3.76\ N_2 + O_2\right) \rightarrow 12\ CO_2 + 13\ H_2O + 69.56\ N_2$$

Thus for an equivalence ratio of 7:

$$C_{12}H_{26} + 2.64\left(3.76\ N_2 + O_2\right) \rightarrow \text{Combustion Products}$$

The mole fractions of the species are:

$$\chi_{\text{dodecane}} = \frac{1}{1 + 2.64 \cdot (4.76)} = 0.07$$

$$\chi_{\text{air}} = \frac{2.64 \cdot 4.76}{1 + 2.64 \cdot (4.76)} = 0.93$$

The viscosity of the mixture is then:

$$\mu_{\text{mixture}} = \frac{0.07 \cdot \left(1.09\ \text{x}\ 10^{-5}\right)}{0.07 \cdot (1) + 0.93 \cdot (0.25)} + \frac{0.93 \cdot \left(3.39\ \text{x}\ 10^{-5}\right)}{0.07 \cdot (4.59) + 0.93 \cdot (1)} = 2.77\ \text{x}\ 10^{-5}\ \text{N} - \text{s/m}^2$$

Density of the mixture ($\rho_{mixture}$) is expressed in the equation below.

$$\rho_{mixture} = \sum_{i=1}^{n} \chi_i \rho_i = \chi_{dodecane} \cdot \rho_{dodecane} + \chi_{air} \cdot \rho_{air} = 0.66$$

Dynamic viscosity was then calculated:

$$\upsilon_{mixture} = \frac{\mu_{mixture}}{\rho_{mixture}} = \frac{2.77 \text{ x } 10^{-5}}{0.66} = 4.19 \text{ x } 10^{-5} \text{ m}^2 / \text{s}$$

Given that the exit velocity of the dodecane - air mixture at $\phi = 7$ is 1.32 m/s (see Appendix E) thus Reynolds number for this mixture was approximated as:

$$\text{Re} = \frac{u_{exit} \cdot \text{exit diameter}}{\upsilon_{mixture}} = \frac{1.32 \cdot 0.0095}{4.19 \text{ x } 10^{-5}} = 300$$

Appendix D
Flame Temperature Correction

Due to radiative, convective, and conductive heat losses the temperature read from the thermocouple bead was less than the true flame temperatures. Thus it was necessary to correct for these losses. This was done with the use of the energy balance equation for the thermocouple bead presented below (Jha et al., 2008, Hariharan, 2004, Chinthamony, 2005).

$$h\, A_b \left(T_g - T_b\right) = \frac{k_w\, A_w \left(T_b - T_\infty\right)}{L} + \sigma \varepsilon A_b \left(T_b^4 - T_\infty^4\right)$$

where;

A_b = Surface area of the bead = $\pi\, d^2$

A_w = Cross-sectional area of the thermocouple wires = $\frac{\pi \left(\text{wire diameter}\right)^2}{4}$

h = Convective heat transfer coefficient between the thermocouple bead and surrounding gases

k_w = Thermal conductivity of the thermocouple wire

L = Length of the thermocouple wire

T_b = Uncorrected thermocouple bead temperature

T_g = True flame temperature

T_∞ = Cold junction temperature or room temperature

σ = Stefan-Boltzmann constant

ε = Emissivity of the thermocouple bead wire

The heat transfer coefficient between the thermocouple bead and surrounding gas was calculated using the following relationships. The diameter of the bead was measured in-house and was found to be 0.25 mm.

$$Nu = \frac{h \cdot \text{bead diameter}}{k_{air}} = 2 + \left(0.4 \cdot Re^{0.5} + 0.06 \cdot Re^{0.67}\right) \cdot Pr^{0.4}$$

$$Re = \frac{u \cdot \text{bead diameter}}{\upsilon_{mix}}$$

where;

k_{air} = Thermal conductivity of air at measured flame temperature

Pr = Prandtl number

u = Burner exit velocity

υ_{mix} = Viscosity of air-fuel mixture

Appendix E
Sample Calculations

Stoichiometric Equations:

$$C_xH_{2y}O_{2z} + a\,(O_2 + 3.76N_2) \rightarrow xCO_2 + y\,H_2O + (3.76a)\,N_2$$

$$a = x + \frac{y}{2} - z$$

$$AF_{stoic} = \frac{a(32 + 3.76 \cdot 28)}{12x + 2y + 32z}$$

For diesel fuel ($C_{14.4}H_{24.9}$):

$$a = 14.4 + \frac{12.45}{2} - 0 = 20.625$$

$$AF_{stoic} = \frac{20.625(32 + 3.76 \cdot 28)}{12 \cdot (14.4) + 24.9 + 32 \cdot (0)} = 14.32$$

For CME ($C_{19}H_{36}O_2$):

$$a = 19 + \frac{18}{2} - 1 = 27$$

$$AF_{stoic} = \frac{27(32 + 3.76 \cdot 28)}{12 \cdot (19) + 36 + 32 \cdot (1)} = 12.52$$

Jet Exit Velocity of Burner:

$$u_{exit} = \frac{\dot{m}_{mix}}{\rho_{mix} \cdot A_{Exit}} = \frac{\dot{m}_{air} + \dot{m}_{fuel}}{\rho_{mix} \cdot A_{Exit}}$$

Given:

$\dot{m}_{air} = 4.2 \text{ x } 10^{-5}$ kg/s

$\dot{m}_{fuel} = 1.99 \text{ x } 10^{-5}$ kg/s

$\rho_{mix} = 0.66$ kg/m^3

$A_{Exit} = \frac{\pi \cdot 0.0095^2}{4} = 7.09 \text{ x } 10^{-5}$ m^2

$$u_{exit} = \frac{\left(4.2 \text{ x } 10^{-5}\right) + \left(1.99 \text{ x } 10^{-5}\right)}{0.66 \cdot \left(7.09 \text{ x } 10^{-5}\right)} = 1.32 \text{ m/s}$$

Emission Index Calculation:

$$EI_{NO} = \left(\frac{\chi_{NO}}{\chi_{CO} + \chi_{CO_2}}\right)\left(\frac{N \cdot MW_{NO}}{MW_f}\right) \cdot 1000$$

Given:

Concentration of NO = 27 ppm

Concentration of CO_2 = 0.9 %

Concentration of CO = 8 ppm

MW_f = 296 kg/kmol MW_{CO} = 28 kg/kmol

MW_{NO} = 30 kg/kmol MW_{CO_2} = 44 kg/kmol

N = Number of moles of carbon in a mole of fuel = 19

$\chi_{NO} = \frac{27}{1 \text{ x } 10^6} = 2.7 \text{ x} 10^{-5}$

$\chi_{CO_2} = \frac{0.9}{100} = 0.009$

$\chi_{CO} = \frac{8}{1 \text{ x } 10^6} = 8 \text{ x } 10^{-6}$

$$EI_{NO} = \left(\frac{2.7 \text{ x } 10^{-5}}{\left(8 \text{ x } 10^{-6}\right) + \left(0.009\right)}\right)\left(\frac{19 \cdot 30}{296}\right) \cdot 1000 = 5.77 \frac{g_{NO}}{kg_{\text{fuel burnt}}}$$

Radiative Fraction of Heat Released:

$$F = \frac{4\pi \ell^2 \cdot q_{corrected}}{\dot{m} \cdot LHV_{fuel}}$$

$$q_{corrected} = q_{total} - q_{back}$$

Each test was run for a time duration of 3 minutes with a sampling rate of 2 Hz, allowing the heat flux to reach a steady value. The data was averaged over this sample time. Next, after the flame was extinguished the background radiation (q_{back}) was obtained and used for correction of the total radiation ($q_{corrected}$). Some sample values obtained for CME at $\phi = 7$ are presented here for the calculation.

q_{total}	= 157.5 W/m^2	q_{back}	= 85.7 W/m^2
ℓ	= 50 cm	$\dot{m}$	= 2.35 x 10^{-5} kg/s
LHV	= 37.4 MJ/kg		

$$q_{corrected} = 157.5 - 85.7 = 71.8 \text{ W/m}^2$$

$$F = \frac{4\pi (0.5)^2 \cdot (71.8)}{(2.35 \text{ x } 10^{-5}) \cdot (37.4 \text{ x } 10^{6})} = 0.26$$

Appendix F
Nomenclature

English

A_i	Pre-exponential factor
B_i	Temperature exponent
AF	Air to fuel ratio
c_p	Specific heat at constant pressure
D	Binary mass diffusion coefficient
EI	Emission index
f_v	Soot volume fraction
E	Total energy
E_i	Activation energy
F	Radiative fraction of heat released
F_L	Visible Flame Length
f_v	Soot Volume Fraction
G	Gibb's function
g	Gravity
g_k	Partial molar Gibb's function
h	Enthalpy of formation
I_o	Attenuated laser intensity
I_s	Incident laser intensity
K	Total number of species
k	Thermal conductivity
k_{fi}	Forward rate constant
k_{ri}	Reverse rate constant
k_λ	Spectral extinction coefficient
ℓ	Distance from flame centerline to pyrheliometer
LHV	Lower heating value
$\dot{m}$	Mass flow rate of liquid fuel
$\dot{m}_o$	Mass through flow rate
MW	Molecular weight
N	Number of carbon atoms
N_k	Number of moles
N_o	Number of chemical species
P	Static pressure
$q_{background}$	Background radiation
$q_{corrected}$	Corrected total radiation
q_{total}	Total flame radiation
R	Universal gas constant
R_r	Source energy due to chemical reaction
Re	Reynolds number
u	Bulk velocity
S	Net rate of production of species by chemical reaction

t	Time
T	Temperature
Y	Mass fraction

Greek

χ	Mole fraction
δ	Flame thickness
ϕ	Equivalence ratio
η	Real part of soot refractive index
κ	Imaginary part of soot refractive index
λ	Wavelength
μ	Dynamic viscosity
ρ	Density
τ	Stress tensor
υ	Velocity vector
ω	molar rate of production

Acronyms

BBO	Beta Barium Borate
CME	Canola methyl ester
FDO	Frequency doubler option
ICCD	Intensified charged coupled device
MS	Methyl stearate
OPO	Optical Parametric Oscillator
PLIF	Planar Laser Induced Fluorescence
SME	Soy methyl ester